NASA/TM—2006–214137

Solar Sentinels: Report of the Science and Technology Definition Team

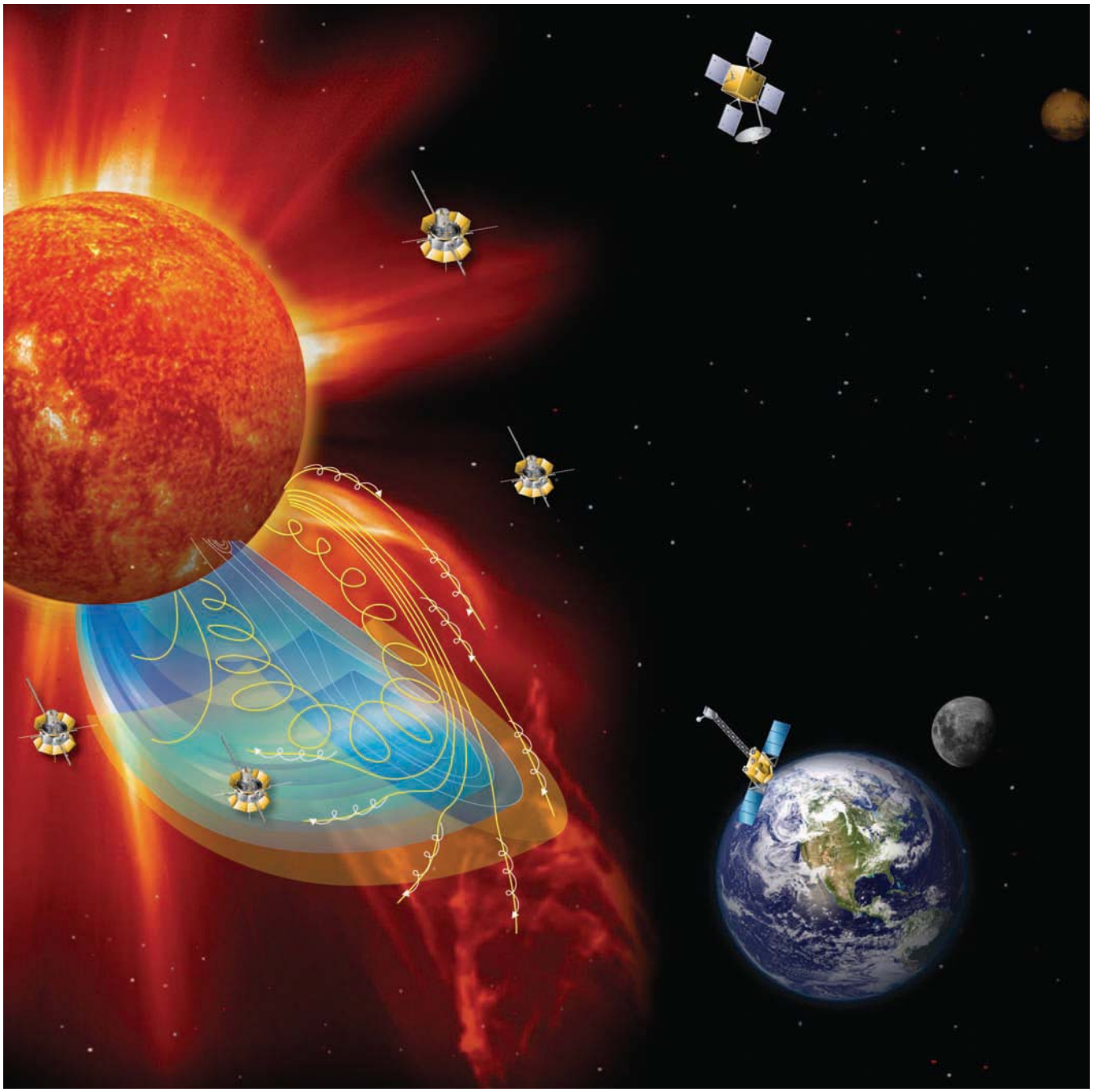

August 2006

The NASA STI Program Office … in Profile

Since its founding, NASA has been dedicated to the advancement of aeronautics and space science. The NASA Scientific and Technical Information (STI) Program Office plays a key part in helping NASA maintain this important role.

The NASA STI Program Office is operated by Langley Research Center, the lead center for NASA's scientific and technical information. The NASA STI Program Office provides access to the NASA STI Database, the largest collection of aeronautical and space science STI in the world. The Program Office is also NASA's institutional mechanism for disseminating the results of its research and development activities. These results are published by NASA in the NASA STI Report Series, which includes the following report types:

- TECHNICAL PUBLICATION. Reports of completed research or a major significant phase of research that present the results of NASA programs and include extensive data or theoretical analysis. Includes compilations of significant scientific and technical data and information deemed to be of continuing reference value. NASA's counterpart of peer-reviewed formal professional papers but has less stringent limitations on manuscript length and extent of graphic presentations.
- TECHNICAL MEMORANDUM. Scientific and technical findings that are preliminary or of specialized interest, e.g., quick release reports, working papers, and bibliographies that contain minimal annotation. Does not contain extensive analysis.
- CONTRACTOR REPORT. Scientific and technical findings by NASA-sponsored contractors and grantees.
- CONFERENCE PUBLICATION. Collected papers from scientific and technical conferences, symposia, seminars, or other meetings sponsored or cosponsored by NASA.
- SPECIAL PUBLICATION. Scientific, technical, or historical information from NASA programs, projects, and mission, often concerned with subjects having substantial public interest.
- TECHNICAL TRANSLATION. English-language translations of foreign scientific and technical material pertinent to NASA's mission.

Specialized services that complement the STI Program Office's diverse offerings include creating custom thesauri, building customized databases, organizing and publishing research results . . . even providing videos.

For more information about the NASA STI Program Office, see the following:

- Access the NASA STI Program Home Page at http://www.sti.nasa.gov/STI-homepage.html
- E-mail your question via the Internet to help@sti.nasa.gov
- Fax your question to the NASA Access Help Desk at (301) 621-0134
- Telephone the NASA Access Help Desk at (301) 621-0390
- Write to:
  NASA Access Help Desk
  NASA Center for AeroSpace Information
  7121 Standard Drive
  Hanover, MD 21076-1320

NASA/TM—2006–214137

Solar Sentinels: Report of the Science and Technology Definition Team

National Aeronautics and
Space Administration

Goddard Space Flight Center
Greenbelt, Maryland 20771

August 2006

Acknowledgments

Individuals from a number of institutions have helped with this study, and the members of the Sentinels Science and Technology Definition Team gratefully acknowledge their contributions.

The Inner Heliospheric Sentinels Engineering Team at the Johns Hopkins University Applied Physics Laboratory was led by Richard Conde and, during earlier stages of the study, by Paul Adamsen II. The JHU/APL team included David Artis, Robert Bokulic, George Dakermanji, Wayne Dellinger, Jack Ercol, Karl Fielhauer, Ted Hartka, Jeff Kelley, Karen Kirby, Binh Le, Jeff Lees, Barbara Leary, Sharon Ling, Perry Malouf, Dave Napolillo, Dave Persons, John Troll, and Bob Wallis. Greg Marr, Linda Kay-Bunnell, and John P. Downing (all at Goddard Space Flight Center) provided additional mission design support for the IHS study.

The Farside Sentinel implementation study conducted at the Jet Propulsion Laboratory was led by Jim Chase, whose team included Juan Ayon, Dick Cowley, Janine Daughters, Sal Distefano, Luke Dubord, Jerry Flores, Mike Fong, Bob Gustavson, Dave Hansen, Gerhard Klose, Ed Mettler, Bob Miyake, Vince Randolph, Yu-wen Tung, Chen-wan Yen, and Xiaoyan Zhou.

The concept for the Near-Earth Sentinel was developed by teams from the Harvard-Smithsonian Center for Astrophysics (UVSC) and the Naval Research Laboratory (WIFCO). The Harvard team included John L. Kohl, Steven R. Cranmer, John C. Raymond, Adriaan van Ballegooijen, Leonard Strachan, Larry D. Gardner, and Peter S. Daigneau; the NRL team included Dennis Socker of NRL and Qian Gong and Robert Hagood, both of Swales Aerospace.

Gang Li and Gary Zank of the University of California at Riverside supplied needed text on modeling the acceleration and transport of energetic particles. Management support for the study was provided by Regan Howard (Orbital Sciences Corporation) and Gifford P. Moak (GSFC). Jennifer Rumburg (GSFC) and Brian Grimm (Paper Cardinal Design) prepared attractive graphics, and Margaret Morris (JHU/APL) and the Technical Communications Group at JHU/APL provided outstanding editorial and production support.

Available from:

NASA Center for AeroSpace Information
7121 Standard Drive
Hanover, MD 21076-1320
Price Code: A17

National Technical Information Service
5285 Port Royal Road
Springfield, VA 22161
Price Code: A10

Table of Contents

Living With a Star Sentinels Science and Technology Definition Team

R. P. Lin, *Chairman*
University of California, Berkeley
Berkeley, CA 94730, U.S.A.

A. Szabo, *Study Scientist*
NASA Goddard Space Flight Center
Greenbelt, MD 20771, U.S.A.

S. K. Antiochos
Naval Research Laboratory
Washington, DC 20375, U.S.A.

S. D. Bale
University of California, Berkeley
Berkeley, CA 94730, U.S.A.

J. M. Davila
NASA Goddard Space Flight Center
Greenbelt, MD 20771, U.S.A.

A. B. Galvin
University of New Hampshire
Durham, NH 03824, U.S.A.

D. K. Haggerty
The Johns Hopkins University
Applied Physics Laboratory
Laurel, MD 20723, U.S.A.

S. W. Kahler
Air Force Research Laboratory
Hanscom AFB, MA 01731, U.S.A.

J. E. Mazur
The Aerospace Corporation
Chantilly, VA 20151, U.S.A.

R. A. Mewaldt
California Institute of Technology
Pasadena, CA 91125, U.S.A.

N. Murphy
Jet Propulsion Laboratory
Pasadena, CA 91109, U.S.A.

G. D. Reeves
Los Alamos National Laboratory
Los Alamos, NM 87545, U.S.A.

P. Riley
SAIC
San Diego, CA 92121, U.S.A.

J. M. Ryan
University of New Hampshire
Durham, NH 03824, U.S.A.

K. Schrijver
Lockheed Martin Solar and Astrophysics Laboratory
Palo Alto, CA 94304, U.S.A.

R. Schwenn
Max-Planck-Institut für Sonnensystemforschung
Katlenburg-Lindau, 37191 Germany

A. J. Tylka
Naval Research Laboratory
Washington, DC 20375, U.S.A.

R. F. Wimmer-Schweingruber
Institut für experimentelle u. angewandte Physik
Christian-Albrechts-Universität zu Kiel
Kiel, 24188 Germany

T. H. Zurbuchen
University of Michigan
Ann Arbor, MI 48109, U.S.A.

Support Staff and Ex Officio Members

K. A. Potocki, *APL LWS Program Manager*
The Johns Hopkins University
Applied Physics Laboratory
Laurel, MD 20723, U.S.A.

R. F. Conde, *APL Engineering Team Lead*
The Johns Hopkins University
Applied Physics Laboratory
Laurel, MD 20723, U.S.A.

H. M. Maldonado, *Study Lead*
NASA Goddard Space Flight Center
Greenbelt, MD 20771, U.S.A.

W. S. Lewis, *Technical Writing Support*
Southwest Research Institute
San Antonio, TX 78228, U.S.A.

M. DiJoseph, *Project Support*
NASA Goddard Space Flight Center
Greenbelt, MD 20771, U.S.A.

M. Guhathakurta, *LWS Program Scientist*
NASA Headquarters
Washington, DC 20546, U.S.A.

C. St. Cyr, *LWS Senior Scientist*
NASA Goddard Space Flight Center
Greenbelt, MD 20771, U.S.A.

H. Opgenoorth, *ILWS Chair*
European Space Agency
Noordwijk, The Netherlands

R. D. Zwickl
NOAA Space Environment Center
Boulder, CO 80303, U.S.A.

Executive Summary: The Living With a Star Sentinels Mission

NASA's Sentinels mission is a multispacecraft mission that will study (1) the acceleration and transport of solar energetic particles (SEPs) and (2) the initiation and evolution of coronal mass ejections (CMEs) and interplanetary shocks in the inner heliosphere. As presently envisioned, the Sentinels mission comprises (1) a constellation of four identically instrumented Inner Heliospheric Sentinels to make in-situ measurements of the plasma, energetic particle, and fields environment as close to the Sun as 0.25 AU as well as multipoint remote-sensing observations of solar X-ray, radio, gamma-ray, and neutron emissions; (2) a Near-Earth Sentinel in Sun-synchronous orbit for ultraviolet and white-light observations of the corona; and (3) a Farside Sentinel in heliocentric orbit at 1 AU to measure the photospheric magnetic field from positions 60° to 120° ahead of the Earth. During the 3-year nominal mission, Sentinels observations will be supplemented by observations both from other spacecraft such as the Solar Terrestrial Relations Observatories (STEREO), the Solar Dynamics Observatory (SDO), and Solar Orbiter and from ground-based observatories such as the proposed Advanced Technology Solar Telescope as well as existing radio and optical telescopes. Theory and modeling will play an integral role in the Sentinels mission during both the development and operations phases of the mission.

Sentinels is a key component of NASA's Living With a Star (LWS) program and as such is designed to advance our knowledge and understanding of those processes and phenomena in the space environment that can adversely affect life and society. ***The Sentinels mission is of particular importance to efforts to characterize, understand, and eventually forecast the radiation environment that will be encountered during human expeditions to the Moon and Mars.***

This summary and the following report describe the results of an intensive 2-year study by the Sentinels Science and Technology Definition Team (STDT) to define the science objectives, measurement requirements and observational strategies, and mission design for the Sentinels mission. The STDT worked closely with engineering teams at The Johns Hopkins University Applied Physics Laboratory and NASA's Jet Propulsion Laboratory

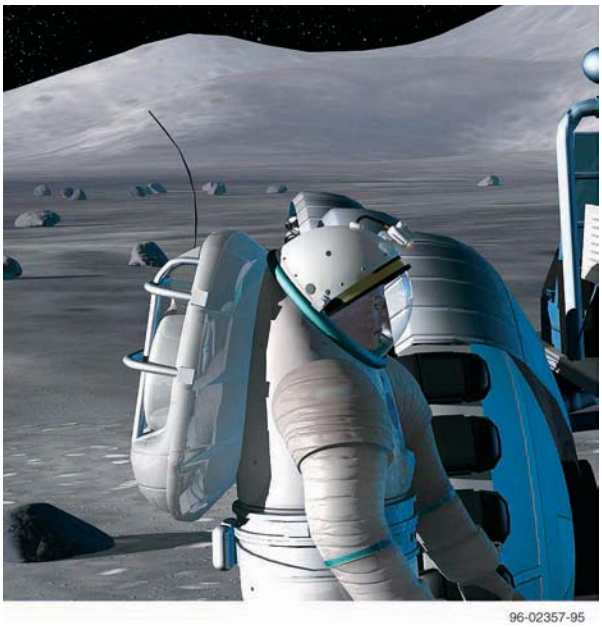

96-02357-95

Intense solar energetic particle (SEP) events will present a serious health hazard for astronauts on future expeditions to the Moon and Mars. Sentinels science will enable the development of a forecasting capability for SEP events.

to ensure that ***the Sentinels mission described in this report can achieve the scientific objectives established by the STDT and can be implemented with no new technology development.***

Energetic Events in the Inner Heliosphere: Sentinels Science Objectives

With ion energies up to tens of gigaelectron volts and electron energies up to hundreds of megaelectron volts, solar energetic particles (SEPs) are one of the principal sources of space radiation and represent a serious threat to both spacecraft systems and astronauts. For example, the Japanese Mars probe Nozomi was crippled by penetrating radiation during an intense SEP event in April 2002, and the mission was eventually lost as a result. Fortunately, no astronauts are known to have suffered from acute radiation sickness as a result of exposure to SEPs. However, studies have shown that the health risk is real and serious. An astronaut caught on the surface of the Moon during the large SEP event of August 1972 and protected only by a space suit could have experienced acute radiation syndrome effects, including severe skin damage, nausea or vomiting, and blood count changes, as well as the early development of cataracts. The radiobiological effects of SEP exposure can be mission-threatening and, in

the case of an extreme event such as the 1859 Carrington event, could even be fatal.[1]

SEPs are produced in association with both solar flares and coronal mass ejections (CMEs). Flare-related or "impulsive" SEP events differ in certain key characteristics from CME-related or "gradual" events. Impulsive events have durations of hours, high electron/proton ratios, and are characterized by $^3He/^4He$, Fe/O, and Fe/C ratios appreciably greater than average coronal and solar wind values, as well as by high average Fe charge states. Gradual events are associated with fast CMEs, occur over a wide longitude range (~100° to 180°), last for days, have low electron/proton ratios, and show low average Fe charge states.

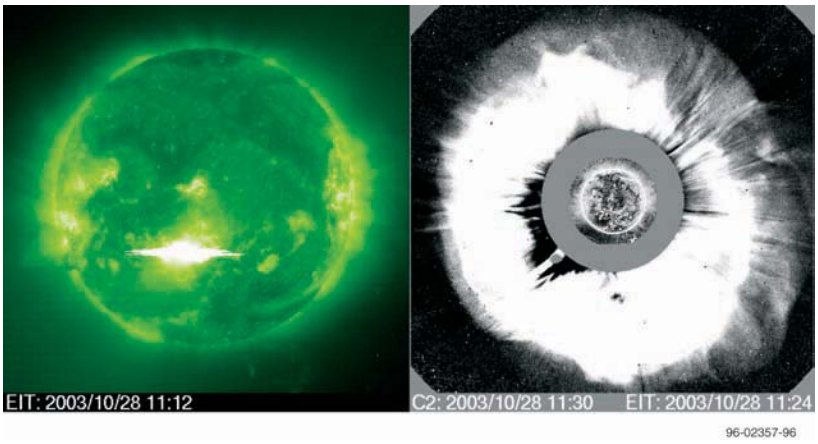

A powerful (X17) flare (left) and halo CME (right) were observed by SOHO during the extreme space weather events of October–November 2003. The SEP event produced by the 28 October solar events was one of the largest observed during the last two solar cycles.

Although the two-class paradigm is a useful classification scheme, recent observations have shown that the distinction between impulsive and gradual events is not as clear-cut as it may seem. While the energetic particles in the most intense events appear to be accelerated predominantly by a CME-driven shock, in many large gradual events enhanced ^3He and Fe abundances as well as higher-than-expected Fe charge states are observed. Do these impulsive-event particles come directly from a flare associated with the CME, or are they relics from previous impulsive events that populate the inner heliosphere and then serve as a seed population to be re-accelerated to higher energy in subsequent gradual events? What are the relative roles of flare acceleration and shock acceleration in such events? Where and when are the particles accelerated at the Sun? A major science objective of the Sentinels mission is ***to determine the roles of CMEs, flares, and other processes in accelerating energetic particles***.

The properties of SEPs accelerated at CME-driven shocks are highly variable. This variability is likely the result of the interplay of many factors, including the composition and distribution of the seed population, the properties of the CME and shock, and the preconditioning of the inner heliosphere by earlier events. Understanding the causes of SEP variability in large gradual events is an essential condition for the development of predictive models. Thus a second major Sentinels objective is ***to identify the conditions that determine when CME-driven shocks accelerate energetic particles.***

The transport of SEPs from their acceleration site through the inner heliosphere to 1 AU and beyond is a problem of critical importance for understanding and eventually predicting SEP events. SEP transport is a complex phenomenon involving a variety of processes: field-line wandering, pitch-angle scattering by turbulent magnetic fluctuations, magnetic focusing by the radially diverging heliospheric magnetic field, adiabatic cooling, and solar wind convection. In the case of shock-accelerated events, the propagation and evolution of the shock must also be taken into account. A particular source of uncertainty in our understanding of SEP propagation is a lack of knowledge of the particle scattering mean free path inside 1 AU. As its third objective, Sentinels will ***determine how energetic particles are transported from their acceleration site and distributed in radius, longitude, and time.***

In order to provide useful warning of SEP events, it is necessary to be able to predict the onset of a CME/eruptive flare from observations of solar conditions. Developing this capability requires achieving a deep physical understanding of the CME/eruptive flare onset. What solar conditions lead to CME onset? By what mechanism is stored

[1]L.W. Townsend, Implications of the space radiation environment for human exploration in deep space, *Radiat. Prot. Dosimetry*, **115**, 44, 2005.

Sentinels Science Goals and Objectives

I. Understand and Characterize the Sources, Acceleration, and Transport of Solar Energetic Particles

Determine the roles of CME-driven shocks, flares, and other processes in accelerating energetic particles
- When and where are energetic particles accelerated by the Sun?
- How are energetic particles observed at the Sun related to those observed in the interplanetary medium?
- What conditions lead to the jets/narrow CMEs associated with impulsive SEP events?
- What physical processes accelerate SEPs?

Identify the conditions that determine when CME-driven shocks accelerate energetic particles
- What are the seed populations for shock-accelerated SEPs and how do they affect SEP properties?
- How do CME/shock structure and topology as well as ambient conditions affect SEP acceleration?

Determine how energetic particles are transported from their acceleration site and distributed in radius, longitude, and time
- What processes scatter and diffuse SEPs both parallel and perpendicular to the mean heliospheric magnetic field?
- What are the relative roles of scattering, solar wind convection, and adiabatic cooling in SEP event decay?

II. Understand and Characterize the Origin, Evolution, and Interaction of CMEs, Shocks, and Other Geoeffective Structures

Determine the physical mechanisms of eruptive events that produce SEPs
- What solar conditions lead to CME onset?
- How does the pre-eruption corona determine the SEP-effectiveness of a CME?
- How close to the Sun and under what conditions do shocks form?

Determine the multiscale plasma and magnetic properties of ICMEs and shocks
- How does the global 3D shape of ICMEs/shocks evolve in the inner heliosphere?
- How does CME structure observed at the Sun map into the properties of interplanetary CMEs?

Determine how the dynamic inner heliosphere shapes the evolution of ICMEs
- How is the solar wind in the inner heliosphere determined by coronal and photospheric structure?
- How do ICMEs interact with the pre-existing heliosphere?
- How do ICMEs interact with each other?

magnetic energy explosively released in the CME/eruptive flare? The fourth major Sentinels objective is ***to determine the physical mechanisms of eruptive events that produce SEPs.*** Because CMEs are the major drivers of space weather at Earth, as well as the primary sources of intense SEP events, this knowledge is also essential for our ability to forecast major geomagnetic disturbances like the storms of October–November 2003.[2] Such severe space weather events can interfere with communications and navigations systems, disrupt satellite operations, and cause electric utility blackouts.

Development of a forecasting capability also requires a knowledge and understanding of what the properties of an interplanetary CME (ICME) are, how they are related to the structures observed at the Sun, how they evolve during the ICME's transit to 1 AU (and beyond), and how they are affected in their evolution by the density and velocity structures of the background solar wind, as well as by interactions with other transients. Thus the fifth and sixth objectives of the Sentinels mission are ***to determine the multiscale plasma and magnetic properties of ICMEs and shocks*** and ***to determine how the dynamic inner heliosphere shapes the evolution of ICMEs.***

Measurement and Observational Requirements

To achieve the Sentinels science objectives, a combination of in-situ measurements and remote-sensing observations is required, although not necessarily from the same platforms. Required in-situ measurements include high- and low-energy ion energy spectra and composition; energetic electrons and protons; suprathermal and energetic (up to

[2]NOAA, *Intense Space Weather Storms October 10–November 07, 2003*, April 2004.

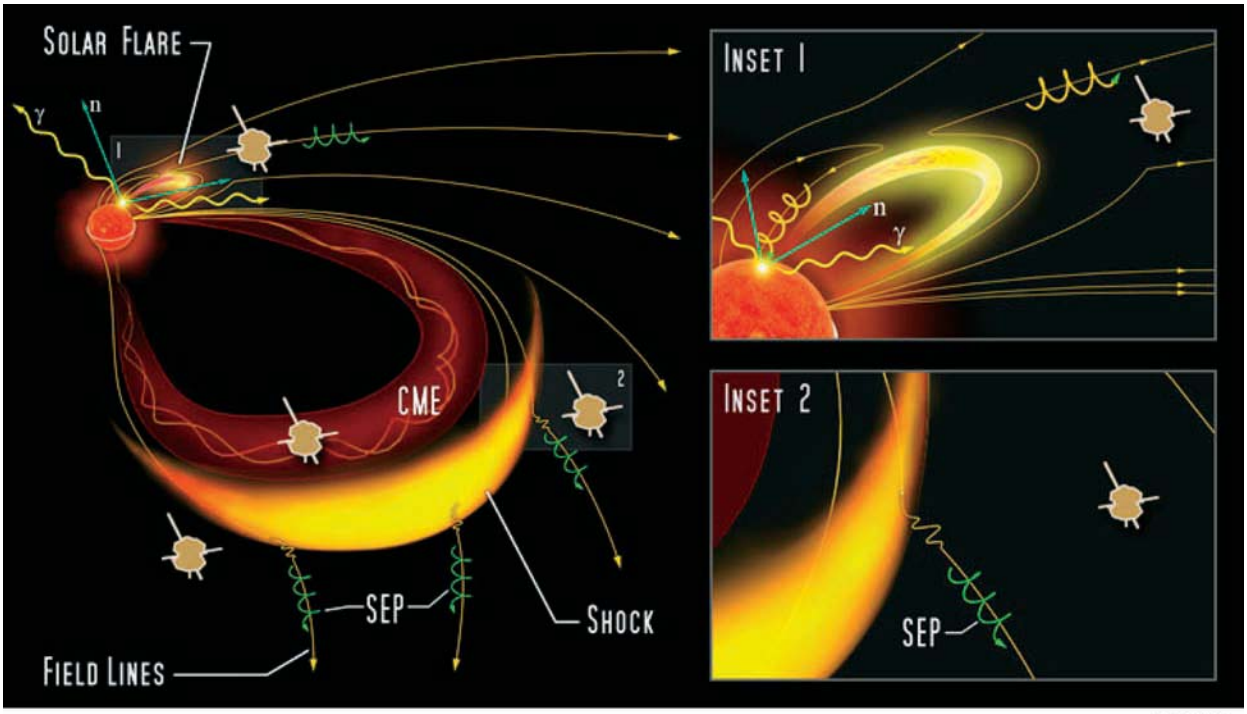

A cartoon demonstrating the need for multiple in-situ observations of SEPs in the inner heliosphere. Simultaneous observations of magnetic field lines connecting back to flare sites (inset 1) and to shock fronts driven by ICMEs (inset 2) are required to determine the relative importance of the associated acceleration processes.

hundreds of keV/nucleon) ion charge states; suprathermal electrons; solar wind ion distributions, composition, and charge state; solar wind electrons; and DC and AC magnetic fields. These measurements are needed to characterize SEPs, their seed populations, the plasmas and fields of the associated transients, and the environment in which they propagate. To characterize the spatial and temporal variations in the SEP spectra and elemental abundances and to study the evolving global structure of ICMEs and shocks as they propagate through the inner heliosphere, simultaneous in-situ measurements should be made from at least four locations, separated in longitude and/or radial distance. Moreover, the in-situ measurements should be made as deep within the inner heliosphere as possible, within 1 to 2 scattering mean free paths (i.e., at radial distances inside 0.35 AU), thus minimizing transport effects and allowing the characteristics of freshly accelerated SEPs and the associated fast shocks, waves, and ICMEs to be determined before significant evolution has occurred. It is desirable that as many SEP events as possible, especially gradual events, be observed within 0.35 AU in order to be able to determine the source of the SEPs and the physics of the acceleration mechanisms. Optimally, the inner heliospheric portion of the Sentinels mission should be flown around solar maximum, when the greatest number of SEP events occur. However, even if this phase of the mission occurs near solar minimum, a statistically meaningful sample of SEP events would be observed.

Critical remote-sensing observations include hard/soft X-rays; neutrons and gamma-rays; radio bursts (type II and III); coronal ultraviolet (UV) and white-light emissions; and photospheric magnetic fields. Observations of radio, X-ray, and gamma-ray emissions and of neutrons in the inner heliosphere will provide crucial information about the location and height of accelerated electrons and ions near the Sun, and combined X-ray, radio, and in-situ electron measurements will allow direct tracing of magnetic field structure and connectivity. UV spectroscopy is necessary to determine plasma conditions in the SEP acceleration region in the corona, while white-light coronagraph observations are needed to observe the onset and initial acceleration of CMEs and to track the evolution of ICMEs out to heliocentric distances

of 0.3 AU, where they can be detected directly. This wide field of view will allow the in-situ ("ground truth") measurements of ICMEs and shocks made inside 0.3 AU to be related to the structure and internal topology of ICMEs (and other coronal structures) imaged by coronagraphs. Measurements of photospheric magnetic fields at heliolongitudes not observable from Earth are needed to provide more realistic boundary conditions for accurate modeling of the heliosphere.

Remote-sensing observations of coronal UV and white-light emissions as well as those of the photospheric magnetic field can be made from spacecraft located at 1 AU. Radio, X-ray, and neutron/gamma ray observations will be made from the inner heliospheric platforms, which will allow stereoscopic and limb occultation measurements to be made, as well as the first-ever measurements of solar neutrons with energies below 10 MeV.

Mission Implementation

The baseline Sentinels mission recommended by the STDT consists of three flight elements: the ***Inner Heliospheric Sentinels (IHS)***, four spin-stabilized spacecraft in elliptical heliocentric orbit with perihelia at ~0.25 AU and aphelia at ~0.75 AU; a 3-axis stabilized ***Near-Earth Sentinel (NES)*** in Sun-synchronous orbit at 1 AU; and a small ***Far-side Sentinel (FSS***) that drifts slowly away from Earth in a heliocentric orbit at 1 AU. The four IHS spacecraft will be identically instrumented to make both the in-situ particles and fields measurements listed above and the remote-sensing observations of radio bursts and X-ray, gamma ray, and neutron emissions. NES will carry a UV spectroscopic coronagraph to determine the physical conditions and mechanisms that govern SEP acceleration near the Sun (1.2 to ~10 R_S), and a white-light coronagraph suite to provide inner-field (1.3 to 4 R_S) and wide-field (4 to 30 R_S) coverage. FSS will be equipped with a simple filter-based magnetograph to provide measurements of the photospheric magnetic field from longitudinal locations between 60° and 180° ahead of the Earth.

The STDT recommends that the Sentinels mission be implemented in stages. The IHS will be developed and launched first, preferably near solar maximum (~2012) to maximize the number of SEP events detected in the inner heliosphere and to provide critical overlap with SDO to determine the conditions for initiation of the flares/fast CMEs that lead to SEP events. NES would be developed in time to have overlapping coverage with IHS to study the coronal acceleration process and the Sun-heliosphere connection. This schedule would also likely result in an overlap with ESA's highly complementary Solar Orbiter mission (planned launch in 2015), which will provide both imaging of the Sun and in-situ measurements, initially from the ecliptic while nearly co-rotating with the Sun and later from higher latitudes. The FSS launch should be timed to provide overlap with Solar Orbiter, since near-Earth ground or space-based magnetograph measurements are expected to be continuously available.

The baseline mission concept for the IHS component of the Sentinels mission calls for four spacecraft to be launched on a single launch vehicle and, through the use of multiple Venus gravity assists, to be placed into slightly different, near-ecliptic heliocentric orbits of approximately 0.25×0.74 AU. The motion of the four IHS spacecraft relative to one another caused by differences in the perihelia and periods of the final heliocentric orbits will result in a number of scientifically desirable orbital configurations, with the spacecraft distributed at different radial and azimuthal positions to make the multi-point measurements discussed above. The IHS orbit has been designed to ensure adequate dwell time close to the Sun.

Sentinels Strawman Payloads	
Inner Heliospheric Sentinels	
High Energy Ion Composition Analyzer	Solar Wind Electron Instrument
Low Energy Ion Composition Analyzer	Search Coil Magnetometer
Solar Energetic Particle Charge State Analyzer	Dual Magnetometer
Energetic Electron and Proton Instrument	Radio/Plasma Wave Instrument
Suprathermal Electron Instrument	X-Ray Imager
Solar Wind Proton/Alpha Instrument	Neutron Spectrometer
Solar Wind Composition Analyzer	Gamma Spectrometer
Near-Earth Sentinel	**Farside Sentinel**
Ultraviolet Spectroscopic Coronagraph	Magnetograph
Wide- and Inner-Field Coronagraph	

NES observations can be performed from a medium-altitude Sun-synchronous orbit like that used by TRACE. Such an orbit will allow nearly continuous observations without the additional costs associated with a geostationary or L1 mission. The baseline FSS orbit design will place the spacecraft 60° ahead of Earth 1.8 years following launch, after which the spacecraft will drift slowly to 120° during the 2-year FSS prime mission phase and to 180° during the subsequent 2-year extended phase. This design provides for a 1.2-year overlap with IHS. Launch on a Taurus is assumed.

Sentinels Spacecraft

The four IHS spacecraft baselined for the Sentinels mission are designed to meet the unique thermal control and power challenges presented by the variations in solar flux over the 0.25 × 0.74 AU IHS orbit. The spacecraft are spin-stabilized, with the spin axis perpendicular to the ecliptic and a rotation rate of 20 rpm. This spin rate reduces the effective solar constant at the spacecraft from 16 to 5 Suns at perihelion. Optical solar reflector material and thermal louvers maintain a core spacecraft temperature of 0° to 25°C, while various passive techniques provide thermal control of exposed subsystems and instruments. Power is supplied by 16 solar panels mounted around the top and bottom of the octagonal spacecraft body and tilted at 45° to maintain the array operating temperature below the 180° C design limit. A peak power tracker architecture is used to regulate and control the power output from the arrays. The X-band telecommunications subsystem uses a gimbaled phased-array high-gain antenna for high-rate downlink and a medium-gain antenna for uplink and low-rate downlink. The two antennas are housed, together with a low-gain antenna, in a thermal-protective radome and mounted on a despun platform located on the top deck of the spacecraft. Data will be stored in the solid state recorders of the redundant command and data handling units and downlinked at a rate that ranges from 750 kbps to 23 kbps depending on the spacecraft–Earth range. In addition to science and housekeeping data, space weather data will be continuously downlinked from each spacecraft. The guidance and control subsystem consists of a spinning Sun sensor and a star scanner for attitude determination and 12 4-N thrusters for attitude control.

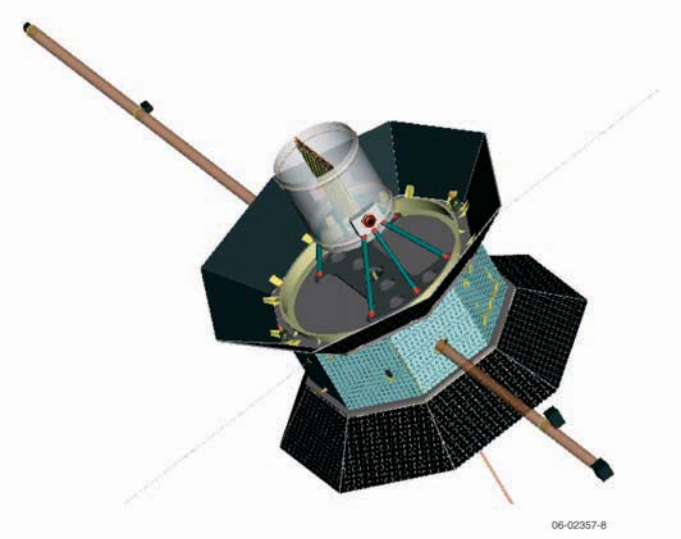

The Inner Heliospheric Sentinels spacecraft design will accommodate the strawman IHS payload and meet the unique thermal and power challenges presented by the mission environment.

The propulsion subsystem is a simple blow-down hydrazine system.

The IHS spacecraft are identically instrumented to make the in-situ and remote-sensing measurements described above. All instruments are mounted within the body of the spacecraft except the radial and axial antennas of the radio and plasma waves instrument, the boom-mounted search coil and dual magnetometers, and the solar wind electron instrument.

The baseline FSS spacecraft is a 3-axis stabilized spacecraft with four deployable solar arrays and an articulating 1.25-m Ka band high-gain antenna. It is designed to be accommodated on a Taurus launch vehicle. The NES presents no unusual mission, spacecraft design, or resource requirements and can be implemented with any of a number of standard spacecraft buses.

Sentinels and the Vision for Space Exploration

NASA's new Vision for Space Exploration (VSE) calls for "a human return to the Moon by 2020, in preparation for human exploration of Mars and other destinations."[3] One of the challenges to be confronted in implementing the VSE is to develop

[3]NASA, *The Vision for Space Exploration*, p. 5, NP-2004-01-334-HQ, February 2004.

the understanding, technologies, and procedures needed to protect astronauts from the hazardous radiation environments that they will encounter on the surface of the Moon and Mars and in transit. The Sentinels mission will contribute to this effort by discovering the physical conditions and mechanisms that govern the production of SEPs and their transport in the heliosphere. The physical understanding gained from Sentinels observations will dramatically improve our ability to model SEP acceleration and transport, which will be a major advance toward our ability to forecast SEP events. ***The STDT strongly recommends that the IHS be launched during the upcoming solar maximum (~2012), which will be the last opportunity before the first manned lunar missions to develop critical knowledge necessary for the development of a space radiation environment forecasting capability.***

Sentinels and Other Living With a Star Missions

The goal of NASA's LWS program is to provide the physical understanding needed to mitigate the adverse effects of space weather. Three missions are planned for launch during the next solar cycle. The Solar Dynamics Observatory (SDO) will study solar magnetic activity and the storage and release of magnetic energy in flares and CMEs. The two flight elements of the Geospace mission—the Radiation Belt Storm Probes and the Ionosphere–Thermosphere Storm Probes—will investigate the response of Earth's coupled magnetosphere-ionosphere-thermosphere system to CMEs and high-speed streams, with particular emphasis on radiation belt enhancements and poorly characterized midlatitude ionospheric disturbances. Sentinels is the third of the planned LWS missions. As an integral element in the LWS program, it will (1) provide contextual information about heliospheric activity for the SDO investigation of active regions emerging from the solar interior; (2) contribute to the Geospace investigation of magnetospheric and ionospheric disturbances by specifying the origin, evolution, and dynamics of geoeffective structures in the solar wind; and (3) enable the development of improved models of energetic events. ***Sentinels will also develop the scientific and technical understanding necessary to implement a future heliospheric space weather warning system by employing real-time capabilities on IHS that allow prototyping and testing of space weather monitoring and forecasting functions.***

Summary

The Sentinels mission will combine multipoint in-situ particles and fields measurements, as well as multipoint remote-sensing observations of solar energetic emissions from as close to the Sun as 0.25 AU and remote-sensing observations of the corona from 1 AU. ***Sentinels will yield breakthrough advances in our knowledge and understanding of the origin and evolution of solar energetic particles, a major source of hazardous space radiation, and of coronal mass ejections, the main drivers of space weather at Earth. The Sentinels mission is thus of central importance to the goals of the Living With a Star program and the Vision for Space Exploration.*** Mission implementation studies conducted in support of the STDT study demonstrate that the Sentinels mission, as described in this report, is fully feasible from an engineering standpoint and can be implemented with no new technology. The STDT recommends that the first flight element of the Sentinels mission, the Inner Heliospheric Sentinels, be launched as close as possible to the next solar maximum.

1.0 Science Objectives and Measurements

The goals of the Sentinels mission are (1) to understand and characterize the production and propagation of solar energetic particles (SEPs) and (2) to understand and characterize the initiation of coronal mass ejections (CMEs) and their evolution (and that of their associated shocks) during transit to 1 AU. Significant progress in our knowledge and understanding of both phenomena, as well as of the background solar wind, has been made during the past 30 years thanks (1) to a wealth of in-situ observations from such spacecraft as ISEE-3, Wind, ACE, SAMPEX, IMP-8, and Ulysses at 1 AU and beyond; (2) to remote-sensing observations from space-based platforms such as Skylab, SOHO, TRACE, and RHESSI as well as from ground-based optical and radio telescopes; and (3) to the pioneering exploratory observations in the inner heliosphere between 1 and 0.3 AU by Mariner 10 and especially the two-spacecraft Helios mission more than a quarter of century ago. Building on the considerable heritage of these earlier missions, the Inner Heliospheric Sentinels (IHS) will yield breakthrough advances in our knowledge and understanding of the origin and evolution of SEPs and transients by making multipoint measurements as close to the Sun as ~0.25 AU, thus observing key features of both phenomena that are washed out by 1 AU. The IHS spacecraft will provide ~100% duty cycle inside ~0.75 AU (the IHS aphelion) and, through simultaneous measurements at four different locations with varying azimuthal and radial separations, will be able to determine and follow the evolving structure of SEP/transient events in the inner heliosphere, which single-point measurements are inherently unable to capture.

The IHS will provide comprehensive and powerful new diagnostics not available on Helios, including (1) in-situ measurements of the composition and charge state of the solar wind plasma, suprathermal seed particles, and SEPs as well as measurements of suprathermal (~1 to 10 keV) electrons, which generate type III solar radio emission; (2) X-ray imaging, which, together with the electron and radio/wave measurements, will allow tracing of the magnetic field lines from the Sun through the inner heliosphere; and (3) ground-breaking neutron measurements at energies from 1 to 10 MeV, as well as gamma-ray measurements, which will make it possible to detect and diagnose SEP acceleration at the Sun. IHS in-situ measurements will be coordinated with supporting observations from both ground-based and space-based assets operating at the time that the IHS spacecraft are launched. During the later mission phases, IHS measurements will be coordinated with observations by the Near-Earth Sentinel (NES) (diagnostic observations of the SEP acceleration region in the high corona and the first-ever coronagraph observations out to ~0.3 AU) and by the Farside Sentinel (FSS) (global magnetograms), as well as with observations by ESA's Solar Orbiter and near-Earth measurements.

Sentinels observational strategies, instrumentation, and supporting observations are discussed in detail in Chapter 3 of this report. The present chapter focuses on the science objectives that follow from the two broad mission goals stated above and describes specific science questions that must be addressed if those objectives are to be achieved. Each of the two main sections concludes with a table listing the measurements that are either required to address the Sentinels science questions or are desirable as supporting measurements. Models to be used in the interpretation of Sentinels data are also noted. Like other Living With a Star (LSW) missions, Sentinels is a mission of "targeted basic research." By making the measurements needed to answer the science questions discussed in the following sections, Sentinels will provide the necessary physical basis for models of SEP acceleration and transport and of CME initiation and propagation. The development of such models will represent a significant step toward achieving the capability to forecast SEP events and predict the geoeffectiveness of CMEs.

1.1 Solar Energetic Particles: Sources, Acceleration, and Transport

Solar energetic particle events were discovered in 1942 with ground-based cosmic ray detectors by *Forbush* [1946]. During the three and a half decades that followed their discovery, it was generally assumed that all SEP events were produced by solar flares. By the mid-1980s, however, it had been established that most large SEP events were also associated with fast CMEs[1] [*Kahler et al.*, 1984],

[1]Coronal mass ejections were discovered with space-based coronagraphs in the 1970s (cf. *Gosling et al.* [1974]).

leading in the early 1990s to a new paradigm classifying SEP events as either impulsive or gradual [*Reames*, 1995] (**Table 1-1**). Impulsive events have durations of hours, have high electron/proton ratios, and are characterized by ^{3}He/^{4}He, Fe/O, and Fe/C ratios appreciably greater than average coronal and solar wind values, as well as by high average Fe charge states ($Q_{Fe} > 18$). The acceleration in these events is presumed to occur in flares, although most such events lack a reported H_α flare; the mechanism is a subject of debate, with at least three mechanisms proposed: stochastic acceleration by magnetohydrodynamic (MHD) waves, DC electric fields, and/or shock acceleration [*Miller et al.*, 1997]. Gradual events are associated with fast CMEs, occur over a wide longitude range (~100° to 180°), last for days, have low electron/proton ratios, and show low average Fe charge states ($Q_{Fe} < 16$). The SEPs appear to be accelerated at the shock driven by the fast CME as it propagates through the corona and the solar wind, presumably by a Fermi process involving multiple scatterings of the SEPs across the shock.

Observations made with ACE and SAMPEX over the last decade have shown that "gradual" events are highly variable in intensity, spectra, and composition and, moreover, that the compositional distinction between the two classes of events is not as clear-cut as the classification scheme described above implies. In many large "gradual" events, enhanced ^{3}He and Fe abundances, as well as higher-than-expected Fe charge states, are observed. These observations have given rise to questions about the sources of the ^{3}He, Fe, and charge-state enhancements and about the relative roles of flare acceleration and shock acceleration in large, intense, proton-rich gradual events.

Table 1-1. Properties of impulsive and gradual events (after *Reames* [1995]).

Particles:	Impulsive	Gradual
	Electron-rich	Proton-rich
^{3}He/^{4}He	~ 1	~ 0.0005
Fe/O	~ 1	~ 0.1
H/He	~ 10	~ 100
Q(Fe)	~ 20	~ 14
Duration	Hours	Days
Longitude cone	< 30°	~ 180°
Radio type	III, V (II)	II, IV
X-rays	Impulsive	Gradual
Coronagraph	–	CME (96%)
Solar wind	–	IP Shock
Flares/year	~ 1000	~ 10

Understanding SEP acceleration at shocks and the variability observed among gradual events (and sometimes within the same event) requires knowledge of the physical conditions in the upper corona and inner heliosphere where the acceleration occurs, as well as of the properties of the shock and the CME driver, both of which are evolving as they propagate outward. Have earlier impulsive flares or CME shocks populated the inner heliosphere with particles that serve as seed populations for further acceleration by CME-driven shocks? What are the relative roles of CME speed and enhanced ambient energetic particle populations on SEP peak intensities? How do shock strength and geometry (quasi-parallel vs. quasi-perpendicular) and the associated waves influence SEP properties?

As SEPs propagate along the Parker spiral interplanetary magnetic field (IMF) away from their acceleration sites, their characteristics and spatial distribution are influenced by various processes such as magnetic field line wandering, pitch-angle scattering, magnetic focusing, and adiabatic cooling. For example, pitch-angle scattering by turbulent magnetic fluctuations along the heliospheric magnetic field will modify the intensity profiles, spectra, and anisotropy of SEPs observed at 1 AU [e.g., *Li, Zank, and Rice*, 2003]. Moreover, recent studies [*Tylka, Ng, and Reames*, 1999; *Ng, Reames, and Tylka*, 1999, 2003] suggest that Alfvén waves amplified by solar energetic protons may control the escape of minor ions from the shock region and affect the resulting elemental abundances seen at 1 AU. Such waves will also scatter the energetic particles back to the shock for further acceleration. Finally, it should be noted that, although SEPs move primarily along the heliospheric magnetic field, transport perpendicular to the average magnetic field also occurs, dispersing the particles in solar longitude and latitude. Ulysses observations of SEPs at high latitudes, for example, have been interpreted in terms of cross-field diffusion [*Dalla et al.*, 2003; *McKibben et al.*, 2001]. The mechanisms responsible for the perpendicular transport of SEPs have not been definitively established.

The first and most important scientific goal of the Sentinels mission is to provide the observations required to determine how SEPs are accelerated and transported in large gradual events, what their seed populations are, and what the conditions in the corona and inner heliosphere are where SEP

acceleration and transport occur. Achieving this goal requires in-situ measurements by the IHS spacecraft as close to the Sun as possible, within ~1 to 2 scattering mean free paths (λ) of the acceleration sites, where freshly accelerated SEPs, the CME/shock, and the upstream/downstream waves can be measured before they are significantly modified or completely dissipated. (Typical values for λ are estimated to be ~0.1 to 0.3 AU.) In addition, high-sensitivity measurements of gamma rays, neutrons, and hard X-rays are required to provide valuable information on SEPs in flare acceleration regions. Longitudinally and radially distributed multipoint observations (from a minimum of four spacecraft) are needed to characterize the spatial and temporal variations in the SEP spectra and elemental abundances as well as the shock seed populations and shock characteristics.

The in-situ measurements by the IHS spacecraft will be supplemented by (a) extreme ultraviolet (EUV) and white-light coronagraphic and spectroscopic measurements from the Near-Earth Sentinel; (b) measurements of the photospheric magnetic field from the Earth, the Farside Sentinel, and Solar Orbiter; and (c) supporting observations from other space- and ground-based assets such as SDO, STEREO, FASR, and ATST. This comprehensive set of measurements will permit current theories of SEP acceleration to be tested and refined and will provide the understanding of the physical processes for CME and flare initiation required for the eventual development of a predictive capability.

The following sections discuss the specific scientific questions relating to SEP acceleration and transport that the Sentinels mission will seek to answer and the measurements required to answer them. The discussion is structured in terms of the following three objectives:

1. Determine the roles of CME-driven shocks, flares, and other processes in accelerating energetic particles.
2. Identify the conditions that determine when CME-driven shocks accelerate particles to high energy.
3. Determine how energetic particles are transported from their acceleration site and distributed in radius, longitude, and time.

The required measurements, along with supporting measurements and models, are summarized in **Table 1-2**, placed the end of Section 1.1 (p. 1–18).

1.1.1. Determine the roles of CME-driven shocks, flares, and other processes in accelerating energetic particles. Until recently, the evidence for a flare origin of energetic ions in small and short-duration impulsive events came mainly from the ion composition and charge states, which are markedly different from those of ions in typical gradual events, as shown in **Table 1-1**. Prior to the ACE mission these two event populations were considered to be separate from one another. However, ACE measurements have exhibited compositional and charge-state anomalies, as if there were mixing of these two populations. It is unclear whether the intrusion of impulsive-event particles comes directly from an associated flare or whether they are relics from previous impulsive events that populate the inner heliosphere and are then re-accelerated to higher energy in subsequent gradual events.

a. When and where are energetic particles accelerated by the Sun? Large SEP events are generally preceded both by a flare (as evidenced by electromagnetic emissions at various wavelengths) and by the launch of a fast CME and the formation of a shock in the corona and interplanetary space. Determining the relative roles of flares and CME-driven shocks in producing SEPs requires accurate measurements of the relative time profiles of the electromagnetic emissions associated with the flare, of the height-time profile of the CME, and of the timing of the energetic particle injection relative to the flare and CME. However, the information needed for timing studies of particle injections is washed out by the effects of scattering off magnetic irregularities as the particles are transported from the Sun to 1 AU. These scattering effects can be large and highly variable from event to event, with scattering mean free paths ranging from ~0.1 to ~1 AU. The detailed magnetic configuration of the inner heliosphere can also come into play [*Larson et al.*, 1997; *Bieber et al.*, 2002; *Ruffolo et al.*, 2006].

Solar impulsive electron events (see *Lin* [1985] for review), which are observed frequently throughout the solar cycle, are an important source of timing information. *Krucker et al.* [1999] and *Haggerty and Roelof* [2002] found that the inferred injection of near-relativistic (> ~30 keV) electrons at the Sun was often delayed by ~10 min with respect to the type III radio bursts at the Sun (**Figure 1-1**), and concluded that the escaping near-relativistic

populations were not directly related to those generating the prompt flare-related emissions. *Simnett, Roelof, and Haggerty* [2002] reported a correlation between near-relativistic electron events and SOHO CMEs and suggested that a CME-driven shock operating at a few solar radii (R_S) above the solar surface is the primary accelerator for the near-relativistic electrons. This interpretation was challenged by *Cane* [2003], however, who argued that the near-relativistic particles and those responsible for the electromagnetic emissions belong to a single population and that substantial scattering during the electrons' transport from the Sun is the primary cause of the delay. Finally, recent detailed timing studies using Nançay Radioheliograph data, together with EUV and white-light imaging of the corona, suggest that the acceleration of near-relativistic electrons is extended in time and results from the restructuring of the corona after the passage of a CME [*Maia and Pick*, 2004; *Klein et al.*, 2005]. In a few solar impulsive electron events where the propagation is nearly scatter-free, *Wang et al.* [2006] found that there are two distinct injections, one at low energies, ~0.4 to 10 keV, early enough to be the source of the type III radio bursts; and a second, about ~10 min later, of higher-energy (>15 to 100 keV) electrons.

The timing question can be resolved through simultaneous observations of low-energy and near-relativistic electrons by the IHS spacecraft positioned at various radial distances from the Sun (e.g., at ~0.7, ~0.5, and ~0.3 AU). If the delay is caused by scattering, the average delay should be systematically smaller the closer to the Sun that the observations are made. On the other hand, if the delay reflects the actual order of things as the SEP-accelerator develops, the average delay will be the same at all radial distances.

The same questions about delays and their implications arise in the study of protons and ions. One of the main reasons why fast CMEs (and not flares) are believed to be the accelerators of SEPs in gradual events is that the arrival of the SEPs at 1 AU is generally significantly delayed from what would be expected if they were injected at the time of the flare and is consistent with acceleration by the CME at altitudes of ~5 to 15 R_S [*Kahler*, 1994]. For example,

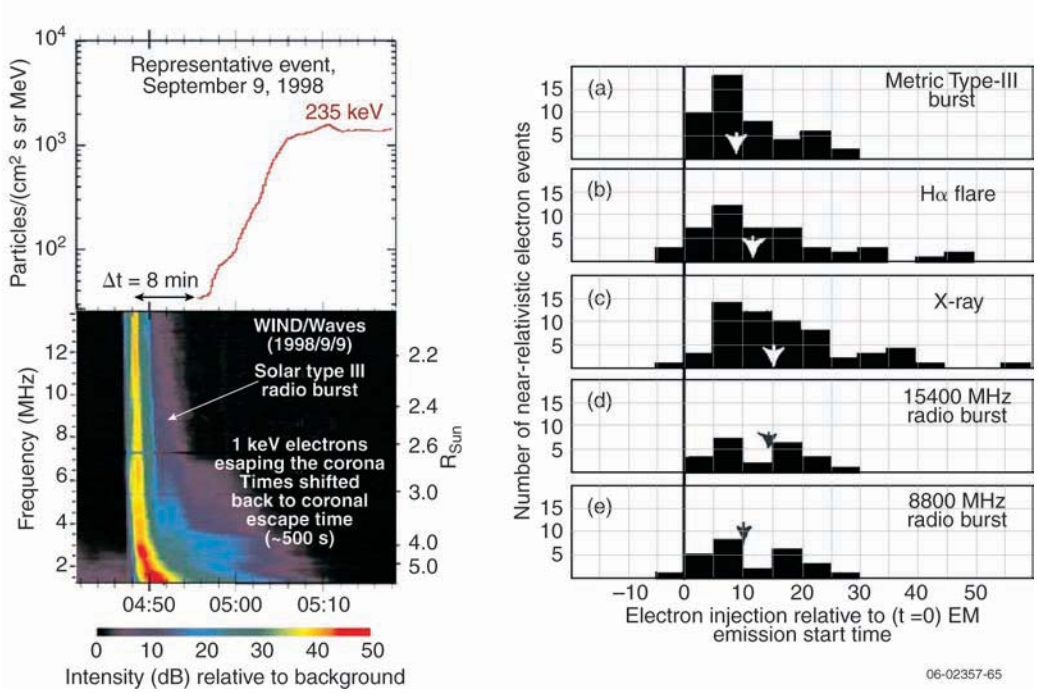

Figure 1-1. Systematic delays between electromagnetic emissions and interplanetary near-relativistic electrons. The left panel shows a representative event in which the onset of >200 keV electrons is delayed with respect to the start of type III radio emission by ~8 min (after correcting for path length and light-travel time). The right panel shows histograms of inferred injection times of near-relativistic electrons at the Sun (in minutes), relative to the onsets of various electromagnetic emissions [*Haggerty and Roelof*, 2002]. The arrows mark the median delay in each panel.

timing studies of the two largest ground-level events (GLEs) seen so far in solar cycle 23 (**Figure 1-2**) show that in both events the production of ~GeV protons peaked during the declining phase of the gamma-ray emissions, which would appear to favor an accelerator other than the flare. Scattering of the SEPs during their propagation to 1 AU, however, would delay the onset of the event, but from observations at 1 AU it is difficult to estimate the duration of the delay. The 20 January 2005 event is the most intense SEP event detected in nearly 5 decades, at energies above a few hundred MeV (and thus the most dangerous for humans in space). The SEPs arrive within minutes after the flare X-ray peak, raising questions about the role of CME shock acceleration. The very limited CME observations (the SOHO coronagraph was quickly saturated by the penetrating SEPs!) indicate that the CME velocity in this event ranged from ~2500 to ~3500 km/s [*Mewaldt et al.*, 2005; *Gopalswamy et al.*, 2005a], implying that the CME was only <2 R_S above the solar surface when the first GeV protons were released. It is uncertain whether a shock could form and accelerate particles to GeV energies in the short time and distance available [*Kahler*, 2005a]. Further, an analysis by *Simnett* [2006] of the timing of the GLE relative to the gamma-ray and other electromagnetic emissions as well as to the relativistic electrons suggests that the GeV protons were accelerated at the flare. Finally, it is interesting that in the 20 January event, both the flare-accelerated proton spectrum from ~10 to ~100 MeV (as derived from RHESSI gamma-ray observations) and the proton spectrum at 1 AU (derived from SAMPEX, ACE, and GOES data) are similar, both as hard as or harder than any spectra observed using these techniques [*G.H. Share*, private communication, 2006]. The implications of these observations for the relative roles of flare acceleration and shock acceleration in this event are not clear.

The number of unanswered questions raised by the 20 January event illustrates the difficulties inherent in attempts to identify the particle accelerator(s) in a particular SEP event based on measurements from 1 AU. An additional complication is introduced into such attempts by our imperfect knowledge of particle transport in the inner heliosphere. That is, although the models used to generate the injection profiles for the ~GeV protons at the Sun [*Bieber et al.*, 2004; *Saiz et al.*, 2005a] are relatively sophisticated, simplifying assumptions in their treatment of particle transport are a major source of uncertainty in the injection profile calculations.

Theoretical studies demonstrate how IHS observations can reduce systematic uncertainties in SEP timing (**Figure 1-3**). *Saiz et al.* [2005b; *Saiz*,

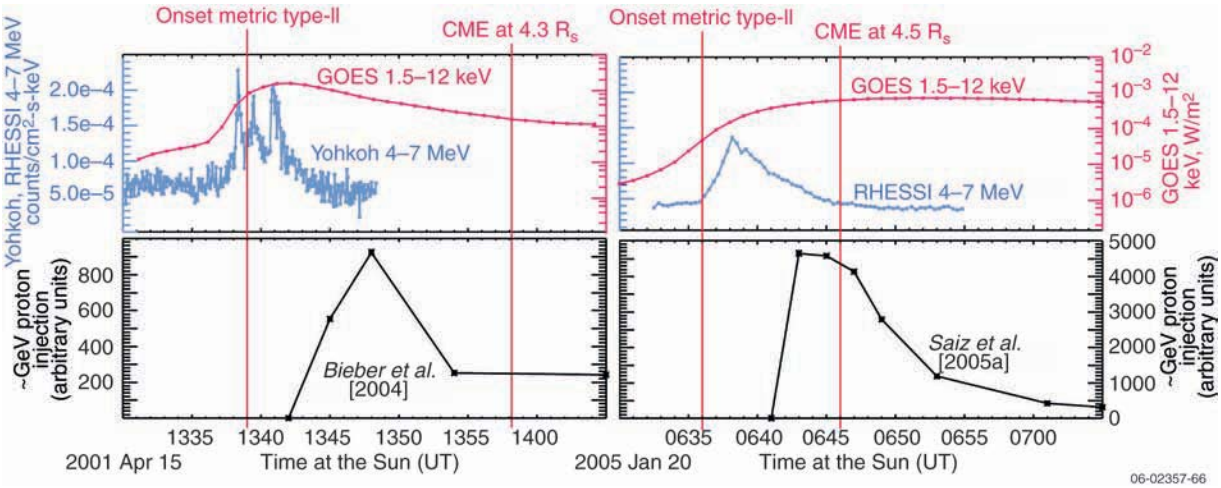

Figure 1-2. Time profiles in the two largest ground level events (GLEs) of solar cycle 23, on 15 April 2001 (left panels) and 20 January 2005 (right panels). The top panels show gamma-rays at 4 to 7 MeV (in blue; left axis) and soft X-rays (in red; right axis). The bottom panels show the injection profile of ~GeV protons at the Sun, as deduced from modeling the response of the Spaceship Earth worldwide neutron-monitor network [*Bieber et al.*, 2004; *Saiz et al.*, 2005a]. All times are corrected for propagation from the Sun. The vertical lines mark the onset times [*Gopalswamy et al.*, 2005a] of metric type II radio emission (indicating the formation of a shock in the low corona) and the first CME observation from SOHO/LASCO.

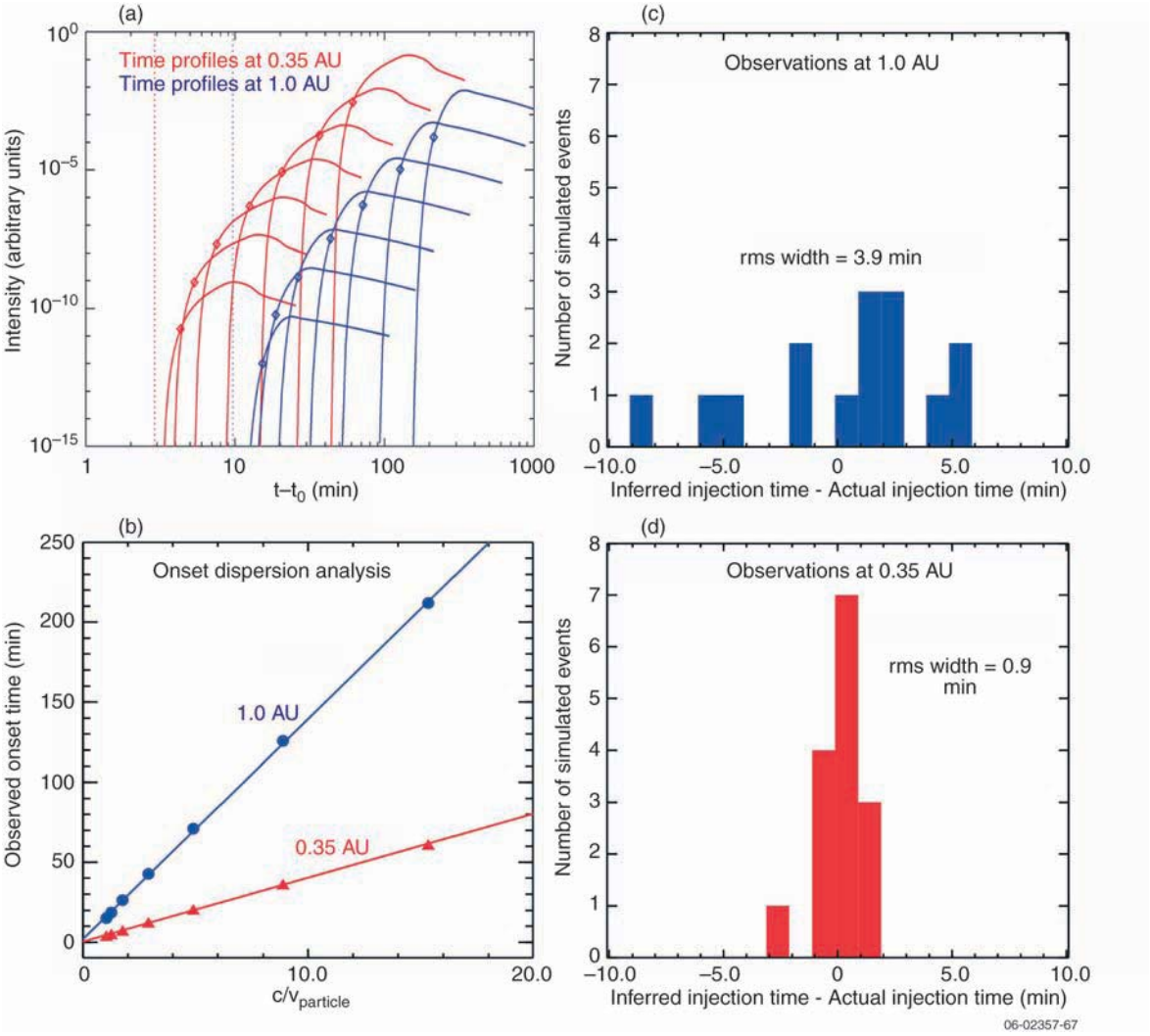

Figure 1-3. (a) Simulated time-intensity profiles for protons at seven energies from 2 to 2000 MeV at 1.0 AU (blue) and at 0.35 AU (red) from *Saiz et al.* [2005b and unpublished data]. Diamonds mark the threshold at 2% of maximum used to define the observed onset. Dotted lines mark times corresponding to path length divided by the speed of light. (b) Onset dispersion analysis based on these simulated profiles. The *y*-intercept of the fitted line gives the time at which particles first departed the Sun; the slope gives the effective path length (in light minutes). (c) and (d) Histograms at 1.0 AU (top) and 0.35 AU (bottom) for differences (in minutes) between the actual injection time at the Sun and the value inferred from velocity dispersion analyses like those in panel b. The simulations demonstrate that the analysis of measurements by the Inner Heliopspheric Sentinels spacecraft at 0.35 AU will yield inferred injection times that are more accurate and less affected by the details of scattering conditions and event structure than times derived from observations at 1 AU.

private communication, 2005] generated synthetic time-intensity profiles for protons at various energies, using numerical solutions of the Fokker-Planck equation and ranges of reasonable assumptions about the duration and shape of the near-Sun injection profile, the interplanetary scattering mean-free-path, and its rigidity dependence. (**Figure 1-3a** shows the simulated time profiles at 1 and 0.35 AU for an extended source injection at the Sun and a constant interplanetary radial scattering mean free path of 0.2 AU.) For each set of assumptions, the synthetic profiles were analyzed to infer the time of first particle injection at the Sun using the same velocity dispersion technique employed in numerous studies of real SEP data [e.g., *Lin et al.*, 1981; *Reames, von Rosenvinge, and Lin*, 1985; *Krucker et al.*, 1999; *Tylka et al.*, 2003] (**Figure 1-3b**).

At 1 AU the error in the injection time was found to vary from +6 to –9 min, with an rms width of ~4 min (**Figure 1-3c**). This spread represents

the potential lack of accuracy in determining the particle injection time. Given the rapid evolution in flare and CME activity at the onset of SEP events, this large systematic uncertainty precludes reaching definitive conclusions about SEP origin. At 0.35 AU (**Figure 1-3d**), however, the study shows that the systematic uncertainties are significantly reduced since the SEPs will have undergone less scattering and stronger focusing, so particle injection times can be established to within ±1 min, regardless of the underlying injection profile. Thus, in-situ measurements by IHS of onset times vs. velocity at different heliocentric radii down to within 0.35 AU will unambiguously determine whether the delays result from uniform interplanetary scattering or from confined acceleration close to the Sun with scatter-free transport to 1 AU. Simultaneous measurements of hard X-rays, gamma-rays, and neutrons will provide accurate timing of particle acceleration by the associated flare, as well as energy spectra and compositional information for those particles for comparison with the SEPs.

In addition to the measurements by IHS, observations from the imaging Sentinels at 1 AU are needed to resolve questions about timing and particle origin. For example, in the two GLEs discussed above and illustrated in **Figure 1-2**, the injection of ~GeV particles began and peaked when the CMEs were below ~4 R_S. If the particles in such events are in fact accelerated by CME-driven shocks, imaging of this region of the corona, with both high spatial resolution and spectroscopic information, will reveal the formation and evolution of the shocks and the concomitant changes in the corona. The fact that most of the GeV particles in the April 2001 and January 2005 events were accelerated and injected into the interplanetary medium within a period of ~10 min suggests that an imaging cadence of ~1 min is needed.

IHS timing, combined with high-spatial-resolution coronal imaging out to at least ~10 R_S and with ~1-min cadence, will enable researchers to identify the site(s) at which particle acceleration occurs and the responsible acceleration mechanism(s); to assess the role of scattering in particle transport; and to evaluate other possible explanations for the observed timing delays, such as acceleration in coronal restructuring following the CME. Resolving the outstanding questions regarding these matters is a necessary condition for the eventual development of reliable SEP prediction models.

b. How are the energetic particles observed at the Sun related to those observed in the interplanetary medium? Recent observations of anomalously enhanced ^{3}He and heavy element (e.g., Fe) abundances and highly ionized charge states (e.g., Q(Fe) ~ +15 to +20) in many large SEP events [*Cohen et al.*, 1999; *Mason, Mazur, and Dwyer*, 1999; *Mewaldt et al.*, 2006] have been interpreted as evidence that remnant material from previous impulsive ^{3}He-rich flares may provide a seed population for further acceleration at CME-driven shocks [*Mason, Mazur, and Dwyer*, 1999]. *Cane et al.* [2003] have proposed that flares contribute directly to major SEP events as well, and have identified three classes of major events based on intensity–time profiles and Fe/O ratios (**Figure 1-4**). The first class consists of events that have enhanced Fe/O ratios at energies >25 MeV/nucleon and steep intensity–time profiles, and are dominated by flare-accelerated particles originating mainly on the western hemisphere. The events in the second class are dominated by shock-accelerated particles with a composition similar to coronal abundances and have more rounded profiles that reach maximum intensities ~1 day after the associated flare. "Two-component" events make up the third class, with a dominant flare-accelerated (high Fe/O) component observed during the early phases and a shock-accelerated component with a

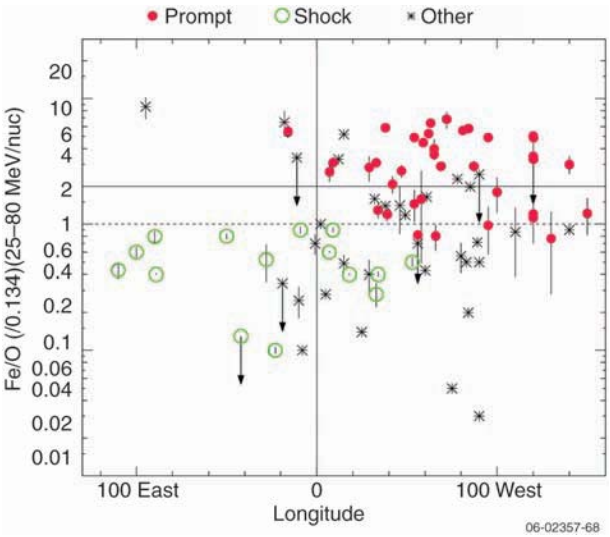

Figure 1-4. Event-averaged values of Fe/O with 25 to 60 MeV/nucleon (normalized to the average SEP value of 0.134 [*Reames*, 1998]) are plotted vs. the longitude of the associated flare event [*Cane et al.*, 2006]. Symbols indicate the SEP profile type.

more or less normal composition (lower Fe/O) seen in the later phases.

Both flares and CMEs are thought to be initiated by magnetic reconnection. In impulsive events, particles accelerated at the flare site are known to escape on open field lines into interplanetary space [e.g., *Reames*, 2002; *Wang, Pick, and Mason,* 2006] (see Section 1.1.1.c). *Reames* [2002], however, suggests that larger CME-associated events involve a closed field topology that does not allow accelerated particles to escape from the reconnection site. According to this view, there should be no significant direct contribution of flare-accelerated particles to large SEP events, so that the only particles that are observed in these events are shock-accelerated coronal/solar wind particles or remnant flare particles. IHS will be able to determine the relative contributions of flare-accelerated and shock-accelerated particles in large SEP events through simultaneous direct measurements of energetic particles at different heliolongitudes. If an admixture of high-energy particles from the flare site is responsible for the ^{3}He and Fe enhancements observed in many of these events, those enhancements will be observed only by those IHS spacecraft that are on field lines connected to the flare site, while IHS spacecraft on field lines not connected to the flare site will observe only shock-accelerated particles.

Knowledge of the near-Sun interplanetary field structure and connectivity will be important for the interpretation of the IHS data. Fast electrons provide ideal tracers of magnetic field connection from the Sun into the heliosphere. The IHS spacecraft can determine their source at the Sun through multipoint (stereoscopic) imaging of their bremsstrahlung X-ray emission, track them as they travel along the magnetic field lines through the interplanetary medium by the stereoscopic radio observations of the type III radio burst that they generate, and then detect them in situ. By analyzing the velocity dispersion of the impulsively accelerated electrons detected in situ, the field line length can be determined in both the quiet solar wind and in interplanetary coronal mass ejections (ICMEs), where the lengths can be several times the typical Parker spiral length [*Larson et al.*, 1997]. Furthermore, the magnetic connectivity back to the Sun can be monitored through IHS measurements of the solar wind electron strahl, i.e., the electrons that continuously flow outward from the hot corona. In addition, IHS observations of dispersionless modulations in the intensity of low-energy solar electron bursts [*Gosling et al.*, 2004] and ions [*Mazur et al.*, 2000] can help in identifying and tracing field lines not connected back to the acceleration region.

c. What conditions lead to the jets/narrow CMEs associated with impulsive SEP events? Early observations of SEPs established the two-class system based on various SEP characteristics shown in **Table 1-1**. The impulsive SEPs were thought to be accelerated in small coronal flares and to escape the corona along pre-existing open field lines overlying the flaring regions. Recently it has been found that some impulsive SEP events are accompanied by coronal jets or fast, narrow (<20°) CMEs. For example, a study of 25 ^{3}He-rich impulsive events showed that the events originated in small active regions located in the western hemisphere close to (within ~4° of) coronal holes [*Wang, Pick, and Mason,* 2006] (**Figure 1-5**). The open flux emerging from the holes was pre-existing and not created during the events and was directed generally earthward. Half of the events were associated with narrow jets observed in the extreme ultraviolet with the SOHO EIT; for some of these events, narrow ejections of coronal material were also observed in white light with the SOHO/LASCO C2. The jets were generally aligned with the open field lines. The EUV jets and white-light counterparts often recurred, with the same active region emitting a series of jets over a period of a day or more. Corresponding recurrent features were seen in the particle intensities measured with the ACE/ULEIS.

One interpretation of these narrow CMEs is that they result from magnetic reconnection between emerging closed field lines and overlying open field lines [*Reames*, 2002]. In this scenario, proposed earlier by *Shimojo and Shibata* [2000], a reconnection region rich in wave turbulence produces the impulsive SEPs and allows the SEPs and hot plasma from the emerging region to escape along newly opened field lines (**Figure 1-6**). In sufficiently large events the plasma would be seen as a narrow CME, but contrary to classical CMEs, no magnetic flux would be expelled from the corona.

What conditions can lead to the production of jets/narrow CMEs and their associated SEP events? We currently have only a few individual cases of coronal jets associated with impulsive SEP events, but several coronagraph and EUV imaging studies

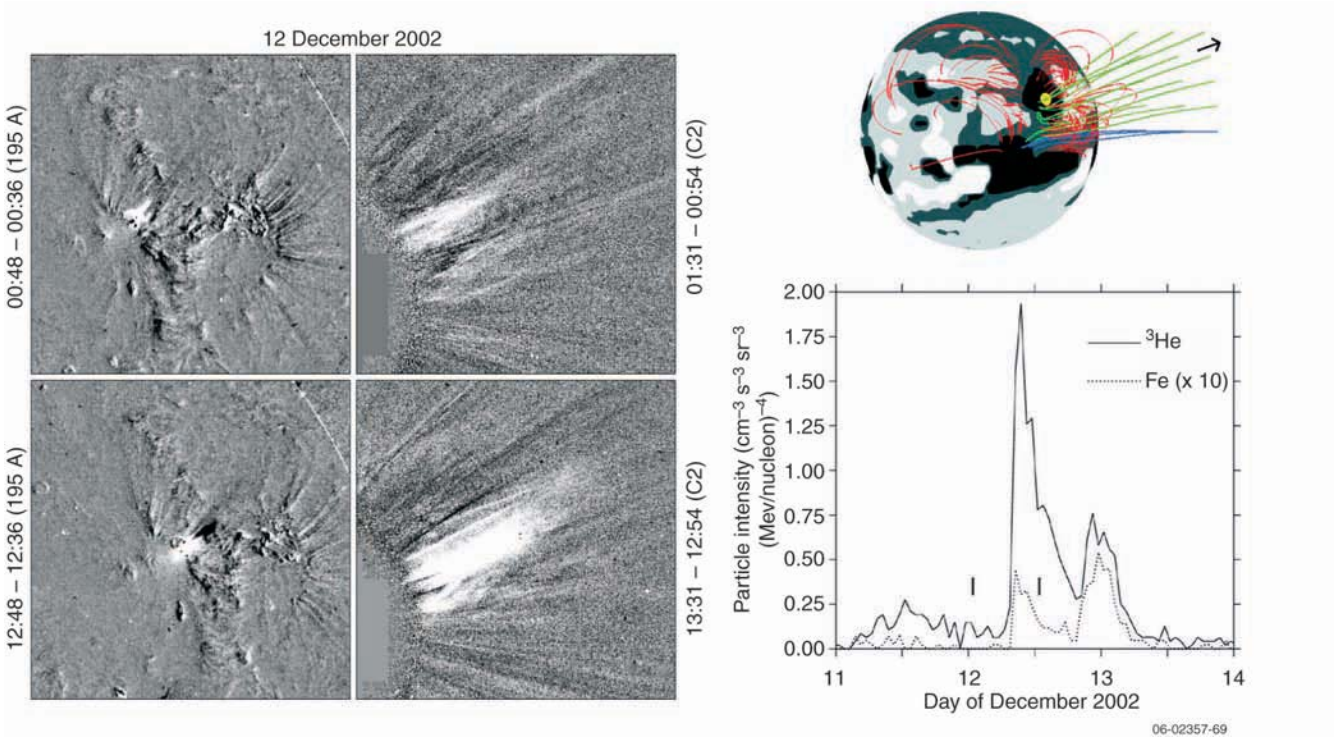

Figure 1-5. Left: SOHO/EIT and LASCO C2 difference images showing a pair of eruptions that occurred 12 hours apart on 12 December 2002. The EUV brightening at 00:48 UT has a characteristic "wishbone" shape strongly suggestive of reconnection between closed and open field lines at an X-type neutral point (see Figure 1-6). Upper right: The field configuration derived by applying a potential-field source-surface extrapolation to photospheric magnetograph data shows that the flare site (yellow dot) is located near open field lines (blue lines are directed into the ecliptic plane and green otherwise; closed field lines are red). Lower right: the intensity profiles of ^{3}He and Fe with 0.32 to 0.45 MeV/nucleon observed by the ACE/ULEIS experiment. The two peaks correspond to the two EIT/LASCO events; vertical bars mark the approximate times of the EUV eruptions (note that 0.38 MeV/nucleon ions take at least 0.25 days to travel ~1.2 AU). From *Wang, Pick, and Mason* [2006].

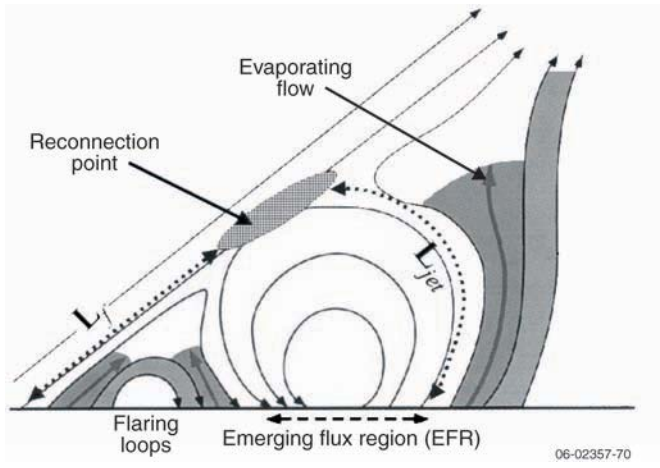

Figure 1-6. Schematic illustrating how emerging closed field lines reconnect with neighboring or overlying field lines, accelerating energetic particles and producing narrow coronal jets [*Shimojo and Shibata*, 2000].

have established conditions leading to jets. The sites are small bipolar magnetic regions located near or inside boundaries of nonpolar coronal holes [*Wang and Sheeley*, 2002] or from compact bipoles inside streamer arcades [*Bemporad et al.*, 2005]. Both jets and impulsive SEP events appear to occur from the same regions in series over periods of up to several days. Observations of many such impulsive SEP events with enhanced sensitivity and more precise injection timings with multipoint inner heliospheric in-situ instruments, together with EUV and X-ray imaging, will allow the source regions and their dynamics to be studied in much greater detail.

d. What physical processes accelerate SEPs? At present there is no unanimity about the processes by which SEPs are accelerated. The

two principal possibilities being actively investigated are acceleration by a CME-driven shock (e.g., *Lee* [2005]) and acceleration by flare-related mechanisms associated with magnetic reconnection (e.g., *Miller et al.* [1997]). In addition, some acceleration may occur as a result of magnetic restructuring of the corona after the passage of a CME [*Maia and Pick*, 2004]. It is likely that SEP events involve acceleration by more than one process, and Sentinels will be able to assess the relative contributions of the different proposed processes to the events that it observes. In addition, SEP observations will make it possible to determine or at least constrain the various physical mechanisms thought to be responsible for particle acceleration at flare sites.

When the two-class paradigm of gradual vs. impulsive SEP events was first proposed, it was assumed that in gradual events particles are accelerated by diffusive shock acceleration, where they are scattered back and forth across a quasi-parallel shock by waves generated by the energetic particles themselves (see *Lee* [2005] and references therein). More recently, it has been pointed out that quasi-perpendicular shocks can easily overtake the energetic particles upstream of the shock even when there is very little scattering by waves [*Webb et al.*, 1995], and the preferential acceleration of flare particles in large gradual events by quasi-perpendicular shocks has recently been investigated [*Tylka et al.*, 2005]. If diffusive shock acceleration at quasi-parallel shocks is important for SEPs, then waves self-generated by the accelerated particles should be present at significant levels. These are also the waves believed to be responsible for the apparent self-limiting of the SEP fluxes observed at 1 AU [*Reames and Ng*, 1998], and they are predicted to be present out to ~0.3 to 0.5 AU. At 1 AU, such waves are only rarely observed and then only waves resonant with protons at energies below a few MeV. Through in-situ observations inside ~0.3 to 0.5 AU, IHS will be able to detect these waves (if present), measure their properties and spatial distribution, and observe the relatively unevolved shock itself. With simultaneous measurements of the distribution of the relatively pristine energetic particles, IHS should provide the first quantitative and realistic assessment of applicability of diffusive shock acceleration theory to SEP acceleration. IHS measurements will also show whether quasi-perpendicular shocks are important, by determining the shock properties, including orientation, with in-situ plasma and field measurements, to compare with the energetic particle measurements.

Imaging observations of solar flare gamma-ray lines and hard X-ray/gamma-ray continuum, emitted by energetic ions and electrons, respectively, show that particle acceleration occurs in flares up to the highest energies observed for SEPs near 1 AU (~MeV to tens of GeV for ions and keV to GeV for electrons). Several different particle acceleration processes have been proposed for flares: parallel electric fields in the magnetic reconnection region, stochastic acceleration by plasma waves and turbulence, and shocks driven by flows from the reconnection region (see review by *Miller et al.* [1997]). There are also intense gradual SEP events observed at 1 AU with no detectable gamma-ray line emission, however, implying that in those events the ions are accelerated where the ambient density is lower (although the current limit, $n < 10^{10}$ cm $^{-3}$, is not very constraining), either by flare-related phenomena higher in the corona or by CME shock waves.

For many, if not most, impulsive SEP events, no associated flares are observed, and the electron spectrum extends down to < ~1 keV, again suggesting that the acceleration occurs high in the corona, since such low-energy electrons would be lost to Coulomb collisions before traveling through much of the corona. As mentioned earlier, recent radio and coronagraph studies of impulsive electron events indicate that the acceleration in those events may be related to jets/narrow CMEs [*Wang, Pick, and Mason,* 2006]. Through in-situ measurements as close to the Sun as ~0.25 AU, IHS may be able to detect these fine-scale jets, and the remnants of the coronal restructuring behind large, fast CMEs before they are washed out. IHS will be able to locate the acceleration region by imaging the accelerated electrons through their X-ray emissions (when present) at the Sun. Stereoscopic X-ray imaging (and limb occultation) from two or more IHS spacecraft will provide information on the altitude of the acceleration region. The IHS multi-spacecraft stereoscopic radio observations can track the electrons, through their type III solar radio emissions, as they escape from the Sun, and trace their propagation in the heliosphere, in the process mapping the structure of the magnetic field lines in the inner heliosphere. Finally, the electrons will be detected in situ at the IHS spacecraft.

The IHS measurements of the SEP ion composition and charge state will provide information on

the conditions (temperature, source composition, density) in the acceleration region and on the acceleration process (**Figure 1-7**). These observations can be compared with the composition of the accelerated ions near the Sun derived from the IHS neutron and gamma-ray observations, and with the NES spectroscopic coronagraph's imaging and spatially resolved measurements of the temperature, density, composition, suprathermal populations, waves and shock passage in the high corona where the acceleration is hypothesized to take place. Accurate measurements of the energy spectrum for electrons and for different charge state ions by the IHS spacecraft close to the Sun will provide a probe of electric field acceleration. Such acceleration should result in a sharp feature in the energy spectrum, and double power-law spectra with relatively sharp breaks have been observed at 1 AU for both SEP electrons and ions.

1.1.2 Identify the conditions that determine when CME-driven shocks accelerate energetic particles. The properties of SEPs accelerated at CME-driven shocks are highly variable. For example, even in events in which CME speeds are the same, SEP intensities can range over ~4 orders of magnitude [*Reames*, 2000] (**Figure 1-8**). This variability is likely the result of the interplay of many factors, including the composition and distribution of the seed population, the properties of the CME and shock, and the preconditioning of the inner heliosphere by earlier events. Understanding the causes of SEP variability in large gradual events is an essential condition for the development of predictive models.

a. What are the seed populations for shock-accelerated SEPs and how do they affect SEP properties? Measurements of SEP elemental and isotopic ratios and ionic charge states suggest (1) that suprathermal ions rather than the bulk solar wind are the primary seed population for particles accelerated by CME-driven shocks and (2) that energetic particles with properties associated with flare acceleration (e.g., enhanced ^{3}He and Fe abundances, highly ionized charge states) are frequently observed in gradual events [*Mason et al.*, 2005; *Mewaldt et al.*, 2006]. A number of different source populations have been proposed to explain these observations.

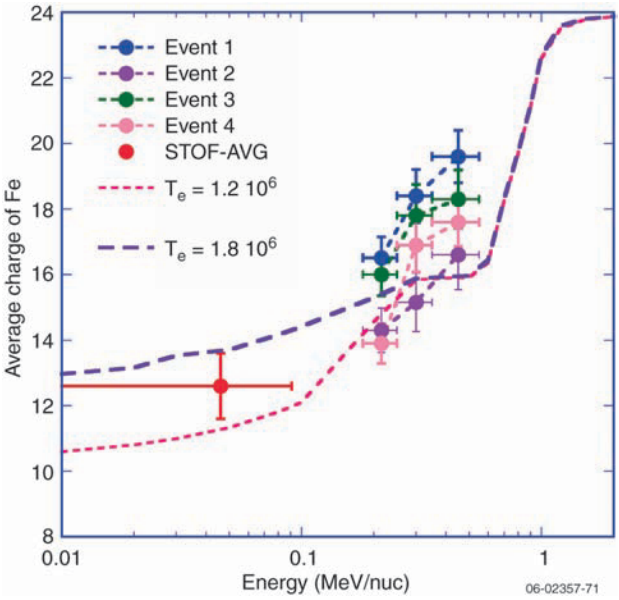

Figure 1-7. Energy-dependence of the mean Fe charge state as observed in several ^{3}He-rich flares [*Klecker et al.*, 2006]. Energy-dependent charge states may reflect the temperature of the source population or be the result of collisional stripping during acceleration, in which case Q is a function of the density in the acceleration region and the acceleration time. The curves assume thermal equilibrium for the source material, but allow for electron stripping during acceleration. Inner Heliospheric Sentinels ionization state measurements will provide information about the source region and acceleration history of energetic particles.

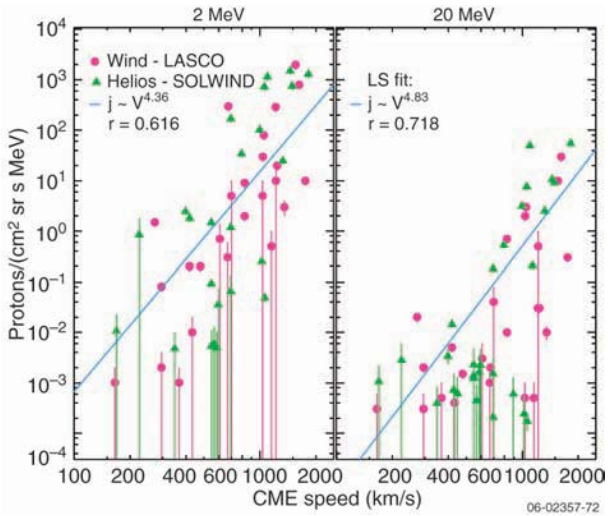

Figure 1-8. Correlation of peak SEP proton intensities at 2 MeV (left) and 20 MeV (right) versus the observed speed of the associated CME from SOHO (circles) and SOLWIND (triangles). There is a clear correlation, but even for events with the same CME speed, the intensities vary over nearly 4 orders of magnitude, suggesting that other factors are also involved in the variability [*Reames*, 2000].

Pre-existing populations of flare-accelerated particles. ACE ^{3}He measurements [*Mason, Mazur, and Dwyer*, 1999] have shown that remnant particles from impulsive events may be an important component of the suprathermal seed population for large, gradual SEP events; several studies have demonstrated that enhanced ^{3}He-levels are a persistent feature of the interplanetary medium during solar maximum [*Wiedenbeck et al*., 2003; *Laivola, Torsti, and Kocharov*, 2003], present even during nominally quiet periods in which no flare activity is presently occurring [*Richardson et al*., 1990] (**Figure 1-9**). When these impulsive-event ^{3}He ions are subsequently overtaken by shocks, they can be accelerated to even higher energies. It has been suggested that suprathermal seed particles from impulsive events also contribute to the enhanced Fe/O ratios and high Fe charge states (Q_{Fe} ~ 20) seen in many gradual SEP events [*Mason, Mazur, and Dwyer*, 1999; *Tylka et al*., 2001; 2005]. However, comparison of Fe ion number densities during quiet or moderately active periods and in Fe-rich SEP events indicates that, except during very active periods, there are not enough remnant suprathermal Fe ions in the inner heliosphere to account for the Fe enrichment observed in gradual and hybrid events [*Mewaldt et al*., 2003, 2006]. In addition to questions about the properties of flare suprathermals in the inner heliosphere and the adequacy of this population as a source for observed fluences at 1 AU, there are a number of unknowns about the nature of their flare source. Do the suprathermals come primarily from the largest flares, whose particles are then dispersed by longitudinal and radial scattering (**Figure 1-10**) (see Section 1.1.3)? Or is the suprathermal population continually replenished by numerous small impulsive events, whose intensities cannot be resolved from background at 1 AU? Do multiple flares from the same active region play a key role in filling the inner heliosphere with suprathermals, thereby providing some uniformity to the compositional and spectral characteristics of the flare suprathermals over a wide longitudinal span?

Suprathermal tails on the solar wind. ACE and Ulysses measurements have revealed the ubiquitous and persistent presence of suprathermal tails on solar wind ion distributions at 1 AU and beyond [*Gloeckler*, 2000]. Such tails are most readily observed for H and He ions, but they are also present for heavy ions. They are commonly observed

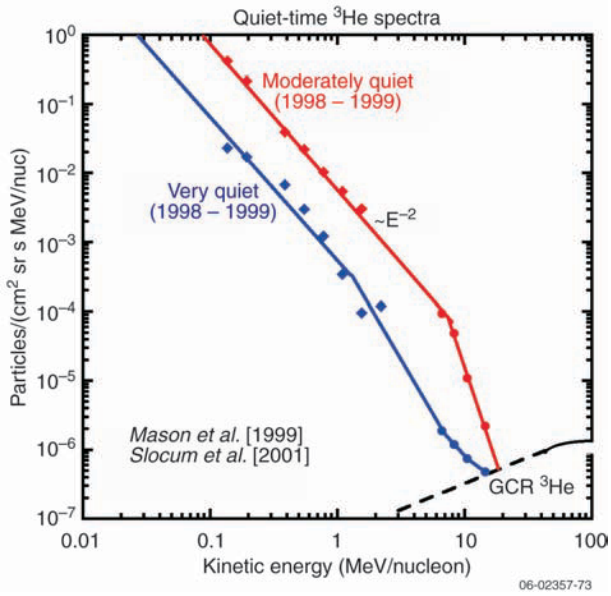

Figure 1-9. Spectra of ^{3}He ions accumulated at 1 AU on days that were very quiet (blue) or moderately quiet (red) with respect to solar activity in 1998–1999. In both cases, significant ^{3}He intensities were observed, suggesting that remnant ions from flare activity can contribute to the seed population for CME-driven shocks [*Mewaldt et al*., 2004].

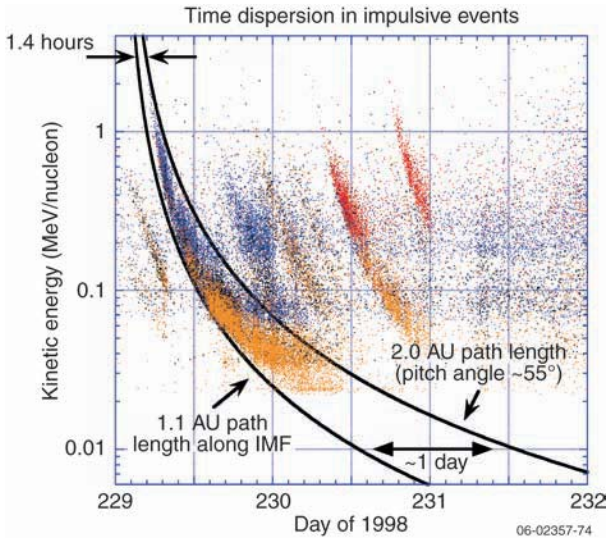

Figure 1-10. A "swoosh plot" representation of an impulsive solar particle event observed by ACE. Each detected ion is represented by a dot, with the vertical coordinate giving its energy and the horizontal coordinate giving its time of arrival. The color indicates the relative density of points. When ions at a few MeV/nucleon arrive, the event lasts only an hour. In contrast, ions at ~30 keV/nucleon arrive over a period of about half a day, implying that they have undergone significant longitudinal dispersion. What is the mechanism for this longitudinal dispersion? And on what timescales does it operate closer to the Sun? [*Mason, Dwyer, and Mazur*, 2000].

downstream of shocks and in co-rotating interaction regions (CIRs), but weaker tails are always present, even during quiet times, far removed from shocks (**Figure 1-11**). The presence of similar tails on He^+, which is a pickup ion created from interstellar neutrals and rare in the bulk solar wind, indicates that the tails can originate in interplanetary space and do not require a solar origin. How the quiet-time tails are produced is unknown; statistical acceleration has been proposed as a possible mechanism [*Fisk*, 2000].

While suprathermal tails have been observed between 1 and 5 AU, it is not known whether they exist in the inner heliosphere, and, if so, what their composition might be or whether they would be intense enough to be a viable source for SEPs (based on ACE and Ulysses results, the intensity of the tails should increase by almost $1/R^2$ closer to the Sun). With multiple spacecraft distributed in radius and longitude between 0.25 and 0.7 AU, IHS will be able to provide information on the composition, distribution, and variability of the hypothesized inner heliospheric suprathermal tail population. IHS data, together with complementary measurements

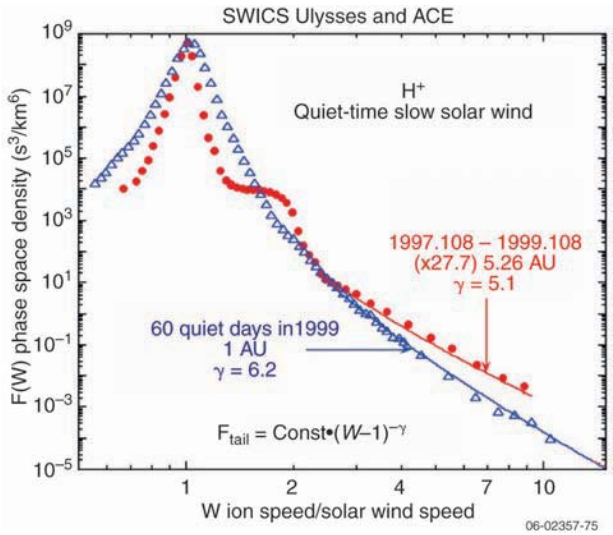

Figure 1-11. Observations of the bulk solar wind and suprathermal tails from the SWICS instrument on ACE (blue) and on Ulysses (red) [*Gloeckler et al.*, 2003]. The Ulysses spectrum is multiplied by $R^2 = 27.7$ to correct for the density decrease due to radial expansion. The origin of these tails is unknown, but they appear to be the product of acceleration processes that operate between the Sun and 1 AU. The quiet-time solar-wind and suprathermal measurements at ACE and Ulysses are compared as a function of *W*, the ion speed divided by the solar-wind speed. Note that the spectrum above $W \sim 2.3$ at Ulysses is stronger and harder than at 1 AU.

from Solar Orbiter and Solar Probe, will characterize this population and illuminate its role in SEP production.

Re-accelerated material from flares associated with CMEs. As discussed above (Section 1.1.1.b), the ^{3}He and Fe enhancements observed in large events may result from the direct injection of material by the flare activity that accompanies the launch of nearly all fast CMEs, if the flare activity occurs within a magnetically "well-connected" longitude range. Such direct injection of flare-accelerated material would eliminate "the need to invoke a population from previous smaller flares" [*Cane et al.*, 2003]. In addition, the directly injected material from the flare may serve as a seed population that undergoes further acceleration by the shock [*Mewaldt et al.*, 2003]. What is the relative contribution of "fresh" (as opposed to "remnant") flare suprathermals? Are there open field lines at the edge of the flaring region or perhaps threading through the CME, along which flare particles can escape into the upstream region? Is there sufficient scattering that the flare particles can then be returned to the CME-driven shock, where they can be further energized?

SEPs from previous CME-driven shocks. Finally. it has been suggested that shock-accelerated SEPs may themselves be another seed population for further acceleration by subsequent CME-driven shocks [*Kahler*, 2001].

The intensity of the SEP seed population has been shown to be an important factor in the extreme variability observed in the intensity of shock-accelerated events [*Kahler*, 2001]. A comparison of the flux of suprathermal Fe ions at ~30 keV/nucleon with the number density of the bulk solar wind suggests how suprathermal variability might contribute to the spread in SEP intensities [*Mason et al.*, 2005]. As illustrated in **Figure 1-12**, the suprathermal intensity measured at 1 AU spans 3 orders of magnitude, while the bulk solar-wind density varies by only a factor of 10. Does the suprathermal intensity in the inner heliosphere, inside 1 AU, show comparable or even larger variations? If so, what causes this variability?

Knowledge of the temporal variability, radial and longitudinal distribution, and composition, intensity, and spectra of the inner heliospheric source material for SEPs is required for understanding, modeling, and eventually predicting SEP events and their

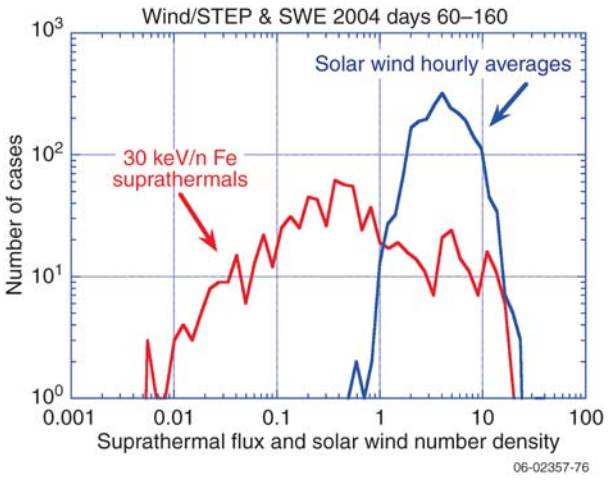

Figure 1-12. Histogram of results from a survey of suprathermal ~30 keV/nucleon Fe intensities at 1 AU and an analogous survey of the bulk solar wind. Whereas the bulk solar-wind density varies by only a factor of 10, the suprathermal intensities span 3 orders of magnitude. The large spread in the intensities of suprathermals, which are believed to be an important seed population for large SEP events, may contribute to the very large event-to-event variation in SEP intensities [*Mason et al.*, 2005].

potential radiation hazards. However, knowledge of these important parameters is severely limited by the fact that they cannot be satisfactorily determined from measurements of suprathermals at 1 AU. That is, because of solar rotation, the spiral configuration of the magnetic field, and the relatively slow speeds of the suprathermals, observations at 1 AU can never sample the same seed population encountered by a CME-driven shock near the Sun. While some information may be obtained from measurements of the suprathermal population at 1 AU one day prior to an SEP event [*Mewaldt et al.*, 2006], such observations are not satisfactory substitutes for direct measurements of the SEP source population in the inner heliosphere, as close to the Sun as possible. (With their perihelia at 0.25 AU, the IHS spacecraft will not measure the suprathermal population in the near-Sun region, inside a few to 10 R_S, where the bulk of the shock acceleration in gradual events is believed to occur. Instead, this region will be sampled by Solar Probe, with its perihelion of 4 R_S [*NASA*, 2005]. The NES spectroscopic measurements of high-energy tails on ion velocity distributions will also provide some of the required information on suprathermal seed population in this region. The IHS, NES, and Solar Probe measurements are highly complementary. Solar Probe will provide a unique "snapshot" look at the suprathermal seed population during its solar flyby, while IHS and NES will characterize the temporal variability and spatial distribution of the suprathermals through extended monitoring from multiple platforms at various radial distances and heliolongitudes.)

b. How do CME/shock structure and topology as well as ambient conditions affect SEP acceleration? Coronal/interplanetary shocks are driven through the solar wind by large, fast CMEs and evolve in response to changing plasma conditions as they move outward from the Sun. A major challenge to understanding SEP acceleration at those shocks is the complexity of the dynamics and spatial structures of both the shock drivers and ambient solar wind streams in the inner heliosphere. Fast CMEs produced in the lower corona gradually decrease in speed as they propagate outward through regions with first rapidly increasing, then slowly decreasing characteristic fast-mode MHD wave speeds [*Gopalswamy et al.*, 2001a]. The stronger B fields, larger Alfvén wave amplitudes, and smaller particle gyroradii allow maximum SEP energies at shocks to scale roughly as $1/R^2$ [*Lee*, 1997; *Zank, Rice, and Wu*, 2000]. Close to the Sun the generally radial magnetic fields should give rise to quasi-perpendicular shocks at CME flanks and parallel shocks above CME leading edges [*Steinolfson*, 1992; *Kahler*, 2004]. SEPs produced at the two kinds of shocks may vary considerably in their properties, but two large SEP events of 2002, interpreted in terms of parallel and perpendicular shock acceleration, were nevertheless attributed to two CMEs with very similar characteristics and solar locations [*Tylka et al.*, 2005].

CME width is apparently an important shock parameter, as CMEs with widths < 60° rarely produce strong interplanetary shocks [*Gopalswamy et al.*, 2001b] or gradual SEP events [*Kahler and Reames*, 2003], even when the CME speeds are high (V > 900 km/s). An important discriminating characteristic between high- and low-intensity SEP events is the presence during the previous ~day of a preceding wide (>60°) CME from the same source region as the primary CME [*Gopalswamy et al.*, 2004] (**Figure 1-13**). However, observations at 1 AU are not sufficient to determine how these higher intensities come about. Do they result from an enhanced seed population produced by the earlier event (see above)? Or does the preceding CME

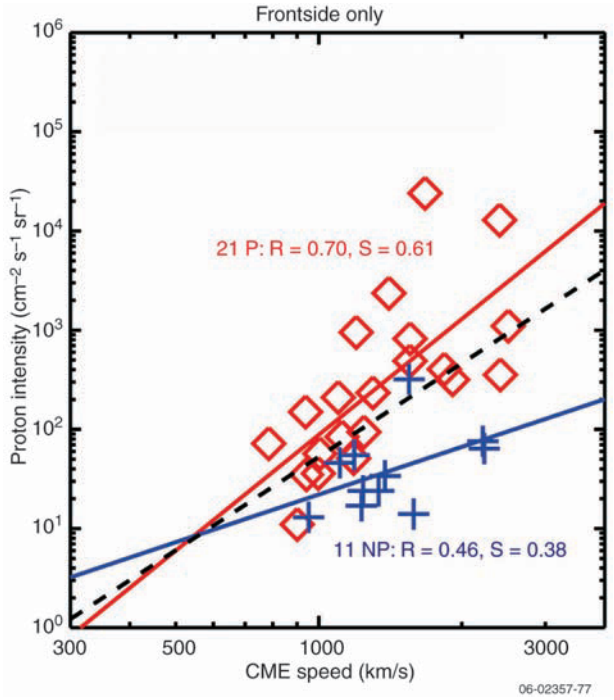

Figure 1-13. Peak >10 MeV proton intensities from GOES vs. observed CME speeds from SOHO. The red diamonds are events in which there was a CME from the same source region during the preceding day. The blue crosses are events with no such preceding CME. The solid lines are regression fits to the two populations. Intensities are higher in the case of preceding CMEs, and there is very little overlap between the two populations. The dashed line is the regression fit to the combined population. The sample includes only events with frontside CMEs [*Gopalswamy et al.*, 2004].

"condition" the interplanetary medium, by changing the ambient waves and plasma in ways that improve the acceleration efficiency at the shock driven by the primary CME?

Although SEP models often assume a single fast-mode MHD shock propagating through an azimuthally uniform flow, the solar wind consists of previous CMEs embedded in slow and fast wind streams. The shock structure and SEP production and transport should be significantly altered when shocks propagate into slower preceding CMEs [*Vandas and Odstrcil*, 2004; *Gonzalez-Esparza et al.*, 2004] or through speed shears in adjacent solar wind streams [*Odstrcil and Pizzo*, 1999b], which could significantly change the shock angles with B. In addition, fast wind regions should be poor candidates for SEP production because of both the higher CME speeds needed to drive shocks and a probable lack of abundant suprathermal ion tails [*Gloeckler*, 2003], but a fast-wind depletion of SEPs has not been found observationally [*Kahler*, 2004].

Further, it is unclear that all inner-heliospheric SEP-producing shocks are forward, fast-mode MHD shocks. Reverse shocks are sometimes seen, generally only beyond 1 AU [*Richardson and Wang*, 2005] in the ecliptic plane, but they could be produced at the trailing edges of expanding CMEs, as observed by Ulysses at high latitudes [*Gosling et al.*, 1994]. At CME speeds below ~900 km/s, slow and intermediate MHD shock waves should form. The intermediate shock waves, characterized by reversals in direction of B_{perp} across the shocks, should form for CME speeds between the Alfvén Mach number and the larger critical Mach number [*Steinolfson*, 1992]. Unlike slow shocks [*Isenberg*, 1986], the intermediate shocks can also accelerate SEPs.

Finally, we have evidence from solar type II radio bursts [*Knock et al.*, 2003] and shock normals at 1 AU [*Szabo*, 2005] for coronal/interplanetary structures that superpose significant perturbations on the large-scale shock structures. For example, observations at 1 AU indicate that the energetic electrons that produce type II radio bursts are counterstreaming from a shock that has a wavy surface [*Bale et al.*, 1999]. From observations at 1 AU, however, we cannot accurately predict whether and what kinds of shocks will form, what their dynamics will be, and how efficiently they will accelerate SEPs. We can anticipate that the numbers and kinds of observed shocks will increase as we probe closer to the Sun (e.g., *Richter* [1991]) with Sentinels. Sentinels will make it possible to track the radial evolution of shocks and ambient conditions throughout much of the inner heliosphere and, through simultaneous observations of the same event over a range of longitudes, to determine the longitudinal structure of CME-driven shocks. In addition, the detailed shock structures, their associated drivers, inhomogeneities, and spatial deformations, as well as their associations with SEP production, will be defined. As mentioned earlier, the magnetic connectivity and large-scale structure can be probed with IHS electrons/radio/X-ray observations. These observations will facilitate the development of time-dependent shock models.

1.1.3. Determine how energetic particles are transported from their acceleration site and

distributed in radius, longitude, and time. The transport of solar energetic particles from their acceleration site through the inner heliosphere to 1 AU and beyond is a problem of critical importance for understanding and eventually predicting SEP events (**Figure 1-14**). SEP transport is a complex phenomenon involving a variety of processes: field-line wandering, pitch-angle scattering by turbulent magnetic fluctuations, magnetic focusing by the radially diverging heliospheric magnetic field, adiabatic cooling, and solar wind convection. In the case of shock-accelerated events, the propagation and evolution of the shock must also be taken into account. A particular source of uncertainty in our understanding of SEP propagation is a lack of knowledge of the particle scattering mean free path inside 1 AU.

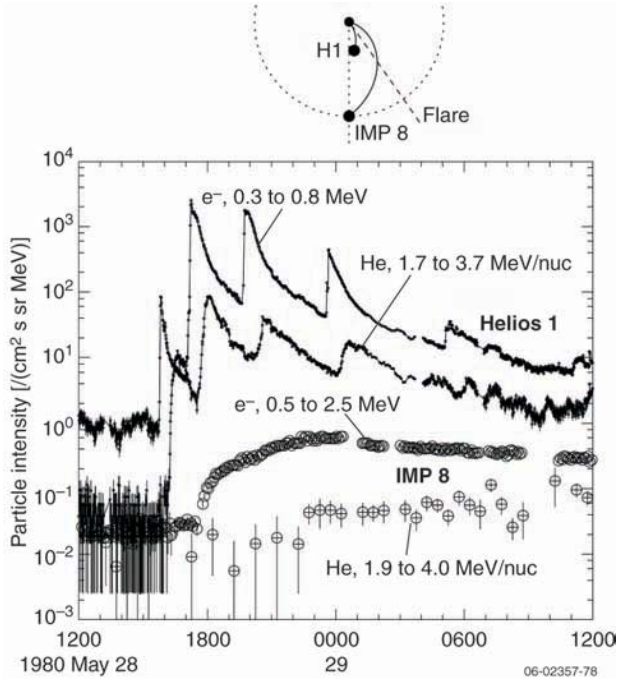

Figure 1-14. Electron and alpha particle time profiles recorded by Helios-1 at 0.3 AU and by IMP-8 at 1.0 AU during a series of impulsive particle events on 28 May 1980 [*Kallenrode and Wibberenz*, 1991]. Based on measured solar-wind speeds, Helios-1 was magnetically connected to W40°, close to the flare sites, while IMP-8 was magnetically connected to W70°. Whereas Helios-1 observed multiple injections, no such structures can be resolved in the intensity-time profile at 1 AU. If both spacecraft were observing the same events (and this is not certain), then this plot vividly illustrates both the effects of radial and longitudinal transport inside 1 AU and the need for observations as close to the Sun as possible [*Wibberenz and Cane*, Multispacecraft observations of solar flare particles in the inner heliosphere, submitted to *Astrophys. J.*].

a. What processes scatter and diffuse SEPs both parallel and perpendicular to the mean heliospheric magnetic field? SEP events observed at 1 AU typically show a rapid rise and slow decay of the particle fluxes, indicative of diffusive transport through the interplanetary medium presumably due to pitch-angle scattering of the SEPs by magnetic spatial fluctuations (waves and MHD turbulence) in the solar wind. In the inner heliosphere the scattering competes with the adiabatic focusing effect of the rapidly decreasing interplanetary magnetic field strength with distance from the Sun ($1/R^2$), sometimes leading to nearly scatter-free propagation in the inner heliosphere. The highly variable propagation of the SEPs is not well understood, nor is the origin of the magnetic fluctuations that do the scattering. MHD turbulence in the solar wind is thought to be generated by nonlinear interaction of Alfvén waves in the inner heliosphere, although this has not been measured experimentally. The evolution of the inertial range of this turbulence and its anisotropy may be important to SEP transport processes (see the discussion in Section 1.2.3.a below).

A process that appears to play a key role, both in shock acceleration and in the subsequent transport of the accelerated particles, is the amplification of Alfvén waves by streaming energetic particles (mostly protons) [*Lee*, 1983; *Tylka, Ng, and Reames*, 1999; *Ng, Reames, and Tylka*, 1999, 2003]. Recent simulations of SEP transport that incorporate wave amplification have demonstrated the effects of this process as it manifests itself in complex temporal and radial variations in SEP intensities and abundances [*Ng et al.*, 2003], and the simulation results generally agree well with observations (**Figure 1-15**). Wave amplification may also be responsible for determining the Q/A dependence of spectral breaks in most large SEP events [*Cohen et al.*, 2005; *Mewaldt et al.*, 2005b; *Li et al.*, 2005]. The SEP abundance variations calculated by the wave amplification model result from the modification of the rigidity-dependent scattering mean free path by the proton-driven wave growth (**Figure 1-16**).

Characterization of the evolving Alfvén wave distributions is essential for an understanding of SEP transport. At 1 AU, wave growth is so slow that it is difficult to detect it against background noise. In the inner heliosphere, however, wave growth is

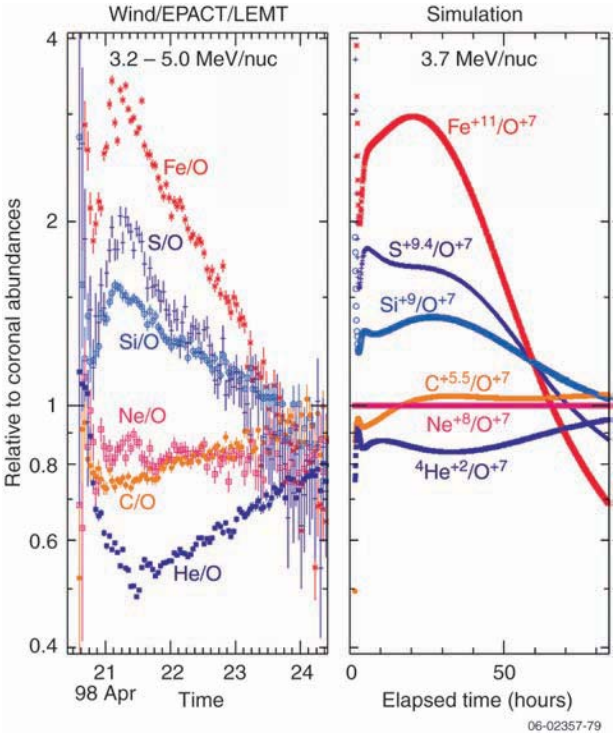

Figure 1-15. (a) Wind/EPACT hourly averaged elemental abundance ratios normalized to nominal coronal values. Data were acquired during the 20 April 1998 SEP event, one of the largest SEP events of solar cycle 23. These minor ions are particularly powerful probes of transport processes: they are genuine "test particles," too few in number to generate significant turbulence in themselves. These heavy ions also come in a wide range of charge-to-mass ratios, so that different ions at the same speed have different rigidities. (b) Simulation of the time-variation of these abundance ratios from the model of shock-accelerated SEP particles coupled to proton-amplified Alfvén waves. Reproducing these time-dependent elemental ratios requires that the model correctly deconvolve velocity- and rigidity-dependent effects in the particle transport. From *Tylka* [2001].

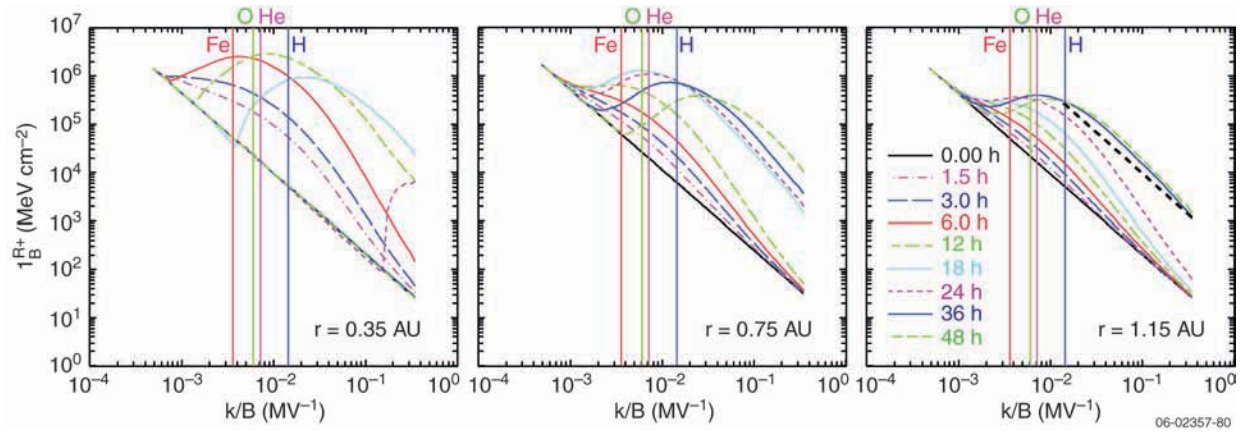

Figure 1-16. Model calculations of amplified wave spectra at various times from *Ng, Reames, and Tylka* [2003]. The three panels are calculations for 0.35, 0.75, and 1.15 AU. (Results are shown for 1.15 AU instead of 1 AU to compensate for the use of a radial magnetic field instead of the Parker spiral.) Vertical lines mark wave numbers that resonate with 2.6 MeV/nucleon Fe^{+14}, O^{+7}, He^{+2}, and H^{+} at cosine pitch angle $\mu = 1$. The black heavy-dashed line in the right panel shows an estimate of the typical background at 1.0 AU, based on observations from *Leamon et al.* [1998]. In this particular calculation, the solar protons are taken to have a relatively high intensity and hard spectrum. Nevertheless, the amplified waves at 1 AU barely exceed this background level. The larger wave growth at smaller radial distances may make it possible to observe these waves in more events than has been possible at 1 AU.

expected to proceed much more rapidly, and the amplified wave intensities there will be significantly larger [*Ng, Reames, and Tylka*, 2003]. Sentinels, therefore, may be able to observe proton-amplified waves in more events, under a larger range of plasma conditions, and over a broader range of wave numbers than is possible for a spacecraft at 1 AU. Such observations would elucidate the role of self-generated waves in modifying particle transport in gradual events and enable the development of improved, physics-based transport models, with more realistic treatments of scattering conditions.

A number of observations indicate that efforts to understand and model SEP transport in the

Table 1-2. Required and supporting measurements and modeling requirements for the Sentinels solar energetic particle (SEP) investigation. *(Italics indicate supporting measurements.)*

Science Objectives	Objective Questions	Required and Supporting Measurements	Modeling Requirements
1.1.1 Determine the roles of CME-driven shocks, flares, and other processes in accelerating energetic particles.	a. When and where are energetic particles accelerated by the Sun?	High/low energy ions/electrons, composition and charge states, suprathermal ions/electrons Neutron/gamma-ray, hard/soft X-rays Radio (type II and III) Coronal plasma conditions and composition *Solar wind ions, composition, and electrons* *Heliospheric DC and AC magnetic fields* *Photospheric magnetic field*	Shock acceleration Flare acceleration Global heliospheric magnetic field
	b. How are energetic particles observed at the Sun related to those observed in the interplanetary medium?	High/low energy ions/electrons, composition and charge states, suprathermal ions/electrons Neutron/gamma-ray, hard/soft X-rays Radio (type II and III) Solar wind electrons PADs (pitch-angle distributions) *Solar wind plasma* *Heliospheric magnetic field* *Photospheric magnetic field*	Shock acceleration Flare acceleration SEP transport Global heliospheric magnetic field
	c. What conditions lead to the jets/narrow CMEs associated with impulsive SEP events?	High/low energy ions/electrons, composition and charge states, suprathermal ions/electrons Neutron/gamma-ray, hard/soft X-rays Radio (type II and III) DC and AC magnetic fields Solar wind plasma Coronal plasma conditions and composition *Photospheric magnetic field*	Shock acceleration Flare acceleration SEP transport Global heliospheric magnetic field Coronal dynamics
	d. What physical processes accelerate SEPs?	High/low energy ions/electrons, composition and charge states, suprathermal ions/electrons Solar wind ions, composition, and electrons Neutron/gamma-ray, hard/soft X-rays Radio (type II and III) DC and AC magnetic fields Coronal plasma conditions and composition *Photospheric magnetic field* *Plasma waves*	Shock acceleration Flare acceleration SEP transport Global heliospheric magnetic field Coronal dynamics
1.1.2 Identify the conditions that determine when CME-driven shocks accelerate energetic particles.	a. What are the seed populations for shock-accelerated SEPs and how do they affect SEP properties?	High/low energy ions/electrons, composition and charge states, suprathermal ions/electrons Solar wind ions, composition, and electrons Hard/soft X-rays Coronal plasma conditions and composition *DC magnetic fields*	Shock acceleration Flare acceleration SEP transport Global heliospheric magnetic field Coronal dynamics
	b. How do CME/shock structure and topology as well as ambient conditions affect SEP acceleration?	High/low energy ions/electrons, composition and charge states, suprathermal ions/electrons Solar wind plasma DC and AC magnetic fields Plasma waves Coronal plasma conditions and composition *Energetic particle charge states* *Solar wind composition* *Solar wind electrons (PADs)*	Shock acceleration Flare acceleration SEP transport Global heliospheric magnetic field CME propagation
1.1.3 Determine how energetic particles are transported from their acceleration site and distributed in radius, longitude, and time.	a. What processes scatter and diffuse SEPs both parallel and perpendicular to the mean heliospheric magnetic field?	High/low energy ions/electrons, composition and charge states, suprathermal ions/electrons Solar wind plasma DC and AC magnetic fields Plasma waves *Solar wind electrons (PADs)*	SEP transport Global heliospheric magnetic field
	b. What are the relative roles of scattering, solar wind convection, and adiabatic cooling in SEP event decay?	High/low energy ions/electrons, composition and charge states, suprathermal ions/electrons Solar wind plasma DC and AC magnetic fields Coronal structures *Solar wind electrons (PADs)*	SEP transport Global heliospheric magnetic field Heliospheric transient model

inner heliosphere must also take into account transport perpendicular to the mean direction of the heliospheric magnetic fields. These observations include fine-scale temporal structure in the intensities of flare-accelerated ions [*Mazur et al.*, 2000]; similar time–intensity profiles seen by two spacecraft widely separated in heliolongitude and heliolatitude [*McKibben et al.*, 2001]; "radio delays" in type III radio bursts [*Cane and Erickson*, 2003]; and anisotropies in the fluxes of 40 to 90 MeV protons measured by Ulysses during the Bastille Day event of 14 July 2000 [*Zhang, Jokipii, and McKibben*, 2003]. Transport in both heliolatitude and heliolongitude has been attributed to a number of different processes. For example, *Mazur et al.* [2000] proposed that the fine-scale temporal structure in the ion intensities resulted from field-line mixing caused by the random-walk motion of the field-line footpoints in the photosphere (see also *Giacalone et al.* [2000].) *Ragot* [1999] has shown that the turbulence in the interplanetary medium should lead to a supradiffusive field-line spreading. As an alternative to field-line mixing *Ruffolo, Matthaeus, and Chuychai* [2003] propose that the ACE/ULEIS observations reflect a filamentary distribution of SEPs in the inner heliosphere caused by their temporary trapping in small-scale topological structures in solar wind turbulence. With increasing radial distance from the Sun, the field lines and SEPs escape from their topological "traps" and diffuse rapidly, producing the substantial SEP dispersion in longitude reported by *McKibben et al.* [2001]. Yet a fourth possibility, suggested recently by *Kaghashvili et al.* [2006], involves spatially and temporally varying turbulence along heliospheric field lines ("intermittent turbulence") and/or spatial inhomogeneities normal to the background magnetic field. The origin of the magnetic and electric fluctuations in the solar wind is presently not understood.

b. What are the relative roles of scattering, solar wind convection, and adiabatic cooling in SEP event decay? When the near-Sun SEP acceleration and injection phases have substantially declined, SEP intensities reach their peak and then begin to decay to background. The exponential decay times τ are expected to reflect primarily the processes of particle scattering, convection by the solar wind, and energy losses through adiabatic expansion of the SEP population. The relative importance of these processes must be understood in order to allow the duration of SEP events to be forecast. The timescale of each of these processes is expected to increase with the solar distance r at which the SEPs are observed. If adiabatic expansion is the principal decay process, then $\tau = 3r/2V\gamma$, where V is the solar-wind speed and γ is the power law exponent of the SEP momentum distribution [*Lee*, 2000]. Observations of ~10 MeV protons generally show that τ ~ 10 to 20 hours for gradual SEP events, with a weak inverse relation between τ and the associated shock speed and a strong inverse relation between τ and energy spectral index [*Daibog et al.*, 2003], as expected if convective and adiabatic losses are dominant effects.

1.2 The Origin, Evolution, and Interaction of CMEs, Shocks, and Other Geoeffective Solar Wind Structures

In addition to investigating SEPs, an equally important goal of the Sentinels mission is to understand the origin and evolution of interplanetary CMEs and their associated shocks as they propagate through the inner heliosphere. Fast CMEs are thought to be the primary sources of intense SEP events and are the main drivers of severe space weather at Earth (e.g., *Gosling* [1993]). For example, the "Bastille Day" solar storm of 14 July 2000, which consisted of a massive filament ejection, an X-class flare, and a fast halo CME, produced an intense gradual SEP event that saturated the detectors of many spacecraft for days and triggered a major geomagnetic storm (Dst_{min} = –301 nT) with associated upper-atmospheric disturbances that led to the loss of a research satellite. Astronauts in the International Space Station were ordered to take cover during the peak of the SEP event as a consequence of this solar eruption. CMEs/eruptive flares, therefore, are a core focus of the LWS program, and are prime science targets for all the upcoming solar/heliospheric missions—Solar-B, STEREO, and SDO. CMEs/eruptive flares also provide a unique opportunity for detailed study of MHD instability and nonequilibrium, processes fundamental to space physics and plasma astrophysics.

The combination of images from SOHO's EIT imager and LASCO coronagraph has shown that the onset of an earthward-directed CME can be observed 1 to 3 days before the main body of the

ICME or any accompanying shock impacts Earth's magnetosphere (e.g., *Brueckner et al.* [1998]). It is thus possible, in principle, to build a satellite warning system that would detect ICMEs well before they arrive at Earth or Mars. The problem, however, is that relativistic SEPs can appear within minutes of CME onset at the Sun, and will therefore reach Earth or Mars with essentially no warning. At present, the observation of an X-ray flare onset by the GOES spacecraft is the earliest possible detection of CME/eruptive flare onset. For most events, flare detection can provide less than an hour warning of SEP onset; and in the case of the large event of 20 January 2005, the detection of the associated X7 flare yielded a warning of only minutes (**Figure 1-17**). In order to provide useful warning of SEP events for the manned space exploration program, we must develop the capability to predict the onset of a CME/eruptive flare from observations of solar conditions. Developing this capability requires achieving a deep physical understanding of the CME/eruptive flare onset mechanism.

While the ability to predict CME onset is a necessary condition for developing a useful forecasting capability, it is not a sufficient one. Both the geoeffectiveness and the SEP-effectiveness of a CME depend on the speed, morphology, and possibly other properties, yet unknown, of the CME/ICME. With respect to the geoeffectiveness of an ICME, its direction and the strength and orientation of its magnetic field as well as its speed are of central importance. Development of a forecasting capability requires a knowledge and understanding of what the properties of an ICME are, how they are related to the structures observed at the Sun, how they evolve during the ICME's transit to 1 AU (and beyond), and how they are affected in their evolution by the density and velocity structures of the background solar wind, as well as by interactions with other transients. Sentinels will address these questions through multipoint in-situ measurements of ICMEs and the ambient solar wind at varying radial and azimuthal locations in the inner heliosphere. These measurements will make it possible to determine the global structure and topology of the ICMEs and, when correlated with in-quadrature coronagraphic observations from the Near-Earth Sentinel, to relate these to the erupting CMEs observed on the Sun. Measurements in the inner heliosphere are particularly important because they will allow Sentinels to capture features that are largely "washed out" by 1 AU.

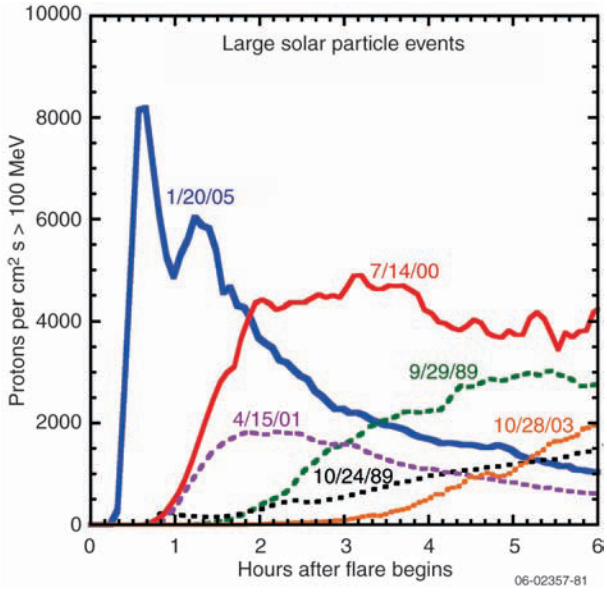

Figure 1-17. Time profiles of >100 MeV protons observed at Earth for some of the largest SEP events observed during the last two solar maxima. The 20 January 2005 event was the fastest rising event in the last 20 years of GOES data [*Mewaldt et al.*, 2005a].

The Sentinels STDT has formulated the baseline CME/ICME investigation in terms of the following three scientific objectives:

- Determine the physical mechanisms of eruptive events that produce SEPs.
- Determine the multiscale plasma and magnetic properties of ICMEs and shocks.
- Determine how the dynamic inner heliosphere shapes the evolution of ICMEs.

In the next sections we consider each of the three science objectives in turn, and discuss how Sentinels will be able to address them. **Table 1-3** at the end of Section 1.2 (p. 1-32) summarizes the measurement requirements for the Sentinels CME/ICME investigation.

1.2.1 Determine the physical mechanisms of eruptive events that produce SEPs. The mechanism for CME onset is still not fully understood, but significant progress has been made in recent years due, in large part, to the new observations from SOHO and TRACE and to major advances in theoretical and numerical modeling. It is widely

accepted that CMEs result from the explosive release of energy stored in the strongly sheared magnetic field of a filament channel. The key observation is that all CMEs and flares are associated with sheared filament channels, which are the only location in the corona where the magnetic field appears to be strongly non-potential, so that substantial energy can be stored. From a large body of theoretical and numerical modeling, the general picture has emerged that a CME represents the catastrophic disruption of the force balance between the upward magnetic pressure gradient of sheared filament field and the downward tension of overlying quasi-potential coronal field (see reviews by *Forbes* [2000], *Klimchuk* [2001], *Low* [2001], and *Linker et al.* [2003]).

To advance our understanding of the physical origins of CMEs and the resulting SEPs and thus to provide a basis of the development of a useful first-principles prediction capability, the Sentinels mission will seek to answer the following three focused science questions: (a) What solar conditions lead to CME onset? (b) How does the pre-eruption corona determine the SEP-effectiveness of a CME? (c) How close to the Sun and under what conditions do CME-driven shocks form?

a. What solar conditions lead to CME onset? Two basic theories have been proposed for CME onset, distinguished primarily by their different assumptions regarding the structure of the pre-eruptive filament channel field (**Figure 1-18**). In one class of models, the pre-eruption topology is that of a twisted flux rope, formed either by emergence through the photosphere or reconnection there [*van Ballegooijen and Martens*, 1989; *Forbes and Isenberg*, 1991; *Amari et al.*, 2003; *Roussev et al.*, 2004]. The flux rope models postulate that the twist increases until some threshold for the occurrence of a loss-of-equilibrium or an ideal instability, such as a kink, is reached. This ideal process is assumed to disrupt the force balance on a fast, Alfvénic, timescale, leading to an explosive eruption. In the second class of models the topology of the filament channel is that of a three-dimensional sheared arcade [*Antiochos et al.,* 1994], and twist is assumed to play essentially no role in either the initial state or the disruption. The critical process that leads to eruption is magnetic reconnection, so these models are inherently non-ideal. These models postulate that reconnection removes overlying field, thereby weakening the downward tension and allowing for an explosive upward expansion of the filament channel. The reconnection models include tether-cutting, in which the reconnection is presumed to occur inside the filament channel [*Moore et al.,* 2001], and breakout, where the onset reconnection occurs above the filament channel in the overlying, quasi-potential field [*Antiochos et al.*, 1999].

In spite of decades of detailed imaging observations at all wavelengths, the topology of a filament channel is still unknown, so that both classes of

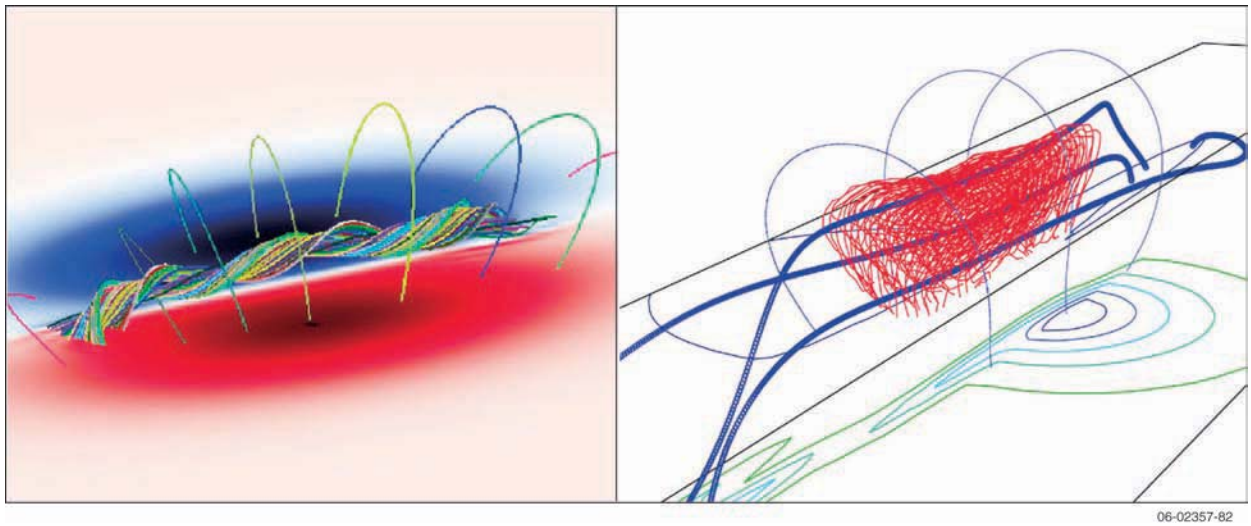

Figure 1-18. Left: Example of the twisted flux rope model from a three-dimensional simulation by *Amari et al.* [2003]. Right: Example of the sheared arcade model from a three-dimensional simulation by *Devore and Antiochos* [2000].

models are still viable. There are two main reasons for this lack of critically important knowledge. First, it is very difficult to measure the coronal magnetic field directly by Zeeman splitting, as in the photosphere. Even if new instrumentation proves capable of measuring the coronal field, the measurements will consist of a complex integration of many features along the line-of-sight because coronal plasma is optically thin. It will be highly problematical for such measurements to distinguish the subtle topological distinctions between a weakly twisted flux rope and a sheared arcade. Second, it is very difficult to infer the magnetic field line geometry from observations of filament channel plasma. The plasma that is easily observed is the cool prominence material, which consists of a collection of small condensations that do not fill a complete coronal flux tube and, hence, do not uniquely outline the field line geometry. At coronal temperatures the filament channel generally appears only as a lack of emission, the so-called cavity. It seems unlikely, therefore, that imaging by itself will be able to reveal the pre-eruption topology responsible for CMEs.

By combining imaging with in-situ measurements of CME magnetic and plasma structure as close to the Sun as possible, Sentinels will be able to determine the pre-eruption flux rope topology and thus will be able to establish the CME onset mechanism. Both the flux rope and the reconnection models predict that, because of the flare reconnection below the eruption, the topology of the ejected filament channel will resemble that of a highly twisted flux rope [*Lynch et al*., 2004]; however, the models predict very different plasma distributions within this structure. In the twisted rope models, the rope is present well before eruption so that the plasma at the axis of the rope should be undisturbed, cold filament plasma. In the reconnection models, on the other hand, the rope forms as a result of the flare reconnection that follows eruption, so the plasma on axis should be heated and energized by reconnection. By measuring the temperatures, charge states, etc. of the on-axis filament plasma of the ejected flux rope, Sentinels will make it possible to test the two classes of models. Of course, this is valid only for CMEs that include the eruption of a cold, dense filament—hence the importance of having imaging data in conjunction with in-situ measurements.

An important point is that the ejected structure will consist of a combination of the filament channel and overlying coronal field and, hence, may not be a single, simple rope. Determining the location of the filament channel and its magnetic axis will be challenging. In addition, the rope is likely to evolve as it moves outward, (see, e.g., *Lynch et al*. [2004]). Consequently, it is essential that the field be sampled as close to Sun and in as many locations as possible in order to pin down the detailed magnetic topology and plasma properties of the ejection, including the innermost structure of the filament channel. Sentinels is designed to address this task. The four IHS spacecraft will provide in-situ measurements at multiple locations close to Sun, while the NES wide-field coronagraph will observe the global topology of the ejection as it passes over the in-situ spacecraft. In addition, the combination of the 2π magnetic field observations from FSS with the next-generation three-dimensional MHD models that will be available by the time Sentinels flies will make it possible to predict the magnetic structure of the ejection, especially that of the large-scale coronal fields. Finally, IHS will use X-ray imaging, stereoscopic tracking of type III radio emissions, and in-situ measurement of the suprathermal electrons to trace magnetic field lines through the inner heliosphere; field line length will be determined through analysis of the velocity dispersion in impulsive events. These observations will provide detailed information on magnetic structure and connectivity. This comprehensive suite of measurements and models will enable us to characterize CME topology and plasma properties in unprecedented detail and therefore allow us to determine the mechanism for CME eruption. This achievement would be a tremendous scientific breakthrough and a major milestone for the LWS program and would provide the foundation for the development of a true first-principles prediction capability.

b. How does the pre-eruption corona determine the SEP-effectiveness of a CME? The active region field and the interaction of the erupting CME magnetic field with the large-scale overlying corona play critical roles in determining the propagation speed and SEP-effectiveness of CMEs. It has been established observationally that fast CMEs capable of driving strong shocks are much more likely to be SEP-effective than slow CMEs; however, as pointed out in Section 1.1.2 above, not all fast CMEs are equally SEP productive [cf. *Reames*, 2000]. Observations indicate that fast CMEs originate

almost exclusively from active regions and, theoretically, it seems evident that only in active regions is the magnetic field sufficiently strong and contains sufficient free energy to produce a large ejection (e.g., *Forbes* [2000]). CME speed and, therefore, kinetic energy have been shown to correlate well with active region magnetic energy (e.g., *Venkatakrishnan and Ravindra* [2003]). From a detailed study of the 2003 "Halloween" events, *Gopalswamy et al.* (2005b) concluded that the extreme size, speed, and SEP productivity of those events were due to the size and energy of the associated active region. In addition to active region structure, the structure of the surrounding global corona also plays an important role in determining CME speed and SEP-effectiveness. For these same Halloween events, *Liu and Hayashi* [2006] concluded that the presence of surrounding or nearby coronal holes substantially enhanced the propagation speeds of the CMEs.

The Sentinels program is designed to make major advances in observing, understanding, and predicting the effect of coronal magnetic fields on CME properties. With the 2π magnetic field coverage and the improved coronal and heliospheric models developed by the Sentinels program, we will be able to determine with unprecedented accuracy the detailed structure of both the active region field that overlies an erupting filament channel and the global coronal field, including any nearby open field regions. In addition, through a combination of imaging with the NES wide-field coronagraph and in-situ measurements by the four IHS spacecraft, Sentinels will be able to measure the speed and size of a CME from its earliest initiation out to the inner heliosphere. These pioneering observations will reveal how the active region and surrounding coronal structure determine CME speed and how magnetic and drag forces subsequently affect CME acceleration.

c. How close to the Sun and under what conditions do shocks form? Fast shocks form when CME speeds exceed the characteristic fast-mode MHD wave speed, which is highly dependent on the magnetic and density distribution in the corona. A recent calculation [*Gopalswamy et al.*, 2001a] compares radial speed profiles through model active regions (AR) and the quiet Sun (QS) (**Figure 1-19**). Type II radio emission is expected to begin when the CME Mach number exceeds 1.4 [*Mann et al.*, 2003], which could occur as low as about 1.2 R_S. Close to the Sun the generally radial magnetic fields should give rise to quasi-perpendicular shocks at CME flanks and parallel shocks above CME leading edges [*Steinolfson*, 1992; *Mann et al.*, 2003; *Kahler*, 2004]. The IHS spacecraft will be able to determine from SEP onsets when the first shock particle emission occurs. It is currently believed that SEP particle generation by CME-driven shocks begins as low as 5 R_S [*Kahler*, 1994] or possibly lower, but remote observation of shocks in this region (falling in the decameter-hectometric wavelength domain of type II radio bursts) are limited only to the fastest and widest of CMEs [*Gopalswamy et al.,* 2001b]. Therefore, in addition to determining the physical mechanism of CME eruption, observing the CME-driven shocks that accelerate particles and the conditions under which they form is essential for the development of a reliable SEP predictive capability.

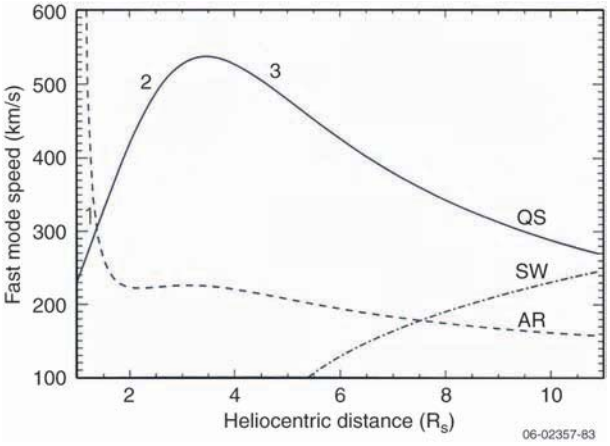

Figure 1-19. Fast-mode MHD speeds for a model active region (AR) and the quiet sun (QS). A typical solar wind speed profile (SW) is shown for comparison [*Gopalswamy et al.*, 2001a].

In addition, the MHD models have now reached a level of sophistication that they can be used to calculate the formation of CME-driven shocks low in the corona using actual observations as input. The main limitations of such models are the numerical resolution and the lack of a robust physical mechanism for CME initiation. We expect that the Sentinels Interdisciplinary Team Modeling Program will increase our capabilities in numerical simulation by orders of magnitude by the time Sentinels flies, and that as discussed above, Sentinels will deliver the understanding required to determine the CME

onset mechanism. Recent studies using SOHO UVCS observations have demonstrated how ultraviolet (UV) spectroscopy and the combination of UV and radio observations can be used to determine the plasma and field conditions in coronal CMEs and leading shocks [*Raymond et al.*, 2000; *Raymond*, 2002; *Mancuso et al.*, 2002, 2003]. At distances of 0.25 to 0.75 AU the IHS spacecraft will be able to determine the shock characteristics and related SEP acceleration directly. By combining next-generation modeling with the advances in UV spectroscopy we expect to be incorporated in the NES/UVSC instrument and with IHS in-situ observations in the inner heliosphere, the Sentinels program will be able both to observe and to model CME-driven shocks as they first form low in the corona and propagate outward, which is an essential step toward first-principles prediction of SEPs.

1.2.2 Determine the multiscale plasma and magnetic properties of ICMEs and shocks. In addition to their role in SEP acceleration, fast CMEs are the principal drivers of severe geomagnetic disturbances. Because of the potentially serious adverse effects of such disturbances on spacecraft, communications and navigation systems, and power transmission grids, developing the ability to predict the occurrence of "geoeffective" events is an important goal for the LWS program. Of particular interest are magnetic clouds (MC)—a subset of ICMEs characterized by a large and smooth rotation of the magnetic field direction, enhanced magnetic field magnitude, and low-plasma β and proton temperature. Owing to their size (~0.25 AU in diameter) and magnetic field structure, the passage of an MC can result in an extended period of strong southward B_z and hence increased transfer of energy, mass, and momentum into the magnetosphere as a result of sustained magnetic reconnection.

The geoeffectiveness of an ICME is determined by its speed and direction and, most importantly, by the structure, orientation, and strength of its magnetic field. While detecting the onset of a fast, earthward-directed CME is important and provides 2 to 3 days of warning that a magnetic storm may occur, it is not sufficient to determine whether the associated ICME will trigger a geomagnetic storm or how severe an eventual storm might be. For example, SOHO observed a fast, intense halo CME on 17 February 2000 (**Figure 1-20**), which was

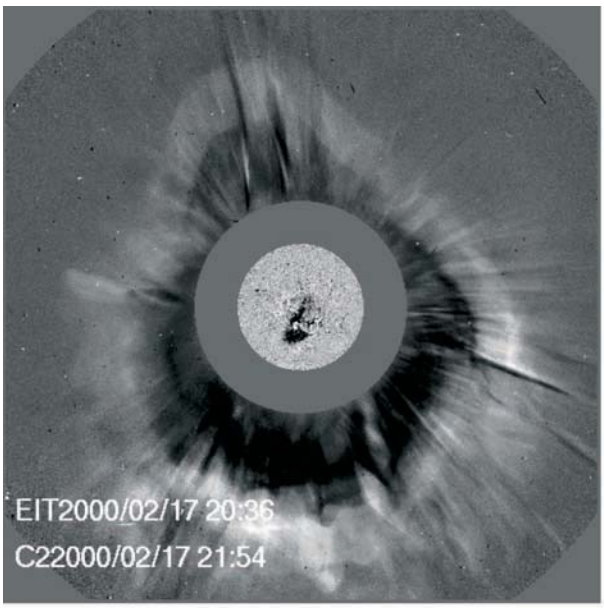

Figure 1-20. Composite of SOHO/EIT and LASCO C2 images showing the filament eruption and halo CME of 17 February 2000.

accompanied by an M-class flare. Although "active to minor storm levels with possible major storming at higher latitudes" were forecast for this event, the halo CME had negligible geoeffectiveness, producing only a minor rise in the Kp index. (Although not geoeffective, the CME did produce an SEP event observed by GOES at $E > 10$ MeV.) Conversely, CMEs that appear much less impressive near the Sun can produce much stronger geomagnetic disturbances.

To complicate the matter further, while there is a very good correlation between ICMEs at 1 AU and coronal CMEs [*Gopalswamy et al.*, 2000], the reverse is not true. Even when limiting the study to only front-side full-halo CMEs, *Michalek et al.* [2004] found that only 83 out of 123 solar events had discernible 1 AU counterparts. What happened to a third of the CMEs? Were they processed by the solar wind so much that they became indistinguishable from the background flow? Or were they deflected by an unusual amount so that they missed Earth?

Because of the importance of ICMEs as SEP accelerators and drivers of geomagnetic activity, understanding and characterizing their properties has been identified as a key science objective of the Sentinels mission. To address this objective, a combination of in-situ measurements, remote-sensing

observations, and modeling studies will be used to answer two key questions: (a) How does the global three-dimensional shape of ICMEs/shocks evolve in the inner heliosphere? and (b) How does CME structure observed at the Sun map into the properties of interplanetary CMEs?

a. How does the global shape of ICMEs/shocks evolve in the inner heliosphere? As noted above, magnetic clouds are an especially geoeffective subset of ICMEs. MCs are conventionally represented as loop-like twisted flux ropes with both legs connected to the Sun (cf. **Figure 1-21**). Their central axes may lie in the ecliptic plane or may be inclined up to 90° from it, with the orientation of the axes and the chirality of the MC's helical fields being generally correlated with the tilt and chirality of the associated erupting filaments [*Webb et al.*, 2000; *Bothmer and Rust*, 1997; *Ruzmaikin, Martin, and Hu, 2003*]. While localized observations from MC passages by single spacecraft can be fitted with simple cylindrical force-free flux rope models [e.g., *Lepping et al.*, 1990], a number of studies (e.g., *Mulligan and Russell* [2001]; *Riley and Crooker* [2004]) have indicated that MCs are not cylindrically symmetric, but should have a flattened, "pancake" shape when viewed in cross-section. The evolution of MCs as they propagate through the inner heliosphere has been simulated with both kinematic models [*Riley and Crooker*, 2004] and MHD models [*Odstrcil and Pizzo, 1999a, 1999b; Vandas, Odstrcil, and Watari*, 2002; *Odstrcil, Riley, and Zhao*, 2004]. These studies have shown how the shape of a magnetic cloud can be deformed by the effect of solar rotation (as suggested by *Marubashi* [1997]) and by the interaction of the ejecta with the ambient solar wind (**Figure 1-22**). The distortion of cloud morphology during propagation through the inner heliosphere will also affect the surface geometry of the associated shocks driven on both the global and local scales, which would have significant impact on particle acceleration processes. In addition to the kinematic and dynamic influences, the development of the flux rope may also be affected by reconnection with the interplanetary magnetic field [*Cargill and Schmidt*, 2002].

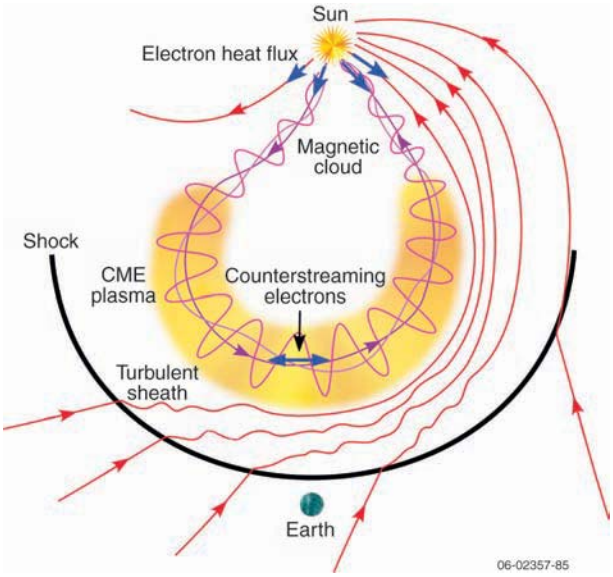

Figure 1-21. Notional structure of ICMEs, as they evolve through the heliosphere. This picture is based mostly on single-point measurements. Multipoint measurements by the Inner Heliospheric Sentinels spacecraft will make it possible to determine the global structure of ICMEs [*Zurbuchen and Richardson*, 2006.]

Magnetic clouds account for only 30% to 50% of all ICMEs observed at 1 AU, with their number varying, according to a recent study, from ~100% around solar minimum to ~15% around solar maximum [*Richardson and Cane*, 2004]. Non-MC ICMEs, which according to this study dominate near solar maximum, have a considerably more complex, disordered magnetic structure [*Burlaga et al.*, 2001]. Burlaga et al. suggest several possible scenarios to account for the complex topologies observed in these ejecta, including collisions among several successive CMEs and the interaction between an MC and a complex ICME that overtakes it. The complex, tangled field observed in the ICME may also simply have been present in the original ejection. A similar explanation is offered by *Richardson and Cane* [2004], who suggest that dominance of complex, non-MC ICMEs around solar maximum reflects the more dynamic, complex coronal magnetic field during periods of increased activity.

While STEREO will make significant progress toward determining the longitudinal extent of MCs at 1 AU, multipoint observations by IHS at radially and longitudinally separated locations within the inner heliosphere are required to determine deviations from the cylindrical symmetry of the Lundquist force-free field (such as flattening of the flux rope); the curvature of the rope axis; the azimuthal (longitudinal) width; the bending of the legs toward the prevailing spiral IMF; the radial and azimuthal

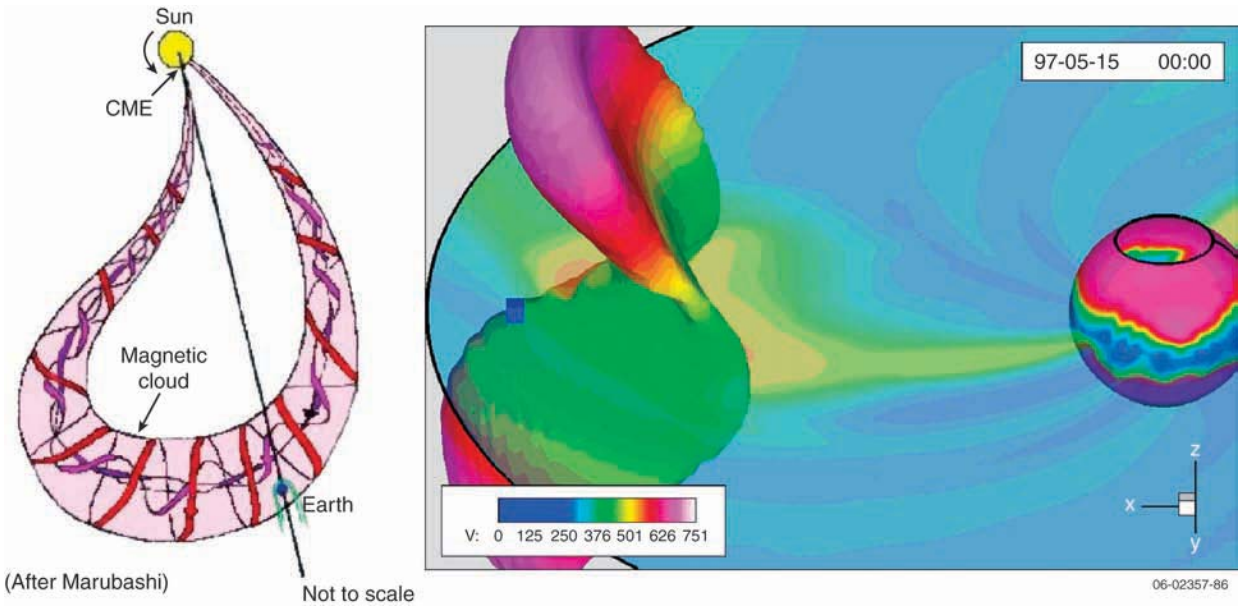

Figure 1-22. Left: A teardrop-shaped magnetic cloud flux rope geometry (after *Marubashi* [1997]). Right: three-dimensional MHD simulation of an ICME [*Odstrcil et al.*, 2004]. The injected cloud is shown as an iso-surface at 25% of maximum density. The color scale shows the flow velocities on the iso-surface and from the solar source surface. The blue box toward the left of this panel shows the Earth's position.

expansion rates, and any variations of magnetic chirality through the MC. In-situ measurements of interplanetary magnetic fields and solar wind plasma with a cadence of 1 to 10 min are required to identify the boundaries of the passing MCs, while electron pitch-angle distributions, electromagnetic plasma waves, and solar wind composition measurements will provide useful additional markers for more complex ejecta. EUV observations of the solar corona will be used to identify the erupting filaments associated with the ICMEs/MCs. In addition, side views of ICMEs in white-light coronagraph images will provide insight into the initial configuration of the ejecta. Multipoint radio observation of type II bursts from interplanetary shocks will allow triangulation and hence determination of shock geometry by remote sensing, significantly augmenting in-situ shock observations. Fine structure in radio type II bursts is generated by multiple quasi-perpendicular contact points at the shock; therefore type II fine structure is a probe of ICME structure, which is likely to evolve with radial distance. Several approximations about MC structure and dynamics will be needed even with sampling by the four IHS spacecraft to adequately characterize the spatial and temporal variations of MCs. Defining the global structures of the non-MC ICMEs will be difficult even with the four IHS spacecraft; but, as mentioned above, magnetic field line tracing by suprathermal electrons (e.g., *Larson et al.* [1997]) will provide powerful diagnostics.

b. How does CME structure observed at the Sun map into the properties of interplanetary CMEs? White-light coronagraph images of CMEs at the Sun typically show a distinct three-part structure composed of a bright loop, a dark cavity, and a bright core [*Illing and Hundhausen*, 1985]. The bright core is believed to consist of cold, dense prominence or filament material; the dark, low-density cavity is thought to be an expanding magnetic flux rope (see, e.g., *Plunkett et al.* [2000] and references therein); and the loop is streamer/coronal material that is swept up as the flux rope moves outward. The relation of the prominence/filament material to the flux rope—i.e., whether or not the prominence is an intrinsic part of the flux rope [*Low*, 1994]—is a question of fundamental importance and a matter of some controversy (e.g., *Gopalswamy et al.*, [1998]; *Leamon, Canfield, and Pevtsov* [2002]; *Rust et al.* [2005]; *Gibson et al.* [2006]).

In-situ observations have, in several cases, revealed the presence of a "plug" of cold, dense

plasma trailing the flux rope, which has been interpreted as remnant material from the erupting filament (the bright core seen in coronagraph images) [*Burlaga et al.*, 1998; *Gopalswamy et al.*, 1998; *Ho et al.*, 2000]. However, filament plasma (indicated by an enhanced He^{+}/He^{++} ratio) has not been observed in the vast majority of ICMEs [*Crooker*, 2004]. The question thus arises, What is the fate of the erupting filament plasma as the CME propagates into interplanetary space? The traditional answer is that the filament is so small relative to the CME that spacecraft simply miss it most of the time. As an alternative explanation, however, *Crooker* [2004] suggests that the filament plasma is present but has lost "its expected low-charge-state signature" because of heating. If cold, dense "untransformed" filament plasma is present in an ICME, multipoint measurements by IHS will increase the likelihood of its being detected. Detection by several spacecraft in different locations will make it possible to determine the spatial extent of the filament material. With respect to the alternative explanation, through composition and charge-state measurements in the ICME early in its evolution, IHS may be able to observe the postulated heating of the filament plasma and loss of its ionization signature as well. Additionally, as noted above (Section 1.2.1.a), detection of cold filament plasma would be evidence for the twisted flux rope model of CME initiation.

ICMEs/MCs are conventionally pictured as closed magnetic structures, with both legs rooted in the corona, and identifiable by the observation of counterstreaming or bidirectional suprathermal electrons. However, several studies of counterstreaming electrons in magnetic clouds have shown that bidirectional flows are often not continuously observed in clouds but are seen only for intervals of varying duration, indicating that "[a]lthough magnetic clouds at 1 AU are observed as coherent structures, most often they comprise a random mix of several intertwined volumes of magnetic open and closed field lines" [*Shodhan et al.*, 2000]. The opening up of an originally closed CME may result from magnetic reconnection between the leg of the CME and the open field of an adjacent coronal hole, a process referred to as "interchange reconnection." This process, possibly driven by the global motion of open field lines, has been proposed as the primary mechanism for preventing the continual buildup of magnetic flux in the heliosphere from the eruption of CMEs [*Crooker et al.*, 2002]. Although interchange reconnection has been widely invoked theoretically as a fundamental process in coronal evolution and in SEP escape, its observational signatures in the heliosphere are far from understood and are the subject of intense debate. The Sentinels observations and modeling are expected to advance our understanding of this fundamental process significantly.

Sentinels will establish the coronal structure of CMEs with coronagraph and spectrograph observations from the NES and correlate these observations with in-situ measurements of the solar wind plasma and magnetic field at least at two different radial locations. Through in-situ measurements at different radial and azimuthal positions, the location and nature of significant topological evolution can be determined. High-sensitivity multipoint observations of suprathermal electrons, coupled with the detection of type III radio emissions and soft X-ray flares, will allow the detailed mapping of magnetic field line connectivity within ICMEs. Observations of helium enhancements and cool filament material within MCs and determination of the exterior configuration of draped fields and displacement of the heliospheric current sheet (HCS) will make it possible to relate MCs to solar source regions.

Composition measurements by IHS will be an important source of information about the evolution of the internal structure of ICMEs. Magnetic clouds often show unusual thermodynamics. The plasma shows unusually high ionic charge states, indicating electron temperatures of several million degrees. Furthermore, their locally observed temperatures and densities indicate extensive heating of these clouds throughout the heliosphere, perhaps resulting from the continuing heat flux from electrons along the magnetic field line. The compositional signatures within an ICME show significant variations [*Lepri et al.,* 2001], which may result from the evolution of the ejecta and mixing of the original content with interplanetary material or might reflect that CMEs contain spatially distinct plasma populations at the time of their initiation [*Antiochos*, 1998]. Solar wind plasma composition observations of the same ICME at different radial locations will thus be essential for determining the evolution of the ICME internal structure.

1.2.3. Determine how the dynamic inner heliosphere shapes the evolution of ICMEs. Predicting the SEP-effectiveness and geo-effectiveness of an ICME requires, in addition to knowledge of CME onset and structure, knowledge of the effects of the interaction with the background solar wind on the structure, speed, and direction of the ICME. The effects of this interaction are illustrated in the right panel of **Figure 1-22** above, which shows how the velocity difference between fast and slow solar wind streams shapes the structure of a simulated ICME (see the discussion of this simulation in Section 1.2.3.b below). Another example of the influence of the interplanetary medium on an ICME is the intensification of the southward fields in the trailing portion of a magnetic cloud that results from its compression by a following high-speed stream. In addition to interacting with the quasi-stationary wind, ICMEs have also been observed to interact with one another, leading in some cases to the formation of transient flows with highly complex magnetic interiors.

Understanding and characterizing the interaction with the ambient solar wind and its influence on the propagation and properties of ICMEs have thus been established as a major objective of the Sentinels mission. Sentinels will (a) measure the background wind and relate the observed velocity, density, and magnetic structures to their coronal sources; (b) investigate the effects of the wind thus characterized on the ICMEs whose evolution Sentinels is tracking through both multipoint in-situ measurements and remote-sensing observations; and (c) provide the first multipoint measurements of the mutual interactions among ICMEs. The following sections develop these aspects of the Sentinels investigation further.

a. How is the solar wind in the inner heliosphere determined by coronal and photospheric structure? Understanding the evolution of ICMEs, with respect to their effectiveness both as SEP accelerators and as drivers of geomagnetic disturbances, requires a knowledge of the state of the ambient quasi-steady solar wind and its relation to source regions at the Sun. The bimodal character of the solar wind—a fast stream originating in magnetically open polar coronal holes and a slower, denser, more variable stream associated with the closed magnetic structures of the streamer belt—has been well documented, as has been the variability of the structure of both the corona and the solar wind with increasing levels of solar magnetic activity [e.g., *Snyder, Neugebauer, and Rao*, 1963; *Rosenbauer et al*., 1977; *Schwenn*, 1990; *McComas et al*., 1998]. Around solar minimum, the corona is characterized by the presence of large coronal holes, with a well-defined belt of streamers encircling the magnetic equator. The quasi-stationary wind is dominated by the high-speed flow. Approaching and at solar maximum, the structure of the corona becomes disordered and chaotic, with streamers and smaller coronal holes observed at all heliolatitudes; and the solar wind consists of variable, slow- and moderate-speed flows, punctuated by the increased passage of transients. As discussed in the next section, ICMEs and associated shocks can be significantly affected by the structure of the solar wind [*Odstrcil and Pizzo*, 1999a, 1999b; *Odstrcil et al*., 2004].

If a coronal hole boundary is inclined by some angle relative to the solar equatorial plane, a high-speed stream will overtake and interact with a slow-speed stream from the streamer belt, producing compression and rarefaction regions that co-rotate with the Sun. The compressed region at the interface of the two streamers is known as a co-rotating interaction region (CIR) [*Gosling and Pizzo*, 1999]. CIRs occur during the declining phase of the solar cycle, when the Sun's magnetic axis is strongly tilted relative to the rotational axis. CIRs are often the site of strong southward B_z; and, passing the Earth in phase with the Sun's rotational period, they are the cause of the geomagnetic storms that recur with a ~27-day period during the declining phase of the solar cycle. ICMEs may interact with CIRs, contributing to the intensity of recurrent geomagnetic storms [*Crooker and Cliver*, 1994; *Crooker and McAllister*, 1997].

In addition to providing contextual information required to understand how ICMEs are modified by their interaction with the ambient solar wind, multipoint measurements by Sentinels in the inner heliosphere, together with remote-sensing observations of the corona and the photosphere, will enable researchers to address fundamental questions about the nature of the solar wind in the early stages of its evolution and about its association with the source regions on the Sun. For example, multipoint measurements by IHS of the solar wind in the early stages of its evolution will provide valuable insights into the evolution of low-frequency magnetic and

plasma fluctuations that may bear the imprint of photospheric and coronal processes (see, e.g., the review by *Goldstein et al.* [1995] and references therein). At higher frequencies, or smaller spatial scales, the character of the heliospheric spectrum becomes turbulent, a signature of its dynamic evolution; and at even smaller scales, energy is dissipated and transferred to heat.

Solar wind MHD turbulence observed at 1 AU is commonly thought to be generated primarily by the transverse gradient in the radial velocity (i.e., shear) that is prevalent in the inner heliosphere [*Roberts et al.*, 1987, 1992] or by nonlinear interaction of Alfvén waves in the inner heliosphere, although this has not been measured experimentally. Helios observed a fully developed inertial range of turbulence dominated by outward-propagating Alfvén waves at 0.3 AU, while at 1 AU the solar wind turbulence is a mixture of inward and outward propagating waves [e.g., *Tu and Marsch*, 1995]. Spectral power law indices of ~5/3 are exhibited by the magnetic, electric (at 1 AU), density, and velocity power spectra. The study of the evolution of the inward-propagating component, the spectral slope, and the anisotropy of MHD turbulence is crucial to understanding the physics of the turbulence cascade process. MHD turbulence is thought to play a key role in the transport of SEPs (as discussed above) and the evolution of the inertial range and its anisotropy may be important to transport processes.

At frequencies of the order of 1 Hz, magnetic and electric fluctuation spectra exhibit a breakpoint, and the spectral slope deviates from ~5/3; this is thought to mark the beginning of the "dissipation" or "dispersion" range of turbulence. At 1 AU, this frequency corresponds to the convected ion gyro or inertial lengths, above which the ions are demagnetized. At shorter wavelengths, the turbulence becomes more electrostatic (at 1 AU [*Bale et al.*, 2005]) and may be responsible for scattering the solar wind ions and electrons and maintaining their relative isotropy [*Kellogg*, 2000]. To fully understand this process of solar wind thermalization, electric and magnetic measurements are required from the inner heliosphere to 1 AU, and the evolution of the breakpoint and electrostatic components must be measured. Models of solar wind acceleration by damping of MHD turbulence also make specific predictions for the evolution of the turbulence. *Coles et al.* [1991] inferred enhanced power in density fluctuations (from IPS measurements) near the expected breakpoint at out to 30 R_S. The compressibility of turbulence in the inner heliosphere will determine if this is representative of the MHD cascade or not.

Solar wind density turbulence also plays a key role in the generation and scattering of interplanetary (type II and III) radio emissions. Langmuir waves generated by SEP electron beams are scattered in the density fluctuations, a process that may affect both the wave growth rate and the radio emission process itself. The parameterization of this process will help us understand the observed radio emissions.

Fine-scale density structures, observed in modern high-resolution coronagraph images (**Figure 1-23**), likely reach 0.25 AU before they are washed out due to stream interactions. These solar wind inhomogeneities are likely coupled to variable flow speeds. This picture can be validated only by making in-situ observations of the solar wind structure at 0.25 AU, coupled with turbulence measurements at larger distances along the same solar wind flow line. The Sentinels mission offers

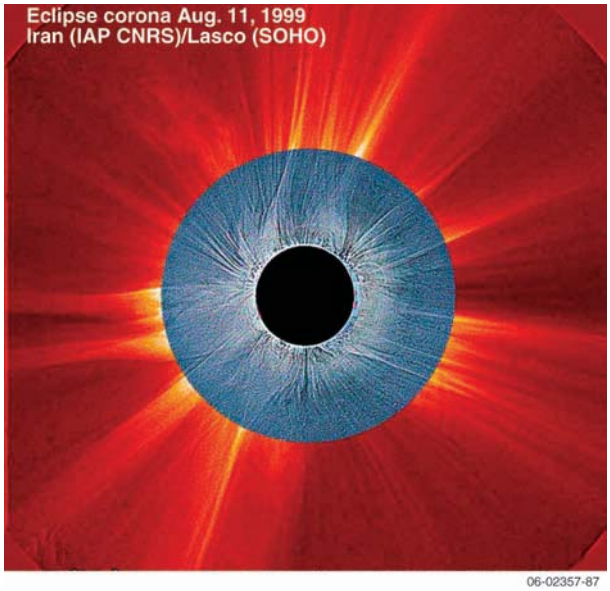

Figure 1-23. Composite image of the corona at the time of the eclipse on 11 August 1999 and approaching solar maximum [*Koutchmy et al.*, 2004]. Instead of being confined to a belt encircling the magnetic equator, streamers are present at all heliolatitudes, a configuration of the corona characteristic of the active Sun. The inner part is the white-light eclipse image obtained in Iran by J. Mouette at 12:03 UT. The outer part is the SOHO/Lasco-C2 image made at 12:06 UT. The imprint on the solar wind of the fine-scale coronal structure is largely washed out by 1 AU, but is expected to be observable by the Inner Heliospheric Sentinels spacecraft at 0.25 AU.

an unprecedented opportunity to characterize the turbulent evolution of the solar wind from 0.25 AU to 1 AU, with profound implications for our understanding of the heliosphere and its connection to the corona as well as for our understanding of energetic particle scattering, field line wandering in the interplanetary medium, and solar wind heating.

b. How do ICMEs interact with the pre-existing heliosphere? The velocity and density structure of the ambient solar wind modifies the speed and structure of ICMEs as they propagate from the Sun to 1 AU and beyond. As noted above, understanding the nature of this interaction and its effects on the properties of an ICME and its associated shock is a necessary condition for developing the capability to forecast the geoeffectiveness (and SEP-effectiveness) of an ICME.

The acceleration/deceleration of ICMEs during their transit to 1 AU has been the subject of several studies [*Gosling and Riley*, 1996; *Gopalswamy et al*., 2000; *Vrsnak and Gopalswamy*, 2002; *Cargill*, 2004]. The effect of the solar wind interaction of ICME velocity is well illustrated by a recent study of ICME/shock propagation times based on Helios in-situ data and Solwind coronagraph observations. The analysis of travel times vs. ICME/shock speeds reveals substantial scatter around the "ideal line" corresponding to the case where ICME speed was not modified by the interaction with the background solar wind (**Figure 1-24**) [*Schwenn et al*., 2005]. The fastest ICMEs/shocks (>1000 km/s) are found to arrive at the location of Helios in approximately the predicted time; however, the large group of slower ICMEs (<500 km/s) arrive substantially earlier than predicted, while the majority of ICMEs with speeds of 750 to 1000 km/s arrive later than predicted. Although there are some uncertainties in the data (e.g., regarding the geometry of the transients observed by Helios), these results suggest that slow ICMEs are post-accelerated by the ambient solar wind, and the fast ones are decelerated, while the fastest of all are unmodified.

As discussed in Section 1.2.2.a, numerical simulations of ICME propagation have shown that the interaction with the background solar wind deforms the shape of ICMEs. For example, in a simulation of the evolution of a halo CME launched on 12 May 1997, the CME is launched into the slow solar wind emanating from the streamer belt [*Odstrcil et al*., 2004] (cf. **Figure 1-22**). As it moves away from the

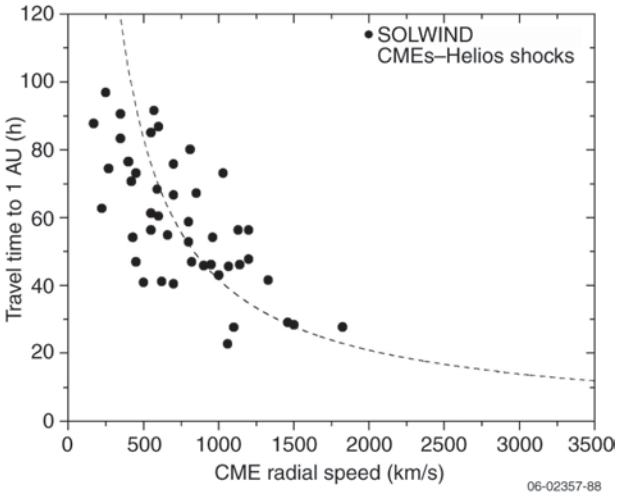

Figure 1-24. The travel time of CME fronts from the Sun to the location of Helios 1 as function of the CME radial speed V_{rad} obtained from the SOLWIND coronagraph. Only those cases were selected where a unique association could be achieved, in particular when Helios 1 was with ±30° near the plane of the sky, and when the angular span of the CME included the Helios orbital plane. The travel time was derived from the moment of first appearance in a coronagraph image and the shock arrival time at Helios 1. The travel times were corrected such that the varying Sun–Helios 1 distances are compensated. All data were adapted from Table 1 of *Sheeley et al.* [1985]. The dotted line denotes the "ideal" line, i.e., where the travel time would exactly correspond to the CME radial speed near the Sun [*Schwenn et al.*, 2005].

Sun, it expands into the northern and southern high-speed streams. The velocity difference between the central part of the ICME in the slow wind and its higher-latitude extensions in the fast wind gives the structure the concave configuration seen in the figure. Significant compression, shock formation, and field line draping occur in the low-latitude region, where the fast CME encounters the streamer belt flow. As demonstrated in earlier MHD simulations, the effect of the solar wind velocity and density structure on the morphology of the ICME (and on the associated distortion of the IMF by shock formation and field-line draping) depends on the initial position of the CME relative to the corotating streamer belt [*Odstrcil and Pizzo*, 1999c].

c. How do ICMEs interact with each other? CME–CME interactions have been observed directly (**Figure 1-25**), detected indirectly through interplanetary radio emissions [*Gopalswamy et al*., 2001c, 2002], and inferred from measurements of the properties of non-MC complex ejecta associated with successive halo CMEs [*Burlaga, Plunkett, and St. Cyr*, 2002]. Such interactions involve the overtaking

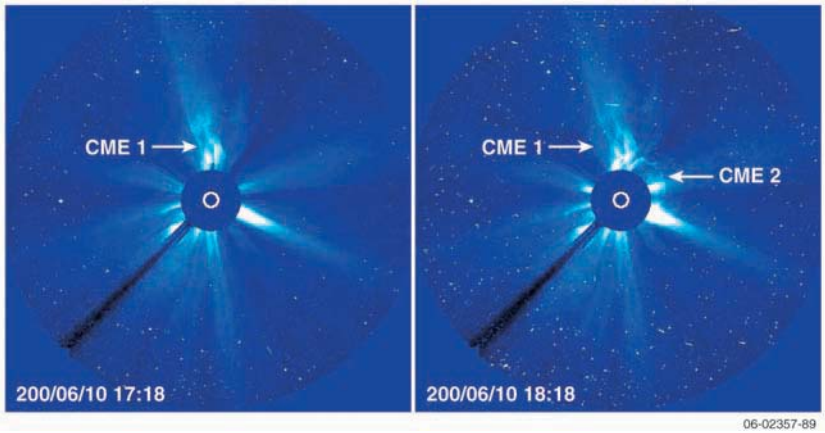

Figure 1-25. The interaction of a slow CME (1) and fast CME (2) observed with the SOHO LASCO instrument on 6 June 2000. This event produced the unusual enhancement in the DH type II radio emission reported by *Goplaswamy et al.* [2001c]. Although not obvious in this pair of images, the collision between the two ejecta altered the direction of propagation of the core of the slower CME.

of slower CMEs by faster ones and can result in the merging of multiple CMEs to form complex transient streams in which the identities of the constituent CMEs are no longer distinguishable [*Burlaga, Plunkett, and St. Cyr*, 2002]. It has recently been proposed that interactions among magnetic clouds can lead to the formation of complex structures consisting of multiple magnetic clouds and the interaction regions between them [*Wang, Ye, and Wang*, 2003]. In addition to modifying the magnetic and plasma structure of the involved ICMEs, the interaction can also alter their trajectory [*Gopalswamy et al*., 2001c] and decelerate fast ICMEs and their associated shocks [*Manoharan et al*., 2004]. A recent three-dimensional MHD simulation of the interaction between two magnetic clouds has identified some of the phenomena involved in the complex interaction [*Lugaz et al*., 2005]. These include the propagation of the shock driven by the second cloud through the first cloud and its merger with the shock driven by the first cloud to form a new, stronger shock; compression and acceleration of the first cloud by the shock driven by the second cloud; reconnection between the two clouds and the formation of a reverse shock; and deceleration of the second cloud by the reverse shock and the cloud's expansion in the lower-density wake of the first cloud. In this simulation, the two clouds can still be distinguished at 1 AU.

A possible role for CME–CME interactions in SEP production was investigated by *Gopalswamy et al.* [2002], who proposed that the SEP-effectiveness of a CME-driven shock is enhanced when the fast primary CME driving the shock overtakes a slower preceding CME. However, *Richardson et al.* [2003] have challenged this hypothesis, arguing, for example, that SEP injections occur before the inferred CME interactions in the ground-level/beamed electron events investigated in their study. Further, *Kahler* [2003] notes that SEP-effectiveness of the shock driven by the primary CME should be diminished rather than enhanced in the region of the preceding CME. Although direct CME–CME interactions appear unlikely to be important for SEP acceleration, the "preconditioning" of the interplanetary environment by the passage of an earlier ICME may influence the SEP-effectiveness of a subsequent ICME [*Gopalswamy et al*., 2004; *Kahler and Vourlidas*, 2005]. For example, closed field lines of the preceding ICME can repeatedly return the particles back to the shock driven by the primary ICME, thus enhancing the efficiency of acceleration [*Gopalswamy et al*., 2004; *Kallenrode and Cliver*, 2001]. The preceding ICME can also greatly enhance the turbulence upstream of the shock, resulting in shorter acceleration times and higher intensities for SEPs [*Li and Zank*, 2005]. Further, the particles accelerated at the preceding ICME and shock may act as seed particles for the following stronger shock, resulting in higher SEP intensities [*Kahler*, 2001].

With NES and the IHS spacecraft in a quadrature geometry, Sentinels will be able to observe the launch of successive CMEs and then measure their plasma and magnetic properties as they interact with one another and evolve during their transit to 1 AU. Observations in the early stages of the evolution of the ICMEs, shocks, and interaction regions will provide information about their detailed plasma and magnetic structure that is largely lost by 1 AU owing to the processing that occurs as structures propagate farther into the heliosphere. Sentinels will also investigate the preconditioning of the inner heliosphere by ICME passage and the influence that such preconditioning has on the SEP-effectiveness of successive ICMEs.

Table 1-3. Required and supporting measurements and modeling requirements for the Sentinels SEP investigation. *(Italics indicate supporting measurements.)*

Science Objectives	Objective Questions	Required and Supporting Measurements	Modeling Requirements
1.2.1 Determine the physical mechanisms of eruptive events that produce SEPs.	a. What solar conditions lead to CME onset?	Solar wind plasma, composition, and magnetic field at <0.3 AU and multiple points Photospheric magnetic fields Coronal plasma, composition/charge state Coronal density structures with in-situ observations inside coronagraph field of view (FOV)	Global heliospheric magnetic field CME initiation CME propagation
		Hard/soft X-rays *2π photospheric magnetic fields*	
	b. How does the pre-eruption corona determine the SEP-effectiveness of a CME?	2π photospheric magnetic fields Coronal plasma, composition/charge state Coronal density structures with in-situ observations inside coronagraph FOV Solar wind ions, electrons, composition, and magnetic fields at multiple points, <0.3 AU	Global heliospheric magnetic field CME initiation CME propagation
		Solar radio emissions *Energetic particles*	
	c. How close to the Sun and under what conditions do shocks form?	Coronal plasma, composition/charge state Radio observations and triangulation of shock fronts	Global heliospheric magnetic field Coronal density
		Photospheric magnetic fields *Solar wind ions and magnetic field*	
1.2.2 Determine the multiscale plasma and magnetic properties of ICMEs and shocks.	a. How does the global shape of ICME/shocks evolve in the inner heliosphere?	Solar wind ions and magnetic field at multiple radial and longitudinal locations EUV imaging of coronal source region Coronal density structures observed in quadrature with in-situ measurements Observation and triangulation of type II radio bursts Suprathermal electrons	Global heliospheric magnetic field CME initiation CME propagation
		Solar wind electron pitch-angle distribution and plasma composition at multiple radial and longitudinal positions *Electromagnetic plasma waves*	
	b. How does CME structure observed at the Sun map into the properties of ICMEs?	Solar wind ion and magnetic field at multiple radial positions inside coronagraph FOV Coronagraph in quadrature Electron pitch angle and solar wind composition at multiple radial positions Suprathermal electrons Solar radio emissions and plasma waves Soft X-ray imaging of flare sites	Global heliospheric magnetic field CME initiation CME propagation
		Coronal plasma and fields *Photospheric magnetic fields*	
1.2.3 Determine how the dynamic inner heliosphere shapes the evolution of ICMEs.	a. How is the solar wind in the inner heliosphere determined by coronal and photospheric structure?	Solar wind plasma, composition, and magnetic field at multiple longitudinal positions Plasma waves Full-disk EUV imaging Coronagraph in quadrature Photospheric magnetic fields	Global heliospheric magnetic field
		Coronal plasma conditions	
	b. How do ICMEs interact with the pre-existing heliosphere?	Solar wind plasma, composition, and magnetic field at multiple radial and longitudinal locations Coronagraph in quadrature	Global heliospheric magnetic field CME initiation CME propagation
		Suprathermal electrons *Solar radio emissions* *Soft X-ray imaging of flare sites*	
	c. How do ICMEs interact with each other?	Energetic particle fluxes Solar wind plasma, composition, and magnetic field at <0.3 AU Suprathermal electrons and radio waves Coronagraph in quadrature Photospheric magnetic fields	Global heliospheric magnetic field CME initiation CME propagation
		Energetic particle composition/charge state *Coronal plasma conditions*	

2.0 Interdisciplinary Research and Modeling

The Sentinels mission is uniquely broad in its scientific range and programmatic scope. The science of Sentinels covers a major fraction of the inner solar system—from the Sun to the Moon and Mars—and a vast range of physical scales, from the AU size of interplanetary coronal mass ejections (ICMEs) to the sub-kilometer sizes expected for flare current sheets in the low corona. To be fully successful, Sentinels must reveal new features of the plasma in the inner heliosphere, produce fundamental advances in understanding the physics of particle acceleration and propagation, enable the development of robust models for critical phenomena such as solar energetic particles (SEPs) and solar wind transients, and deliver capabilities in SEP prediction that will be useful to the Vision for Space Exploration (VSE). These objectives will be achieved only by forming effective partnerships between Sentinels and other major programs, such as the Solar Dynamics Observatory (SDO) and Solar Orbiter. It is clear that all these needs cannot be met by the instrument teams alone, which necessarily must concentrate on the mission hardware. Therefore, the Sentinels Science and Technology Definition Team (STDT) recommends that an Interdisciplinary Science Team (IST) program be established as part of the Sentinels mission. The ISTs, along with the instrument groups led by the instrument Principal Investigators, will form the nucleus of a science community that will reach out to the general science community and to the user base, especially the human spaceflight community. The Sentinels ISTs would encompass the following goals and responsibilities:

1. Provide the broad range of interdisciplinary expertise and skills required for Sentinels to achieve its main science goals.
2. Provide the cross-cutting knowledge and experience required for maximizing the payoff that can be derived from Sentinels science for operational applications.
3. Enable the development of the large-scale models that will be required for the analysis and interpretation of the Sentinels data and for making the transition from Sentinels science to operational tools.

The ISTs would form soon after instrument selection and interact with the hardware groups in all aspects of mission development, including the definition of optimal instrument characteristics, the formulation of observing programs, and in particular, the development of models essential for Sentinels. Modeling will play a critical role in achieving the scientific objectives of the Sentinels mission. Models of various types will provide both local and global contexts for the interpretation of Sentinels data, while Sentinels in-situ and remote-sensing measurements will be used to constrain, test, and improve a wide range of solar and heliospheric models. Ultimately, the advances in modeling made possible by the Sentinels mission will lay a foundation for the transition from research codes into operational tools that can be used for the prediction of space weather phenomena such as SEP events. The accuracy and robustness of these forecasting tools, encoding our newly developed understanding, will be one of the measures of success of the Sentinels program.

To fully exploit the capabilities of existing models and to help develop the next generation of solar and heliospheric models, a significant investment in modeling activities must be made even during the earliest phases of the Sentinels mission. ***Thus the Sentinels STDT recommends that "modeling" be accorded a status equivalent to that of the Sentinels instruments and that it be a prime responsibility of the Interdisciplinary Science Team Program.***

Three types of models are particularly important to Sentinels: (1) global magnetohydrodynamic (MHD) models of the corona and the inner heliosphere; (2) models of transient activity, especially coronal mass ejection (CME) initiation and evolution; and (3) particle acceleration and transport codes. The ultimate goal will be to couple these three model types with the global MHD models providing the background magnetic and field structure used by the transient activity codes, which in turn will calculate the shock structure that the acceleration and propagation models will need. The sections that follow outline the input requirements and validation methodology for each type of model and briefly describe how Sentinels data will be used to validate and improve the models.

2.1 Global MHD Models

Current global MHD models [e.g., *Riley, Linker, and Mikic*, 2001; *Roussev et al*., 2003; *Usmanov et*

al., 2000] can reproduce some aspects of the ambient corona and solar wind conditions (**Figure 2-1**). However, they are limited by the amount and kind of data available to specify the inner boundary conditions. Currently, inner boundary conditions must be derived from observations of the photospheric magnetic field made at Earth and extrapolated to other longitudes. However, this dependence on observations of the photospheric magnetic field at the front-side of the Sun as seen from Earth severely limits the ability of these models to reproduce the global coronal field because considerable evolution of the photospheric (and hence coronal) magnetic field occurs on timescales less than the solar rotation rate. ***To specify more realistic boundary conditions for global MHD models, simultaneous observations of the photospheric magnetic fields at different heliolongitudes are required.***

While current global MHD models are driven by photospheric magnetic field measurements, it is likely that future models will incorporate other remote measurements (white light, X-ray, Extreme ultraviolet Imaging Telescope [EIT], etc.) into the boundary conditions. For example, if sufficiently mature techniques are developed to derive the plasma density, velocity, and temperature in the lower corona from remote-sensing emission observations, such information would provide valuable additional inputs into global coronal models, as these values are currently unknown and must be assumed. At present, however, the primary use of such observations is for model validation. Newer MHD models incorporate coronal thermodynamics (i.e., coronal heating, thermal conduction, and radiation) and can produce simulated ultraviolet and X-ray emission images as output. Comparison of these outputs with observations will allow us to constrain heating mechanisms and ultimately to validate these models.

Comparisons of simulation results with in-situ solar wind plasma and magnetic field measurements are used to validate global heliospheric models. Such measurements have been provided by near-Earth spacecraft at 1 AU as well as, at greater radial distances and above and below the ecliptic, by Ulysses and Voyager. The two STEREO spacecraft, one leading and one following the Earth, will sample the solar wind at different heliolongitudes and, together with observations from near-Earth spacecraft, will provide a picture of the global structure at 1 AU. Missing, however, are in-situ measurements made simultaneously at multiple points within the inner heliosphere, the region where the solar wind evolves at its highest rate. ***Such measurements, along with concurrent photospheric observations, are critical for validation of global models.***

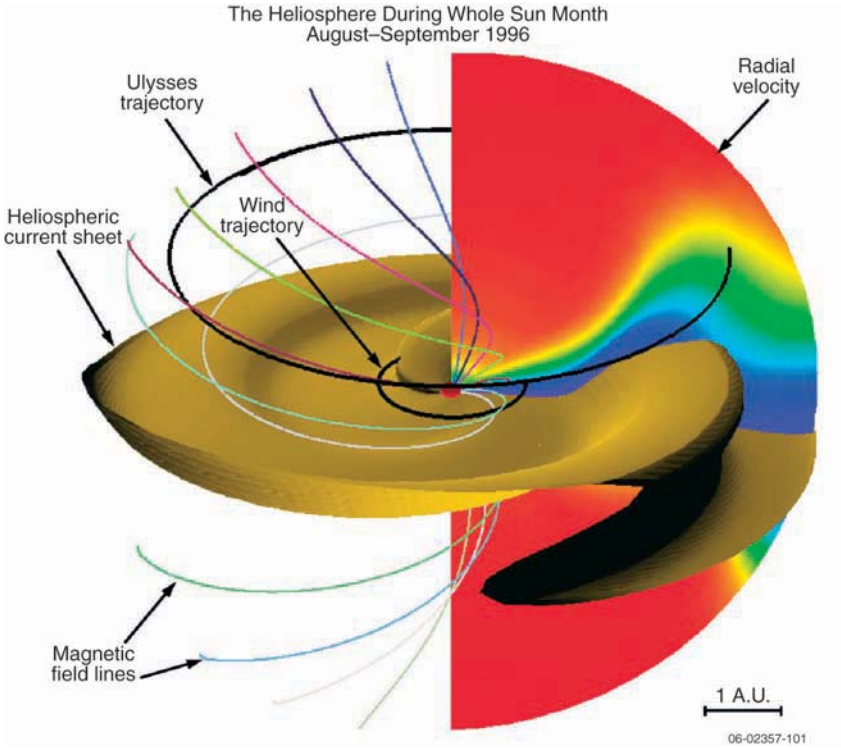

Figure 2-1. Model solution for Carrington rotations (CR) 1912–1913. The heliospheric current sheet (inferred from the isosurface *Br* = 0) is displayed out to 5 AU. A meridional slice of the radial velocity is shown at an arbitrary longitude. Blue corresponds to slowest speeds (750 km/s). Superimposed is a selection of interplanetary magnetic field lines originating from different latitudes. Finally, the trajectories of the Wind and Ulysses spacecraft are marked. Adapted from *Riley, Linker, and Mikic* [2001].

In addition to model validation, Sentinels' combination of remote sensing and in-situ observations can provide important constraints on poorly understood processes such as coronal

heating, thus leading to improved representation of key physical processes within the models. **Table 2-1** summarizes the use of Sentinels data in global MHD models of the corona and inner heliosphere.

2.2 Models of Dynamic Phenomena

In addition to reproducing the steady-state corona and quasi-stationary solar wind, MHD models can also be used to simulate the highly dynamic events such as CMEs and eruptive flares that lead to SEP production. The dynamic MHD models will play a central role in the science of Sentinels, in particular for modeling CME onset and for determining the evolution of the CME and its associated shock in the background solar wind to distances of 1 AU and beyond [e.g., *Roussev et al.*, 2004; *Manchester et al.*, 2005] (**Figure 2-2**). Various models of CME onset have been developed, but these fall generally into two classes: twisted flux rope models [e.g., *Roussev et al.*, 2004; *Lin and Forbes*, 2000] and reconnection models [e.g., *Antiochos, DeVore, and Klimchuk*, 1999]. As discussed in Chapter 1 (Section 1.2.1), both types of models are viable, and the data currently available are not adequate to distinguish between them. However, multipoint measurements of CME plasma properties by the four Inner Heliospheric Sentinels (IHS) spacecraft and spectroscopic determinations of CME physical parameters and global topology by the Near-Earth Sentinel UV and white-light coronagraphs will constrain the models. When combined with the CME onset and evolution models, these measurements will make it possible to discriminate between the different models and ultimately to determine the physical processes responsible for CME initiation and acceleration.

In addition to revealing the physical mechanism for CME onset, dynamics models will play a central role in understanding the propagation of CMEs and the associated shocks in the heliosphere. Many questions concerning the propagation of heliospheric transients, such as the role of reconnection and the interaction of multiple CMEs, have yet to be resolved. Considerable work has already been done by several groups on fully three-dimensional simulations of CME propagation [e.g., *Odstrcil et al.*, 2002; *Manchester et al.*, 2005]. The results of such work can be used directly to interpret the IHS observations and, conversely, the observations will be used to validate and enhance the models. The Sentinels mission, with its multipoint and comprehensive measurements of plasma and fields coupled to the next-generation set of dynamics models, is ideally suited to advancing our understanding of heliospheric dynamics. Furthermore, the dynamics models and observational technology developed by Sentinels will serve as prototypes for an eventual first principles–based prediction capability of heliospheric transients. **Table 2-2** summarizes the use of Sentinels data in CME onset models.

2.3. SEP Acceleration and Transport Models

Theoretical models of SEP acceleration and transport in the (inner) heliosphere have undergone significant development during the past decade. Particular emphasis has been placed on the acceleration of particles by CME-driven shocks to explain gradual SEP events [e.g., *Ng, Reames, and Tylka, 2003*; *Li, Zank, and Rice, 2003, 2005a*; *Lee, 2005*]. Some earlier models of shock-accelerated

Table 2-1. Sentinels data utilization in global MHD models.

Model Type	Supported Science Objectives/Questions	Measurement Requirements		
		For Input	For Validation	For Improvement
Global heliospheric potential field source surface	1.1.1 a,b,c,d; 1.1.2 a,b; 1.1.3 a,b 1.2.1 a,b,c; 1.2.2 b; 1.2.3 a,b,c	2π photospheric magnetic fields	Inner heliospheric magnetic field and plasma parameters	
Global heliospheric: global MHD	1.1.1 a,b,c,d; 1.1.2 a,b; 1.1.3a,b 1.2.1 a,b,c; 1.2.2 b; 1.2.3 a,b,c	2π photospheric magnetic fields	White-light; UV; X-ray; inner heliospheric magnetic field and plasma parameters	Plasma density, velocity, and temparature in the lower corona; inner heliospheric in-situ data assimilated

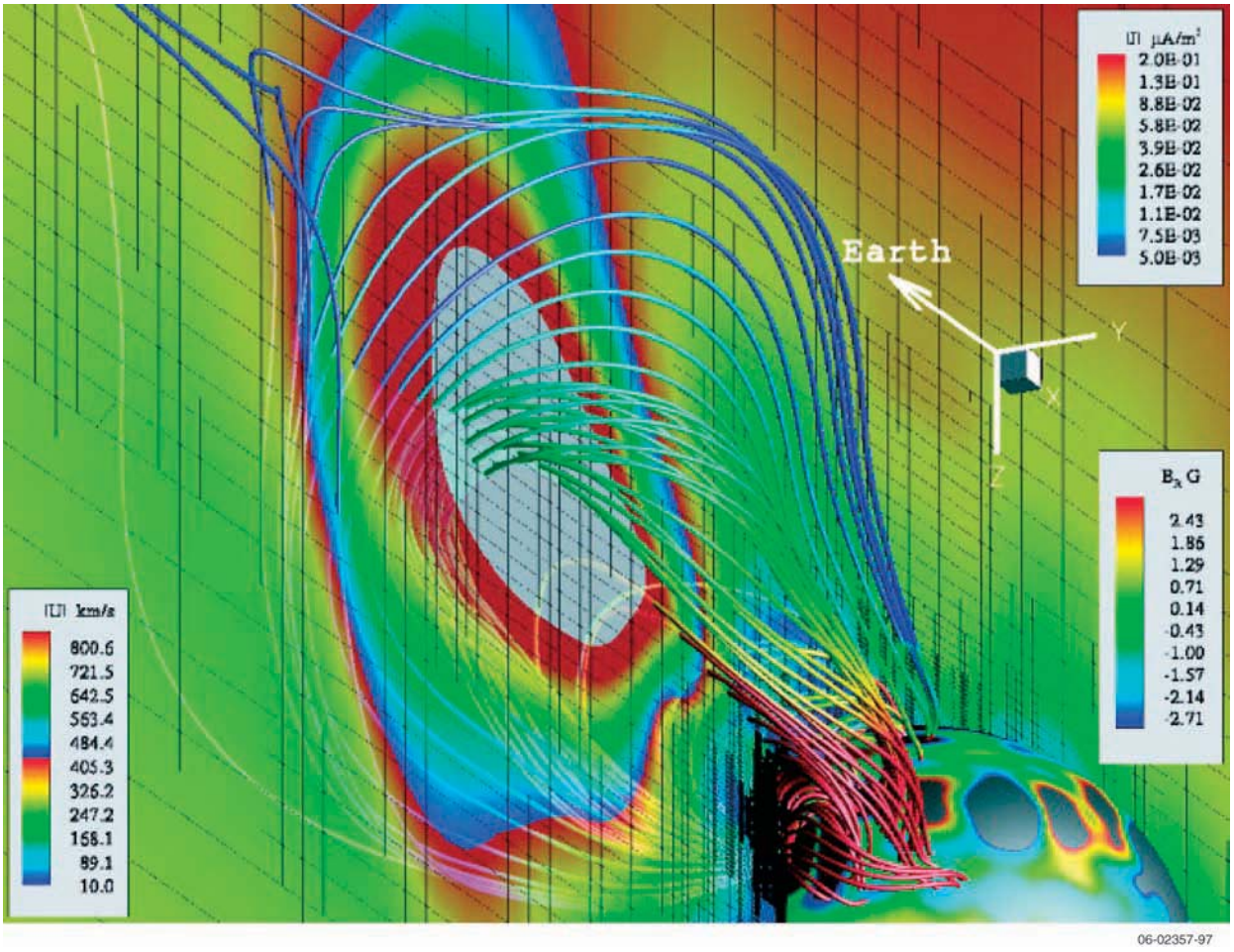

Figure 2-2. Three-dimensional view of a modeled coronal mass ejection [*Roussev et al.*, 2004]. The solid lines are magnetic field lines and the false color shows the magnitude of the current density in units of μAm^2 (see color legend at top right). The magnitude of flow velocity, in units of km/s, is shown on a translucent plane (see color legend to the left). Values in excess of 1,000 km/s are blanked and shown in light grey. The grid-structure on this plane is also shown as the black frame. The inner sphere corresponds to $R = R_S$. The color shows the distribution of radial magnetic field in units of Gauss (see color legend at bottom right). Regions with field strength greater than 3 G are blanked and appear in grey.

Table 2-2. Sentinels data utilization in coronal and heliospheric transient models.

Model Type	Supported Science Objectives/Questions	Measurement Requirements		
		For Input	For Validation	For Improvement
MHD Coronal and Heliospheric Transients Model	1.2.1a,b,c; 1.2.2a,b 1.2.3b,c; 1.1.1a,c,d; 1.1.2b	Photospheric magnetic and velocity fields, coronal XUV images	Coronagraph intensity and velocity; in-situ plasma and fields	Coronal spectroscopic measurements of shock speed and structure; in-situ shock measurements

SEPs do not assume a specific acceleration mechanism but treat the shock as a "black box" from which accelerated particles escape into the heliosphere; these models assume a spectrum for the escaping particles and use it as an input to their transport code [e.g., *Kallenrode and Wibberenz*, 1997; *Lario, Sanahuja, and Heras*, 1998; *Heras et al.*, 1992, 1995]. In an effort to treat the acceleration process at a CME-driven shock and the subsequent transport of energetic particles in the interplanetary medium in more consistent way, later models have explicitly incorporated the diffusive shock acceleration mechanism [*Zank, Rice, and Wu*, 2000; *Li, Zank, and Rice*, 2003, 2005a; *Rice, Zank, and Li*, 2003; *Lee*, 2005]; these models self-consistently calculate the spectra of the particles accelerated diffusely at a propagating shock and compute the subsequent transport of these particles in the inner

heliosphere. Combining the acceleration and the transport of energetic particles is very challenging. For example, energetic particles escaping earlier from the shock complex will alter the turbulence level of the interplanetary medium, which will be experienced by later particles [e.g., *Ng, Reames, and Tylka*, 1999, 2003]. This, in part, reflects the enormous variability of particle time intensity profiles and spectra observed at 1 AU. Acceleration at sites associated with solar flares and unified flare/CME systems has also been studied. These sites may be responsible for so-called impulsive SEPs. **Figure 2-3** illustrates a unified flare/CME system. SEP source regions in the extended corona are indicated.

A key parameter in modeling SEP transport is the particle mean free path, which is related to the level of turbulence in front of a shock and which can be used to parameterize the frequency of pitch-angle scattering. Because SEP acceleration mostly occurs close to the Sun, and because early transport of energetic particles in the inner heliosphere can dramatically alter the time–intensity profile at 1 AU (**Figure 2-4**), IHS observations of turbulence closer to the Sun (~0.25 AU) are needed to improve our understanding of this critical parameter and to better constrain our SEP transport codes. Such improvements in our models will make it possible to make more accurate predictions of SEP time–intensity profiles and spectra at 1 AU, a capability that is particularly important for space weather forecasting.

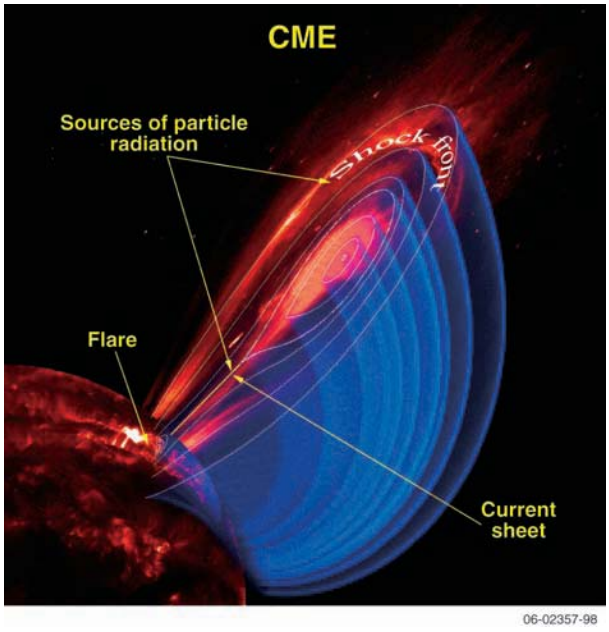

Figure 2-3. Composite illustration of a unified flare/CME system indicating potential solar energetic particle source regions. The LASCO C2 coronagraph image (red image off the limb) shows the CME with a trailing current sheet seen nearly edge-on. A cutaway of the magnetic field structure from a model by Lin and Forbes [2000] is shown by the blue overlay. Post-flare loops are shown on the disk image, which is adapted from a SOHO/EIT image. Adapted from *Kohl et al.* [2006].

Existing SEP acceleration and transport models assume a quasi-parallel shock geometry. However, a model based on non-linear theory has recently been developed to investigate acceleration at quasi-perpendicular shocks [*Zank et al.*, 2006], which has been invoked to explain events characterized by increasing Fe/O as a function of energy [*Tylka et al.*, 2005]. The model predicts quite different time–intensity profiles and spectra for the quasi-parallel and quasi-perpendicular cases. To verify and refine this new model (and to assess the proposed role of quasi-perpendicular acceleration in enhanced Fe/O events), knowledge of the precise magnetic configuration at a CME-driven shock is required: knowledge that the IHS spacecraft will provide.

Ultraviolet spectroscopic and white-light polarimetric observations out to at least 6 R_S are needed to clarify which physical processes are responsible for SEP acceleration. Models of SEP acceleration can be tested by tailoring the models to specific events using remote-sensing constraints and then comparing the model predictions with IHS measurements of CME and SEP properties.

Table 2-3 summarizes the use of Sentinels data in SEP acceleration and transport models.

2.4 Relation to Other Modeling Initiatives

The Sentinels mission falls under the larger umbrella of the Living With a Star (LWS) program, which has a strategic capability initiative as part of the Targeted Research and Technology (TR&T) component to LWS. Some of the models expected to be developed as TR&T strategic capabilities will be applicable to Sentinels. For example, the TR&T is presently calling for the development of a global MHD model as described in Section 2.1 above. Sentinels will use the strategic capabilities developed by TR&T, of course, but will require the models to be expressly tailored to input Sentinels data and to output Sentinels observables. Sentinels will also coordinate with other modeling initiatives,

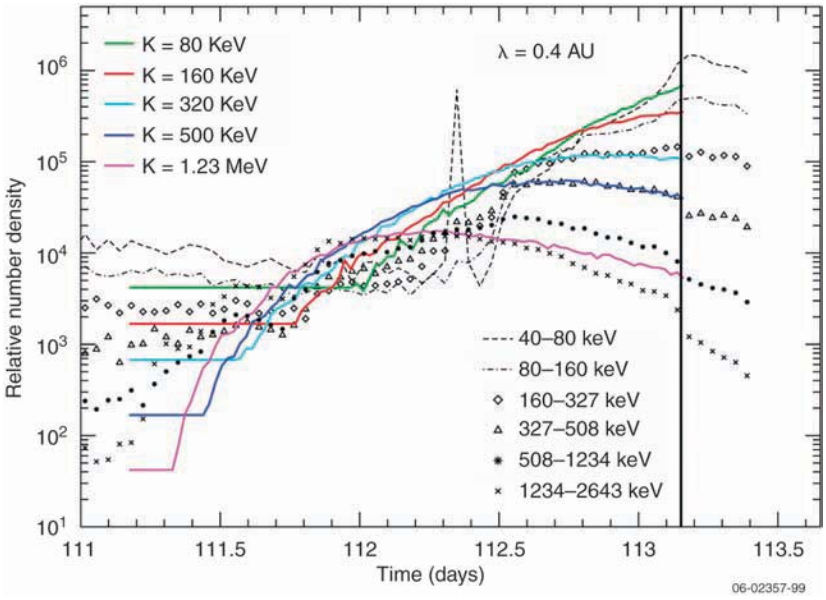

Figure 2-4. Model calculation of the time–intensity profile for the SEP event of 21 April 2002: simulation of CNO particles with kinetic energies per nucleon of 80, 160, 320, and 500 keV/amu and 1.23 MeV/amu are shown, together with the corresponding observational data. The arrival of the shock is represented by the vertical line near time t = 113.15 days. As shown in the figure, we find that the model provides a reasonable intensity profile fit. For example, the predicted curve for particles of K = 1.23 MeV yields almost identical characteristics to those observed. The early rise before the shock arrival signals the earlier acceleration when the shock was still strong. The intensity reaches its maximum and begins to decrease before the shock arrival, suggesting the shock becomes too weak to accelerate particles to this energy. [*Li et al.*, 2005b]

such as the Department of Defense's MURI and the National Science Foundation's CISM programs, which are currently working toward the development of end-to-end models of the Sun-heliosphere-magnetosphere-ionosphere-atmosphere system and are beginning to incorporate energetic particles into their models. The Sentinels mission will be unique in its ability to provide the "front end" inputs for such end-to-end models.

A key role of the Sentinels ISTs will be to coordinate the Sentinels modeling needs with these other modeling programs, especially the LWS-developed models. The ISTs will determine what models need to be developed for the Sentinels program and the optimal strategy for obtaining these models. In some cases this strategy may require building a model "from scratch," in others, adapting pre-existing models developed by other programs. The STDT's recommendations concerning the development and use of models complement the broader policy of LWS. In particular, the STDT recommends (1) an open theory and model policy; (2) partnering with other agencies; (3) maximizing the resources of the Coordinated Community Modeling Center; and (4) supporting both empirical and physics-based approaches. While the goals of the Sentinels mission are primarily science-based, the STDT endorses the broader LWS modeling goals of (1) environmental specification; (2) research into nowcasting; and (3) forecasting.

2.5 Sentinels Models and Societal Benefits

The newly developed models incorporating Sentinels science results will form the basis upon which a future operational space weather forecasting

Table 2-3. Sentinels data utilization in solar energetic particle acceleration and transport models.

Model Type	Supported Science Objectives/Questions	Measurement Requirements		
		For Input	For Validation	For Improvement
Hybrid acceleration and transport (quasi-parallel)	1.1.1.a; 1.1.1.d; 1.1.2.a; 1.1.2.b; 1.1.3	Seed population (proton + heavy ions), shock parameters (compression ratio, Θ_{BN}), upstream turbulence (B)	Observed spectra and time intensity profiles at various locations, SEP composition	Suprathermal seed population, Θ_{BN}
Transport in a turbulent interplanetary medium	1.1.1.a; 1.1.1.d; 1.1.2.a; 1.1.3	Upstream turbulence (B), Θ_{BN}	Time–intensity profiles at various locations	Θ_{BN}

capability can be developed. The envisioned forecasting capabilities are listed in **Figure 2-5**, which shows which Sentinels science objectives or observations will likely contribute to the development of new or improved heliospheric model types. The column on the right shows the likely societal benefits provided by the models once they are validated. Thus, systematic 2π photospheric observations of the

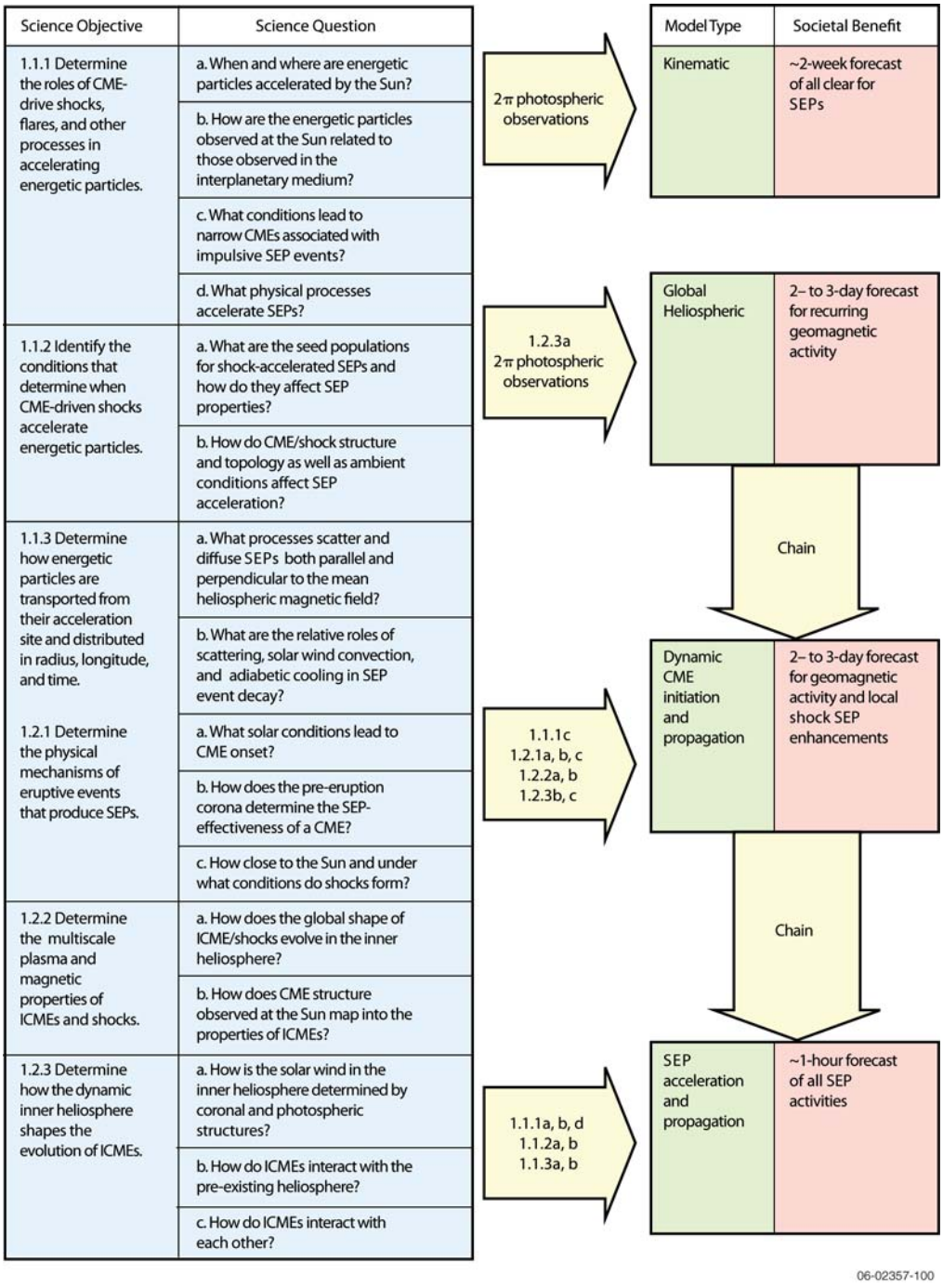

Figure 2-5. Sentinels model traceability table. The first two columns show the Sentinels science objectives. The final two columns depict the resulting model capabilities and the likely societal benefits of these models. Arrows show the connection between the various science objectives and Sentinels observations and the developed models. Also shown is how the various models are expected to be chained together to form a single system.

solar magnetic field will allow "all clear" forecasts with more than 2 weeks of lead time, even with current simple kinematic models. That is, if no significant solar activity is observed on the far side of the Sun, it is highly unlikely that large flares or CMEs will take place when that region rotates to the front side of the Sun. Reliable global heliospheric models will allow the accurate forecasting of recurrent geomagnetic activities due to the arrival of high-speed streams at Earth within the 2- to 3-day propagation time of these streams from the Sun to 1 AU. CME initiation and propagation models will enable the development of forecasting capabilities for transient-induced geomagnetic activities with the same 2- to 3-day lead time. Finally, particle codes would be necessary for any SEP forecasting. It is worth emphasizing that the primary goal of ~1 hour SEP forecasting capability will require the execution of the complete Sentinels program outlined in this report, as it will require the linking or "chaining" of all of the developed models. Therefore, even though Sentinels is not envisioned to provide any operational space weather forecasting capabilities, the program will develop heliospheric modeling capabilities that are necessary ingredients for any future operational system.

3.0 Science Implementation

The Sentinels science objectives require a combination of (1) in-situ measurements by multiple spacecraft operating as deep within the inner heliosphere as possible and (2) remote-sensing observations of the solar corona and photosphere. These measurement requirements are summarized in **Table 3-1**. It is neither necessary nor the lowest cost option, however, to make all of these observations from the same platform. Thus, the baseline Sentinels mission recommended by the Science and Technology Definition Team (STDT) consists of three flight elements:

- The **Inner Heliospheric Sentinels (IHS)**, four spin-stabilized spacecraft in elliptical heliocentric orbit with perihelia at ~0.25 AU and aphelia at ~0.75 AU
- A 3-axis stabilized **Near-Earth Sentinel (NES)** in Sun-synchronous orbit at 1 AU
- A small **Farside Sentinel (FSS**) that drifts slowly away from Earth in a heliocentric orbit at ~1 AU

To address the focused science questions, the four IHS spacecraft will be identically instrumented to make comparisons of in-situ measurements of inner heliospheric solar wind plasma, suprathermal, energetic particles (protons/alphas, electrons, $Z > 2$ ion composition and charge states), magnetic fields, and plasma waves; and of remote sensing (stereoscopic and occultation) measurements of solar/heliospheric radio, soft/hard X-ray, gamma-ray, and neutron observations. The derived baseline strawman payload is described in detail in Section 3.2.

NES will carry an imaging spectroscopic coronagraph to determine the physical conditions and processes that govern solar energetic particle (SEP) acceleration near the Sun (1.2 to ~10 R_S), and a wide field (to ~0.3 AU) coronagraph to directly connect solar imaging to IHS in-situ observations. FSS will carry a simple magnetograph to obtain magnetograms at heliolongitudes not observable from Earth, which, together with magnetograph measurements from the Earth and from Solar Orbiter, will provide near-global coverage of the photospheric magnetic field as input for accurate modeling of the heliosphere.

The first section of this chapter, "3.1 Sentinels Observational Strategy," discusses the observational requirements that determined the minimum design of the baseline Sentinels mission. It is structured in terms of the questions that guided the STDT in developing the Sentinels mission concept. The remaining two sections describe the strawman payloads recommended by the STDT for the each of the Sentinels flight elements and discuss the role of supporting observations in the Sentinels mission.

3.1 Sentinels Observational Strategy

In addition to defining the science goals and objectives for the Sentinels mission and identifying the measurements required to answer the specific science questions described in Chapter 1, the STDT worked closely with engineering teams at The Johns Hopkins University Applied Physics Laboratory (APL) and the Jet Propulsion Laboratory (JPL) to design a mission that (1) is feasible from an engineering point of view with no new technology development, and (2) will allow the Sentinels science objectives to be achieved. Among the critical factors that had to be taken into account in designing the IHS mission were the perihelion distance that the spacecraft need to achieve in order to observe SEPs and transients sufficiently early in their evolution, and the amount of time that the four IHS spacecraft need to spend close to the Sun in order to obtain a statistically useful data set. These and other factors and the scientific rationale for the resulting Sentinels mission design are discussed in the following sections. The engineering aspects of the IHS mission design are covered in Chapter 4, "IHS Mission Implementation." The NES and FSS mission implementations are described in Chapter 5.

3.1.1 How close to the Sun should the in-situ observations be made? The primary objective of Sentinels is to understand SEP acceleration and the source and evolution of solar transients from the corona through the inner heliosphere. This requires in-situ observations that characterize the accelerated SEP particles, their seed populations, the plasmas and fields of the associated transients, and the environment in which they propagate. The SEP measurements should be made within 1 to 2 mean free paths, λ, of the source to minimize propagation effects, allowing the characterization of freshly accelerated SEPs and the associated fast shocks, waves, and interplanetary coronal mass ejections (ICMEs) before significant evolution. Analyses of SEP events observed at ~1 AU

indicate that λ is typically ~0.2 ± 0.1 AU [*Palmer*, 1982]. Closer to the Sun, λ is expected to be larger, since the magnetic field gradient, and therefore the magnetic focusing of SEPs, is more dominant over scattering. Thus, we require SEP measurements within 1 to 2 λ, which we (somewhat arbitrarily) define as inside 0.35 AU. Simultaneous remote-sensing measurements of the acceleration of particles by flares are required to understand their contribution to SEPs. In-situ measurements close to the Sun are also required to observe colliding ICMEs before they overtake each other and to observe fine-scale heliospheric structures that can be connected back to structure in the corona before they are washed out by stream interactions.

The pioneering Helios 1 and 2 and Mariner 10 spacecraft just reached the limits at 0.3 AU, where these kinds of observations are possible, and made the first exploratory measurements. To achieve the Sentinels objectives, however, requires (1) measurements from multiple spacecraft, with at least one spacecraft within ~0.35 AU of the Sun and (2) a comprehensive set of powerful diagnostic in-situ measurements—including suprathermal electrons and ions and ion composition/charge states for solar wind, suprathermals, and low energy SEPs—as well as remote-sensing observations of energetic emissions utilizing multipoint stereoscopic and occultation measurements. Studies by the APL engineering team have established that a single standard launch vehicle using chemical propulsion can, in combination with multiple Venus gravity assists, cost-effectively place four spacecraft well below 0.35 AU. (For details see Chapter 4 and Appendix A.) It was found that a perihelion distance of ~0.25 AU satisfies the measurement requirements while allowing the use of conventional thermal control techniques.

3.1.2 How many in-situ vantage points are required? Multipoint in-situ and remote sensing observations are required to understand SEP acceleration and coronal mass ejection (CME) propagation and evolution. For example, gradual SEP events are believed to be produced primarily at fast CME-driven coronal/interplanetary (IP) shocks, but in the 20 January 2005 event—the most intense observed at high energies (> hundreds of MeV) in almost 50 years—the SEPs arrived so rapidly that their time profile is difficult to explain by CME shock acceleration. Furthermore, the energy spectrum of the SEPs in that event, which was magnetically well-connected to the flare region, is very similar to that inferred from the nuclear gamma-ray line emissions for the flare-accelerated ions. By comparing measurements of SEP energy spectrum and composition over a wide range of longitudes to the energy spectrum and composition of flare-accelerated ions inferred from simultaneous gamma-ray and neutron measurements, we can determine if flares are an important source of SEPs for longitudes that are magnetically well connected (see **Figure 3-1**). By correlating SEP characteristics with the properties of the associated fast CME, shock, and waves, obtained through simultaneous plasma and fields measurements at widely separated points, we can test whether quasi-perpendicular shocks, waves generated by the SEPs, shock surfing, or some unknown physical phenomena are important for SEP acceleration. To probe the importance of seed particles for the SEP production requires correlating seed particle measurements close to the Sun with the SEPs observed farther away on the same magnetic field line.

The multipoint remote-sensing measurements of radio, X-ray, gamma-ray, and neutrons allow the utilization of stereoscopic and limb occultation methods to provide crucial information about the source location and height of accelerated electrons and ions near the Sun. Multipoint measurements make it possible to track impulsively accelerated electrons, first locating them at the Sun and determining their height in the corona through their bremsstrahlung X-ray emission, then following the escaping electrons in the inner heliosphere through their type III radio emission, and finally detecting them in situ and obtaining their field line length through analysis of their velocity dispersion. This method provides direct tracing of the magnetic field structure and connectivity.

The minimum number of IHS spacecraft required for adequate characterizations of either SEP events or transient solar wind structures such as ICMEs follows from the number of free parameters of the simplest phenomenological models. For SEP longitudinal intensities we assume that at least a Gaussian profile fit, with three free parameters, is needed. In addition, a fourth parameter, the radial dependence of the SEP intensities, expressed as a simple power law exponent, is also required. For

Table 3-1. Measurement requirements. "R" denotes measurements required to address the question in whose row they appear; "S" denotes supporting measurements. X = X-rays; PW = plasma waves; C = white-light coronagraph; E = coronal EUV emissions.

KEY
R: Required
S: Supporting
C = white-light coronagraph
E = coronal EUV emissions
PW = plasma waves
X = X-rays

			Inner Heliospheric Measurements (Sonic point < X < 0.5 AU)										Coronal Measurements (0 to 60 R_S)			
GOALS	**Science Objectives**	**Objective Questions**	**Energetic Particles**	**Energetic Particle Composition**	**Energetic Particle Charge States**	**Suprathemals**	**Solar Wind Ions**	**Solar Wind Electrons**	**Solar Wind Composition**	**DC Vector Magnetic Field**	**AC Magnetic Field**	**Radio and Plasma Waves**	**Photospheric Magnetic Fields**	**X-rays, Neutrons, Gamma-Rays**	**Coronal Plasma Conditions**	**Coronal Structures and Velocity**
1.1 Understand and Characterize the Sources, Acceleration, and Transport of Solar Energetic Particles	**1.1.1 Determine the roles of CME-driven shocks, flares, and other processes in accelerating energetic particles**	a. When and where are energetic particles accelerated by the Sun?	R	S	S	R	S	S	S	S	S	R	S	R	S	R
		b, How are the energetic particles observed at the Sun related to those observed in the interplanetary medium?	R	R	R	R-E S-I	S	S	S	S	–	R	S	R	S	S
		c. What conditions lead to the jets/narrow CMEs associated with impulsive SEP events?	R	R	R	R	S	S	S	S	–	R	–	R	S	R
		d. What physical processes accelerate SEPs?	R	R	R	R	–	–	S	–	–	R	S	R	S	S
	1.1.2 Identify the conditions that determine when CME-driven shocks accelerate energetic particles	a. What are the seed populations for shock-accelerated SEPs and how do they affect SEP properties?	R	R	R	R	R	R	R	–	–	S	–	S	S	S
		b. How do CME/shock structure and geometry as well as ambient conditions affect SEP acceleration?	R	S	S	R	S	S	S	R	R	S	R	R	S	R
	1.1.3 Determine how energetic particles are transported from their acceleration sites and distributed in radius, longitude, and time	a. What processes scatter and diffuse SEPs both parallel and perpendicular to the magnetic field?	R	R	R	R	R	R	–	R	R	R-PW	–	–	–	–
		b. What are the relative roles of scattering, solar wind convection, and adiabatic cooling in SEP event decay?	R	R	R	R	R	R	–	R	R	R-PW	–	–	–	–
1.2 Understand and Characterize the Origin, Evolution, and Interaction of CMEs, Shocks, and Other Geoeffective Solar Wind Structures	**1.2.1 Determine the physical mechanisms of eruptive events that produce SEPs**	a. What solar conditions lead to CME onset?	–	–	–	–	R	R	R	R	–	-	R	S (X)	R	R (C+E)
		b. How does the pre-eruption corona determine the SEP-effectiveness of a CME?	S-Lo	S	S	-	R	R	R	R	–	R	R	-	R	R (C+E)
		c. How close to the Sun and under what conditions do shocks form?	–	–	–	–	S	-	–	S	–	R	S	–	R	-
	1.2.2 Determine the multiscale plasma and magnetic properties of ICMEs and shocks	a. How does the global 3D shape of ICMEs/shocks evolve in the inner heliosphere?	–	–	–	R-E	R	S	S	R	–	R, S-PW	–	-	–	R (C+E)
		b. How does CME structure observed at the Sun map into the properties of interplanetary CMEs?	–	–	–	R-E	R	R	R	R	–	R, R-PW	S	R (X)	S	R (C)
	1.2.3 Determine how the dynamic inner heliosphere controls the transit of solar wind structures to Earth and beyond	a. How is the solar wind in the inner heliosphere determined by coronal and photospheric structure?	–	–	–	-	R	R	R	R	–	R-PW	R	–	S	R (C+E)
		b. How do ICMEs interact with the preexisting heliosphere?	–	–	–	S-E	R	R	R	R	–	S	–	S (X)	–	R (C)
		c. How do ICMEs interact with each other?	R	S	S	R	R	R	R	R	–	R	R	–	S	R (C)

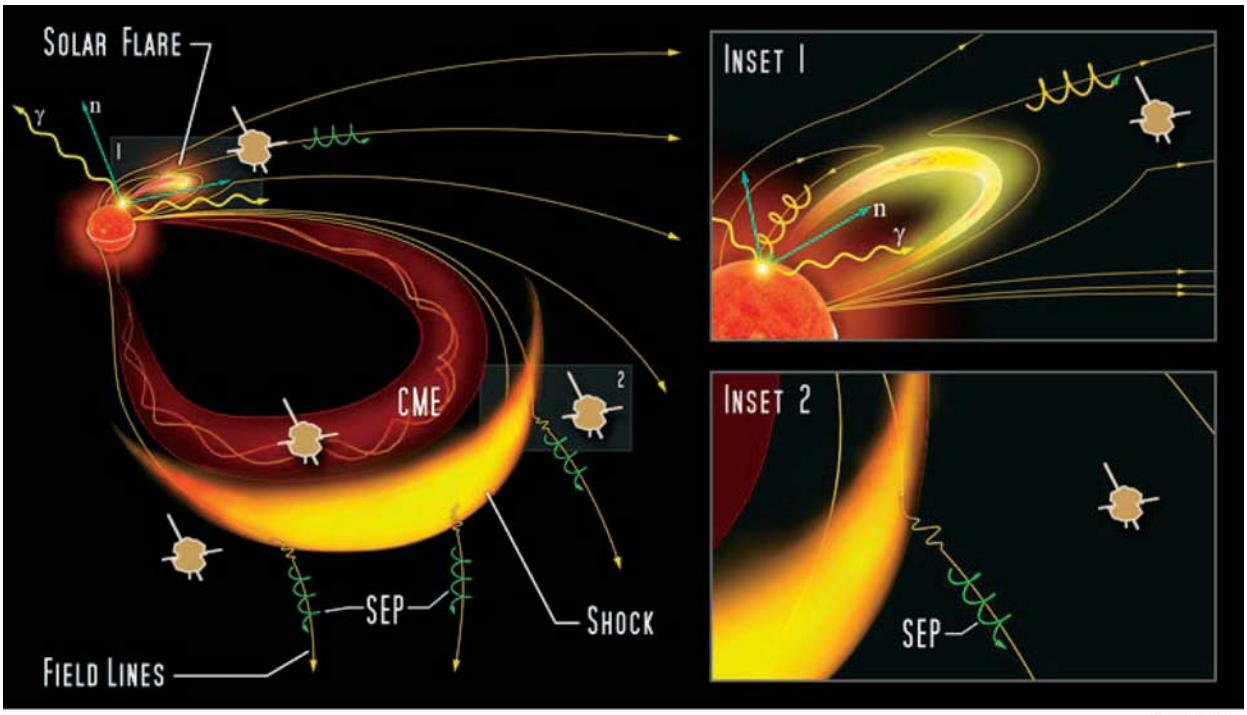

Figure 3-1. A cartoon demonstrating the need for multiple in-situ observations of SEPs in the inner heliosphere. Simultaneous observations of magnetic field lines connecting back to flare sites (inset 1) and to shock fronts driven by ICMEs (inset 2) are required to determine the relative importance of the associated acceleration processes.

ICMEs we assume a magnetic flux rope initially joined to the Sun at both ends. In that case we need measurements at two positions to give the ICME longitudinal extent, or equivalently, the location and radius of the major axis. An additional measurement is required to determine the latitudinal extent, which corresponds to the flux rope radius of the minor axis. The flux rope plane is generally tilted at some angle to the ecliptic, and the cross-section is distorted by a combination of solar wind expansion and solar wind stream interactions, so that at least a fourth IHS measurement is needed to determine the cross-sectional distortion. While the time series of magnetic field and plasma measurements at each of the IHS spacecraft yields information well beyond simple snapshot observations, the ICMEs are also subject to spatially dependent accelerations, shearing, and coronal/IP magnetic reconnections, all of which will require the four spacecraft for the most basic characterizations. Because the optimal situation when all four IHS spacecraft will be in position to observe a single SEP event or ICME structure (i.e., within < 180° longitude) will occur only during a fraction of the mission, these parametric descriptions dictate a minimum configuration of four IHS spacecraft. Additional observations by the NES, FSS, or other spacecraft will certainly be useful and sometimes necessary for adequate characterizations.

3.1.3 How much in-situ observation time is required close to the Sun? Our key requirement is to observe a sufficient number of SEP events, especially gradual events, inside ~0.35 AU to be able to determine the source of the SEPs and the physics of the acceleration mechanism. **Figure 3-2a** shows the expected average number of SEP events per year at 1 AU with proton peak intensities I(>10 MeV) above 10 $cm^{-2}\,sr^{-1}\,s^{-1}$ for the years 2005–2020 (almost all gradual events associated with fast, broad CMEs). An average of ~13.5 events/year are observed for the 3 years around solar maximum and ~2.7 events/year for the 5 years around solar minimum. **Figure 3-2b** shows the integral frequency distribution of gradual SEP events $N(>I) \propto I^{-0.44}$, based on observations at 1 AU made during the last three solar cycles. Gradual events have been identified to I(>10 MeV) ~1 $cm^{-2}\,sr^{-1}\,s^{-1}$ [*Kahler*, 2005], ten times less intense and below, with about the same power law exponent for the frequency distribution. Comparisons of SEP

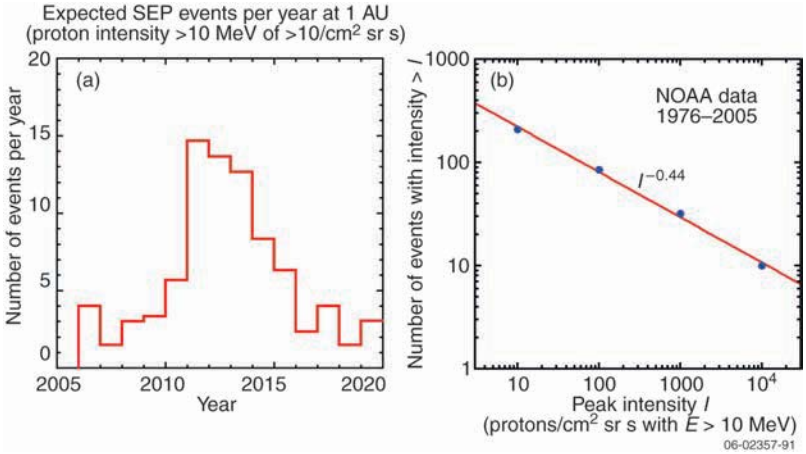

Figure 3-2. (a) Expected number of solar energetic particle (SEP) events per year at 1 AU with proton peak intensities (>10 MeV) above 10 $cm^{-2}sr^{-1}s^{-1}$ extrapolated from NOAA 1976–2005 data and assuming an 11-year solar cycle periodicity. (b) Integral frequency distribution of gradual SEP events based on 1 AU NOAA observations made during the last three solar cycles.

measurements at Helios in the inner heliosphere with IMP-8 at 1 AU indicate that the peak intensity of >10 MeV protons, I(>10 MeV), varies with distance from the Sun approximately as $r^{-2.4}$ [*Lario et al.*, 2006], so we expect ~3.5 times as many events to be detectable at ~0.3(±0.05) AU as at 1 AU, or ~48 events/year with I(>10 MeV) > 10 $cm^{-2}sr^{-1}s^{-1}$ near maximum and ~10 events/year near minimum. For I(>10 MeV) > 1 $cm^{-2}sr^{-1}s^{-1}$, these numbers go up by a factor of ~2.7. To observe a statistical minimum of 10 gradual SEP events at ~0.3 AU requires 0.075 year during solar maximum, or 0.38 year during minimum for I(>10 MeV) > 1 $cm^{-2}sr^{-1}s^{-1}$. Therefore, for a nominal 3-year prime mission, at least 2.5% to 13% duty cycle inside ~0.35 AU (0.3±0.05 AU) is required for the in-situ observations.

Moving the perihelion closer to the Sun does not necessarily result in prolonged stay in the inner heliosphere—the Solar Probe's orbit (~5 AU aphelion) reaches within ~4 R_S of the Sun-center, but spends only 0.8% of its mission within 0.35 AU (**Figure 3-3a**, black dashed line), while one of the Helios spacecraft, reaching only 0.29 AU but with a 1 AU aphelion, spent 8% of its orbit within 0.35 AU (**Figure 3-3a**, red dashed line). As discussed in the previous paragraph, thermal considerations limit the IHS perihelion to >~0.25 AU. To increase the duty cycle inside 0.35 AU, Venus gravity assists (VGAs) can be used to reduce the aphelion to near Venus orbital distance (~0.75 AU). For the IHS orbit design described in Chapter 4 (four spacecraft launched on a single launch vehicle and spread out using slightly different Venus encounters as needed to obtain the required multipoint measurements), the first VGA (a few months after launch) puts the spacecraft into a ~0.5 × 0.88 AU orbit, the second VGA about a year after launch obtains a ~0.32 × 0.77 AU orbit, and the third VGA reaches the ~0.25 × 0.75 AU final orbits (**Figure 3-4a**). Thus, for a nominal 3-year IHS prime mission beginning at the first Venus encounter, at least one IHS spacecraft is inside 0.35 AU for ~14% of the time (**Figure 3-3b**, solid red line).

Figure 3-5 shows the number of gradual SEP events with I(>10 MeV) > 1 $cm^{-2}sr^{-1}s^{-1}$ detected by one spacecraft inside radius R, plotted versus R. For the nominal 3-year mission and a launch near

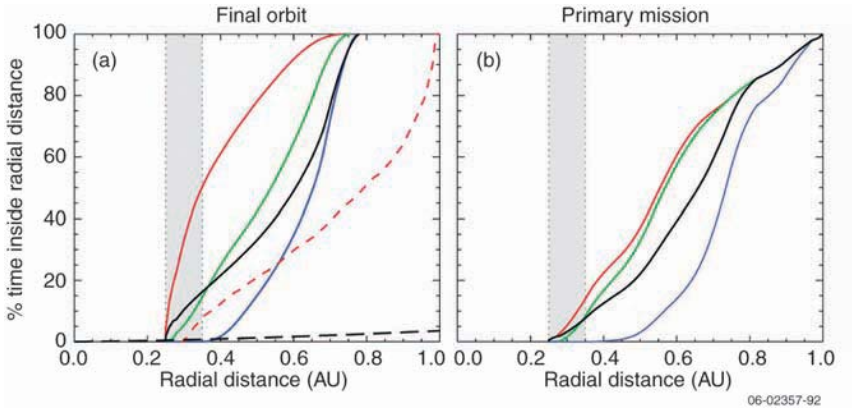

Figure 3-3. (a) The percent of the final orbital period one Inner Heliospheric Sentinels spacecraft (solid black line) spends inside various heliocentric radial distances. For a four-spacecraft constellation, the percent time any one (solid red line), two (solid green line) or three (solid blue line) of the four spacecraft are inside a radial distance is also shown. For comparison the same curve is computed for one Helios (dashed red line) and for the proposed Solar Probe mission (dashed black line). (b) The same quantity computed for the 3-year primary IHS mission that includes over 2 years of Venus encounter orbits.

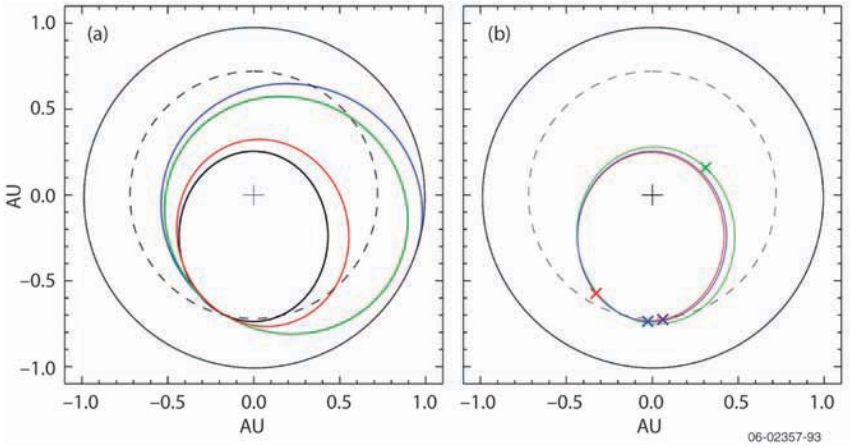

Figure 3-4. (a) Inner Heliospheric Sentinels heliocentric orbit for one of the spacecraft. The blue line depicts the orbit from launch to first Venus encounter (163 days), the green line from first to third encounters (the second encounter is very distant, resulting in only minor orbit corrections) (449 days), and the red line from the third to fourth encounters (449 days). The solid black curve is the desired final orbit. The outer thin black circle is the orbit of Earth and the dashed line is that of Venus. (b) a similar orbit plot showing one possible final orbit scenario for the four IHS spacecraft. The crosses show the locations of the four spacecraft shortly after the insertion of the final spacecraft. The purple spacecraft is in the same orbit as the red, but with a different phase angle. The relative positions change with time due to the different orbital periods.

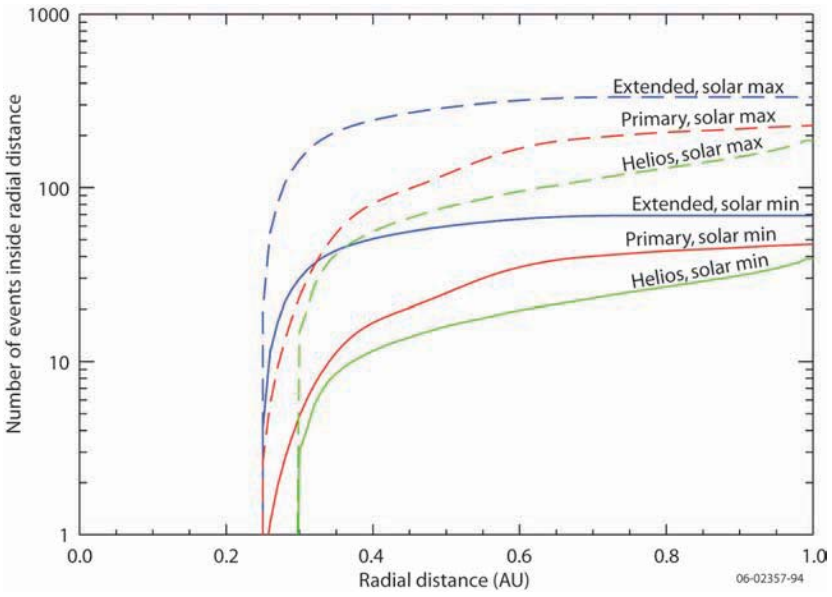

Figure 3-5. The number of gradual SEP events with an intensity I(>10 MeV) > 1 cm^{-2} sr^{-1} s^{-1} detected by the innermost spacecraft inside of radius R, plotted versus R. The red lines are for the primary 3-year mission at either solar minimum (solid) or solar maximum (dashed). The blue curves are for the extended phase of the mission at either solar minimum (solid) or solar maximum (dashed). Note that this calculation underestimates the total number of observed SEP events by perhaps 10% inside 0.35 AU and possibly by as much as a factor of two at 1 AU because it does not account for events that are not observed by the innermost spacecraft because of poor magnetic connection, but are observed by one or more of the more distant spacecraft. For comparison, the same parameter is computed for the orbit of Helios (green) and scaled to the same 3-year mission duration.

solar minimum, we expect to be able to study at least 40 events with four distributed, well-instrumented spacecraft located inside 0.75 AU. For approximately 11 of these events (on average), it is expected that at least one spacecraft will be able to study the event from inside 0.35 AU, a location where it will be possible to learn the most about the acceleration process. A launch at solar maximum will provide up to 5 times as many events. Although there is a range of predictions about the next solar maximum, the best current prediction [*Dikpati et al.*, 2006] finds that the next maximum should be 30% to 50% stronger than the last solar maximum, with the maximum occurring in 2011–2013. It is clear that a 2012 launch would have a great advantage over a 2014, 2015, or 2017 launch because it would provide at least 1 year overlap with solar maximum conditions, greatly increasing the expected number of SEP events that could be studied from close range during the prime mission, and making it very likely that one of the very large events that often occur at the trailing edge of solar maximum would be captured.

The final orbits provide ~51% duty cycle (compared with 8% for Helios) for at least one of the four spacecraft being inside 0.35 AU (**Figure 3-3a**, solid red line). Moreover, 14% of the time at least two spacecraft will be simultaneously inside 0.35 AU (**Figure 3-3a**, solid green line). Thus, an extended IHS mission would be extremely desirable in any case, making it possible to accumulate a large sample set (3 years near solar minimum would provide ~43 events inside

0.35 AU, or ~210 events near solar maximum), and would have an excellent chance to catch one of the most intense gradual event of the solar cycle.

On the other hand, because impulsive SEP events occur far more frequently, IHS should detect more than 50 to 100 such events inside 0.35 AU, even under the most conservative assumptions and for the least advantageous launch window. Thus the IHS orbit design described in Chapter 4 meets the minimum requirement for dwell time close to the Sun.

3.1.4 What relative orbital configurations are required for IHS? Chapter 4 details the possible trajectories of four spacecraft launched by one vehicle and separated in longitude and radial distance by multiple Venus gravity assist maneuvers. The science objectives require the simultaneous observation of the same ICME at different longitudinal and radial positions. Since the typical angular width of ICMEs is on the order of 50° to 60°, two IHS spacecraft are placed in very similar orbits with an aphelion phase shift of ~40°. A third spacecraft at a slightly larger radial distance from Sun will precess between the first two during the 3 years of mission. Finally, a fourth spacecraft could have a significantly different orbit semi-major axis orientation to provide larger relative radial separations (see **Figure 3-4b** for an example of an advantageous orbital configuration). The orbit configuration described is not the only possible scenario, but it demonstrates that the above-outlined measurement requirements can be satisfied in a cost-effective manner.

Measurements from an extremely desirable additional fifth vantage point in the inner (<0.75 AU) heliosphere, and up to ~38° above the ecliptic plane, would be provided by the European Space Agency's (ESA's) Solar Orbiter mission. The MESSENGER and Bepi-Colombo missions to Mercury may provide additional vantage points near 0.3 AU, while the FSS and other near-Earth spacecraft such as the Chinese KuaFu mission could provide additional vantage points near 1 AU. Highly desirable in-situ observations beyond 1 AU could be provided by instrumentation on missions to Mars or to other outer heliosphere destinations.

3.1.5 How can the in-situ measurements be directly connected to the imaging observations of the corona and inner heliosphere? As is evident from **Table 3-1**, a key measurement requirement is to directly connect the structure and internal topology of CMEs (and other coronal structure) imaged by coronagraphs with the in-situ measurements (i.e., "ground truth") of ICMEs and inner heliospheric structure made by IHS spacecraft *within the field of view of the coronagraph*. This will require concurrent wide-field coronagrapic imaging out to ~0.3 AU (~60 R_S), since the IHS spacecraft perihelions are ~0.25 AU. In addition, studies of the SEP source regions (CME shocks and current sheets) in the corona at a few to ~10 R_S will require a UV spectroscopic coronagraph that can measure the physical conditions—such as plasma heating associated with shocks in the corona, enhancements of high-charge-state ions, suprathermal particle populations, etc.—in the acceleration region.

To meet these requirements, the Sentinels STDT recommends implementation of the Near-Earth Sentinel (NES) spacecraft carrying a UV spectroscopic coronagraph (UVSC) and a wide- and inner-field coronagraph (WIFCO). NES could be launched with a modest launch vehicle into a Sun-synchronous low-Earth orbit that can accommodate the required high data rates of these instruments. Simultaneous coverage by IHS and NES of the same CME (as well as the associated energetic particles) is required, but NES could be launched up to ~2 years later than IHS, when the IHS spacecraft are reaching their final inner heliospheric orbits. In the meantime, however, SEP acceleration and propagation and global ICME questions can be addressed with standard coronagraph observations that reach to 20 to 30 R_S, similar to what is currently provided by SOHO/LASCO or expected from STEREO. Such coronagraphic observations are expected to be available, from the Chinese-led KuaFu mission, from NOAA spacecraft, or from ESA's Solar Orbiter.

3.1.6 How much of the Sun's photospheric magnetic field has to be observed? As discussed in Chapters 1 and 2, accurate global heliospheric models require knowledge of photospheric magnetic fields around the Sun. Observations from a single vantage point such as the Earth can provide photospheric magnetic field measurements for ~120° of longitude (180° is not possible due to foreshortening on the limbs), and could lead to as much

as a 10° discrepancy in the longitude of the field line foot points between the modeled and observed interplanetary magnetic field at 1 AU. Solar Orbiter is expected to carry a vector magnetograph and will spend a substantial amount of time on the other side of the Sun with respect to Earth. Thus, measurements by the FSS, separated in longitude from the Earth by 60° to 120°, together with magnetographic measurements by the Solar Dynamics Observatory (SDO) and Solar Orbiter, will provide nearly global coverage for a significant time. The FSS/SDO/Solar Orbiter combination will not provide continuous full-Sun observations, because Solar Orbiter is moving rapidly in its inner heliospheric orbit. However, this optimal configuration will last about a month at a time and recur every 4 months, providing sufficiently long stretches of time (at least one full solar rotation at a time) to test improvements in the accuracy of global heliospheric models. A second FSS spacecraft heading in the opposite direction from the first one would be greatly beneficial.

FSS can be placed into either an Earth-leading or an Earth-lagging orbit at 1 AU. While each configuration has significant advantages, the STDT has adopted the Earth-leading approach, which will allow FSS to image the foot points of the magnetic field lines that intersect Earth and hence are more relevant for studies of SEP transport that focus on near-Earth space weather. There is no requirement for FSS to orbit closer to the Sun than ~1 AU, and in fact cost-effectiveness dictates an orbit near 1 AU. Ideally, FSS should be launched early enough to overlap with SDO (although this is not a requirement, since other space or ground-based magnetographs are expected to be available), but late enough to overlap with Solar Orbiter when it reaches its final orbit.

In addition to photospheric magnetic field measurements, the instrumentation on FSS could make helioseismic measurements that would complement those made near Earth, probing mass flows associated with dynamo activity in the deep solar interior and providing a valuable secondary science return.

3.1.7 What is the optimum timing of the Sentinels mission? To accomplish the science objectives in time to support the first manned lunar mission and fit within the Living With a Star (LWS) funding envelope, the STDT has developed a plan to implement Sentinels in a *staged approach,* to enable the earliest possible launch date for critical elements of Sentinels components. Specifically, IHS would be developed and launched first (preferably in the near-maximum 2012 launch window, as discussed above) to maximize the number of SEP events that would be detected in the inner heliosphere (**Figure 3-2**), and to provide critical overlap with SDO to determine the conditions for initiation of the flares/fast CMEs that lead to SEP events. Moreover, by launching IHS during the upcoming solar maximum, Sentinels would take advantage of the last opportunity to develop critical knowledge necessary for the development of space radiation environment forecasting capability, in time for the first manned lunar missions of the Vision for Space Exploration (VSE). IHS will also have real-time capabilities that allow prototyping and testing of space weather monitoring and forecasting functions, to help develop both the scientific and technical understanding necessary to implement a future heliospheric space weather warning system.

NES would be developed in time to have overlapping coverage with IHS, to study the coronal acceleration process and the Sun–heliosphere connection. This schedule would also likely result in an overlap with the highly complementary Solar Orbiter mission (planned launch in 2015), which will provide both imaging of the Sun and in-situ measurements, initially from the ecliptic while nearly co-rotating with the Sun and later from higher latitudes. The FSS launch should be timed to provide overlap with Solar Orbiter, since near-Earth ground or space-based magnetograph measurements are expected to be continuously available.

3.2 Sentinels Instrumentation

The following sections describe strawman instrument payloads identified by the STDT for each of the three flight elements of the Sentinels mission—the Inner Heliospheric Sentinels, the Near-Earth Sentinel, and the Farside Sentinel—based on the measurement requirements listed in **Table 3-1**.

3.2.1 Inner Heliospheric Sentinels. The IHS strawman payload consists of instrumentation for the in-situ measurement of solar wind plasma, suprathermals, and energetic particles (protons, alpha particles, electrons, composition, and charge states), magnetic fields, radio and plasma waves, and neutron and gamma-ray spectra. The payload also includes an X-ray imager to provide X-ray

imaging and spectroscopy of solar flares and active regions. This suite of instrumentation favors a spin-stabilized spacecraft.

The instruments described in the following subsections are those used by the APL engineering team in defining the mass, power, volume, and accommodation requirements for the baseline IHS spacecraft described in Chapter 4. The STDT chose to specify individual detector systems as instruments, many of which have traditionally been integrated into a single multi-detector instrument package. This approach has artificially increased the number of instruments in the strawman IHS payload. However, it allowed the STDT to identify and seek science justification for all elements of the specified instrumentation suite. As discussed in Chapter 4, the strawman instrument mass and power requirements do not drive the spacecraft bus design.

All instrument designs have significant flight heritage, thus assuring that the payload assumed in the APL engineering study was realistic. It should be stressed that the instruments described here represent only a strawman payload and that other approaches to make the measurements required to achieve the Sentinels mission objectives are possible. The STDT's intention is not to prescribe specific instrument designs but to indicate the measurement capabilities needed to achieve the Sentinels' scientific objectives and to describe one possible implementation of the IHS instrument payload. The instrument specifications and resource requirements for the IHS strawman payload are given in **Tables 3-2** and **3-3**, respectively.

3.2.1.1 Energetic Particle Instrumentation. The IHS science objectives require complete coverage for energetic particles from thermal plasma energies up to 500 MeV/nucleon for ions and up to ~10 MeV for electrons. The strawman IHS payload satisfies this requirement with an energetic particle package that consists of a high-energy ion composition analyzer, a low-energy ion composition analyzer, a low-energy electron and proton instrument, a charge-state analyzer, and a suprathermal electron instrument. To reduce resource demands on the spacecraft, the energetic particle instruments are serviced by a dedicated common data processing unit (DPU) and low-voltage power supply.

High-Energy Ion Composition Analyzer (HICA). The high-energy analyzer is required to measure the composition and energy spectra of energetic nuclei with $1 \le Z \le 28$ from ~3 to 500 MeV/nuc, as well as energetic electrons from ~0.5 to ~10 MeV. Three telescopes are assumed for the strawman instrument: two covering the energy range from 30 to 500 MeV/nuc (called HICA-Hi) and one covering the energy range from 3 to 30 MeV/nuc (called HICA-Lo). As a minimum, the charge resolution should be sufficient to measure the differential intensities of individual elements from H to Ni ($1 \le Z \le 28$). It would also be useful (but is not required to satisfy the minimum science requirements) to extend composition measurements (of element groups if not individual elements) to include nuclei with $30 \le Z \le 83$ that are overabundant in some SEP events associated with impulsive solar flares. It is required that ^{3}He and ^{4}He be separately identified between 3 and 50 MeV/nuc whenever the ^{3}He/^{4}He ratio exceeds 1%. Resolution of isotope ratios such as ^{22}Ne/^{20}Ne and ^{26}Mg/^{24}Mg would be useful for information about mass fractionation processes, but is not required.

Low-Energy Ion Composition Analyzer (LICA). The low-energy ion composition analzyer is required to measure the composition and energy spectra of energetic nuclei with $1 \le Z \le 28$ from ~0.02 to ~3 MeV/nuc, with a goal of extending these measurements down to 0.01 MeV/nuc. As a minimum, the element resolution of this subsystem should be sufficient to measure the differential intensities of even-Z elements from He to Ca, as well as N and Fe. It is required that ^{3}He and ^{4}He be separately identified between 0.05 and 2 MeV/nuc whenever the ^{3}He/^{4}He ratio exceeds 1%. Again, measurements of other isotope ratios such as ^{22}Ne/^{20}Ne and ^{26}Mg/^{24}Mg would be valuable but are not required. It would also be very useful (but is not required) to extend composition measurements to include nuclei with $30 \le Z \le 83$ (element groups, if not individual elements) that are overabundant in some SEP events associated with impulsive solar flares.

The maximum intensity of SEP events appears to scale with distance from the Sun (R) approximately as $R^{-2.5}$ to $R^{-1.6}$ [cf. *Lario et al.*, 2006]. To observe particle populations that range from quiet-time levels near 1 AU to the largest SEP events at 0.25 AU, the IHS composition analyzers should be able to measure intensities from ~0.1 to 10^6 particles/(cm^2 sr s MeV) for ions with energies >10 MeV (HICA) and >0.1 to 10 MeV (LICA). Particle intensities should be measured with a time

Table 3-2. Inner Heliospheric Sentinels instrument specifications

Instrument	Parameter(s) or Quantity(ies) Measured	Sensitivity *Dynamic Range*	Energy Range *Resolution*	Angular Range *Resolution*	Time Integration *Cadence*
High Energy Ion Composition Analyzer (HICA)	Composition and energy spectra of energetic nuclei $1 \leq Z \leq 28$ Energetic electrons	~0.1–10^6 protons/cm^2 s sr for >10 MeV	Ions: ~3–500 MeV/nuc e^-: ~0.5–10 MeV *6 energy bins/decade*	As much of 4π sr as possible *≤45°*	30 s for H; 10 s for e^-; 60 s for $Z \geq 2$
Low Energy Ion Composition Analyzer (LICA)	Composition and energy spectra of energetic nuclei $1 \leq Z \leq 28$	~0.1–10^6 protons/cm^2 s sr for >0.1–10 MeV	Ions: ~0.02–3 MeV/nuc *6 energy bins/decade*	As much of 4π sr as possible *≤45°*	30 s for H; 10 s; 60 s for $Z \geq 2$
Energetic Electron and Proton Instrument (EPI)	Energetic ions and electrons	~5×10^8 particles/cm^2 s sr MeV (protons and e^-)	Ions: ~0.02–10 MeV e^-: ~0.02–1 MeV *6 energy bins/decade*	As much of 4π sr as possible *Ions/e^-: 30°*	Ions/e^-: 10 s (e^- < 1 s for transients)
Suprathermal Electron Instrument (STE)	Distribution functions of suprathermal electrons	~1–10^8 e^-/cm^2 s sr for >2 keV	Suprathermals: ~2–100 keV *E/E ~ 0.20*	As much of 4π sr as possible *Suprathermals: 20°*	Auprathermals: 10 s (<1 s for transients)
Solar Energetic Particle Charge State and Composition Analyzer (SEPQ)	Ionization state of suprathermal through energetic particles $1 \leq Z \leq 28$	~1–10^5 ions/cm^2 s sr for >0.1 MeV *10^4*	10 keV/nuc–1 MeV/nuc *6 energy bins/decade*	As much of 4π sr as possible	15 min
Solar Wind Ion Analyzer (SWI)	3D distribution function of solar wind thermal protons and alphas	Density ~0.1–10^3/cm^3	~150–1500 (2000) km/s ~0.1–12 keV/e (protons) ~0.2–20 keV/e (alphas) (E/Q)/(E/Q) ~ 20	±30° of ecliptic 360° in ecliptic (by spacecraft spin) 5° × 5 ° (or better) resolution	1 min (few seconds in burst mode for transients)
Solar Wind Composition Analyzer (SWComp)	Composition and velocity distribution functions of major solar wind heavies including He, C, O, and Fe	10^7 over entire mission 10^5 at given location	100 eV/q–100 keV/q *E/E ~ 0.05*	±60° from ecliptic *10°*	1–5 min (burst mode to 10 s)
Solar Wind Electron Analyzer (SWE)	Full electron distribution functions	Density to >1000 cm^{-3}	<1–3000 eV *E/E ~ 0.10*	0° to 180° from spin axis ~3° × ~20°	~20 s (<3 s in burst mode for transients)
Dual Magnetometer (MAG)	DC vector magnetic field	0–20 Hz *±64,000*	n/a *0.1 nT accuracy for <1000 nT*	n/a	0.3 s (0.05 s in burst mode)
Search Coil Magnetometer (SCM)	AC magnetic field	5 Hz–20 kHz	<10^{-3} nT/ √Hz at 5 Hz, 10^{-5} nT/ √Hz at 5 kHz	n/a	*> 20 kSPS in burst*
Radio and Plasma Waves (WAVES)	Radio and electromagnetic fields	~DC–16 MHz	<1 mV/m at ~DC ~10^{-19} W/m^2/Hz at 16 MHz	n/a	*0.5 s to 10^7 s (burst)* *4 s for in-situ spectra* *20 s for radio spectra*
Neutron Spectrometer (NS)	Time*-tagged neutron spectra (*at Sun)	0.001 neutrons/cm^2 s *10,000 (may be limited by X-ray dose)*	2–20 MeV *30% at 3 MeV*	Full Sun	Max 30 s in burst mode *Dynamic (burst mode and background mode)*
X-Ray Imager (XRI)	Hard and soft X-ray spectra and imaging	Up to GOES X30 flares	1–150 keV *E/E ~ 0.05*	150° in ecliptic; ±10° out of plane *~20 arcsec*	~20 s (<3 s in burst mode for transients)
Gamma Ray Spectrometer (GRS)	Gamma spectra	5×10^{-3} gammas/cm^2 s at 2.2 MeV *10,000*	0.2–20 MeV *7% at 0.662 MeV*	Full Sun n/a	1 s in burst mode *Dynamic (burst mode and background mode)*

Table 3-3. Inner Heliospheric Sentinels instrument resource requirements.

Instrument	Mass (kg)	Power (W)	Data Rate (bps)
High Energy Ion Composition Analyzer (HICA)	8.0	5.00	600
Low Energy Ion Composition Analyzer (LICA)	2.0	1.7	400
Solar Energetic Particle Charge State and Composition Analyzer (SEPQ)	4.0	4.00	300
Energetic Electron and Proton Instrument (EPI)	2.5	2.3	500
Suprathermal Electron Instrument (STE)	1.0	1.0	250
SEP DPU and Low Voltage Power Supply (SEP DPU/LVPS)	6.5	6.50	N/A
Solar Wind Ion Analyzer (SWI)	4.1	4.00	1000
Solar Wind Composition Analyzer (SWComp)	6.0	6.00	950
Solar Wind Electron Analyzer (SWE)	1.5	1.50	350
Search Coil Magnetometer (SCM)	0.5	0.15	200
Dual Magnetometer (MAG)	1.5	1.00	400
Radio and Plasma Waves (WAVES)	5.2	3.00	600
Neutron Spectrometer (NS)	3.9	3.00	50
X-Ray Imager (XRI)	2.0	2.00	200
Gamma Ray Spectrometer (GRS)	2.3	0.48	100
Instrument DPU (IDPU)	3.0	3.30	N/A
Instrument Subtotal	**54.0**	**44.9**	**5900**
Plus 30% margin	**70.2**	**58.4**	**7670**

resolution that is no worse than 30 s for protons and 1 min for $Z \geq 2$ nuclei.

Near the Sun energetic ions may be highly anisotropic and beamed along the interplanetary magnetic field, which can vary considerably in direction. The instruments should therefore be mounted so as to sample as much of 4π steradians as possible. At the very least the instruments should take advantage of the spinning spacecraft to determine the magnitude and direction of first-order anisotropies with an angular resolution of $\leq 45°$.

Because HICA and LICA will most likely be allocated at most a few hundred bits per second (bps), it is essential that onboard particle identification be used to sort abundant species into a matrix of species versus energy at a rate of at least 100 particles/s. The energy resolution of these bins should be no worse than six intervals per decade.

Energetic particle composition instruments in the ~0.02 to ~3 MeV/nuc and ~3 to 500 MeV/nuc energy ranges have considerable heritage. Instrument designs that could be adapted to meet the IHS requirements (assuming modern, low-power, electronics) have flown on IMP-7 and -8, Helios, Voyager, ISEE-3, Ulysses, SAMPEX, Wind, and ACE and will be flown on STEREO.

Energetic Electron and Proton Instrument (EPI). EPI will measure energetic electrons from ~20 keV to ~1 MeV and energetic ions from ~20 keV to ~10 MeV total energy. Based on previous experience it is expected that high-resolution, low-energy ion composition instruments such as LICA are inefficient at measuring protons. The total ion energy measured by EPI is intended to complement the low-energy composition instrument by providing these observations.

Energetic electrons will be highly anisotropic and beamed along the interplanetary magnetic field. To measure the electron distribution function properly, EPI must sample as much of 4π steradians as possible. EPI is required to have an angular resolution along the spin axis of better than ~30° and needs to be mounted on the spacecraft to observe nearly full 4π steradians. As with the electrons, the low-energy protons are expected to have widely varying angular distributions with both gyrotropic and non-gyrotropic distributions. It is especially important that EPI be able to determine the magnitude and

direction of first-order proton anisotropies covering nearly 4π steradian. Nearly complete measurements of the low-energy proton distribution function are required to extend the capabilities of physics-based predictive SEP models, to distinguish between electron and ion acceleration mechanisms, and to develop and validate inner-heliospheric transport models.

Based on particle intensities scaled from the largest peak flux event observed at 1 AU during solar cycle 23, EPI should be capable of measuring intensities up to ~5 × 10^8 particles/(cm^2 sr s MeV). Because it is likely that this instrument will be allocated at most a few hundred bps, it is essential that the instrument have processing capabilities to reduce the required telemetry.

Energetic electron and ion instruments in the ~0.02 to ~1 MeV electron and ~0.02 to ~10 MeV ion energy range have significant flight heritage. Instrument designs that could meet the IHS requirements have flown on ACE, Ulysses, and WIND and will be flown on STEREO.

Solar Energetic Particle Charge State and Composition Analyzer (SEPQ). SEPQ will measure the ionization state of suprathermals and energetic particles ($1 \leq Z \leq 28$) in the energy range of less than tens of keV/nuc to a few hundred keV/nuc. Examples of instruments that could meet this requirement have been flown on ISEE-3, Ulysses, ACE, and SOHO [*Hovestadt et al.*, 1978; 1995].

A primary IHS objective is to identify the suprathermal seed populations that are accelerated by shock or other transient solar phenomena to produce solar energetic particles. Ion composition is one tool available to distinguish populations, but is usually insufficient given uncertainties in the role of particle rigidity (momentum per unit charge). The SEPQ ionization state measurements will provide key information about the sources of He-Fe ions. Ionization state measurements can uniquely identify the role of pickup ions, for example, and establish how rigidity organizes the particle data. SEPQ targets the suprathermal energy range where such particles are likely to participate in further acceleration by shocks. IHS' combination of suprathermal and solar wind ion charge state measurements will make it possible to trace the ion origins and histories.

SEPQ should be able to sample intense particle events without saturation. The suprathermal energy range, where particle intensities are naturally high, along with the expected radial dependence of event intensity, together afford a modest geometry factor (<0.1 cm^2 sr). The high particle intensities allow for a collimation system with smaller acceptance angles and thus allow the possibility of good charge state resolution ($\Delta Q/Q << 1$). Lower-intensity ^{3}He-rich particle events can be measured nearer to perihelion. With a spacecraft spin normal to the ecliptic, more than one sensor head (e.g., looking above and below the ecliptic plane) may be required to account for large particle anisotropies within 1 AU. There is thus a trade space of instrument resources (multiple heads), charge state resolution, and any requirements to observe high anisotropies.

Onboard event processing will be required to accommodate a data rate of at most a few hundred bps. The onboard spectral and charge-state bins should include the most abundant mass groups, augmented with a low rate of fully analyzed pulse-height events for detailed analysis and verification of the binning algorithms.

The ionization states of higher-energy ions (several to 100 MeV/nuc) are also of great interest for determining the sources of high-energy SEPs, but measurements even to a few MeV/nuc using a deflection technique would require instrument resources that are outside the scope of Sentinels mission. (The only currently viable technique for the higher energies uses a particle sensor in low-Earth orbit, along with the Earth's magnetic field as a rigidity selector.)

Suprathermal Electron Instrument (STE). STE covers the primary energy range (~2 to 100 keV) for electrons in impulsive, electron/^{3}He-rich events, which are the most common SEP events (>~1000/year near solar maximum). This energy range includes the impulsively accelerated solar electrons that generate type III radio emission, the shock-accelerated electrons that produce type II radio emission, and the superhalo electrons (whose origin is unknown) that are present in the interplanetary medium even during the very quietest times. The impulsive SEP event electrons provide ideal tracers of magnetic field connection from the Sun into the heliosphere. They can be located at the Sun through their bremsstrahlung X-ray emission (imaged by the XRI instrument), tracked as they travel along the magnetic field lines through the interplanetary medium by the type III radio bursts that they generate (by triangulation with the WAVES instruments

on IHS), and detected in situ by the STEs on the IHS spacecraft. By analyzing the velocity dispersion of these impulsively accelerated electrons, the field line length can be obtained in both the quiet interplanetary medium and in ICMEs, where the lengths can be several times typical Parker spiral length. Electron injection profiles and spectra in impulsive and gradual SEP events will be determined from STE measurements. Comparison of these data with XRI measurements of the spectrum, temporal profile, and location of the X-rays produced by electrons of the same energies at the Sun will provide detailed information about electron acceleration and escape in impulsive SEP events.

The primary requirement for STE is very high sensitivity compared with plasma electron instruments, since the electron fluxes at these energies are many orders of magnitude lower than solar wind plasma core or halo electrons. High sensitivity can be obtained through arrays of silicon semiconductor detectors (SSDs) with thin entrance windows, combined with state-of-the-art low-noise electronics to achieve energy thresholds below ~2 keV. Such SSD arrays in a pinhole camera configuration can provide angular resolution of better than ~20° over a nearly full three-dimensional field. Energy resolution of $\Delta E/E \sim 20\%$ would allow the accurate measurements of the electron distribution function required to quantitatively test wave–particle interactions for the production of the plasma waves that produce type III radio emission. Temporal resolution should be ~10 s (with < 1 s for transient studies using a burst memory). Pitch-angle sorting using onboard magnetometer measurements would provide physically meaningful data compression. Instrument designs that could meet these requirements have been developed for STEREO.

3.2.1.2 Solar Wind Plasma Instrumentation. The solar wind plasma instrumentation baselined for IHS consists of a Solar Wind Ion Analyzer (SWI), a Solar Wind Composition Analyzer (SWComp), and a Solar Wind Electron Analyzer (SWE).

Solar Wind Ion Analyzer (SWI). SWI is required to measure the three-dimensional distribution functions of solar wind protons over the energy range 0.1 to 10 keV with a goal of 20 keV (150 to 1500 km/s with a goal of 2000 km/s) over all solar wind conditions. Solar wind bulk parameters for density, vector velocity, heat flux, kinetic temperature, and temperature anisotropy should be provided with a typical time resolution of 1 min (one spin, ~3 s, resolution in burst mode for proton moments for shock studies). Measurements of solar wind alpha-particles (He^{+2}), singly charged helium He^{+} (often observed in ICME-related solar wind), and helium isotopic ratios ($^3He/^4He$) must be provided either by SWI or SWComp or both.

Solar wind ion distribution functions typically exhibit non-Maxwellian features, including non-thermal tails, secondary peaks in velocity, and temperature anisotropies generally along the magnetic field direction. There can also be differential streaming among different ion species. These characteristics, as well as compositional signatures (proton/alpha ratio, ratio of high to low first ionization potential [FIP] elemental abundances, ionic charge state distributions), are observed to vary for different types of solar wind flows (such as high-speed solar wind from coronal holes, slow solar wind, and ICMEs) and at their interplanetary boundaries (such as magnetic sector boundaries, compressive and rarefaction regions). It is important that SWI and SWComp have sufficient resolution and be sufficiently intercalibrated to provide meaningful interspecies comparisons.

Solar wind ions come from the sunward direction and are highly anisotropic. The minimum required field of view for solar wind is nominally ±30° above and below the ecliptic and ±30° in the ecliptic plane. More extended fields of view are desirable for studying particle acceleration processes at shocks and other heliospheric phenomena, such as pickup ions. Typically, the spinning of the spacecraft naturally covers a 360° in-ecliptic field of view, as well as the aberration angle effect. In-ecliptic directional determination and angular resolution for solar wind protons should be a couple of degrees or better, out-of-ecliptic to within a few degrees.

SWI will need to be able to make measurements both for the full spectrum of solar wind conditions and over the full orbital range of the IHS spacecraft (1 to 0.3 AU). The typical dynamic range of solar wind proton density at 1 AU is a few tenths to a couple of hundred protons/cm^3. Because solar wind density typically scales as R^{-2} with distance from the Sun, the innermost orbits of the Sentinels will increase the required upper sensitivity range for density to >2000 protons/cm^3, with a goal of ~4000 protons/cm^3. In addition to density, kinetic

temperature, heat flux, and interspecies velocity differences exhibit radial gradients in the inner heliosphere. SWI, and where applicable SWComp, should be capable of measuring the full dynamic range of these parameters with sufficient resolution to determine the radial gradients.

Because of the likelihood of extremely limited telemetry, at most a couple of hundred bits per second, it will be essential to have onboard processing providing (as necessary) species separation, solar wind tracking, moment calculations, distribution function characterizations, and prioritization of returned distribution functions. Heritage solar wind ion instruments have flown on spinning spacecraft such as Helios 1 and 2, Wind, and ACE; on 3-axis stabilized spacecraft such as SOHO; and will soon be flown on STEREO.

Solar Wind Composition Analyzer (SWComp). SWComp is required to measure the composition, charge state, and velocity distribution functions of solar wind ions between He and Fe from 100 eV/q to 100 keV/q. The key measurements include (1) the dynamic properties (velocities, thermal properties) of solar wind heavy ions in the inner heliosphere; (2) ionic (charge state) composition of ions as a signature of the source regions of solar wind and CMEs and their association with flares; (3) elemental composition as a signature of the solar wind source regions; and (4) distribution functions extended into the suprathermal range to probe shock acceleration processes and to relate suprathermal particles to the composition of high-energy particles accelerated in the heliosphere. As a minimum, charge resolution should allow resolution of all key charge states of He, C, and O and of the average charge states of Si and Fe. The elemental resolution should allow measurements of He/O, C/O, Fe/O, and Si/O in order to measure signatures of the first ionization potential (FIP) effect. ^{3}He and ^{4}He should be separately identified in the entire energy range. The energy resolution requirements should be 5%, and the angular resolution should be ~10° in all directions.

The SWComp field of view should spin in the ecliptic, covering at least a latitude range of ±60° from the ecliptic plane, and the entire 0° to 360° range within one spacecraft spin. The time of one spacecraft spin is sufficient for all fast measurements.

The dynamic range of SWComp should accommodate the R^{-2} density dependence of all components, as well as the range of abundance ratios at any given R. The velocity, temperature, and density of the most abundant species should be measured within one spacecraft spin period in a burst mode. Typical time-resolution requirements are ~1 or several minutes.

The solar wind composition experiment described here has heritage from instruments such as those that have been flown on ACE, Wind, Ulysses, and MESSENGER and that will fly on STEREO.

Solar Wind Electron Analyzer (SWE). SWE should be capable of measuring the full distribution function of electrons over the energy range <1 to ~3000 eV, which covers the spacecraft photoelectrons and the extremely cold (Tec < 1 eV) solar wind core electrons that provide a tracer of ejected cold prominence material in ICMEs; the typical thermal core population; and the halo and strahl population. SWE should have an angular resolution of ~3° in at least one dimension (~20° in the other) for measurements of halo/strahl directionality, and full three-dimensional angular coverage to allow tracing of the topology of the interplanetary magnetic fields, in particular, of ICME fields even when the IMF rotates far out of the ecliptic. The energy resolution should be ~10% to resolve the thermal electron distribution; control of the instrument's external potential may be needed to obtain this resolution at the lowest energies. The dynamic range should accommodate the measurements from 0.25 to 0.75 AU distance from the Sun. The temporal resolution can be typically ~20 s, but with much faster measurements, <~3 s (spin period), available for studying transient phenomena, such as shocks, using a burst memory.

Accurate measurements of cold solar wind core electrons, often found in ICMEs, require that the incoming electron trajectories not be significantly distorted by electric potentials on the spacecraft exterior surfaces, i.e., that the spacecraft be electrostatically clean. The spacecraft exterior surfaces (except for solar panels) should be conductive, and SWE should be mounted on a boom to minimize electrostatic effects.

Designs based on standard top-hat (symmetric quadraspherical) electrostatic analyzers (ESAs), with a 180° fan-shaped field of view oriented perpendicular to the spacecraft spin axis, can cover the full three-dimensional sky in a single spin. Such ESAs have been flown successfully on many spacecraft missions such as Wind, FAST, ACE, etc. The

measurements can be sorted into pitch-angle bins for physically meaningful data compression, using the onboard magnetometer measurements (already successfully implemented on space mission such as Wind).

3.2.1.3 Magnetometer (MAG). Knowledge of the interplanetary magnetic field strength and direction is critical for the identification and characterization of magnetic clouds/ICMEs, interplanetary shocks, and discontinuities. Moreover, magnetic field lines are the pathways for energetic particles; hence, determining their global topology is essential for the success of Sentinels.

Global topology observations will require a magnetometer that can measure the full range of interplanetary magnetic fields in the region between 0.25 and 1 AU. Based on Helios observations, and in agreement with heliospheric models, the magnitude of the steady magnetic fields is in the 0 to 100 nT range, with occasional high field transients reaching values of no more than 500 nT. An absolute accuracy of 0.1 nT and a time cadence of 10 s is sufficient to identify global heliospheric structures. A range of ±64,000 nT is desirable for calibration of the instrument on the ground.

The identification of the internal structure of interplanetary shocks and the level of magnetic field turbulence in the inner heliosphere will be critical for establishing the prevalent mechanisms of particle acceleration. Due to the rapid motion of the very steep gradient shock structures, a magnetic field time cadence of 0.3 s will be minimally required, with the ability to generate 0.05-s resolution short-period burst data.

In addition, it is desirable to characterize the breakpoint in the magnetic fluctuation spectrum (which is thought to mark the onset of dissipation) over the radial distance range of IHS. This breakpoint occurs at ~1 Hz at 1 AU, and is expected to vary with radial distance and solar wind conditions. To accomplish this, the MAG's frequency response must overlap that of the Search Coil Magnetometer (SCM), ideally sampling at 10 Hz or higher.

Magnetometers that can satisfy the above requirements are well within current technological capabilities and have extensive heritage from instruments flown on ACE, Wind, Ulysses, Helios, or Voyager. The measured ambient fields are comparable to typical spacecraft-generated fields. The MAG instrument requires a stringent magnetic cleanliness program and the placement of the sensor on a boom so that the spacecraft-generated DC fields at the sensor are no more than 0.1 nT and AC fields no more than 0.01 nT. The baseline IHS payload includes two sensors, one at the tip of the 5-m boom, the second located 2 m inboard from the first on the same boom to allow the precise determination of the spacecraft-generated magnetic fields.

3.2.1.4 Search Coil Magnetometer (SCM). The solar wind is rich in magnetic fluctuations, from DC to the electron cyclotron frequency. Ion cyclotron, Alfvén, and whistler waves are observed in the ambient solar wind and at shocks and discontinuities. The MHD cascade appears to proceed to short wavelength kinetic Alfvén waves, which appear at tens of hertz in the spacecraft frame. Whistler waves in the ambient solar wind are thought to control the evolution of solar wind electron heat flux, and hence to control thermal conduction. Electromagnetic whistlers occur at up to one-half the electron cyclotron frequency in the plasma frame. Ion cyclotron waves may be convected from the solar wind acceleration region out to IHS perihelion, where they would be observed at near the proton gyrofrequency.

SCM will measure magnetic fluctuations on three orthogonal axes from several hertz up to approximately 10 kHz, the local electron cyclotron frequency at Sentinels perihelion (0.25 AU). Similar instruments have flown on the FAST and Cluster missions (and will be flown on THEMIS) and could be adapted for Sentinels. SCM should have sensitivity at low frequencies that allows overlap with MAG at several hertz (order of 10^{-3} nT/$\sqrt{\text{Hz}}$) and a sensitivity of approximately 10^{-5} nT/$\sqrt{\text{Hz}}$ at a few kilohertz. The SCM instrument must be boom-mounted to be far (3 m or more) from spacecraft-generated noise sources, which fall off as $1/r^3$ from the spacecraft. In addition, the SCM must be mounted more than 1 m away from any other sensor or sources of noise. The SCM signal processing can be combined with the radio and plasma waves (WAVES) instrument and should follow a signal path similar to the electric sensors.

3.2.1.5 Radio and Plasma Waves Instrument (WAVES). WAVES will measure electric field fluctuations from near DC to radio frequencies of 16 MHz on a set of ~40-m (tip-to-tip) spin-plane wire electric antennas and a 5-m rigid electric antenna mounted on the spacecraft spin axis. WAVES can

also provide signal processing for the search coil magnetometer (SCM). Similar instruments have been flown on ISEE, Ulysses, Wind, and STEREO; an instrument for Sentinels would benefit from miniaturization efforts.

A variety of electromagnetic and electrostatic plasma waves will be present in both the ambient solar wind (as an extension of the MHD cascade and a thermalizing agent) and at shocks, discontinuities, type-III electron beams, reconnection events, and structures internal to CMEs. A DC electric field due to solar wind convection will be present, as well as DC fields in shocks and reconnecting current sheets. Electric and magnetic spectra and waveforms should be measured with sufficient time and spectral resolution to allow mode identification up to the electron cyclotron frequency.

The quasi-thermal noise (QTN) spectrum of electric fluctuations in the solar wind has a peak near the electron plasma frequency and has several features that allow precise measurement of the core and halo electron densities and temperatures, permitting intercalibration with the plasma analyzers. The QTN has also been used to measure the solar wind bulk velocity. Measurement of the QTN requires sensitive electric fluctuation measurements from ~2 kHz to 1 MHz, with frequency resolution sufficient to fit the spectrum, typically $\Delta f/f$ of a few percent.

Radio emission is generated in the interplanetary medium by electron beams accelerated in impulsive solar flares (type III radio emission) and at strong (CME-driven) interplanetary (IP) shocks (type II emission); these emissions occur at the local electron plasma frequency (and harmonic). Sensitivity should be sufficient to see the galactic nonthermal spectrum, e.g., better than 10^{-18} W/(m^2 Hz) at 10 MHz.

WAVES is capable of generating several megabytes/s of data and thus requires considerable onboard processing at the instrument level. For example, a waveform sampling scheme will be necessary to identify nonlinear features in plasma waves. Cross-spectral processing will aid in identifying wave modes such as whistler, kinetic Alfvén, and ion cyclotron waves.

The baseline IHS mission design calls for the spacecraft spin axis to be normal to the orbital plane. However, should it be possible to implement the IHS spacecraft as Sun-pointed spinners, WAVES could provide excellent measurements of the DC electric field in the solar wind. Such measurements would be unique and would elucidate the dissipation mechanism of solar wind turbulence, by providing a measurement of the index of refraction of the turbulence. It would also provide excellent measurements of cross-shock electric fields, which are important to many shock acceleration mechanisms. To make such measurements the electric antennas must be equally illuminated by the Sun, which is most easily implemented on a Sun-pointed spinner.

Successful implementation of a radio and plasma waves instrument requires electromagnetic cleanliness (EMC) at both spacecraft and instrument levels. An EMC committee should be formed to provide compatibility requirements, test plans, and review of instrument and harness designs. The STEREO EMC effort is an example of such a program.

3.2.1.6 Neutron and Gamma Ray Spectrometers. Neutron and gamma-ray line emissions are produced by the nuclear collisions of energetic (~1 to >~100 MeV/nuc) ions with the solar atmosphere. Because they are neutral, neutrons and gamma-rays propagate outwards, unaffected by the solar magnetic field, and can be detected remotely. They thus provide an invaluable source of information about the temporal behavior and spectral character of accelerated energetic ions at the Sun.

Solar gamma-rays have been successfully measured at 1 AU on a near-continuous basis since 1980, but there are only a handful of successful neutron measurements. The IHS orbit, with a perihelion of 0.25 AU, will open a new window in the neutron spectrum, allowing measurement of neutrons with energies below 10 MeV. Neutrons at these energies have never before been measured because the neutron lifetime is of order 1000 s, so most neutrons decay in flight before reaching Earth. IHS neutron measurements thus hold great potential for new discoveries.

Neutron measurements are highly complementary to gamma-ray line measurements; measuring both over a wide spectral range makes it possible to disentangle the composition or metallicity of the target corona and chromosphere and the population of energetic ions. Some gamma-ray measurements suggest that there is an abundance of heavy ions in the energetic particle population, for example, but these results are model dependent. Measuring neutrons can confirm or refute these conclusions.

Measurements of gamma-ray continuum emissions produced by electron bremsstrahlung also provide information on accelerated relativistic electrons.

Gamma Ray Spectrometer (GRS). The gamma-ray spectrometer consists of a scintillation detector, possibly segmented or using phoswich techniques to minimize background, with photomultiplier read-outs to provide an efficient line spectrometer with high spectral resolution and sensitivity from ~0.2 to >~20 MeV. This instrument will use standard techniques and methods, but may be able to take advantage of new scintillator materials such as lanthanum bromide that can provide energy resolutions a factor of 3 better than NaI (~1.5% at 3 MeV) with the stopping power and photopeak efficiency of CsI above 1 MeV. Count-rate spectra should be telemetered every 1 s in a compact one-dimensional array compatible with, but no poorer than, the energy resolution. The instrument should be able to handle count rates of 10^5 s^{-1} and should be protected from the intense flux of lower energy X-rays and penetrating SEPs. There should be minimal material between the instrument and the Sun, preferably without significant variation with spin. Similar scintillation detector gamma-ray spectrometers have been flown on SMM, OSO-7, and Yohkoh.

Neutron Spectrometer (NS). The neutron spectrometer must be designed to accurately measure the energy of each detected neutron. This capability is essential for removing the effects of velocity dispersion so that the time in the solar event when the neutron left the Sun can be determined. Furthermore, the solar neutrons must be distinguished both from solar gamma-rays or charged particles and from gamma-rays, neutrons, or charged particles produced by cosmic-ray interactions within the spacecraft. This requirement is especially important if quasi-steady neutron emission is to be distinguished from local background. Ideally, NS will image the Sun in neutrons and employ techniques that can reduce or eliminate background. Such techniques have existed in the laboratory for decades and were used on the Compton Gamma Ray Observatory. Compact versions are now being developed for the surveillance of special nuclear material for homeland security applications. The difficulty of measuring neutrons further requires that as much of the instrument as possible be active material for the direct detection of neutrons, placing strong constraints on any shielding or collimating materials.

NS should provide a spectrum of solar neutron counts as a function of neutron production time at the Sun. Ideally this could be computed onboard, thus requiring a minimal amount of telemetry bandwidth for the final two-dimensional array. The NS instrument should be programmable so that lower levels of data can be transmitted for careful ground study and/or diagnosis. The instrument should have sensitivity from 2 to at least 20 MeV. The energy resolution drives the precision of the neutron production-time data, i.e., 30 s. If mounted on a spinning spacecraft, the NS should have 360° field of view and a uniform response. Full neutron detections may approach 20 s^{-1} with count rates in individual elements 100 times that rate.

3.2.1.7 X-ray Imager (XRI). XRI will directly detect and image electron acceleration and energy release in flares and other transients, allowing the relationship between flare particle acceleration and the SEP events measured in situ to be studied. At the Sun, the accelerated electrons colliding with the solar atmosphere produce bremsstrahlung X-ray emission whose spectral, temporal, and spatial characteristics are measured by XRI, while the accelerated ions produce neutrons and gamma-ray emissions that are detected by the NS and GRS instruments. In addition, XRI will provide GOES-like soft X-ray measurements of flare and active region thermal (>2 MK) plasmas, but with imaging of individual flares/active regions over the entire side of the Sun visible from the IHS spacecraft.

Stereoscopic imaging from the multiple IHS spacecraft will make it possible to directly determine the X-ray emission heights of each source component. Limb occultation of sources from one IHS spacecraft allow high coronal X-ray emission to be cleanly detected and normalized by unocculted measurements from another IHS spacecraft, providing unique insights into the vertical transport of energetic electrons into coronal loops. Furthermore, flux and imaging intercomparisons of directly observed events on two or more IHS spacecraft can be used to determine the X-ray directivity (and hence electron beaming) of individual source components. Correlation of STE and XRI observations will be used for magnetic field line tracing and to investigate electron acceleration and escape in impulsive SEP events (see the discussion of STE in Section 3.1.2.1 above).

Although the spinning IHS spacecraft do not support conventional imaging, XRI utilizes a simple scanning technique to provide real-time soft and hard X-ray imaging and spectroscopy of solar flares and active regions over the entire visible solar surface. A pair of compact, orthogonal collimators rapidly modulate the incident X-ray fluxes as the spacecraft spins. The time-modulated fluxes yield two orthogonal high-quality one-dimensional solar images with ~20 arcsec resolution (equivalent to 5 to 15 arcsec at 1 AU). The imager has a self-contained aspect system, so precise alignment is not required. Cadmium-zinc-telluride (CZT) and silicon pin diode detectors behind the collimators measure the X-ray flux from ~1 to ~150 keV with good spectral resolution ($\Delta E/E$ ~5%). Temporal resolution of ~20 s in normal mode and ~3 s (spin period) during transients (stored in a burst memory) can be accommodated with a telemetry rate of a few hundred bits per second. Location and intensity information on the active regions and flares can be compressed onboard to a few bits per minute for inclusion in real-time beacon mode telemetry.

3.2.1.8 Instrument DPU. The IDPU provides the interface between the instruments and the spacecraft commad and data handling (C&DH) system. The IDPU will coordinate science operations onboard and control the instrument burst memory for high-time-resolution data. It will collect, format, and forward instrument telemetry to the C&DH, and decode and implement spacecraft commands and timing signals. The IDPU will also extract and format the space weather data from the science telemetry stream and forward it to the C&DH system. The IDPU will coordinate high-speed telemetry snapshots from the various instruments when the environment is active, playing those data back as part of the regular instrument telemetry stream. Depending on the spacecraft design and instrument locations, one or more IDPUs may be needed. Similar IDPU designs have flown on various missions such as FAST, RHESSI, and STEREO.

3.2.2 Near-Earth Sentinel (NES). The role of the NES is to characterize (1) the source regions for SEPs; (2) the properties of CMEs and flare/CME current sheets; and (3) the connection between the imaging of the near-Sun inner heliosphere and in-situ measurements of IHS (see the description of NES in Chapter 5 and Appendix D). The primary instruments baselined for NES are an **Ultraviolet Spectroscopic Coronagraph (UVSC)** and a **Wide- and Inner-Field Coronagraph (WIFCO).** Both instruments have heritage from SOHO and STEREO.

3.2.2.1 Ultraviolet Spectroscopic Coronagraph (UVSC). The NES/UVSC will be used to characterize CMEs, including the CME-driven shocks and current sheets that are believed to be the source regions of SEPs. The UVSC should have sufficiently high sensitivity and a wide enough spectral range to be able to determine line profiles for atoms and ions of many different charge-to-mass ratios, including helium, the most dominant species after hydrogen. This capability requires a sensitivity that is 2 orders of magnitude higher than that of the SOHO/UVCS instrument, as well as a spectral range that is wider than that of the SOHO/UVCS. To satisfy the Sentinels science objectives, the telescope should have an external occulter placed at a large enough distance from the primary mirror to provide a large unvignetted aperture and sufficient stray light suppression capability to be able to observe coronal structure and SEP source regions from heliocentric heights of 1.2 to 10 R_S. The inner field of view is significantly closer to the disk than was achievable with earlier space-based coronagraphs. This is particularly important for characterizing CMEs and their associated current sheets right after their formation close to the coronal base.

UVSC's cadence must be high enough to capture the evolution of fast CME events. For detailed studies of CMEs, flare/CME current sheets, corona streamers, and polar plumes, a spatial resolution of at least 5 arcsec is needed. UVSC should have a high enough spectral resolution to determine proton and minor ion velocity distributions (thermal and non-Maxwellian). Doppler shifts will also be used to determine bulk velocities along the line of sight. Determination of elemental abundances and charge states of ions in coronal plasmas can be used to identify the origin of particles detected in situ with the IHS spacecraft. In addition, UVSC should be capable of measuring coronal electron temperatures, including departures from a Maxwellian velocity distribution. When combined with white-light density measurements, UVSC observations will be used to determine bulk outflow velocities with the Doppler dimming/pumping technique [*Withbroe et al.*, 1982].

The range of spectroscopic diagnostic techniques should be sufficient to characterize SEP source regions to the extent that all plasma parameters included in theoretical models can be determined. Descriptions of solar wind source regions should be sufficient to characterize high- and low-frequency MHD waves believed to be responsible for the primary acceleration of the solar wind in the extended corona.

3.2.2.2 Wide- and Inner-Field Coronagraph (WIFCO). The WIFCO consists of two coronagraphs, a wide-field coronagraph (WFC) and an inner-field coronagraph (IFC). The IFC will be used to record the onset, structure, and initial acceleration of CMEs and possibly shocks in SEP source regions low in the corona and near the solar limb.[1] The WFC will be used to detect CMEs and shocks near the Sun and far from the Sun, out to where they are sampled in situ by the IHS near perihelia.

Wide Field Coronagraph (WFC). The minimum WFC requirements appropriate for determining the involvement of CMEs and shocks in SEP acceleration can be described in terms of field of view, temporal resolution, and image quality. The field of view should be circular and Sun-centered, with a half field angle extending from 3 to at least 60 R_S. The temporal resolution should be sufficient to track the evolution of shocks and fast CMEs associated with the acceleration of SEPs. The fastest of the 10,000 CMEs recorded by LASCO [*Brueckner et al.*, 1995] was 3200 km/s, on 10 November 2004; the second fastest 2800 km/s; and 36 have been above 2000 km/s. Since the maximum proper motion of a 2000 km/s CME is 1 R_S in 5.8 min, these structures would be well recorded with WFC cadences of 2 min inside 6 R_S; 10 min inside 12 R_S; and 20 min from 12 to 60 R_S.

Image quality can be expressed in terms of exposure, spatial resolution, exposure time, and masking of coronal structure by energetic particles during radiation storms. When both signal and background profiles are taken into account, the exposure sufficient to detect CMEs and shocks in the outer field of view will need to be about 12 times that achieved in 19 s with LASCO/C3, which detects shocks to about 25 R_S. A polarization analysis capability is recommended to improve knowledge of the three-dimensional distribution of the CMEs and shocks with respect to the IHS spacecraft. The ideal spatial resolution would be about 30 arcsec/pixel, where spatial resolution is dominated by detector pixelation, but it could be as high as about 100 arcsec, since the structures are relatively broad [*Vourlidas et al.*, 2003]. Exposure time short enough to avoid image smear beyond about 30 arcsec for fast CMEs and shocks is about 10.8 s. Energetic particles incident on the WFC image detector can mask CME and shock data during SEP events. Good WFC imagery can be maintained during the worst storms with multiple short 3-s exposures (peak masked fraction ~0.1; 13.5 × 13.5 μm pixel), obtained within the image blur time, which are efficiently scrubbed onboard for energetic particles before summing to a single final image. It is estimated that with an entrance aperture of 21 mm (about twice as large as that of LASCO/C3) and with an image summing and energetic particle scrubbing capability, a single 3-s exposure would be adequate for distances < 25 R_S and that five 3-s exposures summed onboard would be adequate for 60 R_S.

Inner Field Coronagraph (IFC). The IFC should have a Sun-centered circular field of view that, at its inner limit, approaches the solar limb to capture events that are out of the plane of the sky. To detect CME substructure, IFC's spatial resolution needs to be better than 10 arcsec (transverse to the radial direction). The timing of CME onset should be accurate to about 1 min in order to relate the coronagraphic observations with SEP timing analysis using IHS data. The acceleration and velocity of the fastest CMEs should be observable, since these are associated with shocks and SEP acceleration. Approximately eight images of a fast (≥2000 km/s) CME can be used to determine velocity and acceleration before it passes beyond the outer 4 R_S field of view cutoff. The IFC exposure time should be short enough (e.g., 0.5 s) that fast CME image smear and energetic particle masking of the image at the CCD are minimal.

A classical Lyot coronagraph will detect the required CME and shock density signatures in the electron, or K-corona, with a simple and compact instrument operating with a broad passband in the

[1] As an alternative to the IFC, an externally occulted visible light coronagraph (VLC) which employs the long boom required by the UVSC instrument could be included. Such an instrument could provide images of coronal density structures and bulk flows with a 10-s cadence and with "eclipse-like" clarity (5 arcsec resolution in both the radial and tangential directions).

visible region of the spectrum where the K-corona signal peaks. A polarization analyzer will enhance the contrast of the polarized K-corona Thomson-scattered photospheric photon signal in the presence of the unpolarized scene F-corona and instrumental backgrounds. Internal occultation is required to achieve high spatial resolution near the inner field limit (~1.3 R_S). With a compact instrument this type of occultation limits the outer field cutoff to about 4 R_S due to the scattering of solar disk light by the objective into the coronal image.

3.2.3 Farside Sentinel (FSS). Several payload options were considered in the Farside Sentinel implementation study conducted by an engineering team at the JPL (see the description of FSS in Chapter 5 and Appendix D). Payloads considered by the JPL team ranged from a simple magnetograph to a full payload complement comprising, in addition to the magnetograph, coronagraphs and instruments for the in-situ measurement of particles and magnetic fields. While a full instrument complement would certainly be useful, the essential measurements to be provided by the FSS are of the photospheric magnetic field. We therefore restrict the discussion here to a description of a concept for the **Farside Sentinel Magnetograph (FSM)**.

The FSM will provide photospheric magnetograms over a range of heliographic longitude separations from Earth with a spatial resolution up to 1500 km at disk center. These data will be used (1) to extend the range of photospheric boundary conditions used by models of the heliospheric magnetic field and (2) to determine the magnetic field conditions in the photosphere that are associated with eruptive events.

Making solar remote-sensing observations from beyond Earth orbit imposes severe constraints on both the volume of data that can be returned and the available mass for instrumentation. Current flight magnetographs are capable of providing all the necessary measurements to support the Sentinels science goals; however, they are difficult to accommodate because of their mass (~50 kg). To alleviate this problem the FSS could use a filter-based magnetograph, weighing ~10 kg and consuming 20 W of power. There are several possible implementations for the FSM, including solid etalon Fabry-Perot interferometers (FPI) (e.g., *Rust* [1986]; *Bonaccini* [1988]) or magneto-optical filters (MOF) (e.g., *Cacciani and Fofi* [1975]; *Tomczyk et al.* [1995]), each with different advantages and disadvantages. The strawman design selected for Farside and described here is a MOF magnetograph, which offers high stability and can be implemented with a compact optics design because of the inherently large field of view of the filter, with the compromise that the choice of operating line is limited (the K 770 nm line is assumed, although other lines are available (see *Murphy et al.* [2005] and references therein). The FSM will be capable of measuring longitudinal and vector magnetic fields in the mid-photosphere, with a varying cadence determined by the available telemetry rate. Longitudinal magnetograms, calculated onboard the spacecraft with an assumed compression factor of 2.5 and an angular resolution of 2 arcsec (i.e., a spatial resolution of 1500 km at disk center) and a 3-min cadence will be returned with an instrument data rate of 37 kbps and form the basic data set.

An attractive science option would be to return vector magnetograms. This will require significantly more telemetry bandwidth, as it is necessary to determine the four Stokes parameters at several wavelength positions across the spectral line [*Graham et al.*, 2002]. The FSM will measure all four Stokes parameters at five wavelength positions, resulting in a data volume of 134 Mb per magnetograph, assuming the above spatial resolution and compression. While returning this volume of raw data would require an extremely high telemetry rate (~750 kbps for a 3-min cadence), onboard processing can significantly reduce the required data volume. An enhanced magnetograph option was studied that could return vector magnetograph data at 158 kbps. This would allow the return of the longitudinal and transverse magnetic field magnitudes and the transverse field angle, together with some ancillary data, at a 3-min cadence.

In addition to magnetograph data, the FSM will be capable of measuring the velocity field in the photosphere via the Doppler shift of the chosen spectral line and returning Dopplergrams as an important secondary science product. As with vector magnetic fields, the return of Dopplergram data requires a high bandwidth. The enhanced magnetograph telemetry mode would allow the return of Dopplergram data with an angular resolution of 2 arcsec (1500 km at disk center) collected at a 45-s cadence, which is close to the acoustic cutoff frequency. Combined with

data collected on or near the Earth, these data would allow local helioseismology studies over an extended baseline, probing more deeply within the Sun than is currently possible with near-Earth assets.

3.3 Supporting Observations

Supporting measurements from both ground-based observatories and other spacecraft will provide valuable contextual information for the interpretation of Sentinels data, in particular the in-situ data acquired by the Inner Heliospheric Sentinels. The following sections briefly outline some of the facilities and missions that are proposed, planned, or under development and that can provide supporting observations to maximize the scientific yield of the Sentinels mission.

3.3.1 Supporting Ground-Based Observations. Remote-sensing observations in support of the Sentinels mission will be provided by both ground-based radio and optical telescopes. Radio observations will yield information about the nonthermal and thermal signatures of CMEs, electron trajectories (through type III bursts), shock waves (through type II bursts), and post-CME structures (through stationary type IV bursts), large-scale magnetic field structure and topology (through Faraday rotation measurements), and solar wind density and turbulence (interplanetary scintillation measurements). Optical observations, at both visible and infrared wavelengths, will supply contextual information about the emergence of magnetic flux, coronal magnetic field and topology, transient eruptions, active regions, and the quiet Sun.

In addition to radio telescopes already in operation in the U.S. and other countries, two advanced radio telescope arrays that are expected to come on line during the next decade will contribute significantly to the Sentinels mission. The proposed 100-plus-antenna **Frequency-Agile Solar Radio-telescope (FASR)** array will perform imaging spectroscopy with extremely high temporal, spatial, and spectral resolution over 3 decades of radio frequency, from 30 MHz to 30 GHz. This capability will represent a significant increase over current imaging at 5 frequencies (432 to 164 MHz) by the Nançay Radioheliograph and at 17 and 34 GHz by the Nobeyama Radioheliograph and will improve our ability to conduct quantitative studies of the buildup and release of magnetic energy in the corona. FASR will accurately measure coronal magnetic fields, image CMEs both off the limb and on the disk, and measure flare- and shock-accelerated energetic electrons from the upper chromosphere through and beyond the coronal heights (to at least 2.5 R_S) at which energy release is believed to occur, thus helping to characterize the onset of energetic phenomena subsequently observed by Sentinels.

The **Mileura Widefield Array–Low Frequency Demonstrator (MWA-LFD)** will be an array of 500 phased-array antennas, clustered in sub-arrays of 16 dipoles, each operating at 80 to 300 MHz and spread over a 1.5-km diameter. MWA-LFD will be located at a radio-quiet site in Western Australia. The primary goal of MWA-LFD is to demonstrate the capabilities of a digital array for conducting groundbreaking heliospheric and astrophysical science through wide fields of view, high sensitivity, and multiple beam capabilities. The heliospheric goals of MWA-LFD are to characterize the density, velocity, and magnetic field of the inner heliosphere, from the outer corona to interplanetary space, and to image and localize solar radio bursts with an angular resolution of several arcminutes and accuracy of a few arcseconds for compact emission regions. Interplanetary scintillations will be used to determine solar wind velocity and density. The Faraday rotation of galaxies in the MWA-LFD field of view will be used to remotely measure the magnetic field, with particular emphasis on CMEs. It is estimated that hundreds of radio sources would be available within 60 R_S of the Sun to obtain rotation measurements with about 5-min time resolution. MWA-LFD is expected to be fully operational within the next 2–3 years.

Ground-based optical observations in support of the Sentinels mission will be provided by telescopes already in operation in the United States and other countries and with the planned **Advanced Technology Solar Telescope (ATST)**. ATST's large 4-m aperture and use of adaptive optics will enable it to overcome the limitations to which existing ground-based optical telescopes are subject, allowing it to achieve the high spatial, temporal, and spectral resolution needed to probe the small-scale magnetic processes that play a fundamental role in solar activity. While existing facilities provide a coronal magnetic field sensitivity of about 1 G and have coarse spatial resolution, ATST will achieve sub-Gauss field

sensitivities, along with an angular resolution of 0.1 arcsec or better (comparable to TRACE coronal imagery). ATST will be used to study the origin, structure, and dynamics of magnetic flux ropes and the structure, dynamics, and heating of the chromosphere and corona. ATST observations will provide an important context for relating IHS in-situ observations of SEPs and transient structures to their solar sources. ATST first light is currently expected to occur in 2014.

3.3.2 Supporting Space-Based Measurements. Ground-based remote-sensing observations supporting the Sentinels mission will be complemented by measurements from a number of space-based observatories that are to be launched during the coming decade. The first of these is **STEREO**, which will place two nearly identical spacecraft, instrumented with both remote-sensing and in-situ instruments, into a heliocentric orbit at 1 AU. One spacecraft will lead the Earth, the other will follow, providing three-dimensional stereoscopic views of CMEs as they propagate through the inner heliosphere toward Earth. An imaging package comprising two white-light coronagraphs, an extreme ultraviolet (EUV) imager, and a heliospheric imager will observe the onset of CMEs and track their evolution, while the SWAVES instrument, through measurement of type II bursts in the decametric–hectometric wavelength range, will determine the location and evolution of the CME-driven shocks. Although only a 2-year prime mission is planned, it is conceivable that STEREO will still be operational after the Sentinels misson has begun and will thus be able to provide both remote-sensing observations and in-situ measurements at 1 AU in support of the Sentinels science investigation. STEREO will be launched in August 2006.

STEREO will be followed by the **Solar Dynamics Orbiter (SDO),** the first Living With a Star mission, which is scheduled for launch into geosynchronous orbit in 2008. With a 5-year prime mission and a planned 5-year extended mission phase, SDO will overlap with IHS (assuming a launch by 2015), allowing significant coordination between the two missions. EUV/UV observations with SDO's Atmospheric Imaging Assembly (AIA) will provide information about the three-dimensional structure and dynamics of the corona, the reconfiguration of the coronal fields and the onset of CMEs, flares, and filament eruptions, and the propagation of CMEs. This information can be correlated with the Sentinels heliospheric SEP measurements and X-ray/neutron/gamma-ray observations of coronal energy release.

ESA's **Solar Orbiter** will fly concurrently with Sentinels and will be the principal space-based source of supporting observations for the Sentinels mission. Launch is nominally scheduled for 2015, and operations (prime mission plus extended phase) are expected to continue through 2023. Solar Orbiter will be placed in an elliptical heliocentric orbit, with perihelion as close as 0.22 AU and inclination increasing from near-equatorial to 35° heliolatitude during the extended mission. During its perihelion passes, the spacecraft will co-rotate with the Sun, allowing Solar Orbiter to track the evolution of a particular feature or region over a period of days. Solar Orbiter's payload will comprise both remote-sensing and in-situ packages. The in-situ instrumentation is expected to be similar to that carried by the IHS spacecraft and will make measurements of energetic particles, solar wind plasma, neutrons, and fields that can be correlated with IHS measurements. The spacecraft will also carry a dust detector, which can provide information about "inner source" pickup ions produced from dust grains as a possible source of SEP seed particles. Solar Orbiter's remote sensing package will include a coronagraph, EUV and X-ray imagers, and a visible-light imager and magnetograph and will provide high-resolution observations of coronal structure and dynamics. Solar Orbiter's remote-sensing observations of the corona from as close to the Sun as 45 R_S can be related to the in-situ data acquired by both the Orbiter and the IHS and will contribute significantly to the accomplishment of the Sentinels science objectives.

Although **Solar Probe** is currently not included in the NASA budget, the recently completed mission definition study [*NASA*, 2005] has demonstrated that a flyby mission to as close as 3 R_S above the Sun's surface is technically feasible and could, in principle, be operational during the Sentinels mission. Such a mission would provide unique contextual information about the energetic particle, solar wind, suprathermal, and neutron populations well inside the perihelia of IHS and Solar Orbiter. Of particular relevance to the Sentinels mission would be the information that Solar Probe would be able

to provide on the SEP seed population near the Sun, a region that IHS will not be able to sample.

Finally, a potential source of supporting data for Sentinels is the Chinese National Space Agency's **KuaFu-A**, one of the elements of a three-satellite mission being planned to study the response of the geospace system to solar disturbances. The KuaFu-A spacecraft would be stationed at the L1 libration point and equipped with both remote-sensing and in-situ instruments. It would provide continuous imaging at extreme and far ultraviolet wavelengths of the source regions of eruptive events, track the propagation of CMEs/shocks through the inner heliosphere, and measure SEPs, as well as the background solar wind and IMF.

4.0 Implementation of the Inner Heliospheric Sentinels Mission

Of the three flight elements in the LWS Solar Sentinels program, the Inner Heliospheric Sentinels (IHS) mission is the most challenging in terms of mission design and implementation. The engineering staff at The Johns Hopkins University Applied Physics Laboratory (APL) was therefore tasked to conduct a detailed engineering and mission design study to demonstrate the feasibility of a mission that would fully address the objectives for in-situ science as defined by the STDT and discussed above in Chapter 2. Key mission and spacecraft design drivers include:

- Minimize the perihelion distance and maximize the portion of the orbit within 0.3 AU of the Sun
- Spacecraft attitude control through spin-stabilization to provide required instrument fields-of-view
- Launch of all four spacecraft on a single launch vehicle
- Operation in the challenging thermal environment near perihelion
- A mission life of 3 years with a goal of 5 years
- Spacecraft downlink capable of returning specified science data
- Goal of continuous transmission of space weather data

The sections that follow describe the baseline IHS mission designed by the APL team with significant input from the Sentinels STDT. The STDT-provided measurement requirements strongly favor a spinning spacecraft with the spin axis pointing ecliptic north.

4.1 Baseline Inner Heliospheric Sentinels (IHS) Mission Design

The baseline mission concept for the IHS component of the Sentinels mission calls for four identical, spinning spacecraft to be launched on an Atlas V-541 and, through the use of multiple Venus gravity assists, to be placed into slightly different, near-ecliptic heliocentric orbits of approximately 0.25 × 0.74 AU. The first Venus flyby will occur 3 to 6 months after launch, depending on the launch date. Two of the spacecraft (Sentinels-1 and Sentinels-2) will perform three Venus flybys; the first and third flybys will be separated by approximately 674 days (three Venus orbital periods). Sentinels-3 and Sentinels-4 will perform four flybys; the first and fourth flybys will be separated by approximately 899 days (four Venus orbital periods). Perihelion of the final heliocentric orbit is 0.25 AU for the Sentinels-1 and Sentinels-4 and slightly larger than 0.25 AU for Sentinels-2 and Sentinels-3. The motion of the four IHS spacecraft relative to one another caused by differences in the perihelia and periods of the final heliocentric orbits will result in a number of scientifically desirable configurations of the IHS constellation (cf. Section 3.1, "Observation Strategy," above).

4.1.1 Baseline orbit. Given a baseline IHS launch mass (with margin) of ~3192 kg, a heliocentric orbit of about 0.25 × 0.74 AU can be achieved with launch energies (C_3) that range between 20 and 30 km^2/s^2 according to the launch date selected. For launch energies within this range launch opportunities will occur every Earth–Venus synodic period (~584 days). Orbit trajectories were evaluated for launch dates in 2012, 2014, 2015, and 2017 (**Table 4-1**). For all dates evaluated, the required C_3 was calculated to

Table 4-1. Inner Heliospheric Sentinels launch opportunities. The declination of launch asymptote (DLA) is the declination of the post-launch hyperbolic excess velocity with respect to Earth.

Launch	First Venus Flyby	C_3 (km^2/s^2)	DLA (deg)	VHP Venus (km/s)	Heliocentric Ecliptic Inclination (deg)
3/1/2012	6/10/2012	26.5	21.7	10.56	0.3
3/11/2012	6/12/2012	24.0	20.8	10.65	0.5
3/21/2012	6/13/2012	24.3	20.4	10.95	0.6
1/29/2014	7/20/2014	27.8	24.2	11.06	1.3
2/8/2014	7/25/2014	27.5	22.6	11.30	0.8
2/18/2014	7/28/2014	28.0	20.5	11.43	0.6
8/26/2015	2/14/2016	26.5	–23.0	11.22	0.0
9/4/2015	2/14/2016	23.6	–22.2	10.93	0.0
9/15/2015	2/14/2016	26.2	–20.6	10.91	0.0
2/27/2017	9/5/2017	27.7	20.4	10.32	0.5
3/9/2017	9/9/2017	24.4	18.1	10.28	0.9
3/19/2017	9/13/2017	22.7	16.0	10.32	1.3

be less than 30.0 km^2/s^2, the heliocentric ecliptic inclinations ranged between 0.0° and 1.3°, and the hyperbolic excess velocity (VHP) with respect to Venus was greater than the 10 km/s required to achieve a heliocentric orbit with a perihelion of 0.25 AU. For the baseline IHS mission, a launch date of September 4, 2015, was assumed. For this launch date, a final orbit with a perihelion of ~0.25 AU, an aphelion of ~0.74 AU, and a heliocentric ecliptic inclination of 0° can be achieved with a C_3 of 23.6 km^2/s^2 and a Venus VHP of 10.93 km/s. The characteristics of the baseline orbits for the four IHS spacecraft are summarized in **Table 4-2. Figure 4-1** illustrates the Venus flyby trajectories and final orbit for Sentinels-1.

For all of the orbital scenarios studied, the Venus flybys are separated by integer multiples of the Venus orbital period. As a result, the perihelion right ascensions of the IHS spacecraft are not significantly separated. If desirable from a science perspective, however, significant angular separation among the spacecraft at perihelion could be achieved by separating the flybys by non-integer multiples of Venus' orbital period. (This change would also alter the heliocentric ecliptic inclination.) For a September 4, 2015, launch this option yields the following orbital characteristics:

- 0.25 × 0.74 AU final orbit, 127.52-day period, 3.21° ecliptic inclination
- Three Venus flybys: (1) 2/14/2016; (2) 12/4/2016; and (3) 2/26/2018 (flyby 2 + 449.4 days)
- Minimum flyby altitude 4929 km

The right ascension of perihelion is ~86° greater than in the September 4, 2015, baseline case. Comparison of the post-Venus flyby 3 perihelion shown in **Figure 4-1b** with that in **Figure 4-1a** clearly illustrates the appreciable difference in angular separation that can be achieved by modifying the intervals between Venus encounters. (Similar results would be expected for the other launch dates studied.) The angular separation of perihelion would be slightly larger for larger VHPs and slightly smaller for smaller VHPs.

4.1.2 Launch vehicle selection. A survey of NASA-approved launch vehicles was undertaken to determine their lift mass capabilities as a function of C_3 (**Figure 4-2**). The Atlas V and Delta IV were found to be the only vehicles currently in the U.S.

Table 4-2. The baseline IHS orbits for a September 4, 2015 launch.

Spacecraft	Venus Flybys	Minimum Flyby Altitude (km)	Final Orbit (AU)	Period (days)	Ecliptic Inclination (deg)	Position Relative to Sentinels-1
Sentinels-1	F1: 2/14/2016 F2: 9/26/2016[a] F3: 12/20/2017[b]	1079	0.25 × 0.74	127.15	0	—
Sentinels-2	F1: 2/14/2016 F2: 9/26/2016[a] F3: 12/20/2017[b]	1079	0.28 × 0.76	136.93	0	Drifts ~180° from Sentinels-1 in 2.5 years; drift rate not constant
Sentinels-3	F1: 2/14/2016 F2: 9/26/2016[a] F3: 5/9/2017[c] F4: 8/1/2018[d]	902	0.26 × 0.74	129.23	0[e]	Drifts toward Sentinels-1 over 5 years after Sentinels-1 final VGA; drift rate not constant
Sentinels-4	F1: 2/14/2016 F2: 9/26/2016[a] F3: 5/9/2017[c] F4: 8/1/2018[d]	902	0.25 × 0.74	127.15	0[e]	44.0° ahead of Sentinels-1 at flyby 4 (heliocentric)

[a]Flyby 1 + 224.7 days
[b]Flyby 2 + 449.4 days
[c]Flyby 2 + 224.7 days
[d]Flyby 3 + 449.4 days
[e]Ecliptic inclination of 2° between flybys 2 and 3

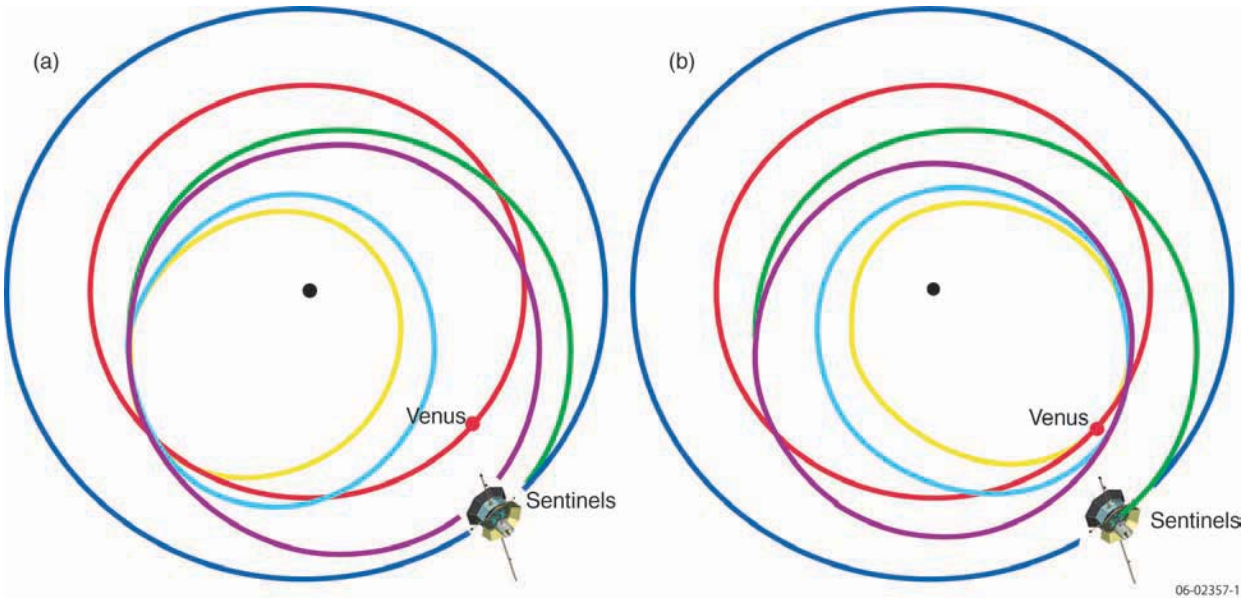

Figure 4-1. (a) A heliocentric view of the Sentinels-1 trajectory for a September 4, 2015 launch. There are three Venus flybys. The trajectory is green from launch through the first Venus flyby, purple after the first Venus flyby, cyan (light blue) after the second Venus flyby, and gold after the third Venus flyby. The Earth and Venus orbits are blue and red, respectively. (**b)** The same for a modified Sentinels trajectory.

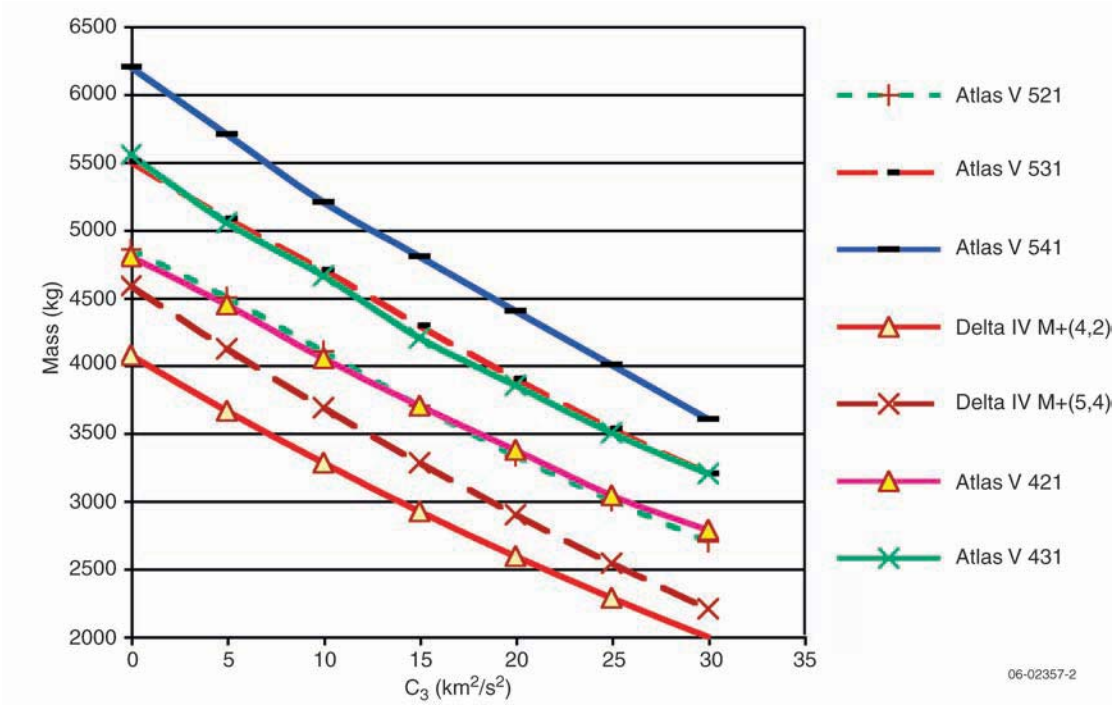

Figure 4-2. Lift mass as a function of C_3 for the set of potential launch vehicles evaluated for the IHS mission. The "H" or "heavy" versions of these vehicles were not considered for reasons of cost.

inventory capable of lifting several thousand kilograms to C_3 of 30 km^2/s^2. Based on the margined stack mass of ~3192 kg and the IHS C_3 requirement of 26.5 km^2/s^2, the Atlas V-541 (a 5-m fairing) has been baselined as the IHS launch vehicle (3605 kg capacity). If a 4-m fairing would suffice, the Atlas V-431 could be used (3390 kg capacity). Should the launch mass increase beyond the capabilities of the above launch vehicles, an Atlas V-551 (3925 kg capacity) could be used.

4.2 Mission Operations Concept

The timeline of key mission events for the September 4, 2015, baseline mission, from launch through the Venus flybys to the attainment of the final heliocentric orbits, is presented in **Table 4-3**.

4.2.1 Launch, separation, and spacecraft deployment. The four IHS spacecraft will be launched in a stacked configuration. (A radial configuration, with the four spacecraft stowed radially like flower petals, was also considered, but the stacked confguration was selected because of its simplicity, low risk, and relatively low cost. See Appendix B.) At launch (L) + 2 hours spacecraft separation will begin. At this time, the launch vehicle and the spacecraft stack will be in full Sun and spinning at ~3 rpm. The spacecraft release sequence will be initiated and timer-controlled by the upper stage and will involve a total of seven separation events, occurring 20 minutes apart: one for each of the four spacecraft and each of the three inter-spacecraft support structures (**Figure 4-3**). During spacecraft deployment, the spin-axis of the upper stage will be pointed 5° off ecliptic north and its direction altered between separations so that the four Sentinels are deployed around a circle, thus avoiding collisions with each other. (**Figure 4-4**). Typical achievable separation rates range from 0.5-3.0 m/s. Assuming a separation velocity of 1.0 m/s, each deployed item will be spaced 2800 m from the launch vehicle before the next deployment. In addition, owing to the tilt of the spin axis the separation of the items will increase with time. (Details of

Table 4-3. Timeline of key mission events from launch to attainment of final operational orbits for the four IHS spacecraft.

Date	Mission Event
September 4, 2015	Launch (L)
L + 2 hours:	Release of first IHS spacecraft (Sentinels-1)
L + 2 hours 40 min	Release of second IHS spacecraft (Sentinels-2)
L + 3 hours 20 min	Release of third IHS spacecraft (Sentinels-3)
L + 4 hours	Release of fourth IHS spacecraft (Sentinels-4)
September 14–17, 2015	First trajectory correction maneuver (TCM), Earth–Venus leg (Sentinels-1, 2, 3, 4)
January 30–February 2, 2016	Final TCM, Earth–Venus leg (Sentinels-1, 2, 3 ,4)
February 14, 2016	Flyby 1 (Sentinels-1, 2, 3, 4)
February 28–March 2, 2016	First TCM, first Venus–Venus leg (Sentinels-1 ,2, 3, 4)
September 11–14, 2016	Final TCM, first Venus–Venus leg (Sentinels-1, 2, 3, 4)
September 26, 2016	Flyby 2 (Sentinels-1, 2, 3, 4)
October 8–11, 2016	First TCM, second Venus–Venus leg (Sentinels-1, 2, 3, 4)
April 27–28, 2017	Final TCM, second Venus–Venus leg (Sentinels-3, 4)
May 9, 2017	Flyby 3 (Sentinels-3, 4)
May 24–25, 2017	First TCM, third Venus–Venus leg (Sentinels-3, 4)
December 5–6, 2017	Final TCM, second Venus–Venus leg (Sentinels-1, 2)
December 20, 2017	Flyby 3 (final, Sentinels-1, 2)
March 3, 2018	First post-flyby-3 perihelion, Sentinels-1 (0.25 AU)
March 14, 2018	First post-flyby-3 perihelion, Sentinels-2 (0.28 AU)
July 17–18, 2018	Final TCM, third Venus–Venus leg (Sentinels-3, 4)
August 1, 2018	Flyby 4 (final, Sentinels-3, 4)
October 14, 2018	First post-flyby-4 perihelion, Sentinels-4 (0.25 AU)
October 16, 2018	First post-flyby-4 perihelion, Sentinels-3 (0.26 AU)

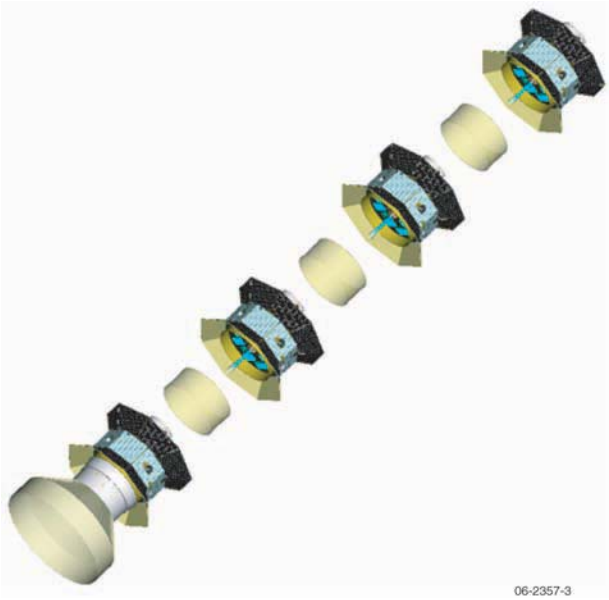

Figure 4-3. The four IHS spacecraft and three interspacecraft support structures in the stacked configuration.

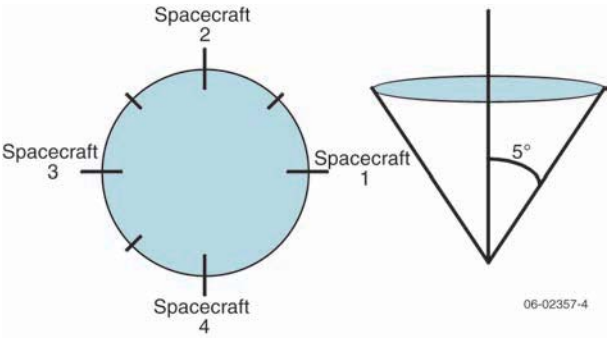

Figure 4-4. Separation vector directions for the four Sentinels.

the analysis of the spacecraft release and separation sequence are presented in Appendix A.)

At separation, each spacecraft will be spinning at ~3 rpm, with its spin axis pointed approximately due north of the ecliptic plane. This attitude is stable and will allow the spacecraft to enter a power-positive state. When each spacecraft senses its separation, a stored sequence of commands will run automatically. The transponder and medium-power transmitter will be turned on and transmit spacecraft status at 1000 bps through the aft low-gain antenna (LGA), which is fixed to the bottom deck of the spacecraft and will be operational immediately upon separation. The star scanner, accelerometers, and Sun sensor attached to the primary command and data handling (C&DH) subsystem will be turned on. The guidance and control (G&C) subsystem will determine how far the spacecraft spin axis is from being orthogonal to the ecliptic plane. Based on the expected upper-stage pointing accuracy and tip-off angle, this angle will likely be small and not need adjustment. However, if the angle exceeds a threshold, the G&C subsystem will "burp" the thrusters and initiate an autonomous spin-axis correction maneuver to orient the spacecraft spin axis normal to the ecliptic plane. (The catalyst bed heaters for the two thrusters needed for this maneuver will be turned on prior to launch.) Once the maneuver is completed (or if it is not necessary), the catalyst bed heaters will be turned off. After the initial sequence of stored commands has been executed, the spacecraft will remain in a passive state awaiting ground commands. The batteries are expected to be fully recharged within 12 hours. (In launch configuration the spacecraft will be on internal power, with only essential systems on to minimize the load on batteries; once on orbit and during separation from the upper stage, the solar arrays will be illuminated, allowing the batteries to recharge.)

4.2.2 Navigation. DSN 2-way range and Doppler data will be used for spacecraft navigation. DSN delta-differential one-way ranging (DDOR) data may be used prior to Venus flybys. From launch to L + 2 weeks the IHS spacecraft will be tracked nearly continuously. From L + 2 to L + 4 weeks, there will be five DSN passes per week; and from L + 4 to L + 6 weeks, three DSN passes per week.

For the Venus flybys, there will be three DSN passes per week from flyby minus 5 weeks to flyby minus 1 week, and 1 DSN pass per day from flyby minus 1 to flyby plus 1 week.

During the nominal mission phase, there will be two 8-hour DSN tracking passes every 3 weeks per spacecraft (additional passes will be required for solid-state recorder (SSR) playback; see Section 4.2.6 below). A solar conjunction of 50 to 60 days (see Section 4.2.7 below) should not be a problem, assuming accurate orbit determination beforehand. Moreover, the effects of the solar conjunction are not expected to last as long for the tracking data as for the high-rate science data.

4.2.3 Early operations. The ground assets required during initial spacecraft contact are detailed in Appendix A. During the first week

after launch, the mission operations team will initiate maneuvers to correct the spin axis orientation and increase the spin rate from 3 to 20 rpm. The health of primary and redundant spacecraft components will be checked. At approximately L + 11 days, there is sufficient power available from the solar arrays to operate the despun platform. Redundant pyros will be fired to release the platform, and the G&C subsystem will be commanded to control platform pointing. Once platform control is operational, the medium-gain antenna (MGA) can be used for the uplink and downlink. After the link is checked out with the MGA, the high-gain antenna (HGA) can be used for downlink, while the MGA will continue to be used for uplink.

Between L + 10 days and L + 13 days the first trajectory correction maneuver (TCM) for each of the four IHS spacecraft will be performed. The ΔV for this first TCM is estimated to be 30 m/s (**Tables 4-4** and **4-5**). (The maneuver may be broken up into several separate burns.) One spacecraft will be maneuvered per day over the 4-day period. The initial TCM will be performed to ensure that the four spacecraft arrive at Venus at different epochs. Small changes to the TCM will allow the Venus flyby epochs to be separated by 15 to 30 minutes. This will ensure spacecraft separation at the first Venus flyby, while also ensuring that the separation is not larger than ~100,000 km, as desired for science checkout during the Earth-to-Venus transfer. With periapses of the first Venus flyby separated by ~30 minutes, it is estimated that, for a September 4, 2015, launch, two IHS spacecraft would be separated by ~20,000 km at the first Venus flyby and by a maximum of ~50,000 km during the Earth-to-Venus transfer.

During the TCM the medium-power transmitter and aft LGA will be used for both uplink and downlink. After each maneuver is completed, use of the MGA for uplink and of the HGA for downlink will be resumed. Radio tracking before and after the TCM will allow ground navigators to calculate each spacecraft's orbit.

Table 4-4. Preliminary ΔV requirement for Sentinels-1 and 2.

Maneuvers	ΔV (m/s)
Trajectory Correction Maneuver 1 (TCM1, Earth–Venus leg)	30
Post-TCM1 to Venus Flyby 1	10
Venus Flyby 1 to Venus Flyby 2	10
Venus Flyby 2 to Venus Flyby 3	10
Total	60

Table 4-5. Preliminary ΔV requirements for Sentinels 3 and 4.

Maneuvers	ΔV (m/s)
Trajectory Correction Maneuver 1 (TCM1, Earth–Venus leg)	30
Post-TCM1 to Venus Flyby 1	10
Venus Flyby 1 to Venus Flyby 2	22
Venus Flyby 2 to Venus Flyby 3	23
Venus Flyby 3 to Venus Flyby 4	10
Total	95

4.2.4 Instrument checkout and calibration. Solar array power generation will increase by 20 W by approximately L + 26 days, enabling the start of instrument checkout. Instruments must be checked out individually or in small groups until 45 days after launch, when the solar array output will be sufficient to power the complete instrument payload. Instrument checkout must be completed prior to the final pre-Venus TCM to allow selection of the spacecraft for each trajectory based on instrument functionality. For all identified launch opportunities in the 2012–2017 time frame, there is at least a 3-month gap between launch and the first Venus flyby (the gap is 5 to 6 months for all but the launches in 2012). The final TCM will take place approximately 12 to 15 days before the actual Venus flyby, leaving at least 1.5 months for instrument checkout.

The magnetometer (MAG) must be powered when the 5-m boom is deployed; and, as a goal, the search coil magnetometer (SCM) should be powered when the 3-m boom is deployed. The solar wind electrons (SWE) instrument will be off when the 3-m boom is deployed, however, and the WAVES instrument will also be off when the wire antennas and axial antenna are deployed.

4.2.5 Venus flybys. In addition to the two TCMs performed during the Earth–Venus leg of the orbit, two TCMs will be performed on each of the Venus–Venus legs (cf. **Table 4-3**). The ΔV requirements for these maneuvers are shown in **Tables 4-4 and 4-5**. Preliminary analysis of the Sentinels-3 and Sentinels-4 trajectories indicates the possible need

for an additional 25 m/s ΔV between Venus flyby 1 and flyby 3 compared with the allocation for Sentinels-1 and Sentinels-2; however, further analysis may identify solutions to reduce or eliminate this additional ΔV. The IHS propulsion subsystem can provide 100 m/s ΔV (not including margin) for these maneuvers, which is sufficient to meet these requirements.

For all of the orbits studied, there will be a solar eclipse of up to 25 minutes during each Venus flyby. This will require that the spacecraft be powered by the battery. The spacecraft will therefore be placed in a minimum-power configuration during the flyby, with the instruments turned off. No Earth occultation periods occur during the Venus flybys analyzed in this study, and thus no communications blackouts are anticipated. (The occurrence of a communications blackout during a flyby would not be a significant problem in any event because no critical maneuvers are conducted during the actual flyby.) DSN coverage will be increased around the flybys to allow for accurate navigation

4.2.6 Science data acquisition. IHS science data will be collected and returned using a "store and forward system." Science data will be collected 24 hours/day at a low rate from the instruments and stored on the SSR. During each spacecraft's one 8-hour DSN pass per week, the stored data will be played back to the ground at a high rate. Some of these passes can be combined with the tracking passes required for navigation (see Section 4.2.2).

Once the solar array output has increased enough to support the instrument load, the entire instrument suite will be turned on and the data recorded on the SSR in the primary C&DH subsystem. Redundant recording on the SSR in the backup C&DH subsystem will begin once the solar array output has increased enough to support that additional load. The medium-power transmitter will be used for communications until the solar array output has increased enough to support the high-power transmitter. **Table 4-6** gives the spacecraft-to-Sun ranges where each of these modes will be in effect. During science data acquisition the MGA will be selected for uplink and the HGA for downlink. Although the rate at which instrument data are recorded is constant, the downlink rate will vary greatly depending on the spacecraft–Earth range. The effect of this highly varying rate is discussed below in Section 4.10, Mission Data Management.

Table 4-6. Instrument and communications modes.

Spacecraft Mode	Solar Distance (AU)
Instruments off and medium power transmitter on	1–0.88
Instruments and medium-power transmitter on and science data non-redundantly recorded on one SSR	0.88–0.85
Instruments and medium-power transmitter on and science data redundantly recorded on both SSRs	0.85–0.67
Instruments and high-power transmitter on and science data non-redundantly recorded on both SSRs	0.67–0.65
Instruments and high-power transmitter on and science data redundantly recorded on both SSRs	0.65–0.25

The solar distances at which the various instrument and communications modes can be implemented are a function of the size of the solar array, spacecraft bus power, instrument power, and transmitter power levels selected. If the instrument power requirement increases, then the distance from the Sun at which instruments are turned on must decrease, given the size of the solar array, and the solar distance at which the high-power transmitter is turned on will decrease also. Beyond a certain point, however, an increase in the instrument power requirement may reduce the amount of time that the instruments can be operated below a scientifically acceptable level. In this case, the size of the solar array would have to be increased.

During science data acquisition the downlink will be configured to transmit space weather data whenever the spacecraft is not in contact with the DSN. See Section 4.2.9.

4.2.7 Solar exclusion. When the angle between the spacecraft–Earth and Sun–Earth lines is between 2° and 3°, solar scintillation effects will render X-band communications unreliable. Once the angle is less than 2°, no communications at all will be possible. During these periods, the Sentinels must operate completely autonomously. The number and length of these periods will depend on the specific trajectory and launch date. For the baseline September

4, 2015, launch date, the number of days of solar exclusion (for a 2° and 3° Earth–Sun angle) for the Sentinels-1 and Sentinels-3 trajectories are shown in **Figure 4-5**.

As can be seen from the bottom panel of **Figure 4-5**, the longest period of solar exclusion lasts 60 days (a 3° Sun-Earth-Probe angle is assumed), although the low-rate telemetry and tracking exclusion period is likely to be less than 60 days. The IHS spacecraft must therefore be able to operate independently for 60 days. An initial analysis indicates that the DSN will have sufficient knowledge of spacecraft location after 60 days to re-establish communications. Prior to the beginning the solar exclusion period, the MGA will be selected for downlink, which will aid in downlink acquisition at the end of the exclusion. While science operations can continue during the period of solar exclusion, onboard time accuracy used to time-stamp science data will degrade because there will be no contacts to correlate spacecraft time to ground time. Time accuracy will degrade from 10 ms to 60 ms over the course of a 60-day exclusion period. Initial analysis indicates that the spin axis will move less than 1° during any 60 days, so that no autonomous spin-axis control should be required even during the longest period of solar exclusion.

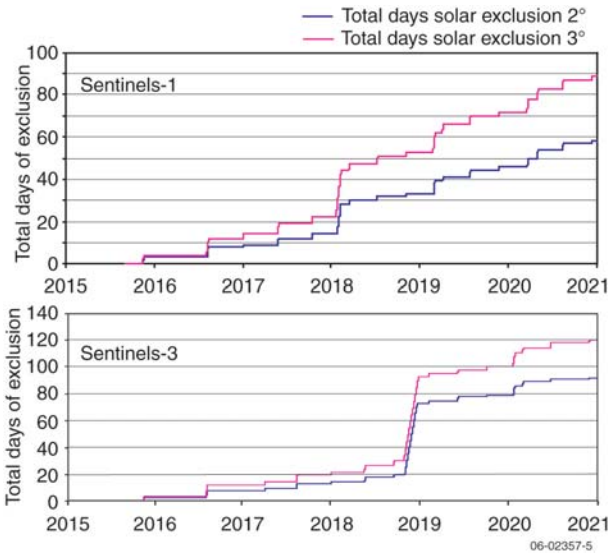

Figure 4-5. Days of solar exclusion for Sentinels-1 (top) and Sentinels-3 (bottom) for a September 4, 2015 launch date. The intervals of solar exclusion for Sentinels-2 (Sentinels-4) are nearly identical to those for Sentinels-1 (Sentinels-3).

4.2.8 Emergency operations. The C&DH subsystem includes fault detection functions to determine when the spacecraft should enter a safe mode. In safe mode, the telecommunications subsystem will use the aft LGA and medium-power transmitter for communications. The aft LGA does not depend on proper operation of the despun platform. The downlink bit rate will be set to 10 bps, and the uplink bit rate to 7.8 bps, ranging will be turned off, and a short downlink transfer frame format will be selected. This configuration will maximize chances for DSN acquisition and allow a downlink to be established even at the maximum expected spacecraft–Earth range. The telecommunications subsystem will be periodically cycled between its two redundant sides to mitigate any single-point failure. To ensure that the spacecraft is in a power-positive state all instruments and non-critical loads will be turned off. The spacecraft safe mode includes a "last-ditch" function that will perform an autonomous spin-axis correction if the angle between the spin axis and the ecliptic plane exceeds a certain threshold.

4.2.9 Space weather data. Each spacecraft will transmit low-rate space weather data whenever it is not in contact with the DSN and there is sufficient power to run the instruments and the medium-power transmitter (see **Table 4-6**). The high-power transmitter will be used when sufficient solar array power is available; otherwise the medium-power transmitter will be used. In addition to variations due to transmitter selection, the space weather data rate varies as a function of spacecraft-to-Earth range. The space weather link supports multiple data rates between 10 and 500 bps. The HGA is always used for the space weather link.

The spacecraft downlink will include space weather information even when the spacecraft is in contact with DSN. The science operations center can opt to strip out these data and forward them to organizations that want them, since those organizations will not have the ground station resources to receive the high-rate data transmitted by the spacecraft to the DSN.

4.3 Mission Environment

The two environmental factors of primary relevance to the IHS mission are (1) the thermal

environment at and near perihelion and (2) solar energetic particle radiation.

4.3.1 Solar flux. The large variation in solar flux between aphelion and perihelion is a significant design driver for the both IHS thermal control and power subsystems. The most extreme thermal environment that the spacecraft will encounter will be at perihelion, where the solar constant is about 2.1 W/cm^2, or 16 times that at 1 AU. However, thermal analysis shows that, for a spacecraft spinning at the nominal rate of 20 rpm, the solar constant at 0.25 AU will be reduced by about a factor of three, from 16 to 5 Suns. The IHS spacecraft do not have a special thermal protection system to shield the bus and payload from direct solar exposure. Instead, optical solar reflectors (OSRs) are used to manage solar heating and, in combination with louvered radiators and special protective measures for exposed components such as antennas, to maintain spacecraft and payload temperatures. The OSRs will reflect ~90% of the incident solar energy.

As discussed in Section 5.8, the power subsystem must be designed to accommodate the changes in solar array output associated with the variations in the solar flux over the IHS trajectory. The power requirements at 1 AU determine the array size, while the flux at 0.25 AU determines what fraction of the array is packed with OSRs. Hence the two limits determine the minimum surface area, and therefore the size of the spacecraft bus.

4.3.2 Radiation. The exposure to solar energetic proton radiation that the IHS spacecraft would experience during a 5-year mission was evaluated using the assumption of a 1/R^2 radial dependence of the energetic protons. The 1/R^2 dependence assumes diffusive transport from the Sun to the Earth. Dose-depth curves for two different launch dates, 2012 and 2015, were calculated. A finite slab model was used to simulate locations near the periphery of the spacecraft, while a spherical geometry was used for locations near the center of the spacecraft.

Although for a 2012 launch the spacecraft would spend slightly more time near solar maximum than for a 2015 launch (2.4 vs. 2.1 years), they would be farther from the Sun early in the mission during the solar maximum period than the spacecraft launched at 2015 would be. With the 1/R^2 dependence the energetic proton intensity increases significantly with decreasing distance from the Sun. The worst-case total radiation dose was found to be that for the 2015 launch.

At 75 mils Al depth (nominally the spacecraft skin and a box wall yielding ~0.5 g/cm^2) the predicted slab dose is 6.0 krads (**Figure 4-6**). At 511 mils Al or 3.5 g/cm^2 near the center of a light spacecraft the predicted spherical dose is 2.6 krads. Other electronics locations will yield doses between these two values. These are very low doses compared with most missions and can be easily accommodated by most space electronics. Even upscreened commercial parts such as flash memories can operate in this environment. The exception to this dose range would be any hardware protruding from the spacecraft or placed on a boom for which the spherical geometry at shallow depths (75 mils Al) yields 25.0 krads. Higher doses would also be experienced for any shield depth of less than 50 mils Al or 0.34 g/cm^2.

It should be noted that while worst-case fluence may be acceptable, the peak intensity that will be experienced by the IHS spacecraft in the inner heliosphere will undoubtedly be larger than is experienced by instruments at 1 AU. This should be taken into account in designing instruments for the Sentinels.

Figure 4-7 is a plot of the cumulative dose versus mission year for missions launched in 2012 and 2015, both with a 1/R^2 dependence for the proton fluence. For either launch date the spacecraft receive about 3 krad per solar-max year and less than 1% of that per solar min year, resulting in 12.4 krad for the 2015 launch and 8.5 krad for the 2012 launch.

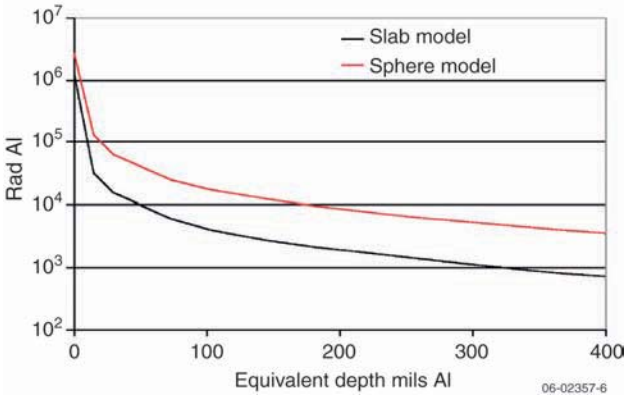

Figure 4-6. Worst-case radiation dose depth for the Inner Heliospheric Sentinels (2015 launch, 1/R^2 radial proton fluence dependence).

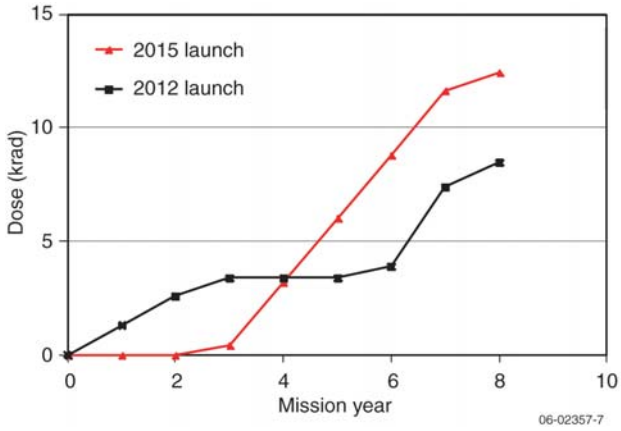

Figure 4-7. Profiles of Inner Heliospheric Sentinels cumulative radiation dose versus time (cumulative dose under 75 mils Al; $1/R^2$ radial proton fluence dependence).

No design margin has been included in these estimates, since the solar proton spectra used are at the 90% confidence level; that is, it is expected that these values would be exceeded in only 1 of 10 such IHS missions.

4.4 Spacecraft Overview

The IHS spacecraft design will accommodate the scientific payload defined by the STDT and meet the unique power and thermal control challenges presented by the mission environment. The spacecraft concept is illustrated in **Figure 4-8**, which shows one of the Sentinels in its flight configuration; and a block diagram of the major components is shown in **Figure 4-9**. This section provides an overview of the baseline design and summarizes the mass and power requirements. The individual subsystems and related design issues are described in subsequent sections.

4.4.1 Spacecraft description. The four IHS spacecraft are identically instrumented and virtually identical in overall design (but see Section 4.5 below). Each spacecraft is a solar-powered spinner, with a mechanical structure consisting of a central octagon, a top deck, a middle deck, and a bottom deck. The octagon consists of eight removable panels with cutouts for booms, instrument apertures, and thrusters. The decks are made of aluminum honeycomb covered with aluminum face sheets.

Thermal control of the IHS spacecraft is passive and uses conventional materials, which enables the use of standard space-grade electronic parts. The eight side panels are covered with optical solar reflector (OSR) material, and thermal louvers are mounted on the bottom deck to modulate the flow of heat to space. At spacecraft temperatures below 0°C, the louvers are fully closed; at temperatures above 20°C, they are fully open. Because the louvers do not receive direct solar illumination, conventional louver materials can be used.

Spacecraft power is provided by fixed solar panels that project above and below the spacecraft body. The solar cell strings are packaged with OSRs. This approach, used on Helios, will maintain the arrays at acceptable operating temperatures (≤180°C) even at the worst-case solar distance of 0.25 AU. A lithium–ion battery provides power during launch, before the solar arrays are illuminated, and is available for use during propulsion events if the solar array power is inadequate. The power subsystem uses a peak-power tracking (PPT) architecture, allowing a small solar array to handle

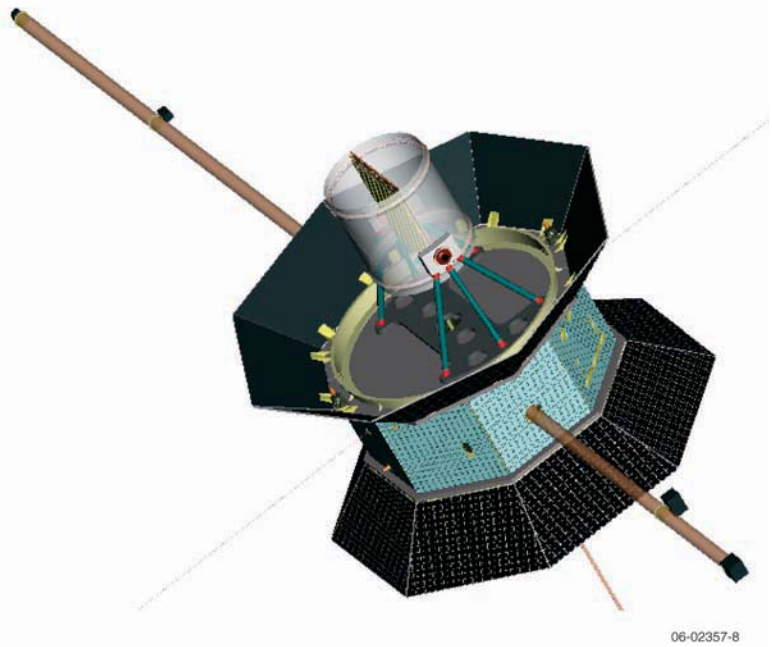

Figure 4-8. One of the four Inner Heliospheric Sentinels spacecraft in deployed configuration.

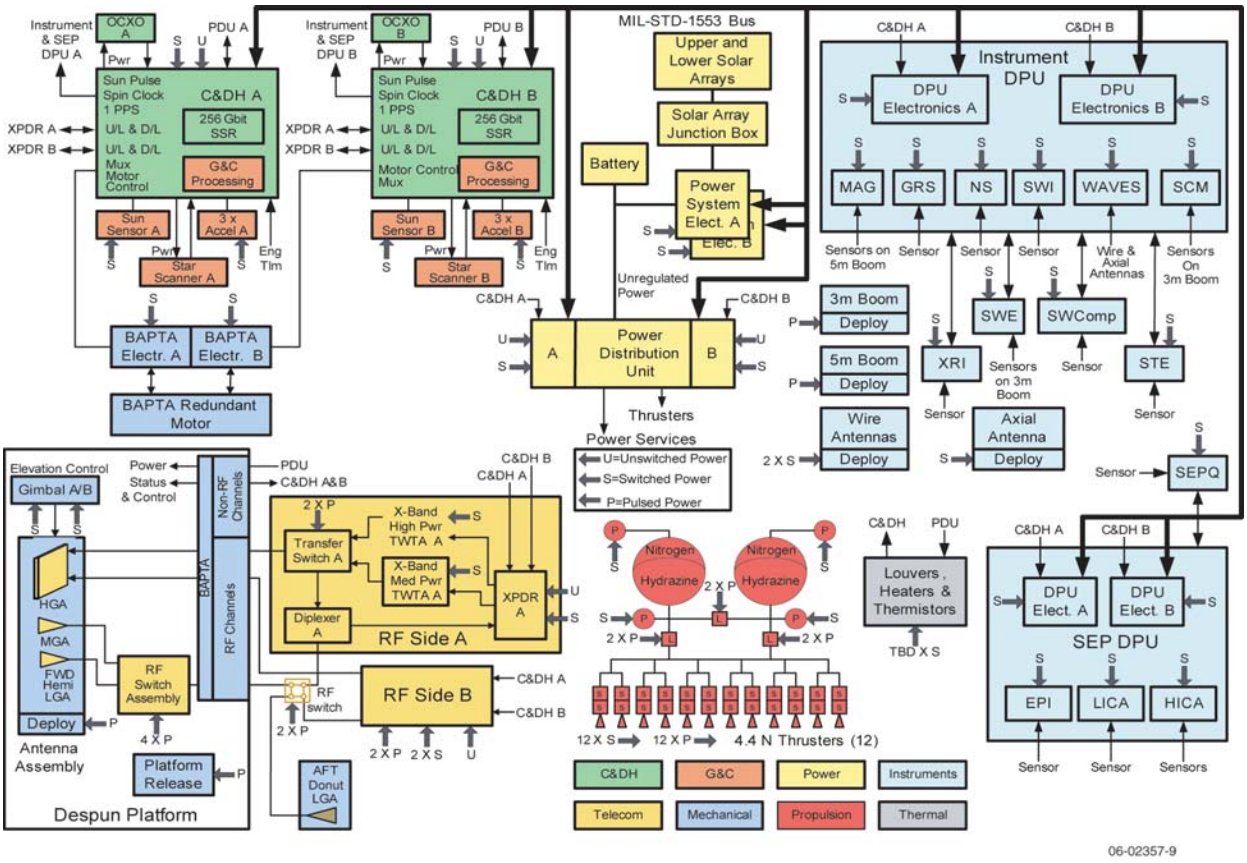

Figure 4-9. Block diagram of the Inner Heliospheric Sentinels spacecraft.The two teardrop propulsion tanks are mounted in the middle deck. Spacecraft electronic boxes and the instruments are located on the aft side of the top deck, both sides of the middle deck, and the forward side of the bottom deck. Solar arrays project above and below the spacecraft body. They are mounted 45° off normal to the spin axis to reduce their maximum temperature. Except for the instrument apertures, the body of the spacecraft is covered with optical solar reflectors (OSRs) to reduce the amount of solar energy received by the spacecraft while at close solar distances.

the wide range of current–voltage (I-V) characteristics experienced between solar distances of 0.25 and 1.0 AU. This system is used on TIMED and MESSENGER. The power distribution unit (PDU) provides unswitched, switched, and pulsed power.

An X-band coherent communications subsystem incorporates redundant transponders, redundant medium- and high-power transmitters, a high-gain phased-array antenna (HGA), a medium-gain antenna (MGA), and two low-gain antennas (LGAs). During normal operations data is downlinked through the HGA and commands uplinked through the MGA. Both of the LGAs are used during early operations and one LGA is used for emergency mode communications. The HGA and MGA are housed within a thermal-protective radome and mounted, together with one LGA, on a despun platform. The second LGA and communications subsystem electronics are mounted on both sides of the bottom deck. The despun platform is located on the top deck of the spacecraft and controlled via a bearing and power transfer assembly (BAPTA) by the guidance and control (G&C) subsystem to counteract the spin of the spacecraft and point the HGA at Earth. The antenna assembly is gimbaled to allow steering of the HGA and MGA in elevation. The HGA and MGA azimuth angle is controlled by adjusting the azimuth angle of the entire platform using the BAPTA.

The IHS command and data handling (C&DH) subsystem consists of a primary and a backup C&DH unit and two oven-controlled crystal oscillators. The C&DH subsystem performs command and data handling, G&C processing, data storage, and fault protection functions. Each C&DH unit consists of a CPU, a solid state recorder (SSR), a power converter board, and two interface boards.

Software that runs in the CPU stores instrument data in files on the SSR so that data can be played back in a priority order. During periods of low solar array output, only one C&DH unit is fully powered. When there is sufficient power, the backup C&DH unit is powered and will redundantly record instrument data. The oven-controlled crystal oscillators provide precision timing.

The G&C subsystem consists of a spinning Sun sensor and a star scanner for attitude determination and twelve 4-N thrusters for attitude control. The spacecraft is stable in its spinning configuration. However, solar pressure effects are expected to necessitate occasional attitude corrections to maintain the spin axis to within 1.0° of orbit normal. The G&C subsystem controls the despin motor and the HGA gimbal to maintain high-rate communications with Earth.

The propulsion subsystem is a simple blow-down hydrazine system with 100 m/s capability. The twelve attitude control thrusters provide thrust and torques along any spacecraft axis. The propulsion subsystem can tolerate several thruster failures and still be fully functional.

All instruments are connected to either the instrument data processing unit (DPU) or the solar energetic particle (SEP) DPU. Some of the instrument electronics are located inside the DPUs and some are located externally. The instruments do not connect directly to the C&DH subsystem; rather the two DPUs interface to the C&DH subsystem and in turn provide command and data handling interfaces to the instruments. The C&DH subsystem provides Sun pulse and spin clock signals to the DPUs, which in turn buffer and provide the Sun pulse and spin clock signals from the primary C&DH unit. Instruments are powered whenever there is sufficient power from the solar array, that is, whenever the spacecraft-to-Sun distance is less than 0.88 AU.

Spacecraft system margins are listed in **Table 4-7**.

4.4.2 Spacecraft and mission reliability. The IHS spacecraft design incorporates redundant subsystems to minimize the risk of failure and to ensure mission reliability (**Figure 4-10**). Components that are not fully redundant (battery, motor

Table 4-7. Spacecraft system margins.

System Margin	Requirement	Capability	Margin
Spacecraft dry mass[a]	503.7 kg	654.8 kg	30%
Propellant[b]	36.5 kg	42.5 kg	16%
Power			
Solar array, 1 AU	210 W	282 W	34%
Solar array, science and medium-power transmitter[c]	279 W	363 W	30%
Solar array, science and high-power transmitter[d]	432 W	561W	30%
Thermal[e]	–20° to +50°C[f]	0° to +25°C	At least 20°C
Radiation tolerance (5 year mission with 75 mils Al shielding, 2015 launch)	6 krad	>15 krad	>9 krad
Guidance and control (G&C)			
Spin axis control	1°	0.2°	400%
Spin axis knowledge	0.5°	0.1°	200%
HGA pointing	0.8°	0.49°	63%
Instrument data rate	5900 bps	7670 bps	30%
Data storage	180×10^9 bits	275×10^9 bits	53%

[a]Additional mass margin available based on launch vehicle capability.
[b]Tanks can be loaded with another 2.0 kg of propellant total.
[c]Additional power margin available by delaying instrument turn-on until closer to the Sun.
[d]Additional power margin available by delaying high-power transmitter turn-on until closer to the Sun.
[e]Not including instrument apertures.
[f]Some instruments may have a maximum operating temperature in the range of +20 to +40°C. These will be handled as special cases; they have much higher survival temperatures.

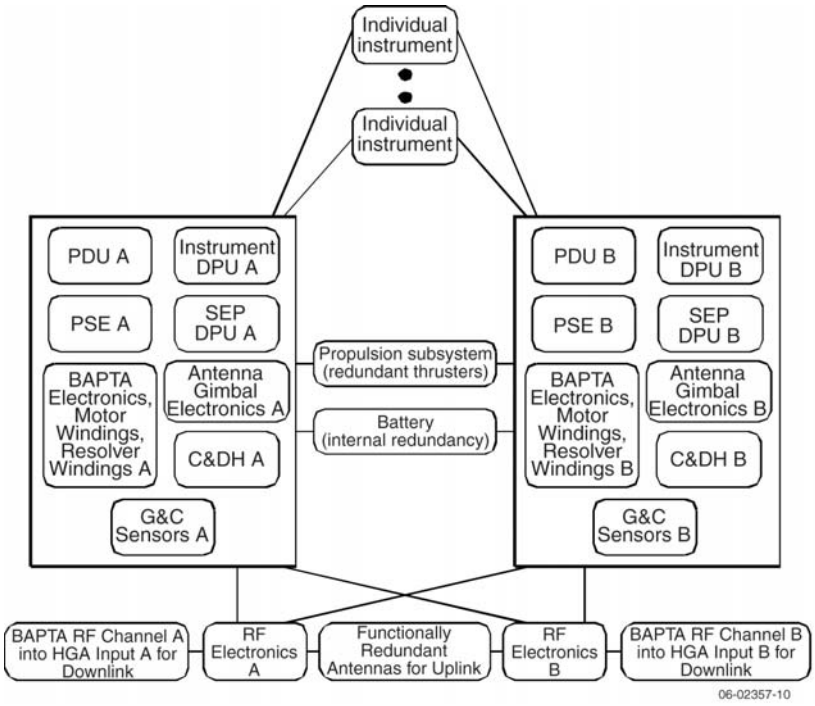

Figure 4-10. Redundancy of the Inner Heliospheric Sentinels spacecraft.

mechanisms) have partial redundancy. The C&DH and communications subsystems are cross-strapped: C&DH side A can operate with communications side B and vice versa. The communications subsystem has functionally redundant antennas for uplink purposes (the MGA and aft LGA) and two redundant paths through the BAPTA into the HGA for downlink. Elsewhere, block redundancy is used instead of cross-strapping to reduce spacecraft complexity and to simplify spacecraft integration, test, and mission operations.

4.4.3 Mass and power budget summaries. **Table 4-8** summarizes the **mass budget** for the payload and each of the spacecraft subsystems. The mass numbers represent the current best estimate. A 30% margin is added to account for unanticipated growth and any launch reserves. The masses of the four spacecraft will vary slightly owing to slight differences in the mass of the central support cylinder required by each spacecraft's relative position in the stacked launch configuration as well as by the related difference in the amount of propellant carried by each spacecraft. (The bottom spacecraft in the launch stack needs to support the most mass and is therefore the heaviest. The second-to-the-bottom spacecraft is the second heaviest, and so forth.) The structure mass shown in T**able 4-8** is the average structure mass. The propellant mass is also an average.

The baseline spacecraft configuration has fixed solar arrays and a non-deployed HGA. This configuration reduces complexity, risk, and cost, but other configurations have lower mass. Spacecraft configurations with folded solar arrays and a deployed HGA can reduce the total launch mass by approximately 500 kg, although this approach increases complexity, risk, and cost (see Appendix A, section 17).

The **power requirements** for the IHS spacecraft (**Table 4-9**) are based on current best estimates plus a 30% margin. The power required by the spacecraft in launch configuration (second column from the left) is 120 W, which will be provided by the battery. This requirement directly determines the battery capacity. The estimates given in the third column from the left (despun platform off, instruments off, medium power transmitter on) represent the minimum power required by the spacecraft at 1.0 AU. This requirement determines the size of the solar array. The fourth column (despun platform on, instruments off, medium power transmitter on) shows the minimum solar array output required to turn on the despun platform and commence high rate communications. The fifth column (despun platform on, instruments on, medium-power transmitter on) shows the minimum solar array output required to power the complete instrument payload. The solar array will output this power at Sun distances less than 0.88 AU. The final column (instruments on, high-power transmitter on) gives the minimum solar array output needed to power the high-power transmitter. The solar array can output this power at Sun distances less than 0.67 AU.

4.5 Mechanical Design

The structural subsystem of the IHS spacecraft is designed to accommodate the science payload and other spacecraft subsystems, to allow

Table 4-8. Mass budget summary.

Category	Mass (kg)
Instrument payload	70.5
Guidance and control subsystem	12.7
Command and data handling subsystem	11.2
Power subsystem	80.7
Structure subsystem (average)	161.6
Propulsion subsystem	23.2
Telecommunications subsystem	73.1
Thermal subsystem	25.5
Harness subsystem	45.3
Spacecraft Dry Mass Total (average)	**503.7**
Margin of 30% (average)	151.1
Spacecraft Dry Mass with margin (average)	654.8
Spacecraft Dry Mass Total (top spacecraft)	614.1
Spacecraft Dry Mass Total (bottom spacecraft)	695.9
Propellant and Pressurant (average)	43.0
Mass of one Observatory (average)	**697.8**
Mass of Four Observatories	2791.3
Jettisoned support cylinders w/ 30% margin	89.0
Separation and Jettison System w/ 30% margin	312.0
Total launch mass with margin	**3192.4**

the four spacecraft to be stacked for launch within the launch vehicle fairing, and to provide the necessary stiffness and strength to handle the launch loads experienced by the spacecraft in this stacked configuration. The main spacecraft structure consists of eight aluminum isogrid panels that form an octagonal "exo-skeleton," sandwiched by aluminum octagonal-to-circular transition pieces (see **Figure 4-11**). Panels forming the octagon can be individually removed to allow access to components during integration and test of the spacecraft. The thickness of the panels and cylinders varies according to the position of the spacecraft in the stack. Mounted outside this structure are eight lightweight OSR-covered panels with cutouts for instrument apertures, booms, and thrusters. Within the structure three aluminum honeycomb decks carry the payload and subsystems. The middle deck, to

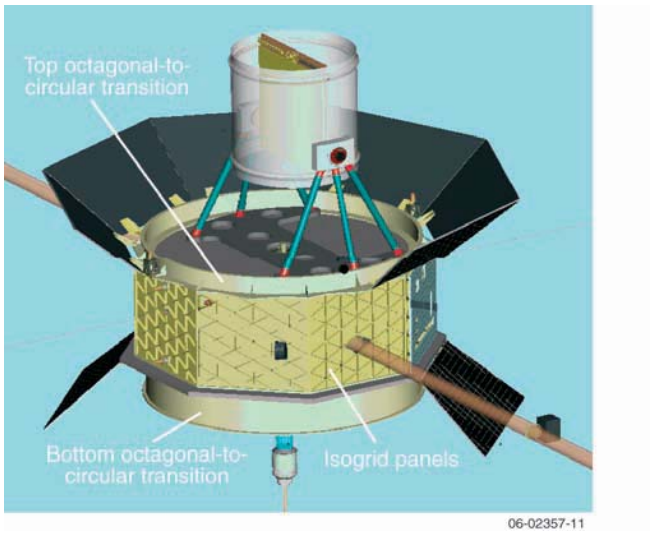

Figure 4-11. Spacecraft load-bearing structure exposed by removal of OSR and solar array panels.

Table 4-9. Power budget summary.

System	Launch Config. (W)	Despun Plat. Off Instruments Off Med-Pwr Xmtr On (W)	Despun Plat. On Instruments Off Med-Pwr Xmtr On (W)	Despun Plat. On Instruments On Med-Pwr Xmtr On (W)	Despun Plat. On Instruments On High-Pwr Xmtr On (W)
Instrument Payload	0.0	0.0	0.0	69.0	69.0
G&C	0.0	2.0	2.0	2.0	2.0
C&DH	24.0	24.0	24.0	27.0	27.0
Power	24.0	44.0	44.0	44.0	44.0
Propulsion	19.6	3.6	3.6	3.6	3.6
Communications	11.2	65.2	81.7	81.7	231.7
Thermal	8.8	67.9	67.9	47.9	47.9
Harness	1.3	3.1	3.3	4.1	6.4
Total	**88.9**	**209.8**	**226.5**	**279.4**	**431.6**
Margin of 30%	26.7	62.9	68.0	83.8	129.5
Total with Margin	**115.6**	**272.7**	**294.5**	**363.2**	**561.1**

which the propulsion system is integrated, is permanently installed. The remaining forward and aft decks can be removed and installed, with mounted components, as a unit. The despun platform (carrying the forward LGA, MGA, and HGA communications antennas) is mounted on the top, or forward, deck. Solar arrays are mounted at each end of the spacecraft, fanning out from the body at a 45° angle. The arrays are rotated about the spin axis by 22.5° relative to one another to reduce the ripple in the output power. The total array area is 9 m^2.

4.5.1 Launch configuration. In the launch configuration the four spacecraft are connected by three spacer rings and are stacked on top of each other and secured by "clamp-band" separation systems. The stack height is approximately 7.5 m. The HGA is rotated by 180° to provide a more compact profile, and the instrument booms and wire antennas are stowed. The despun platform is locked into place. The stack geometry allows the spacecraft to fit tightly within a 4-m extended extended payload fairing (XEPF) envelope on an Atlas V launch vehicle (**Figure 4-12**). A 5-m medium fairing is baselined to provide substantial envelope margin.

4.5.2 Deployed configuration. Upon separation, each spacecraft will be a major axis spinner with a moment-of-inertia (MOI) ratio of between 1.05 and 1.15. This is a sufficiently stable ratio for early operations until deployments are made. Approximately two weeks after separation, the launch locks on the despun platform will be released and the HGA will be rotated 180° about its gimbal into its operational configuration. Once the spinning spacecraft is in its final deployed configuration (see **Figure 4-13**), with the

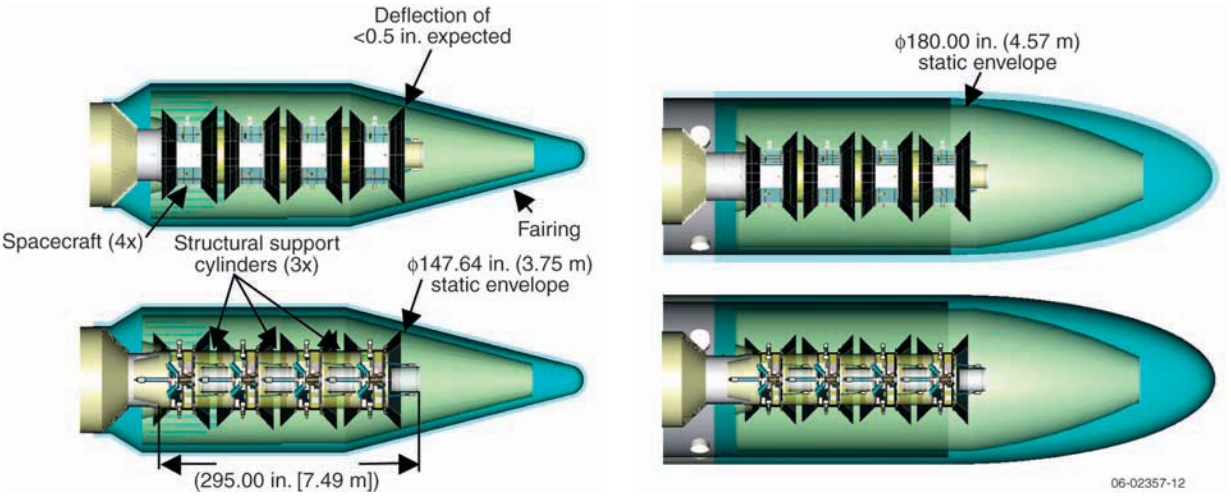

Figure 4-12. The four Inner Heliospheric Sentinels spacecraft stowed in (a) the 4-m fairing on an Atlas V-431 and (b) the 5-m fairing of an Atlas V-541.

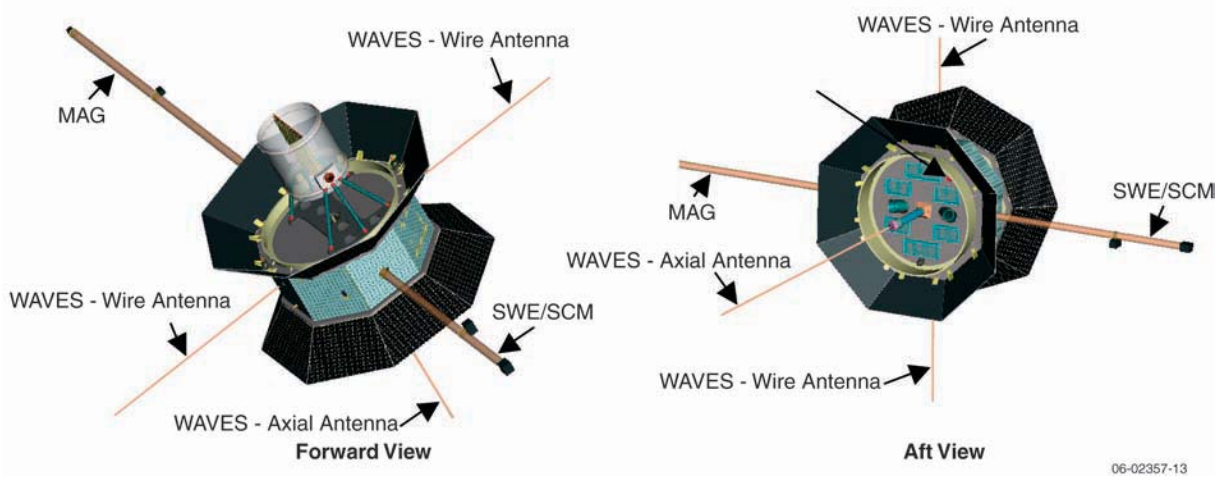

Figure 4-13. Deployed configuration of the Inner Heliospheric Sentinels spacecraft.

instrument booms and WAVES antennas deployed, it will be very stable with an improved MOI ratio of approximately 1.5.

4.5.3 Instrument accommodation. The IHS mechanical design will accommodate the baseline instrument payload specified by the STDT (**Figure 4-14** and **Table 4-10**). The Solar Wind Electron (SWE) instrument and the Search Coil Magnetometer (SCM) are mounted on a 3-m boom, and the Dual Magnetometer (MAG) is mounted on a 5-m boom with one sensor at

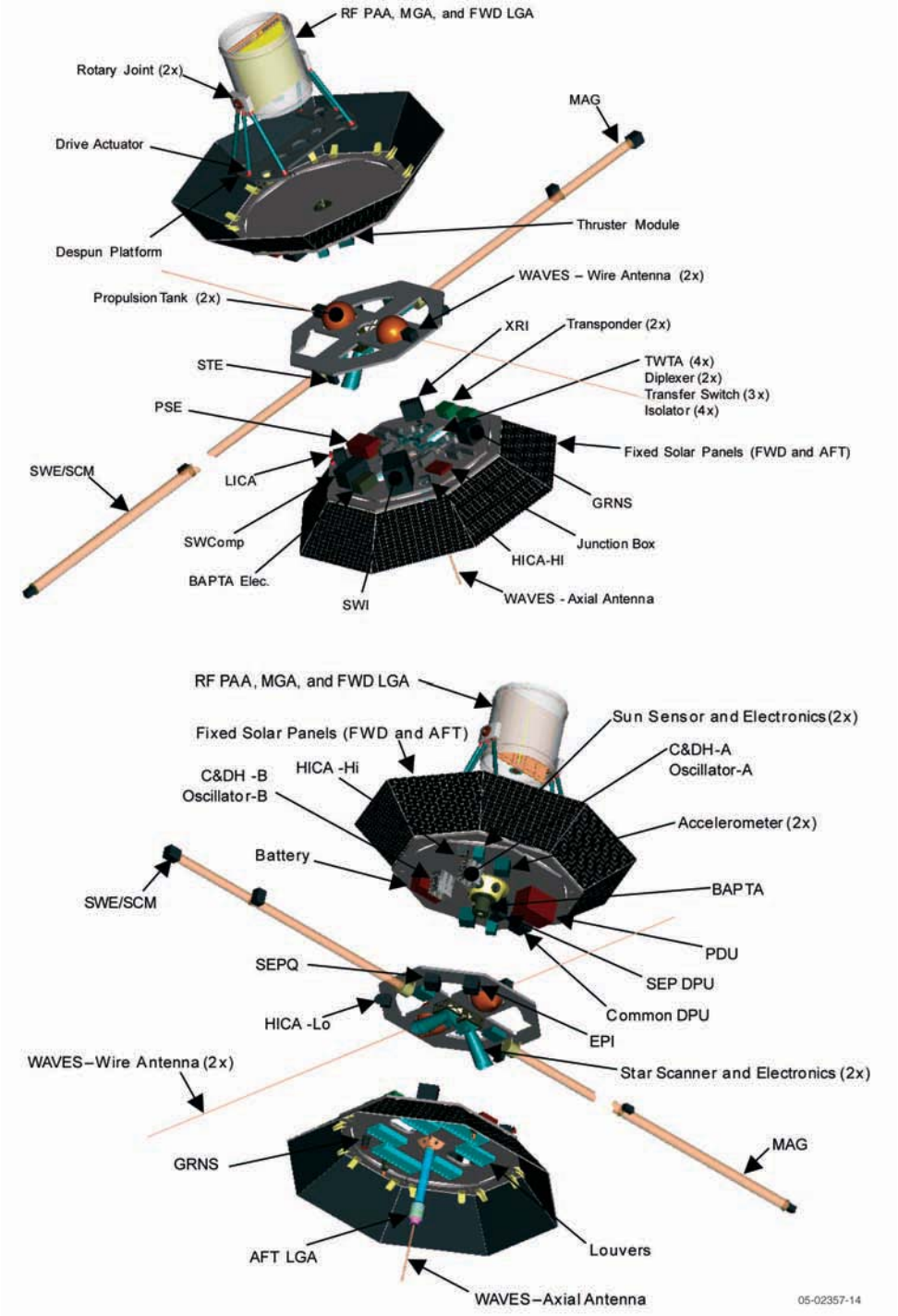

Figure 4-14. Two views of the Inner Heliospheric Sentinels spacecraft, showing the locations of the science instruments and the spacecraft subsystems.

Table 4-10. Instrument fields-of-view and placement

Instrument	Requested FOV	Accommodated FOV	Sensor Placement	Additional Requirements
HICA-Hi (2 sensors)	60° full cone	As requested	Two sensors on opposite sides pointing ±20° up/down	–
HICA-Lo	130° NS × 20° Ecl	100° × 20°	FOV centered on ecliptic plane	–
EPI	120° NS × 16° Ecl.	100° along spin axis by 16°	Several small sensors in bus	–
LICA (2 telescopes)	44° NS × 16° Ecl.	As requested	Two sensors FOV centered on ±26° above/below ecliptic	–
STE	180° NS × 5° Ecl.	100° NS × 5° Ecl.	FOV centered on ecliptic plane	–
SEPQ	10° NS × 40° Ecl.	As requested	Two sensors FOV centered on ±15° above/below ecliptic	–
SWI	60° × 60°	As requested	FOV centered on ecliptic	Conductive surfaces near instrument < 10 s of eV
SWComp	90° NS × 5° Ecl.	As requested	FOV centered on ecliptic plane	
SWE	180° NS × 20° Ecl.	As requested	On boom >2 m from body	Spacecraft potential at spacecraft must be < 10 V
MAG (2 sensors)	–	–	On 5-m boom at tip and at 3 m	magnetic cleanliness: DC ≤ 0.1 nT; AC ≤ 0.01 nT at sensors
SCM	–	–	On same boom as SWE, but 1 m farther out	EMC
WAVES	–	–	Two 20-m radial wire antennas 5-m axial boom	EMC
NS	Full Sun	Full Sun w/some obstructions	Coaxial with rotation axis	–
XRI	10° NS × ±150° Ecl.	As requested		–
GRS	Full Sun	Full Sun w/some obstructions	Coaxial with rotation axis	–

NS = north-south; Ecl = ecliptic

the tip of the boom and the second sensor at 3 m. The WAVES sensors are a 5-m axial antenna that extends from the bottom deck of the spacecraft and two 20-m wire antennas mounted 90° away from the HICA-Hi apertures. The rest of the payload is housed inside the spacecraft. Instrument FOVs are given in **Table 4-10** and illustrated in **Figures 4-15** and **4-16**.

4.5.4 Subsystem accommodation.

Communications. The communications subsystem electronics are mounted on the bottom deck of the spacecraft. The HGA, MGA, and one LGA are gimbal-mounted within a radome on the despun platform; the aft LGA is on a fixed boom that, when stacked for launch, nests within the HGA radome of the spacecraft beneath it. The despun platform is

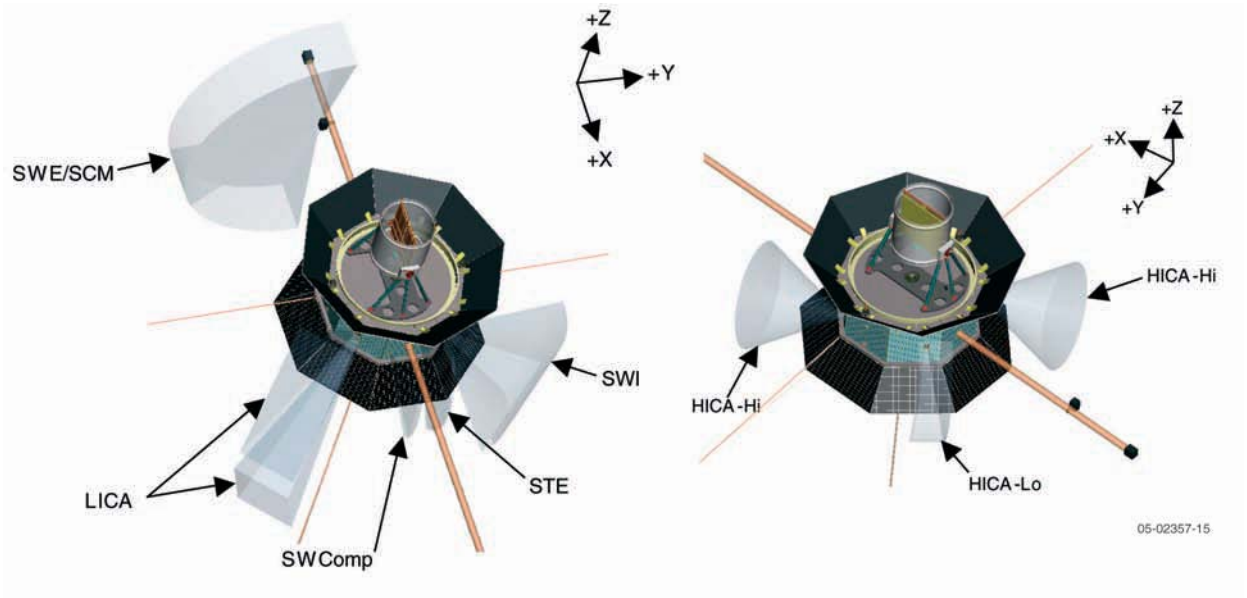

Figure 4-15. Instrument fields-of-view.

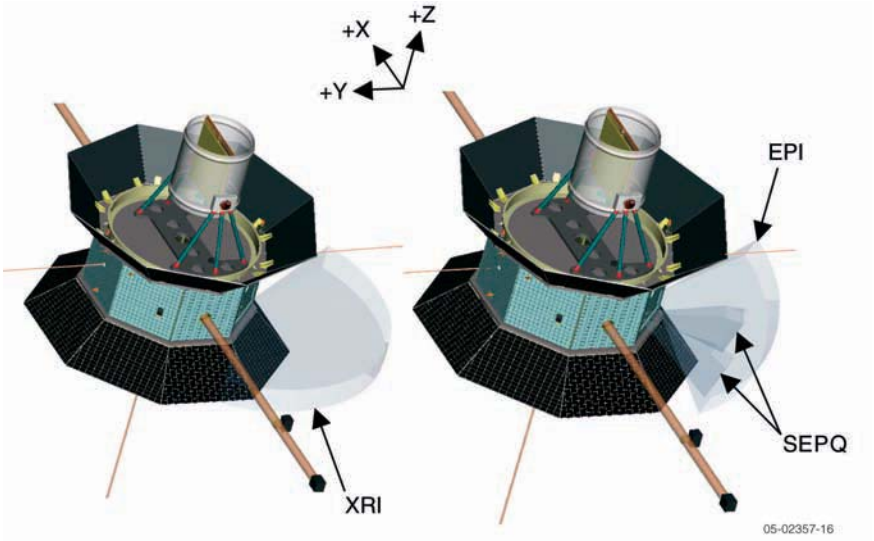

Figure 4-16. Instrument fields-of-view.

controlled by the BAPTA mounted to the top deck and counterrotates relative to the main body of the spacecraft to keep the HGA and MGA oriented toward Earth.

Propulsion. Two conisphere propellant tanks are supported within the main body of the spacecraft by brackets on the middle payload deck. Propellant lines internal to the spacecraft run to the twelve thrusters. Thrusters are placed on brackets to achieve the proper stand-off and orientation. Cut-outs in the outer OSR panels allow the needed thruster clearance. Some plume impingement will occur for thrusters oriented along the axis.

Thermal. Eight lightweight OSR-covered panels are mounted around the octagon support structure to reduce the amount of solar radiation absorbed by the spacecraft. The thermal design calls for 1-m^2 louvered radiator area on the aft deck.

Harness. The harness includes shielding to meet science electromagnetic compatibility requirements.

4.5.5 Structural design and analysis. The four IHS spacecraft will be launched in a stacked configuration (**Figure 4-12**). The launch loads are transferred through the stack through the octagonal isogrid support structures, the octagonal-to-circular transition pieces, and the three interspacecraft spacer cylinders. To evaluate key trades between stiffness, stack height, total support structure mass, launch mass, and boundary conditions, the spacecraft stack was modeled as a cantilevered beam with a cylindrical cross-section. To satisfy Atlas launch vehicle requirements the lateral frequency of the stack must be at least 2.5 Hz. Using

published clampband stiffness, this beam-bending model returned 10.5 Hz for the stack in bending, greatly exceeding the minimum Altas requirement.

A configuration trade study was completed that demonstrated a structure using aluminum transitions (top and bottom) with an aluminum isogrid octagon could meet structural and mass requirements. Structure mass was minimized by allowing the individual thicknesses of each segment to vary based on the line load to be carried, with the diameter held constant at 1.67 m. A Saab separation system was baselined for each of the six separation joints between spacecrafts and support cylinders. The Atlas D1666 clampband is the baseline vehicle interface joint. Based on published values from the payload planners guide, the spacecraft stack meets the structural requirements for the D1666 payload adapter.

4.6 Thermal Control

The diverse thermal environments experienced by the IHS spacecraft present a unique thermal design challenge. Most components such as spacecraft and instrument electronics are well coupled to the internal structure via conduction mounting. Minimal power is dissipated on the despun platform. The solar arrays and main cylinder side panels are thermally isolated from the main core structure by means of conductive isolation and high-temperature multilayer insulation (MLI). Spacecraft radiators on the bottom deck utilize louvers to minimize heat leak near aphelion and to maximize radiator area at perihelion. (The performance characteristics of the louvered radiator baselined for the IHS were demonstrated in thermal vacuum testing of the New Horizons spacecraft.) The louvers always have a field of view to cold space because they are oriented in the direction parallel to the spacecraft spin axis and are baffled by the tilted solar arrays (**Figure 4-17**). The louvers are used to balance the waste electronics heat and the unavoidable heat leak through the multilayer insulation (MLI) to maintain a core spacecraft temperature of between 0°C and 25°C. Heaters and electronic or mechanical thermostats are used to maintain the temperature of the propulsion system at or above 10°C.

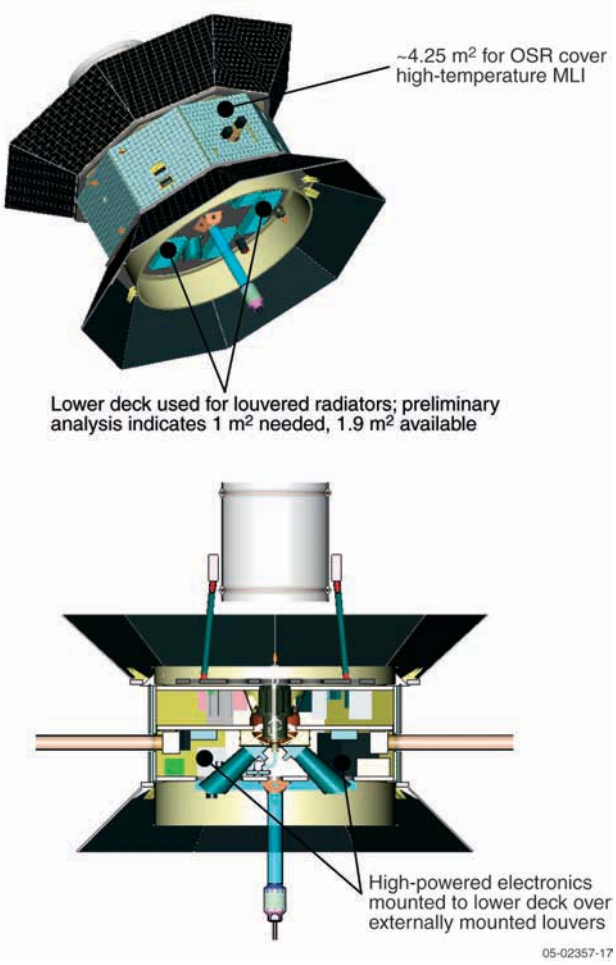

Figure 4-17. OSRs and louvered radiators provide passive thermal control of the IHS spacecraft.

4.6.1 Thermal analysis. The Thermal Synthesizer System (TSS) and SINDA were used to perform a thermal analysis of the IHS spacecraft design for conditions near perihelion ("hot case") and near 1 AU ("cold case.") In addition, in order to establish the lowest possible perihelion distance, thermal control requirements for the solar arrays were studied for perihelia between 0.20 AU and 0.35 AU. The fraction of the solar array that must be packed with OSR (the "packing factor") to keep solar array temperatures below 180°C was evaluated for this perihelion range. The packing factor is directly correlated with solar array size, and the study made it apparent that the size of the solar arrays would have to be at least a factor of two larger at 0.20 AU than at 0.25 AU (**Figure 4-18**), which would entail an unacceptable increase in mass. As a result, 0.25 AU was confirmed as the baseline perihelion for the IHS mission.

Thermal analysis: hot case. The heat sources assumed in the hot case analysis were the absorbed

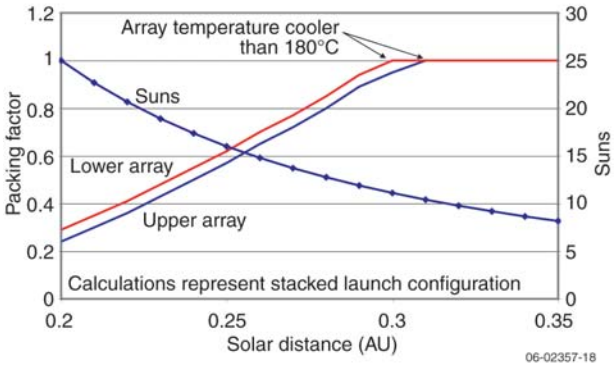

Figure 4-18. Packing factor as a function of solar distance needed to maintain upper and lower solar array temperatures at 180°C.

solar flux at 0.25 AU and the heat dissipated by the spacecraft electronics. As shown in **Figure 4-19**, with an MLI performance of 0.03, at 0.25 AU the absorbed heat flux from each side panel to the core IHS spacecraft was calculated to be approximately 30 W/m^2, or, when multiplied by the side panel surface area, 125 W. (0.03 is the nominal MLI performance determined during thermal vacuum testing of the MESSENGER spacecraft.) The worst-case heat dissipated by the electronics was estimated to be 250 W. These two values, plus an additional 25 W as uncertainty margin, yielded a worst-case thermal load of 400 W. To manage this load and maintain the spacecraft core temperature at 25°C, calculations showed that a radiator area of approximately 1 m^2 (louvers fully open) is required. If needed, however, additional louvered radiator area

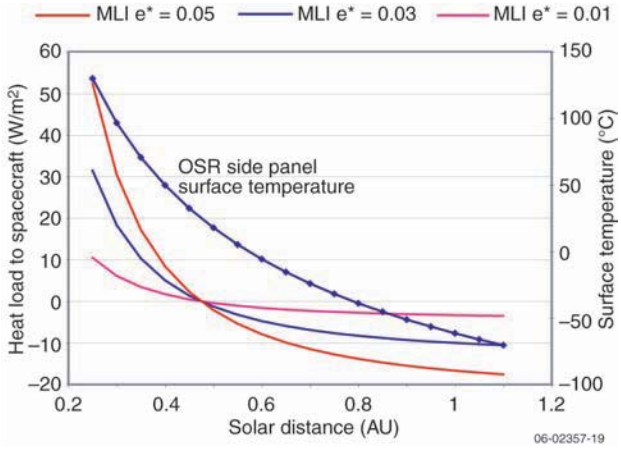

Figure 4-19. Heat load analysis with the spacecraft spin axis normal to the Sun.

could be added to the lower deck, since only about one-half of the area is used for spacecraft thermal control.

Thermal analysis: cold case. The cold case analysis was performed for the conditions at launch and during early operations, when the spacecraft will be near 1 AU. Because the OSRs reflect ~90% of the incident solar radiation, the aphelion solar environments were ignored and only heat dissipated by the spacecraft electronics was considered. For the cold case, a worst-case minimum internal electronics heat dissipation of 95 W was calculated. The IHS louvers will be fully closed at temperatures at or below 0°C and fully opened at temperatures at or above 20°C. Given the performance characteristics of the MLI and louvers, the core temperature of the spacecraft with the louvers closed will be above zero. Since propulsion components are the most sensitive to cold conditions, heater power has been budgeted for propulsion tanks, lines, and valves to ensure component regulation at or above 10°C at all times.

4.6.2 Thermal accommodation of spacecraft subsystems. The antennas, digital Sun sensors (DSS), and thrusters are located where they will be exposed to direct solar illumination. These subsystems require special protection to ensure proper operation during perihelion portions of the mission. Thermal design and fabrication techniques developed for the MESSENGER spacecraft can be used to maintain acceptable operating temperatures for these exposed components. Because the IHS spacecraft will be spinning at 20 rpm, the equivalent solar constant at the spacecraft will be reduced from 16 Suns to 5 Suns. This is significantly less than the 11 Suns to which the equivalent MESSENGER subsystems will be exposed, suggesting that the thermal control techniques developed for MESSENGER will provide substantial margins for the IHS mission.

Telecommunications. The MGA and HGA on the despun platform are protected with a single cylindrical radome. The portion of radome in front of the antennas consists of Q-Felt between two layers of Nextel 312-AF10 cloth. The remainder of the radome is a lightweight composition of metallized Kapton between layers of Nextel cloth. The three low-gain antennas are protected by a wrapping of Q-Felt/Nextel construction.

The IHS radomes will maintain the antenna hardware at temperatures below 200°C at perihelion and should provide substantial thermal margin. (MESSENGER antennas were tested to 315°C).

While they receive no direct solar input, the high power traveling wave tube amplifiers (TWTAs) have a thermal dissipation of 100 W. The TWTAs are kept cool by mounting them close to the center of the bottom deck and thermally coupling them to radiators located on the other side of the deck. A preliminary thermal analysis predicts that the maximum TWTA baseplate temperature can be kept below 50°C with a thermal doubler located at the bottom of the TWTA. Typical TWTAs of this type have a maximum baselplate temperature of 85°C, giving 35°C of operating temperature margin for Sentinels. If required, the temperature could be further lowered by adding thermally conductive plugs in the honeycomb deck.

Propulsion. As is done on MESSENGER, the IHS thrusters are mounted in a manner that minimizes solar input into the thruster nozzles, which are recessed behind structural panels covered with MLI and OSRs. Thruster valves are heat sunk to decks that are always kept at temperatures above 0°C. Thruster heaters maintain thruster temperatures above 10°C during aphelion phases of the mission.

Guidance and control. The IHS spacecraft use redundant modified digital Sun sensors developed by Adcole for the MESSENGER mission. This sensor has been thermally qualified to operate from –100° to +200°C and has a solar-attenuating neutral density filter that reduces incident solar intensity at the sensor by approximately 1 order of magnitude.

4.6.3 Thermal accommodation of instruments. There are two classes of instruments from a thermal standpoint: those mounted on spacecraft decks and those located on booms. Each type is accommodated differently.

Deck-mounted instruments. Apertures of deck-mounted instruments are exposed to direct solar illumination. Instrument temperatures can be controlled to practical levels by coupling these instruments directly to the deck or to radiators as shown in **Figure 4-20.** Instruments and instrument electronics can transfer heat via conduction to spacecraft decks that are maintained at 0° to +25°C. They can also be isolated from the spacecraft structure and have a dedicated radiator for thermal control. The dedicated radiator can be implemented in the spacecraft deck design or in the instrument design. The impact of solar illumination through the aperture can be minimized using three different techniques: the aperture can be covered with a thin metallic foil shield; the detector can be positioned so that it is not directly exposed to the solar input; or the aperture size can be reduced. An example of the effect of aperture size on detector temperature for a specific instrument with a 100-cm^2 radiator is shown in **Figure 4-21**. This analysis must be repeated to get the result for a different instrument.

Boom-mounted instruments. Boom-mounted instruments such as the magnetometer are sensitive to solar illumination. A passive thermal control design using an OSR shroud on Sun-facing surfaces will reflect most of the solar energy. Radiators located on non-Sun-facing surfaces will dissipate the heat that does penetrate the shroud. A preliminary thermal analysis indicates that when the spacecraft is at 0.25 AU, the magnetometer outer surface temperature (inside the shroud) can reach 100°C. This condition was

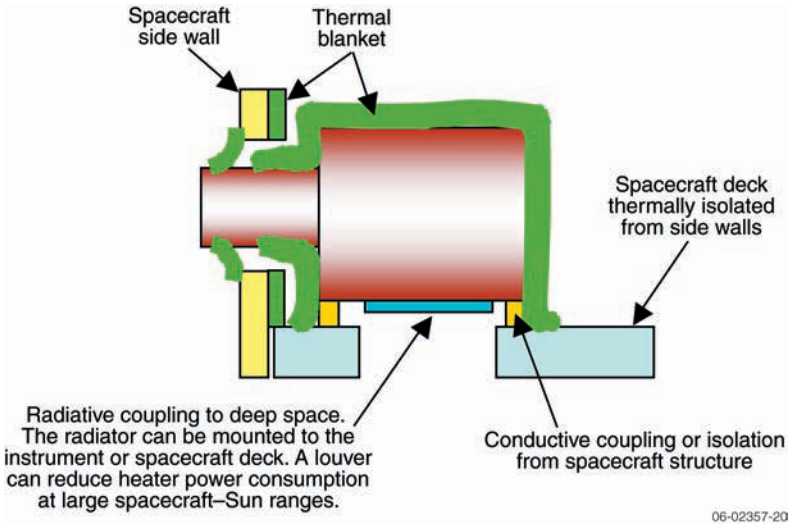

Figure 4-20. Typical instrument accommodation on spacecraft deck.

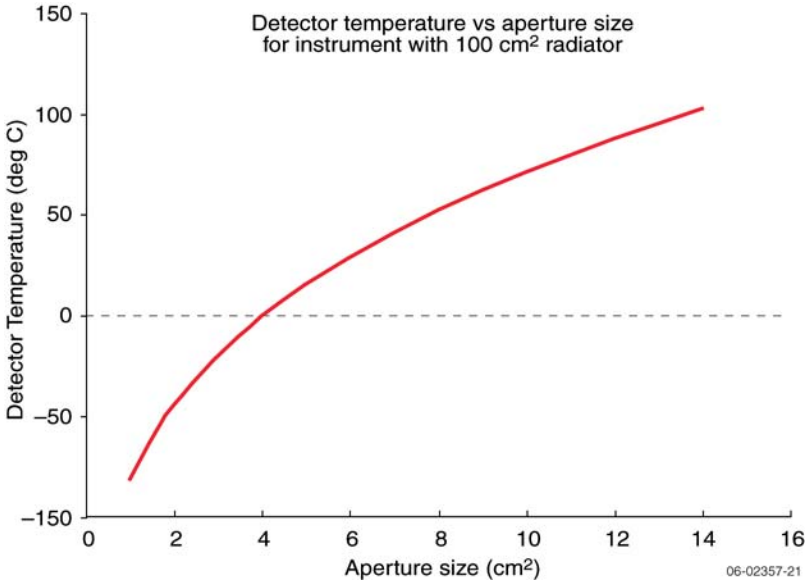

Figure 4-21. Effect of aperture size on detector temperature.

acceptable for the MESSENGER magnetometer design. The temperature of boom-mounted instruments can be further controlled by isolating sensitive components and by varying the radiator size.

4.7 Power Subsystem

The power for the IHS spacecraft is provided by two solar arrays, one mounted at the top of the spacecraft and one at the bottom. In addition to the solar arrays, the IHS power subsystem consists of the solar array junction box, a 20-Ah lithium-ion battery, power system electronics (PSE), and a power distribution unit (PDU) (**Figure 4-22**). Variations in solar flux from 0.25 to 1 AU impose severe requirements on the design of this subsystem. The maximum-power-point voltage of the solar array is expected to range from 40 to 95 V. A peak power tracker (PPT) architecture with strong heritage from MESSENGER isolates the battery and power bus from the variations of the solar array voltage and current characteristics and maximizes the solar array power output over the mission's highly varied solar array operating conditions. A similar PPT architecture is used on many interplanetary spacecraft where solar panel temperature variations are large (e.g., Rosetta, Mars Express, Venus Express, Dawn, and MESSENGER).

4.7.1 Power subsystem architecture. Triple-junction solar cells, with an efficiency of 28.5%, are baselined for the IHS solar arrays. The total array area is 9 m^2. The solar array design derives from that used on MESSENGER, which will operate under similarly extreme thermal conditions. A single PPT with seven converter modules controls the power generated by the arrays; the seventh converter provides redundancy in case one converter fails. The loads are connected directly to the battery. The nominal bus voltage is 28 V and can vary from 22 to 34 V, depending on the state of charge of the battery.

Lithium–ion technology was selected for the IHS battery because of its high energy density. The battery consists of eight-cell strings used in parallel and includes one more string than needed in case one string fails. The cells have internal switches that will open and isolate a string in case of cell failure. This approach avoids the need for a second, backup battery, which would add to the mass of the spacecraft. Lithium–ion batteries are being used on the European Space Agency's Rosetta, Mars Express, and Venus Express planetary missions and have been selected for the NASA's Living With a Star Solar Dynamics Observatory (SDO).

The battery capacity is determined by the power required from launch until the solar arrays are fully illuminated, which will occur when the upper stage is oriented normal to the ecliptic and begins to rotate at 3 rpm. The battery depth of discharge (DOD) during launch is estimated to be approximately 50%. The solar arrays are not sized to support thruster operation at 1 AU, so the battery may be needed during thrusting events if the solar array power is not adequate. Battery DOD during the thruster preparation and burns will be less than 10%.

Battery charge control is achieved by charging the battery to a preset voltage. Once the desired state of charge is reached, the voltage control loop forces the charge current to taper to a low value. If the spacecraft loads and the battery charge

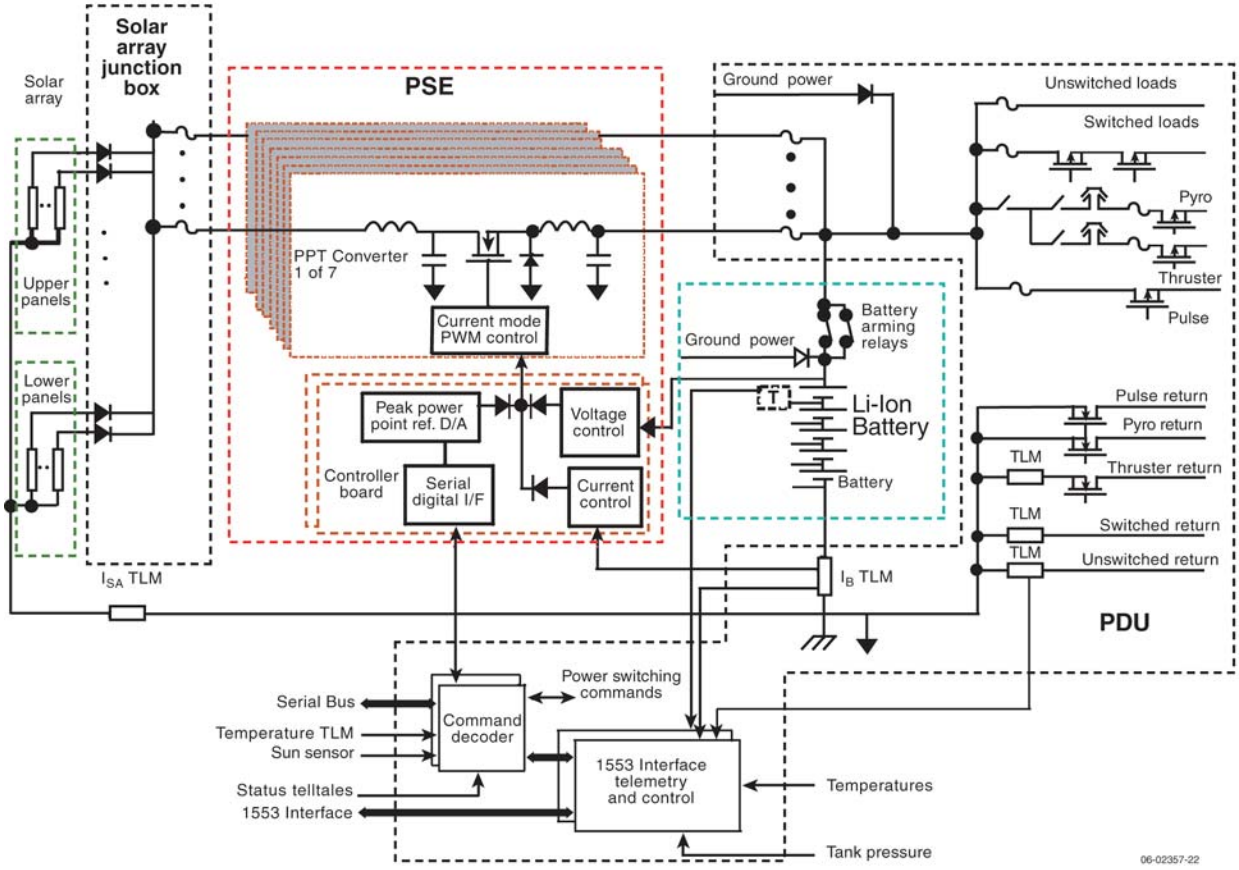

Figure 4-22. Block diagram of the Inner Heliospheric Sentinels power subsystem.

requirements exceed the available solar array power, the power system will operate in the peak power tracking mode. During this mode of operation, the solar array voltage will be varied to maintain peak power from the solar array. The solar array voltage control signal is determined by the PPT algorithm executed by the spacecraft C&DH processor.

The PDU contains the circuitry for the spacecraft pyrotechnic firing control, power distribution switching, load current, and voltage monitoring, fuses, external relay switching, power system relays, propulsion thruster firing control, and propulsion latch valve control. The PDU is internally redundant. The telemetry collected by the PDU is sent to either of the C&DH processors through MIL-STD-1553 busses.

The power subsystem design is single-point-failure tolerant. Fault detection and correction are performed by the C&DH processor.

4.7.2 Solar array design. Each solar array consists of 8 non-deployed solar panels mounted at a tilt of 45° to the spin axis. The upper and lower arrays are mounted with a 22.5° offset from each other in order to minimize the power ripple generated by the spacecraft spin. The rows of solar cells are placed between rows of OSRs to form strings similar to the arrangement used on the MESSENGER solar panels (**Figure 4-23**). Each panel has an integral number of strings. To minimize the magnetic field induced by the currents in the strings, adjacent strings are placed with alternating current polarity whenever possible, and the strings are back-wired such that each string return runs under its cells. The IHS solar panel electrostatic and magnetic cleanliness will be similar to that of the STEREO solar panels.

The top and bottom solar arrays have different packing factors (fraction of the surface composed of OSRs) to ensure that they both operate at

Figure 4-23. MESSENGER solar panel showing the use of OSR to maintain array operating temperature within acceptable limits.

approximately the same temperature even though the top array is partially blocked from radiating by the HGA. The top array is packed with 55% solar cells, and the bottom array with 60% solar cells. Because both arrays operate at about the same temperature, a single PPT can be used for both. Both arrays are tilted 45° to the spin axis to reduce the array operating temperature. Because of the thermal environment in which the IHS spacecraft will fly, the IHS solar arrays are designed to operate at a temperature of ~180°, which is higher than the typical maximum operating temperature for spacecraft solar arrays (100°). (The MESSENGER solar panels are qualified to operate at 150°C and to survive short-duration temperatures up to 270°C.) Platinum wire sensors placed in small-bored cavities beneath the solar-cell-side face sheet are used to measure the solar panel temperatures.

The cover glass on each solar cell is a 0.15-mm-thick cerium-doped microsheet with magnesium fluoride anti-reflective coating. The panel substrates are aluminum honeycomb core with composite face sheets. The graphite-cyanate-ester materials on the panel face sheets are chosen for their high thermal conductivity. The side of the panels on which the solar cells are attached is insulated with Kapton, co-cured with the graphite fiber face sheet.

The solar array strings are isolated with string de-coupling diodes, which are placed inside the spacecraft in the solar array junction box to protect them from the high temperatures of the solar array panels. The survival of the individual cell bypass diodes at the maximum expected panel temperature and current will be verified.

Bombardment by solar energetic protons will be the predominant cause of radiation damage to the solar cells. The estimated total radiation dose that the arrays will receive over a 5-year period is about $5.3 \times 10^{+11}$ equivalent 10-MeV protons/cm^2, resulting in a degradation of the solar panels by about 8%, which was included in the solar array analysis.

4.7.3 Power subsystem performance. The performance of the IHS power subsystem was modeled for one of the IHS spacecraft for a 2012 launch. **Figure 4-24** shows the predicted power available to spacecraft loads. (660 W is the maximum power that the PPT can provide to the loads.) The analysis included the effects of solar array degradation resulting from solar enegetic particle bombardment, variations in illumination intensity, and solar array power processing losses. The

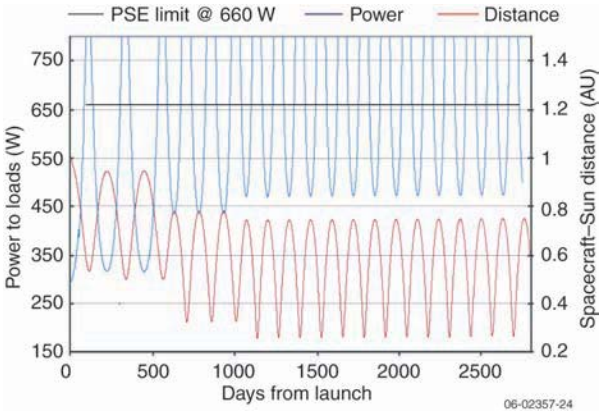

Figure 4-24. Predicted available load power during the mission. Analysis shows the Sentinels-4 spacecraft power for the 2012 launch.

minimum power occurs after launch at 1 AU. Other power minima occur at aphelia.

4.8 Communications Subsystem

The IHS communications subsystem must satisfy a number of requirements. The HGA and associated power amplifiers must provide for the return of the science data. The system must provide antenna coverage to enable robust communications and navigation (both uplink and downlink) over all mission scenarios, including early post-launch operations, routine operations, and emergencies. The system must be compatible with the DSN and associated CCSDS standards. Finally, the system must provide for a space weather downlink whenever the spacecraft are not in communication with the DSN.

4.8.1 Subsystem implementation. The block diagram in **Figure 4-25** shows the baseline design of the communications subsystem. The system operates in the deep space X-band frequency range with a 7.2 GHz uplink and 8.4 GHz downlink. A despun platform is required to point the HGA and MGA at Earth. The entire communications subsystem except for the antennas is located on the bottom deck of the spacecraft bus. This configuration simplifies the removal of waste heat from the power amplifiers. Three RF channels and 50 non-RF channels cross the despun boundary. A bearing and power transfer assembly (BAPTA) carries all signals across the despun boundary; it incorporates the necessary rotary joints and redundant motors to despin the platform. The communications subsystem electronics are block redundant to ensure against single-point failures. Each redundant side includes a deep space transponder, two TWTAs and associated isolators, a transfer switch, diplexer, and high-pass filter. Two levels of TWTA power are used to tailor the downlink bit rate capability to the power available based on the widely varying spacecraft–Sun distances (**Figure 4-26**). A medium-power TWTA (25 W_{RF}, 50 W_{DC}) provides communications when the spacecraft is outside 0.67 AU, and a high-power TWTA (100 W_{RF}, 200 W_{DC}) is used at distances inside 0.67 AU. The HGA is optimized for transmit-only operation, with high-pass filters at its inputs to prevent TWTA output noise from interfering with transponder receiver operation. A diplexer is used to combine the transmit and receive signals for the MGA and LGAs.

The HGA is a mechanically steered flat panel, a configuration that minimizes mass. It is 0.7 × 0.7 m in size with a 3-dB beamwidth of approximately 2.5°. The HGA is gimbaled in elevation by up to +15°/–7° to keep it pointed at Earth. The gimbal holds the HGA in a compact position during launch and, after separation and early operations, rotates the HGA approximately 180° into an operational state with a clear field of view past the

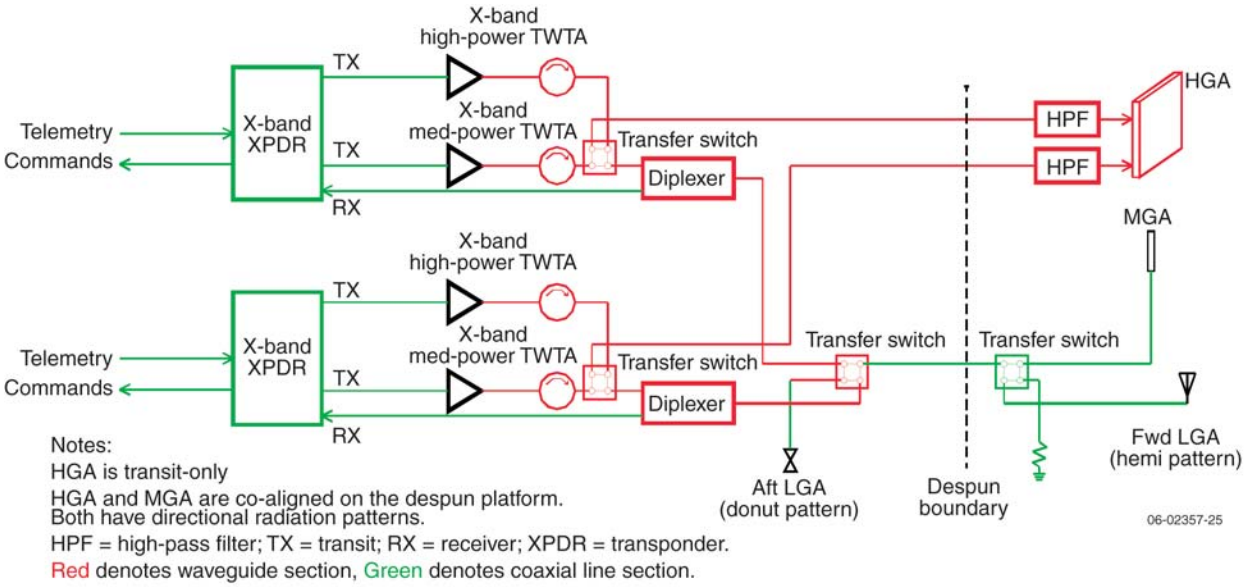

Figure 4-25. Block diagram of the Inner Heliospheric Sentinels communications subsystem.

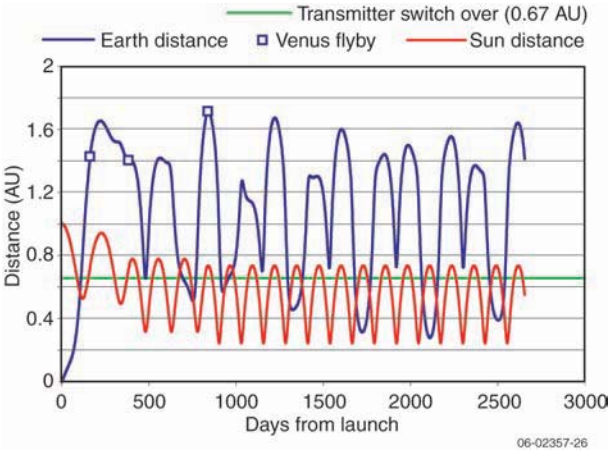

Figure 4-26. Earth and Sun distances as a function of mission day for the Sentinels-1 spacecraft (typical of all four spacecraft).

solar arrays at all necessary gimbal angles. In line with the gimbal axis are two multi-channel RF rotary joint feedthroughs. The gimbal motor is located off the gimbal axis on the despun platform deck and drives the rotary joints with a shaft drive linkage (see Appendix A).

The MGA consists of two linear arrays of helices (transmit and receive) fed through the broad wall of a waveguide. It has a 3-dB beamwidth of approximately 6° in azimuth and 90° in elevation and provides routine uplink communications and low-bit-rate downlink communications. The MGA resides with the HGA and is gimbaled in elevation with it.

The aft LGA is a conical corrugated horn radiating into a parabolic reflector that produces a "donut" pattern similar to that of a dipole. It is used for early launch operations and for emergencies such as a despun platform anomaly. The forward LGA is located on the bottom of the HGA to ensure hemispherical coverage before the HGA is gimbaled into its operational position. The combination of forward and aft LGA patterns gives nearly spherical coverage about the spacecraft for early post-launch operations.

4.8.2 Link performance. Link budget analyses were performed to verify the science return capability and the robustness of the design for early operations, science return, emergency mode, and space weather. Use of the 34-m DSN antennas was assumed for routine operations, of the 70-m DSN antennas for emergency operations, and of the 10-m ground antennas for space weather. Use of the medium-power TWTA was assumed for Sun distances > 0.67 AU; otherwise the higher-power TWTA was used. The science downlink data rate varies from 23 to 750 kbps (limited by spectrum regulation issues) over the mission profile.

Table 4-11 lists the specific downlink assumptions for each mode and the corresponding link analysis results. The analysis showed that the science downlink is capable of supporting a bit rate of 276 kbps with a margin of 3 dB at an Earth distance of 1 AU; this result was provided as an input to the more detailed science return analysis discussed in Section 4.10, Mission Data Management. The emergency mode link margin was found to exceed 3 dB using the aft LGA (donut pattern) at the maximum Earth distance. The analysis also demonstrated that in early operations the aft LGA can be used at 1000 bps out to an Earth distance of 0.1 AU (37 days after launch) and that the space weather downlink can support a bit rate of 10 bps at the maximum mission distance.

Although not shown, link analysis results for the uplink indicate adequate margins for all mission phases. A minimum operational uplink bit rate of 125 bps is assumed. The emergency mode uplink bit rate is 7.8 bps.

4.9 Command and Data Handling Subsystem

The C&DH subsystem baselined for the IHS mission is an integrated system that performs guidance and control as well as command and data handling functions. The C&DH requirements for the IHS mission are typical of those for spacecraft programs and can be met with flight-proven and/or industry-standard designs and components.

4.9.1 C&DH subsystem architecture. The C&DH hardware consists of a primary and a backup C&DH unit, two oven-controlled crystal oscillators (OCXOs), and a data bus **(Figure 4-27**). The C&DH subsystem is block redundant; either side can be selected as the controller. The C&DH subsystem is cross-strapped to the communications subsystem but not to the instrument DPUs, G&C sensors, or BAPTA electronics.

Each C&DH unit includes five daughter cards that adhere to the 6U compactPCI standard: a

Table 4-11. Downlink analysis assumptions and results

Parameter	Operational Scenario			
	Early Operations	**Science**	**Emergency**	**Space Weather**
Frequency[a]	X-band	X-band	X-band	X-band
Bit rate (bps)	1000	276,000	10	10
Earth distance (AU)	0.1 AU (37 days after launch)	1.0	1.7 (max. Earth distance)	1.7 (max. Earth distance)
RF transmit power (W)	25	100	25	25
Passive loss (dB)	3	1	3	1
Spacecraft antenna	Aft LGA (gain = 0 dBic)	HGA (gain = 35.6 dBic)	Aft LGA (gain ≥0 dBic over ±8°)	HGA (gain = 35.6 dBic)
Spacecraft pointing loss (dB)[b]	0	0.7	0	0.7
Ground antenna	34-m BWG	34-m BWG	70-m	10-m
Ground conditions	90% weather 20° elev.	90% weather 20° elev.	90% weather 20° elev.	Clear conditions
G/T (dB/K)	52.6	52.6	60.2	32.3
Simultaneous ranging	Yes	Yes	No	No
Coding	Turbo, R = 1/6, short frame	Turbo, R = 1/6, long frame	Turbo, R = 1/6, short frame	Convolutional R = 1/2
Receiver system implementation loss (dB)	1.5	1.5	2.5	3.0
Link Margin (dB)[c]	**3**	**3**	**4.8**	**6.9**

Notes:
(a) X-band is at 7.2 GHz receive and 8.4 GHz transmit
(b) HGA pointing error is 0.8°.
(c) Link margin is relative to the power needed to achieve a frame error rate of 1×10^{-4}

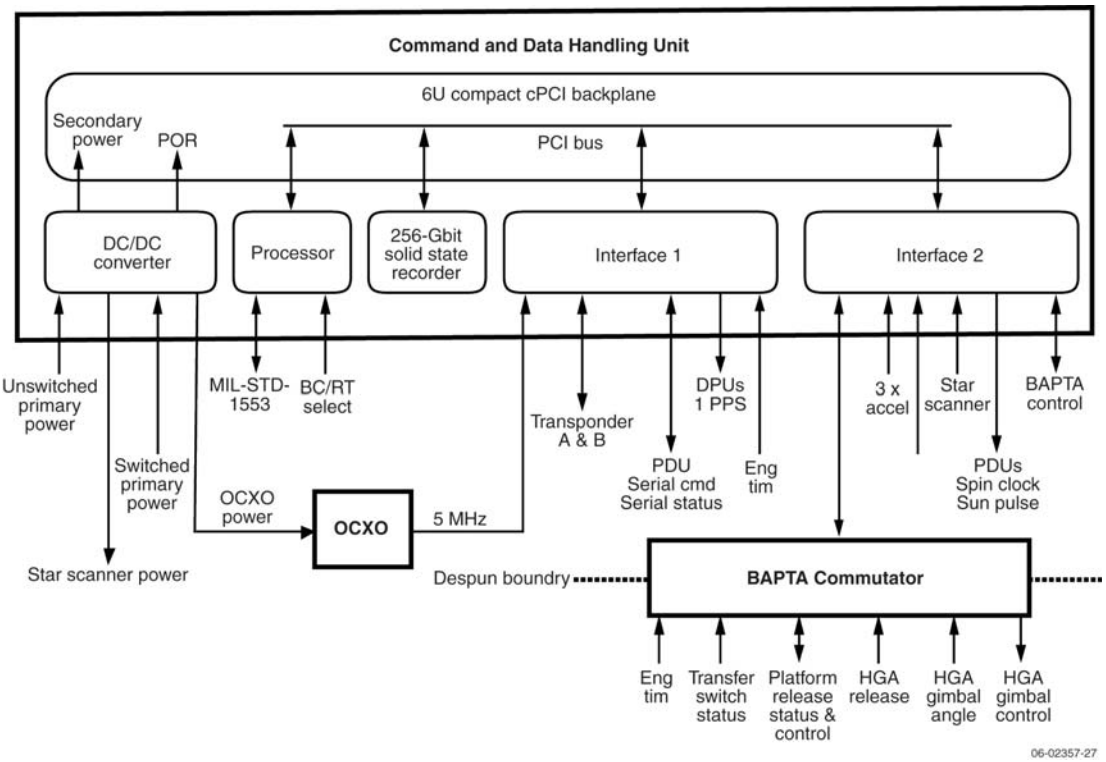

Figure 4-27. Block diagram of the Inner Heliospheric Sentinels command and data handling subsystem.

processor, an SSR, two interface cards, and a DC/DC converter card. A processor throughput of 10 to 20 MIPS should be adequate for the IHS mission and is not a significant design driver. Data rates are low, with an SSR record rate of 8326 bps and a maximum SSR playback rate of less than 750 kbps. Downlink data rates range from 10 bps to 750 kbps. The PCI backplane can easily accommodate both the SSR and downlink data rates. The required SSR capacity is about 180 billion bits (see Section 4.10.3 below); however, a capacity of 275 billion bits should be easily attainable with current flash memory or near-term SDRAM memory technology. The DC/DC converter board provides regulated voltages for the OCXO and star scanner as well as for the internal C&DH subsystem loads.

The OCXO provides precision timing for the C&DH subsystem. For an accuracy of 10 ms, an oscillator with a frequency uncertainty of 8 ppb would be needed, assuming that the spacecraft time is correlated to ground time on a weekly basis.

The C&DH supports a MIL-STD-1553 data bus for communicating with the instrument DPUs, PSE, and PDU. This bus can easily accommodate the required data rates.

4.9.2 Despun platform signal management. The despun platform requires about 50 signal and power lines to be passed through the BAPTA. This can be accommodated by available BAPTAs. These signals are needed to power, control, and monitor the status of the antenna gimbal and RF switches, and to deploy the antenna assembly and release the despun platform.

4.9.3 Sun pulse processing. An important function of the C&DH subsystem is to process the "raw" Sun pulse from the Sun sensor and to output the processed Sun pulse together with a spin clock pulse to the instrument DPUs with non-cross-strapped interfaces. The spin clock generates 4096 ± 1 pulses per spin. The Sun pulse and spin clock signals are used by the instruments to bin measurements based on the angle between the instrument aperture and the Sun. The duration of the Sun pulse will vary significantly with distance from the Sun. This variation in pulse width would introduce an offset between measurements made at different spacecraft–Sun distances if the rising edge of the pulse were used to initiate the binning. To avoid this offset, the C&DH processes the "raw" Sun pulse from the Sun sensor so that the rising edge of Sun pulse sent from the C&DH to the instruments occurs in the center of the Sun pulse from the Sun sensor.

4.9.4 Data rates. The baseline composite raw instrument data rate is 5900 bps. The C&DH adds another 200 bps of engineering data needed to interpret the instrument data. This engineering data include Sun pulses, time tags, and spacecraft attitude data. Packet headers added to these instrument and engineering data will increase the data rate by 5%. The data rate is further increased by 30% to add data margin, for a total rate of 8326 bps.

The C&DH generates downlink data at bit rates ranging from 10 bps to 750 kbps. The expected bit rates for different modes are shown in **Table 4-12.**

4.9.5 C&DH flight software. The IHS C&DH flight software has no unusual or stressing requirements. The low data rates and spin-stabilized bus simplify the real-time processing that the C&DH software must implement. A typical software implementation that meets IHS requirements follows. The software would be implemented in C code running under the VxWorks real-time operating system. The G&C attitude determination and control algorithms would be implemented as tasks executing concurrently with other tasks that constitute the C&DH functionality. The primary flight processor boots to an application that becomes the 1553 bus controller and actively controls the spacecraft, performing all G&C and C&DH functions. The backup flight processor, when powered, boots to an application that operates as a remote terminal on the 1553 bus and can record science data to the SSR in parallel with the primary flight processor.

The primary flight processor C&DH software manages the telecommunications uplink and downlink using CCSDS protocols for data handling. Commands are received in CCSDS telecommand

Table 4-12. Downlink data rates for mission modes

Mode	Downlink data rates
Early operations	1,000–10,000 bps
Space weather	10–500 bps
SSR dump	23–750 kbps
Emergency	10 bps

packets that are either processed by the C&DH software or dispatched to the G&C tasks or to other subsystems on the 1553 bus, as indicated by an operation code contained in the packet header. The C&DH software supports storage of command sequences, or macros, which can be executed by a time-tagged command stored in flight processor memory.

The C&DH software collects engineering and science data from the instruments and manages the storage of those data on the SSR in the form of files. The files are stored in a directory structure that implements the priority scheme described in Section 4.10.1. The instrument DPUs packetize their data prior to sending the data to the C&DH. The C&DH software can be configured to interleave CCSDS transfer frames of real-time telemetry packets with frames of SSR playback data. SSR playback is managed using the CCSDS File Delivery Protocol (CFDP). CFDP provides a mechanism to downlink files from the SSR using a handshake with the CFDP client in the ground system software. This protocol automatically manages retransmission of any file fragments lost due to data dropouts without requiring retransmission of the entire file, and file transmissions may be suspended and resumed between passes. No operator intervention is required to manage the retransmit process.

In addition to supporting standard command processing, data handling macro storage and uplink/downlink function, the C&DH software includes an autonomy evaluation engine that supports fault detection and correction. Data collected from all subsystem are stored in a memory buffer and can be referenced by uploaded autonomy rules. Each rule can monitor one or more telemetry points, perform computations, and execute a specified command if the premise of the rule evaluates "true" for a designated number of consecutive times. Typically the command is an instruction to execute a stored macro that performs a corrective action. This design allows for autonomy rules to be developed and uploaded without requiring software changes.

The C&DH software supports receipt of code, parameter, and rule uploads, and downlink of these items or flight software data structures. Additionally, the flight software maintains a number of history logs, event logs, and anomaly logs that may be downlinked to support anomaly investigation. The flight code implements a software watchdog that services a timer that forces a reset of the processor should any critical task fail to execute during the allotted time.

4.10 Mission Data Management

The distance between the IHS spacecraft and Earth will vary substantially because of the mission trajectories. Except during the early operations phase, when the spacecraft is close to Earth, the spacecraft–Earth distance will range from about 0.3 AU to 1.7 AU. The RF transmit power will vary by a factor of 3 based on the power available for the transmitter. As a result, the downlink data rate will vary greatly, from a peak of 750 kbps down to 23 kbps. But while the downlink data rate varies by a factor of ~33, the instrument data rate is constant. The SSR must therefore have the capacity to accommodate the difference between the SSR record and playback rates. Depending on the DSN strategy, there can be times when data will accumulate on the SSR for almost a year and then be dumped in a few months during a period of downlink at a high data rate.

4.10.1 Science Data Latency. Science data latency refers to the period between the time when a set of data is recorded on the SSR and when it is downlinked. The key factors determining latency are shown in **Table 4-13.** Data are recorded at three different priority levels:

- ***High-priority data*** are the highest-priority data on the SSR and are always downlinked first. These data consist of a subset of instrument data identified by ground command prior to being recorded on the SSR. The total amount of high-priority data on the SSR is limited to 1 Gbit. Once the high-priority data area on the SSR is filled up, no further high-priority data are recorded.
- ***Continuous science data*** have the next-highest priority. These data are allocated 4720 bps (without margin or headers). They consist of a subset of instrument data identified by ground command before the start of the recording process.
- ***Burst science data*** have the lowest priority. These data are allocated 1180 bps (without margin or headers). The subset of instrument data to be recorded as burst science data can be changed by command from the instrument or the SEP DPU or by ground command. There are multiple

Table 4-13. Primary factors affecting science data latency.

Parameters Driving Science Data Latency	Value
Instrument data rate	5900 bps, 8326 bps with engineering telemetry, margin & overhead
Data at each priority level	80% continuous science (highest priority); 20% burst science (lowest priority)
RF transmit power	100 W_{RF} or 25 W_{RF}, depending on available power
HGA gain	Gain assumes 0.7 × 0.7 m phased array antenna
Solar distance power available for high power transmitter	0.67 AU based on instrument and high-power transmitter power load
Solar distance power available for instruments	0.88 based on instrument power load
Science operations start date	Assume 2 months after launch
DSN strategy	Two cases: non-optimized 8 hours/week; improved by only dumping SSR during periods of high data rate
Trajectory	IHS trajectories 1-25, 2-25, 3-25, 4-25 with launch on September 4, 2015

priority levels of burst science data. The priority levels are set by ground or DPU command. The priority level of data already stored on the SSR also can be changed by ground command.

Latencies are calculated independently for continuous science and burst science data. Data are downlinked in order of priority. No burst science data are dumped from the SSR until all of the continuous science data have been dumped.

Latency plots for two different trajectories are shown in **Figure 4-28**. The latencies assume a simple DSN strategy, with 8 hours of SSR dump time per spacecraft per week. The plots show a large buildup of data on the SSR during the first year of the mission. During this period, the spacecraft–Earth distance is large (which reduces the downlink data rate) and the spacecraft–Sun distance is large, which means that the medium-power transmitter must be used instead of the high-power transmitter. The link with the medium power transmitter has one third of the data return capability of the link with the high-power transmitter.

4.10.2 Deep Space Network strategy. Reducing DSN costs can be a significant factor in reducing the overall mission cost. It is therefore important to consider ways in which data can be returned as efficiently as possible, thus minimizing the DSN pass time and hence the cost. One strategy is to dump the SSR only on days when the downlink bit rate exceeds the median bit rate. The latency plots shown in **Figure 4-29** dump 10 hours per week when the bit rate is above the median, and do not dump at all when the data rate is less than the median, for an average of 5 hours per week. Another strategy is to download 8 hours per day from the nearest spacecraft.

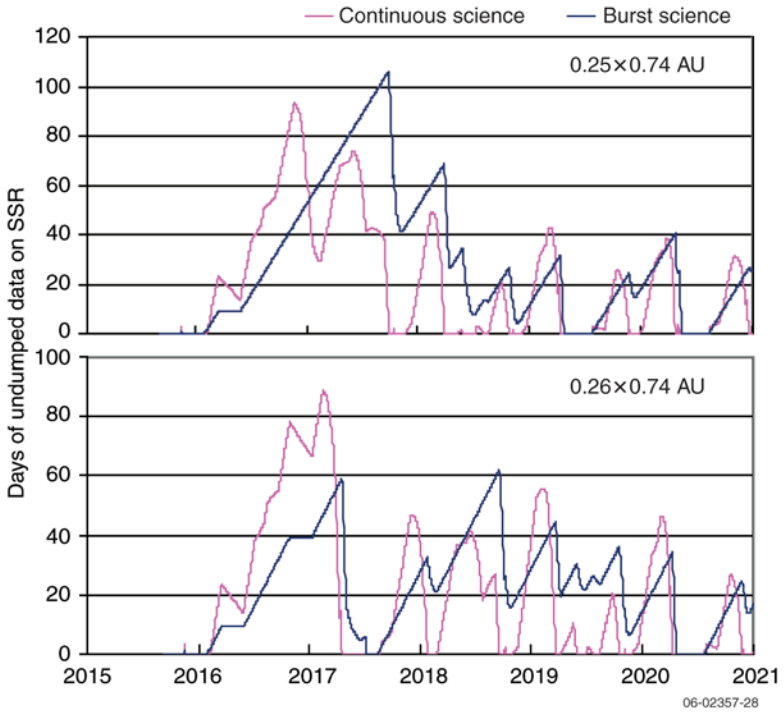

Figure 4-28. Science data latency with simple DSN strategy for two trajectories, Sentinels-1 (top) and Sentinels-3 (bottom).

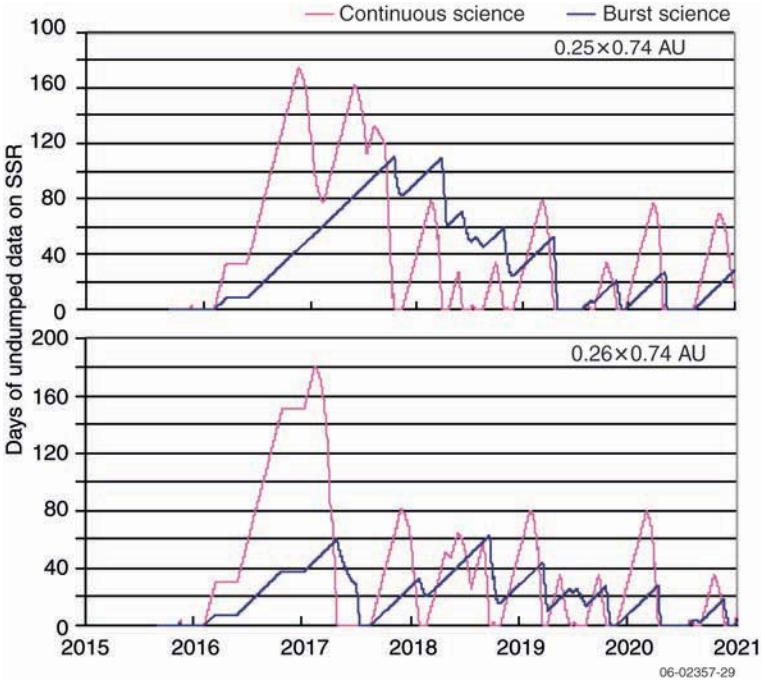

Figure 4-29. Science data latency with improved DSN strategy for two trajectories, Sentinels-1 (top) and Sentinels-3 (bottom).

Ultimately, the strategy selected must take into account the fact that DSN costs do not scale linearly with the number of hours used.

4.10.3 Solid-state recorder capacity. The required SSR capacity is related to the DSN strategy, because a strategy that provides for SSR dumps only during periods of high downlink data rate will cause a greater accumulation of data on the SSR. The amount of data that accumulates in the SSR for a strategy of 10 DSN hours per spacecraft per week during periods of high data rate, and no DSN hours for periods of low data rate, is shown in **Figure 4-30**. The maximum amount of data on the SSR is about 180 Gbits. A 256-Gbit single board SSR is feasible now with flash memory technology, and will be feasible in the near future with SDRAM memory technology.

4.11 Guidance and Control Subsystem

The G&C subsystem determines and controls the spacecraft spin axis direction and spin rate and the spin phase of the despun platform; executes ΔV maneuvers for orbit control; and controls the pointing of the HGA. Spin-axis control involves precession of the spin vector in inertial space, nominally controlled to point perpendicular to the spacecraft orbit plane. Changes to orbit geometry are accomplished through ΔV maneuvers. The G&C design provides the ability to perform ΔV maneuvers in any direction without requiring any precession maneuvers, thus simplifying operations and reducing propellant mass. HGA pointing control involves control of the despun platform pointing to achieve the correct azimuthal pointing and control of the antenna gimbal to achieve the correct elevation angle. The G&C subsystem baselined for the IHS mission employs standard techniques and components that have been proven on many previous missions.

4.11.1 G&C subsystem architecture. The G&C subsystem consists of a star scanner and spinning Sun sensor for spin axis and spin phase determination and 12 4-N thrusters for maneuver control. Accelerometers are used to assist in the closed-loop control of nutation resulting from propulsive maneuvers. (Active nutation control would be required only if future analysis indicates that propellant slosh alone would not damp out nutation sufficiently fast.) Only two thrusters are required for any given

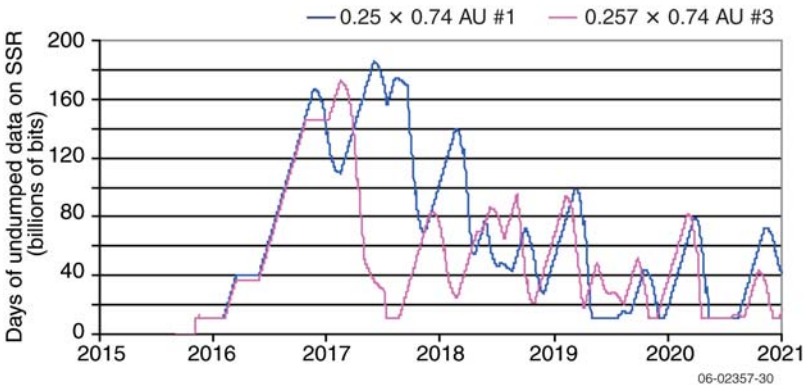

Figure 4-30. Data buildup on the solid-state recorder for a strategy of 10 DSN hours per spacecraft per week during periods of high data rate, and no DSN hours for periods of low data rate for the two trajectories.

maneuver. This minimizes the power necessary for each maneuver by reducing the required number of powered catalyst bed heaters. Redundant hardware is provided for all G&C sensors. The 12 thrusters provide redundancy and flexibility for any ΔV maneuver.

G&C commands and algorithms are processed by the C&DH subsystem. Earth and spacecraft orbit ephemerides are required for antenna pointing and are input as parameters to the C&DH processor, which outputs thruster commands, antenna pointing commands, and spin-axis and spin phase estimates. No instrument data are used for the attitude determination and control functions. **Figure 4-31** is a simple diagram of the G&C subsystem, and **Table 4-14** gives the characteristics of the baseline components. Additional detail can be found in the spacecraft block diagram presented in Section 4.4 (**Figure 4-9**).

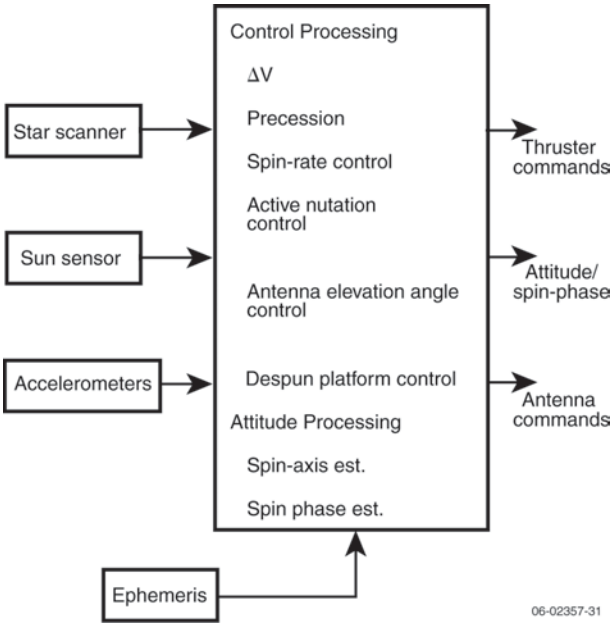

Figure 4-31. Block diagram of the Inner Heliospheric Sentinels guidance and control subsystem.

Table 4-14. Baseline components of the guidance and control subsystem.

G&C Component	Mass (kg)	Power (W)	Volume (mm)
Adcole Sun sensor	1.25	1	Sensor head: 127 × 102 × 76 Electronics box: 66 × 66 × 50
TNO-TPD Star-mapper	4.1	0.5 (secondary power)	Sensor head: 482 × 366 × 180 Electronics box 61 × 182 × 170
Honeywell QA3000 Accelerometers	1	1.5	150 × 150 × 150

4.11.2 Attitude determination. Knowledge of the spin axis direction to within 0.5°, 3σ, is required. The star scanner is used to determine the direction of the spin axis, while the spinning Sun sensor is used to determine the spin rate and spin phase. The spin rate is calculated from the time measured between Sun pulses. (If desired, timing information from the Sun sensor could be augmented with star-scanner timing measurements.) The spin phase can be determined from the spin rate and Sun pulse timing.

Estimation of spin-axis attitude, spin rate, and spin phase are performed onboard the spacecraft for use in maneuver processing. Additional post-processing can be performed on the ground to increase the accuracy of these estimates if desired. However, onboard processing is fully capable of meeting the mission requirements.

4.11.3 Attitude control. To meet the IHS science requirements, the G&C subsystem must be able to control the spin axis to within 1.0°, 3σ, of orbit normal. In addition, the subsystem must be able to increase the spin rate to 20 rpm and maintain it, perform ΔV maneuvers, and provide active nutation control.

Spacecraft attitude is controlled with the 12 thrusters. Paired thrusters are used for all attitude control maneuvers, providing nearly pure torque and minimizing undesired orbit perturbations. **Figure 4-32** illustrates the layout of the 12 thrusters. Spin-up and spin-down are accomplished with opposing, tangentially pointed thrusters t5/t8 and t6/t7, respectively. The spin axis direction is controlled through precession maneuvers, which use opposing, radially pointed thrusters t9/t12 or t10/t11. Radial ΔV maneuvers can be performed with thruster pairs t9/t11 or t10/t12, and axial ΔV maneuvers use thrusters t1/t2 or t3/t4.

Spin-rate control maneuvers are initiated by ground command and specified in terms of thruster on-time. The burn time is calculated from the desired spin-rate change,

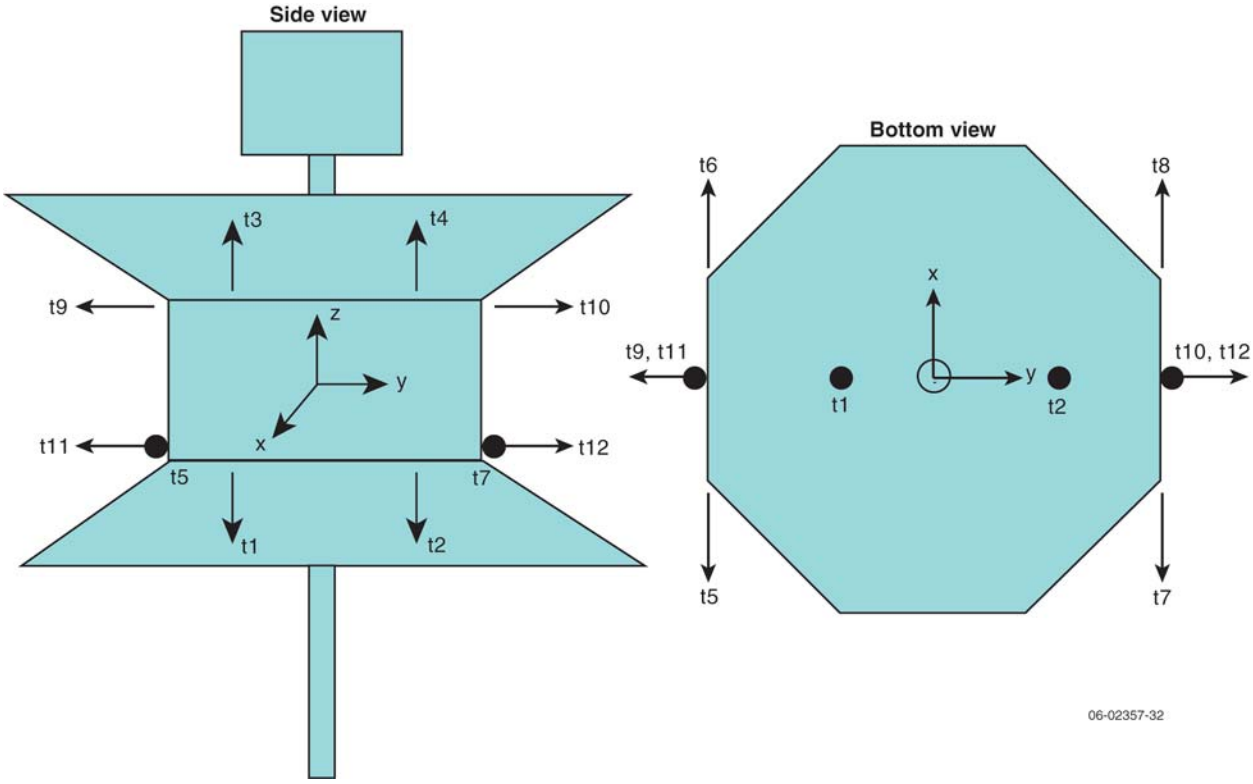

Figure 4-32. Thruster locations as viewed from the side (left) and the bottom (right) of the spacecraft.

calibrated thruster performance, and the estimated spacecraft mass properties. (Spacecraft mass properties are maintained on the ground and uplinked to the spacecraft.)

Axial and radial ΔV maneuvers are also specified in terms of thruster on-time. Burn time for axial ΔV values is calculated from the desired magnitude of the ΔV, calibrated thruster performance, and estimated spacecraft mass. Selected thrusters are turned on for the specified burn time. Radial ΔV maneuvers use the same parameters for calculating the total thrust time; however, the thrusters must be pulsed over a revolution. Generally, the thrust is commanded over one-quarter of a revolution, and the start of the pulse is timed relative to the Sun pulse. Precession maneuvers are performed in a fashion similar to a radial ΔV maneuver, except that opposing thrusters are used.

As designed, the spacecraft is a major-axis spinner at separation, thus minimizing the need for immediate propulsive maneuvers. However, it is possible (but unlikely) that the spacecraft may have to perform an autonomous precession maneuver soon after separation, due to launch vehicle insertion errors. To simplify ground operations and allow for the possibility of autonomous maneuvers, maneuver calculations should be performed onboard the spacecraft by the flight software. The operators on the ground would provide the necessary data (for example, maneuver magnitude, thruster performance, thruster pair, spacecraft mass properties, etc.), and the flight software would calculate the thruster on-times.

The use of booms and long wire antennas on spinning spacecraft is not new (e.g., WIND, FAST), and thus is not of great concern. These appendages are generally benign except when a spacecraft maneuver is being performed. For example, during a precession maneuver the spacecraft precesses as the thrusters fire, but the wire antennas take considerable time to "catch up." Proper analysis of the flexible mode issues should be performed during spacecraft development. Boom excitation by solar inputs may cause the IHS spacecraft to experience a nutation problem like that experienced by Ulysses, whose architecture is similar to that of the IHS spacecraft. (The WIND and FAST architectures are similar to those of Ulysses and IHS and have not exhibited the nutation problems that Ulysses did.)

Of particular concern is the axial boom, which will require sufficient rigidity to avoid excitation, within the limits of allowable structure and mass. Active nutation control is part of the baseline architecture, as described above, and can be used to damp any nutation. Passive nutation control can be added if early analysis shows that active control requires an excessive amount of propellant.

4.11.4 Center-of-mass/center-of-pressure offset. Solar radiation produces pressure on exposed surfaces of the spacecraft. The pressure decreases with the square of the distance from the Sun, and so at 0.25 AU, the perihelion distance for IHS, the effect is 16 times greater than at 1 AU. Thus what is normally negligible is of potential concern for the IHS spacecraft. An offset between the spacecraft center of mass and the center of pressure (CM-CP offset) can create a precession torque that will, over time, cause the spacecraft spin axis to precess. Over the course of an orbit the spin axis will wobble in an almost circular motion as the solar radiation changes direction relative to a fixed heliocentric coordinate frame. If the CM-CP offset is great enough, the spin axis could eventually tilt beyond the allowed 1.0° deviation from orbit normal, thus requiring a precession maneuver to get back within specifications.

Propellant mass is directly related to the number of maneuvers that must be performed over the life of the mission. Moreover, the solar pressure effect could force an autonomous precession maneuver during the 60-day blackout period. Thus, to minimize both propellant mass and the need for autonomous maneuvers, it is necessary to minimize the CM-CP offset.

The main body of the IHS spacecraft is very symmetrical, which tends to place the center of pressure at the geometric center of the body. However, the IHS spacecraft has a long, relatively thin boom protruding from the bottom deck and a large, radome-shielded antenna at the top which serves as a "sail." To determine the center of pressure, careful analysis of the final geometry of the spacecraft, as well as modeling of the spacecraft's material properties, will be needed. (The type of material determines whether the solar flux is absorbed, diffusely reflected, or specularly reflected.) Fortunately there is a large body of literature concerning the modeling of solar pressure torques, particularly for Earth-orbiting spacecraft such as the TOPEX/POSEIDON spacecraft and the GPS satellites. These satellites require very good modeling of the spacecraft position. Application of these previous studies will improve the solar pressure modeling of the IHS spacecraft. Once the center of pressure has been calculated, judicious placement of hardware can reduce the CM-CP offset, as can the extension of the appropriate solar panel (upper or lower). Another alternative is to bias the spin axis off of orbit normal in a way that the wobble is centered around zero. For example, if the magnitude of the wobble is predicted to be 1°, then bias the spin axis to start at -0.5° and let it grow to +0.5° before it decreases again.

Figure 4-33 illustrates the estimated propellant required given a particular CM-CP offset. The pressure at perihelion is approximately 10 times greater than at aphelion; however the spacecraft spends less time at perihelion than aphelion. As a result of these two characteristics of the orbit, the spin axis does not return to its original direction after one orbit. There will be a slow "walking off" of the axis over time. If the CM-CP offset is small, the magnitude of the wobble is small, and so it is the slow "walking off" that dictates how many maneuvers are required. This is illustrated in **Figure 4-33** for CM-CP offsets up to around 9 cm. When the CM-CP offset becomes large enough, the magnitude of the wobble increases to the point of violating the 1° requirement every orbit. This result can be seen in **Figure 4-33** by the rapid increase in required propellant for a CM-CP offset greater than 9 cm. After this point the propellant mass is dictated by the magnitude of the wobble.

In the current configuration of the IHS spacecraft, the CM-CP offset is about 10.9 cm. No attempt has been made to minimize the offset for this study. Given this offset, it is estimated that the IHS spacecraft will require a procession maneuver once per orbit, or roughly every 122 days. At this rate, and based on the mass flow rate of the thrusters, it is estimated that 0.9 kg of propellant would be required for this number of maneuvers. The propellant mass budget includes 1 kg for these maneuvers, not including the added margin. The data indicate that the current spacecraft design can acceptably manage the solar pressure torque. While the CM-CP offset is an important issue and

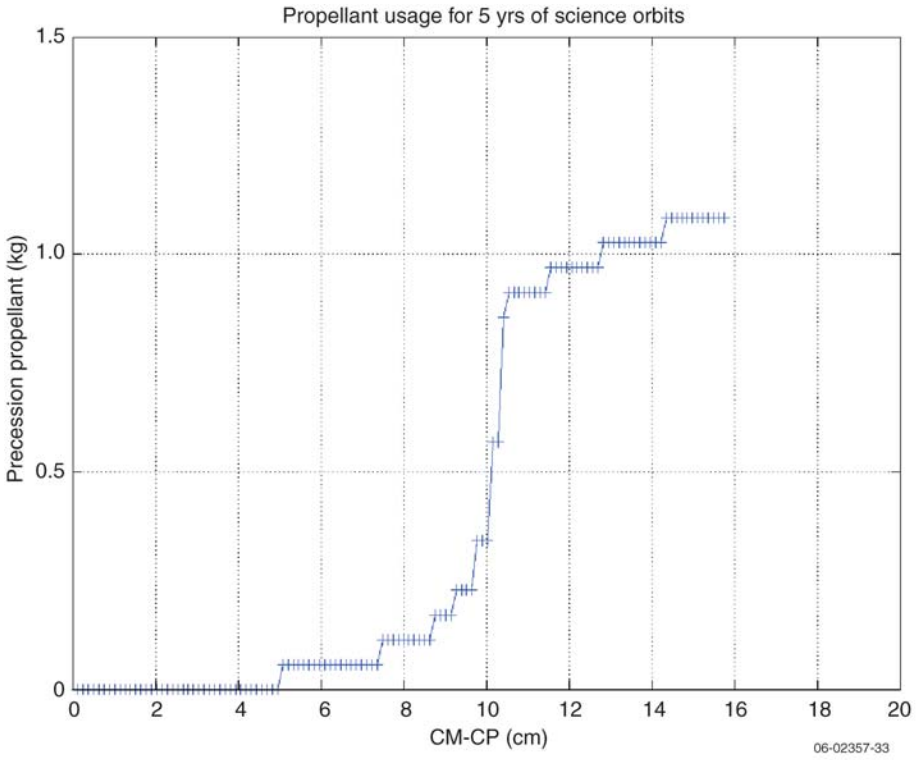

Figure 4-33. Inner Heliospheric Sentinels propellant usage based on the center-of-mass to center-of-pressure offset.

every attempt would be made in the final spacecraft design to reduce it to zero, management of the offset is technically feasible and of low risk. For example, the Helios spacecraft did not require a precession maneuver to correct for solar pressure effects in its entire 12-year life.

4.11.5 High-gain antenna control. The G&C subsystem controls the pointing of the HGA so that the spacecraft can provide continuous space weather data. Platform azimuth and antenna gimbal angles are calculated from ephemeris data, knowledge of current time, and spin-axis direction. Earth and spacecraft orbit ephemeris data, in inertial coordinates, are provided to the spacecraft by ground operations, typically in the form of polynomial coefficients. The frequency at which these data are updated depends on the orbit; however, once the spacecraft reach their final science orbits, these data will require only infrequent updates.

Table 4-15 gives an antenna pointing budget. The predicted antenna pointing capability is 0.49°. The required antenna pointing performance (used in the RF downlink analysis) is 0.8°.

4.11.6 G&C subsystem performance. Performance requirements for the IHS spacecraft are not overly stringent. Pointing control of a spinning spacecraft to within 1.0° is easily achievable with the selected 4-N thrusters. Spin-axis attitude estimation of 0.5° is easily attained with the star scanner and onboard processing. In fact, previous missions indicate that performance closer to 0.1° is achievable; on RHESSI, ground post-processing of attitude data has demonstrated performance on the order of 0.02°. **Table 4-16** provides a summary of the estimated capabilities of the IHS G&C subsystem. The techniques and hardware for attitude estimation and control baselined for the IHS spacecraft are well established and have been demonstrated on previous missions involving spinning spacecraft, including Wind, Polar, and RHESSI. New development is not required.

4.11.7 Spacecraft stability at separation. The inherent spin stability of the spacecraft and interspacecraft structures will prevent tumbling upon separation. However, the spacecraft will wobble when released from the upper stage. This wobble

Table 4-15. Antenna pointing budget.

	Azimuth (deg)	Elevation (deg)	Basis of Estimate
Attitude knowledge	0.25	0.25	Expected performance of sensor
Attitude control: nutation[(a)]	0.05	0.05	New Horizons analysis
Principle axis alignment	0.10	0.10	CONTOUR analysis
Platform resolution (azimuth)	0.003		Vendor specification
Gimbal "slop" (elevation)		0.05	STEREO analysis
Thermal	0.20	0.20	Initial analysis
RF calibration error	0.05	0.05	Initial analysis
RSS error	0.34	0.35	
Total RSS error		0.49	

[(a)]Most attitude control error is taken out by antenna pointing adjustments.

Table 4-16. IHS G&C subsystem capabilities.

Capability	Requirement	Estimated Capability	Margin
Spin-axis control	1.0°	0.2°	400%
Spin-axis knowledge	0.5°	0.25°	100%

will naturally decay as a result of damping by propellant slosh. The spacecraft mechanical design must prevent any contact between segments during separation.

4.12 Propulsion Subsystem

The propulsion system baselined for the IHS mission (**Figure 4-34**) is a blowdown system similar to almost every hydrazine propulsion system flying today. Twelve thrusters provide a thrust of 4.48 N each for ΔV maneuvers and angular momentum management. The thrusters can apply orbit maneuver ΔV in all required directions. The thrusters are manifolded together, and parallel latch valves control propellant to the thrusters. Each thruster has series-redundant control valves to protect against leakage.

The hydrazine propellant and nitrogen pressurant are stored in two custom conispherical tanks whose pressure decreases as propellant is depleted. Latching valves isolate the thrusters from the tanks for ground safety and system reliability (i.e., in case of a thruster leak), while manual service valves are used for testing and loading the system on the ground. The latching valves also allow for propellant balancing between the two propellant tanks. Surge suppression orifices keep transient pressures within appropriate levels, and the pressure transducers are used together with temperature telemetry to gauge propellant and monitor system performance in flight.

The propellant load was determined based on the performance of a representative thruster (the Aerojet MR-111c) that has an extensive flight and test heritage and that meets or exceeds all IHS requirements. The total maximum required usable hydrazine propellant load calculated is 42.5 kg, including margin (**Table 4-17**). The ΔV requirement is 100 m/s, which requires 37.3 kg of propellant. For a 5-year mission an additional 5.2 kg of propellant is required for attitude control. To accommodate this calculated propellant load, together with trapped propellant, pressurant, and the range of inlet pressures for which the thruster has been

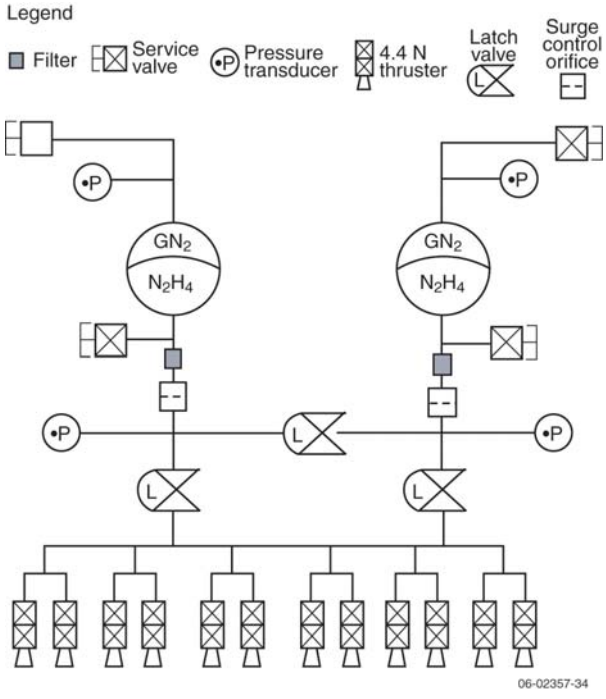

Figure 4-34. Propulsion system functional schematic.

Table 4-17. Propellant mass budget.

Propellant Budget	Mass (kg)
Nondeterministic ΔV (100 m/s) **Nondeterministic ΔV (100 m/s) +15% margin**	32.5 **37.3**
G&C propellant **G&C propellant required +30% margin**	4.0 **5.2**
Pressurant	0.5
Total Propellant and pressurant with margin	**43.0**

qualified, each tank requires a volume of 30.56 L. An additional 1.0 kg of propellant could be loaded into each tank, extending the life of the propulsion system from 5 to 10 years. The tanks baselined for the IHS spacecraft are a new design and would need to be flight qualified. However, components with signficant flight heritage are available for all of the other elements of the propulsion subsystem.

5.0 Implementation of the Remote Sensing Sentinels

The measurement requirements derived from the Sentinels science objectives (listed in **Tables 1-2** and **1-3** in Chapter 1) call for remote sensing of the structure and plasma characteristics of the solar corona and for 2π photospheric magnetic field observations. Because of the high telemetry rates associated with imaging instruments, particularly the UV and white-light coronagraphs, and their stricter pointing and stability requirements, the Sentinels STDT has determined that the most cost-effective way to return the highest-quality solar observations is to use platforms located at 1 AU. Only the 2π photospheric observations require a platform on the far side of the Sun. The STDT recommends that the magnetograph be flown on a different platform from that carrying the coronagraphs, and thus designed the smallest possible focused mission to the far side of the Sun. The coronagraphs will be kept on a spacecraft in low Earth orbit, thus minimizing launch and telemetry requirements.

This chapter summarizes the design of the two remote sensing Sentinels platforms, the Farside Sentinel (FSS) and Near-Earth Sentinel (NES). More engineering details of possible implementations of FSS and NES can be found in Appendices D and E, respectively.

5.1 The Farside Sentinel (FSS)

The implementation of the FSS was studied by an engineering team at the Jet Propulsion Laboratory (JPL). Their task was to identify the smallest and most cost-effective design that is technically feasible and will provide the required measurements. The JPL team developed a number of options, which are detailed in Appendix D. Here the simplest design is described.

Since photospheric magnetic fields can be determined only for about 120° of the visible surface of the Sun from a single vantage point, due to limb foreshortening, complete 2π observations would require three independent platforms evenly distributed around the Sun. The LWS Solar Dynamics Observatory (SDO) will provide the necessary photospheric observations from a near-Earth location. Rather than proposing two additional FSS spacecraft to observe the Sun's far side, the STDT recommends that a partnership be formed with the ESA Solar Orbiter, a spacecraft that is envisioned to carry a capable magnetograph and will spend substantial periods of time on the far side of the Sun. This would allow NASA to focus on implementing a single far-side mission while still obtaining the required 2π coverage. Once the various components are in place, the FSS–SDO–Solar Orbiter constellation would provide complete solar equatorial coverage every 4 to 5 months. Coverage would last more than a solar rotation period at a time.

Because of Solar Orbiter's orbital symmetry, it is equally feasible to place FSS into either an Earth-leading or an Earth-lagging orbit. Significant scientific advantages are associated with both options. However, the STDT has determined that an Earth-leading orbit, which will allow the foot points of interplanetary field lines intersecting the near-Earth environment to be observed, has the highest priority for studying solar energetic particle (SEP) acceleration and transport. Should a second Earth-lagging far-side mission be required at a later time, a spacecraft virtually identical in design to the one described here for the Earth-leading platform could be used.

5.1.1 Orbit Design. The primary measurement requirement of the FSS is to provide solar photospheric magnetic field observations from 60° to 180° ahead of Earth from a nearly constant radial distance of ~1 AU. To maximize the possible overlap between the Inner Heliospheric Sentinels (IHS) and FSS, orbit solutions with the shortest cruise time to 60°, relying on the smallest possible launch vehicle, were sought. For a small spacecraft bus carrying only a magnetometer, a Taurus launch vehicle can achieve a heliocentric orbit that will place FSS at 60° ahead of Earth in 1.8 years. Then, during a 2-year prime phase of the mission, the spacecraft would drift to 120°, reaching 180° in an additional 2 years (see **Figure 5-1**).

5.1.2 Instrumentation. The primary instrument carried by FSS is a magnetograph that will provide photospheric magnetograms with a spatial resolution of up to 1500 km at disk center. The large distance of FSS from Earth and the focused nature of this mission impose severe constraints on instrument telemetry rates and mass. The STDT recommends using a filter-based magnetograph, which would provide significant mass and power savings

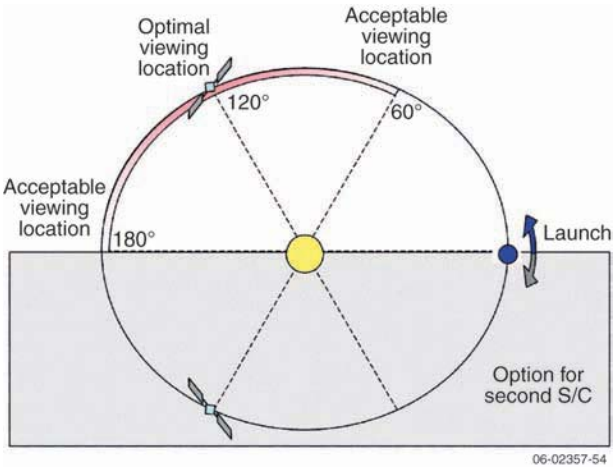

Figure 5-1. Orbits for Earth-leading and Earth-lagging Farside Sentinels (FSS). Only the Earth-leading FSS is currently under consideration.

(~10 kg, 20 W) compared with current magnetograph designs. The available telemetry rate allows the return of longitudinal magnetograms with around a 3-min cadence. The impact of optional additional instruments (coronagraphs and an in-situ package) was also studied, but would likely result in transitioning to a larger, Delta II class launch vehicle.

5.1.3 Spacecraft Bus Design. The primary constraints for the FSS spacecraft bus design are that it fit inside the 1.4-m fairing of a Taurus launch vehicle and that its total mass be kept below the 445-kg launch vehicle capability while still returning the required science telemetry. A 440-kg fully margined total launch mass cubic bus design with four deployable solar arrays (see **Figure 5-2**), an area of 2.24 m^2, and producing 890 W, plus an articulating 1.25-m-diameter Ka band high-gain antenna, satisfies the launch vehicle and 115-kbps science collection data rate requirements. The spacecraft is 3-axis stabilized with 20 arcsec pointing control and better than 5 arcsec pointing stability. All of the spacecraft components can be built using currently available parts and technologies.

5.2 The Near-Earth Sentinel (NES)

The role of NES is (1) to characterize the coronal source regions of SEPs and CMEs by using UV spectroscopy and white-light polarimetry of the extended corona and (2) to relate the IHS in-situ measurements to the large-scale density structures imaged with a white-light coronagraph whose field of view extends to 0.3 AU. Because NES will be very similar to recent solar remote sensing missions, specific spacecraft bus options were not studied in detail. The emphasis instead was placed on instrument studies aimed at extending UV spectroscopic coronagraph and white-light coronagraph capabilities. A Smithsonian Astrophysical Observatory team studied improvements for a spectrographic coronagraph, and a Naval Research Laboratory team investigated white-light coronagraph implementations. The results of these engineering feasibility studies are summarized below.

5.2.1 Orbit Design. The NES measurement requirements can be satisfied from a TRACE-like 650 km altitude, Sun-synchronous orbit that allows nearly continuous observations without the additional costs associated with a mission in geostationary orbit or in orbit at L1. Such orbits are routinely calculated and executed for NASA missions.

5.2.2 Instrumentation. The primary instruments on the NES are the UV Spectroscopic Coronagraph

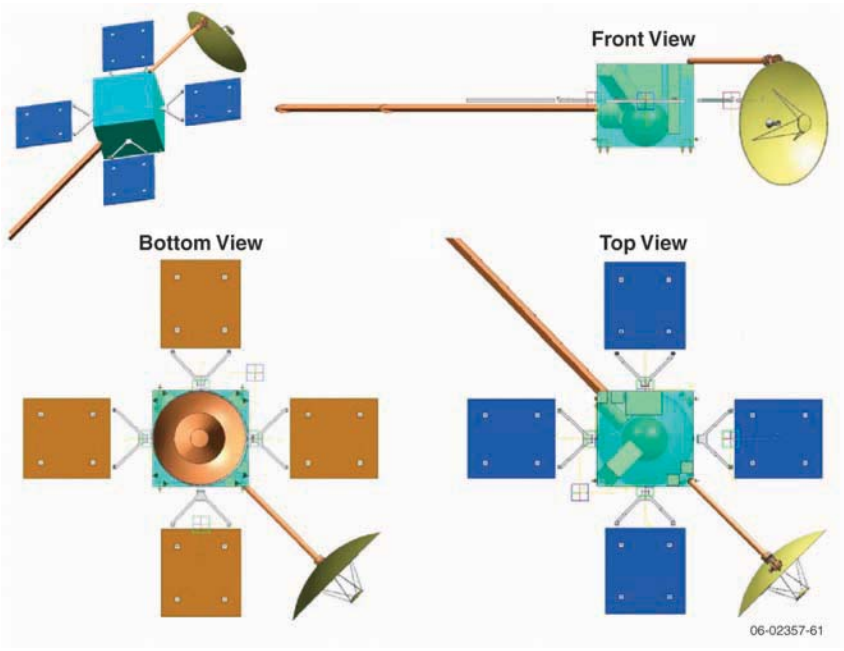

Figure 5-2. Possible FSS spacecraft configuration.

(UVSC) and the Wide- and Inner-Field Coronagraph (WIFCO). UVSC is a large-aperture, high-sensitivity spectroscopic coronagraph to characterize the coronal source regions of SEPs (including CME shocks and/or current sheets) and CMEs. It uses a linear occulter at the end of a 13-m boom to provide a sufficiently large unvignetted collection aperture. The large-aperture telescope mirrors and improved mirror coatings for UVSC will provide up to 2 orders of magnitude higher sensitivity and a wider spectral range than UVCS on SOHO. This will allow the determination of line profiles for atoms and ions of many different charge-to-mass ratios, including helium, thus providing proton and minor ion velocity distributions (thermal and non-Maxwellian) as well as bulk velocities along the line of sight. UVSC will have a high enough cadence to describe the evolution of fast CME events with a spatial resolution of at least 5 arcsec.

WIFCO comprises the Wide-Field Coronagraph (WFC) and Inner-Field Coronagraph (IFC). The requirement for the WFC is to detect CMEs and shocks to ~60 R_S from Sun disk center. The temporal resolution should be sufficient to track these structures, requiring a cadence of ~2 min inside 6 R_S but increasing to ~20 min at 60 R_S. Engineering studies have established that such a telescope is feasible by expanding the entrance aperture diameter of a SOHO/LASCO/C3-like coronagraph to 21 mm. WFC will employ a 4096×4096 CCD with 3-s exposure times that can be integrated onboard for larger radial distances from the Sun. The instrument would have a mass less than 15 kg and produce 230 kbps without compression.

The IFC will make white-light observation of the lower corona in order to image the initiation and early evolution of shocks and CMEs. This dedicated corongraph will be used to detect density structures down to ~1.3 R_S, rather than requiring a compromised WFC to do it. A classical Lyot coronagraph will be able to detect the required CME and shock density signatures in the electron-scattered corona (or K-corona), with a simple and compact instrument operating with a broad passband in the visible region of the spectrum where the K-corona signal peaks. Internal occultation is required to achieve high spatial resolution near the inner field limit (~1.3 R_S). For a compact instrument, this type of occultation limits the outer field cutoff to about 4 R_S due to the scatter of solar disk light by the objective into the coronal image. Thus the inner field limit requirement on the WFC can be relaxed to around 3 R_S, simplifying the design of that instrument. This provides sufficient overlap between the IFC and WFC field of views to allow continuous tracking of density structures from ~1.3 to ~60 R_S. The IFC design has a strong heritage from the STEREO/SECCHI/COR1 coronagraph and would provide better than 10 arcsec of spatial resolution with 1-min cadence.

The long boom required by the UVSC instrument provides a unique opportunity to include an optional high-resolution, large-aperture visible light coronagraph (VLC) in place of the IFC. The externally occulted VLC can provide polarized brightness images of the corona from 1.2 to 10 R_S with "eclipse-like" clarity, i.e., with 5-arcsec spatial resolution in both radial and tangential directions. It can obtain images of coronal density structures and determine CME bulk flows with a 10-s cadence.

The instrument feasibility studies summarized above demonstrate that all NES instruments involve mature designs and can be built using current technology.

5.2.3 Spacecraft Bus Design. Because the NES will fly in a standard low Earth orbital environment and has no unusual resource requirements, the Sentinels STDT did not undertake a detailed study of the NES spacecraft bus. NES can be implemented with currently available spacecraft buses.

6.0 References

Amari, T., et al., Coronal mass ejections: initiation, magnetic helicity, and flux ropes. I. Boundary motion-driven evolution, *Astrophys. J.*, **595**, 1231, 2003.

Antiochos, S. K., The magnetic topology of solar eruptions, *Astrophys. J.*, **502**, 181, 1998.

Antiochos, S. K., R. B. Dahlburg, and J. A. Klimchuk, The magnetic field of solar prominences, *Astrophys. J*., **420**, L41, 1994.

Antiochos, S. K., C. R. DeVore, and J. A. Klimchuk, A model for solar coronal mass ejections, *Astrophys. J.,* **510**, 485, 1999.

Bale, S. D., et al., The source region of an interplanetary type II radio burst, *Geophys. Res. Lett.*, **26**, 1573, 1999.

Bale, S. D., et al., Measurement of the electric fluctuation spectrum of magnetohydrodynamic turbulence, *Phys. Rev. Lett.,* **94**, doi:10.1103/PhysRevLett.94.215002, 2005.

Bemporad, A., et al., A new variety of coronal mass ejection: streamer puffs from compact ejective flares, *Astrophys. J.*, **635**, L189, 2005.

Bieber, J. W., et al., Energetic particle observations during the 2000 July 14 solar event, *Astrophys. J.*, **567**, 622, 2002.

Bieber, J. W., et al., Spaceship Earth observations of the Easter 2001 Solar Particle Event, *Astrophys. J*., **601**, L103, 2004.

Bonaccini, D., Infrared imaging filter with lithium niobate double channel Fabry Perot interferometer, *NOAO Preprint 179*, 1988.

Bothmer, V., and D. M. Rust, The field configuration in magnetic clouds and the solar cycle, in: *Coronal Mass Ejections*, Geophysical Monograph 99, eds. N. U. Crooker, J. A. Joselyn, and J. Feynman, p. 139, American Geophysical Union, Washington D.C., 1997.

Brueckner, G. E., et al., The Large Angle Spectroscopic Coronagraph (LASCO), *Solar Phys*., **162**, 357, 1995.

Brueckner, G. E., et al., Geomagnetic storms caused by coronal mass ejections (CMEs): March 1996 through June 1997, *Geophys. Res. Lett.*, **25**, 3019, 1998.

Burlaga, L. F., et al., A magnetic cloud containing prominence material, *J. Geophys. Res.*, **103**, 277, 1998.

Burlaga, L. F., et al., Fast ejecta during the ascending phase of solar cycle 23: ACE observations, 1998-1999, *J. Geophys. Res.*, **106**, 20,957, 2001.

Burlaga, L. F., S. P. Plunkett, and O. C. St. Cyr, Successive CMES and complex ejecta, *J. Geophys. Res.*, **107**, doi:10.1029/2001JA000225, 2002.

Cacciani, A., and M. Fofi, The magneto-optical filter. II. Velocity field measurements, *Solar Phys.*, **59**, 179, 1979.

Cane, H. V., Near-relativistic solar electrons and type III radio bursts, *Astrophys. J.*, **598**, 1403, 2003.

Cane, H. V., and W. C. Erickson, Energetic particle propagation in the inner heliosphere as deduced from low-frequency (<100 kHz) observations of type III radio bursts, *J. Geophys. Res.*, **108**, 1203, 2003.

Cane, H. V., et al., Two components in major solar particle events, *Geophys. Res. Lett.*, **30**, 8017, doi:10.1029/2002GL016580, 2003.

Cane, H. V., et al., The roles of flares and shocks in detemining SEP abundances, *J. Geophys. Res.*, in press, 2006.

Cargill, P., On the aerodynamic drag force acting on interplanetary coronal mass ejections, *Solar Phys*., **221**, 135, 2004.

Cargill, P. J., and J. M. Schmidt, Modelling interplanetary CMES using magnetohydrodynamic simulations, *Ann. Geophys.*, **20**, 879, 2002.

Cohen, C. M. S., et al., New observations of heavy-ion-rich solar particle events from ACE, *Geophys. Res. Lett.*, **26**, 2697, 1999.

Cohen, C. M. S., et al., Heavy ion abundances and spectra from the large solar energetic particle events of October–November 2003, *J. Geophys. Res.*, **110**, A09S16, doi: 10.1029/2005JA011004, 2005.

Coles, W. A., The solar wind density spectrum near the Sun: Results from Voyager radio measurements, *J. Geophys. Res*., **96**, 1745, 1991.

Crooker, N. U., Solar and heliospheric geoeffective disturbances, *JASTP*, **62**, 1071, 2000.

Crooker, N. U., Filament eruptions in CMEs and implications for ICMEs, *Presentation at SHINE 2004*, June 27–July 2, 2004, Big Sky, MN.

Crooker, N. U., and E. W. Cliver, A postmodern view of M-regions, *J. Geophys. Res.*, **99**, 23,383, 1994.

Crooker, N. U., and A. H. McAllister, Transients associated with recurrent storms, *J. Geophys. Res.*, **102**, 14,0041, 1997.

Crooker, N. U., J. T. Gosling, and S. W. Kahler, Reducing heliospheric magnetic flux from coronal mass ejections without disconnection, *J. Geophys. Res.*, **107**, 10.1029/2001JA000236, 2002.

Daibog, E. I., Statistical properties of SEP event flux declines, *Adv. Space Res.*, **32**, 2655, 2003.

Dalla, S., et al., Properties of high heliolatitude solar energetic particle events and constraints on models of acceleration and propagation, *Geophys. Res. Lett.*, **30**, ULY 9-1 doi:10.1029/2003GL17139, 2003.

DeVore, C. R., and S. K. Antiochos, Dynamical formation and stability of helical prominence magnetic fields, *Astrophys. J.*, **539**, 954, 2000.

Dikpati, M., et al., Predicting the strength of solar cycle 24 using a flux-transport dynamo-based tool, *Geophys. Res. Lett.*, **33**, doi: 10.1029/2005GL025221, 2006.

Fisk, L. A., et al., Ubiquitous statistical acceleration in the solar wind, in: *Acceleration and Transport of Energetic*

Particles Observed in the Heliosphere: Proceedings of the ACE-2000 Symposium, January 5–8, 2000, Indian Wells, CA, AIP Conference Proceedings 528, eds. R. A. Mewaldt et al., p. 229, AIP Publishing Services, Melville, NY, 2000.

Forbes, T. G., Review on the genesis of coronal mass ejections, *J. Geophys. Res.,* **105**, 23,153, 2000.

Forbes, T. G., and P. A. Isenberg, A catastrophe mechanism for coronal mass ejections, *Astrophys. J.*, **373**, 294, 1991.

Forbush, S. E., Three unusual cosmic-ray increases possibly due to charged particles from the Sun, *Phys. Rev*., **70**, 771, 1946.

Giacalone, J., J. R. Jokipii, and J. E. Mazur, Small-scale gradients and large-scale diffusion of charged particles in the Heliospheric magnetic field, *Astrophys. J.*, **532**, L75, 2000.

Gibson, S. E., et al., The calm before the storm: the link between quiescent cavities and coronal mass ejections, *Astrophys. J.*, **641**, 590, 2006.

Gloeckler, G., Ubiquitous suprathermal tails on the solar wind and pickup ion distributions, in: Solar Wind 10, *AIP Conf. Proc. 679*, eds. M. Velli, R. Bruno, and F. Malara, p. 583, AIP Publishing Services, Melville, NY, 2003.

Gloeckler, G., et al., Elemental composition of the inner source pickup ions, *J. Geophys. Res.*, **105**, 7459, 2000.

Goldstein, M. L., D. A. Roberts, and W. H. Matthaeus, Magnetohydrodynamic turbulence in the solar wind, *Ann. Rev. Astron. Astrophys.*, **33**, 283, 1995.

Gonzalez-Esparza, A., A. Santillan, and J. Ferrer, A numerical study of the interaction between two ejecta in the interplanetary medium: One-and two-dimensional hydrodynamic simulations, *Ann. Geophys.*, **22**, 3741, 2004.

Gopalswamy, N., et al., On the relationship between coronal mass ejections and magnetic clouds, *Geophys. Res. Lett.*, **25**, 2485, 1998.

Gopalswamy, N., et al., Interplanetary acceleration of coronal mass ejections, *Geophys. Res. Lett.*, **27**, 145, 2000.

Gopalswamy, N., et al., Near-Sun and near-Earth manifestations of solar eruptions, *J. Geophys. Res.*, **106**, 25,261, 2001a.

Gopalswamy, N., et al., Characteristics of coronal mass ejections associated with long-wavelength type II radio bursts, *J. Geophys. Res.*, **106**, 29,219, 2001b.

Gopalswamy, N., et al., Radio signatures of coronal mass ejection interaction: Coronal mass ejection cannabalism? *Astrophys. J.*, **548**, L91, 2001c.

Gopalswamy, N., et al., Interacting coronal mass ejections and solar energetic particles, *Astrophys. J.*, **572**, L103, 2002.

Gopalswamy, N., et al., Intensity variation of large solar energetic particle events associated with coronal mass ejections, *J. Geophys. Res.*, **109**, A12105, doi:10.1029/2004JA010602, 2004.

Gopalswamy, N., et al., Coronal mass ejections and ground level events, in: *Proc., 29th Int. Cosmic Ray Conf.*, August 3–10, Pune, India, 2005a.

Gopalswamy, N., et al., Coronal mass ejections and other extreme characteristics of the 2003 October–November solar eruptions, *J. Geophys. Res.*, **110**, A09S15, doi:10.1029.2004JA010958, 2005b.

Gosling, J. T., The solar flare myth, *J. Geophys. Res.*, **98**, 18,937, 1993.

Gosling, J. T., and V. J. Pizzo, Formation and evolution of corotating interaction regions and their three dimensional structure, *Space Sci. Rev.*, **89**, 21, 1999.

Gosling, J. T., and P. Riley, The acceleration of slow coronal mass ejections in the high-speed solar wind, *Geophys. Res. Lett.*, **23**, 2867, 1996.

Gosling, J.T., et al., Mass ejections from the Sun—A view from SKYLAB, *J. Geophys. Res.*, **79**, 4581, 1974.

Gosling, J. T., et al., A new class of forward-reverse shock pairs in the solar wind, *Geophys. Res. Lett*., **21**, 2271, 1994.

Gosling, J. T., et al., Correlated dispersionless structure in suprathermal electrons and solar energetic ions in the solar wind, *Astrophys. J.*, **614**, 412, 2004.

Graham, J. D., et al., Inference of solar magnetic field parameters from data with limited wavelength sampling, *Solar Phys.*, **208**, 211, 2002

Haggerty, D. K., and E. C. Roelof, Impulsive near-relativistic solar electron events: Delayed injection with respect to solar electromagnetic emission, *Astrophys. J.*, **579**, 841, 2002.

Heras, A. M., et al., The influence of the large-scale interplanetary shock structure on a low-energy particle event, *Astrophys. J.*, **391**, 359, 1992.

Heras, A. M., et al., Low energy particle events: Modeling the influence of the parent interplanetary shock, *Astrophys. J.*, **445**, 497, 1995.

Hovestadt, D., et al., Nuclear and ionic charge distribution particle experiments on ISEE-1 and ISEE-C spacecraft, *IEEE Trans. Geosci. Electron., GE-16*, **3**, 166, 1978.

Hovestadt, D., et al., CELIAS—Charge, Element and Isotope Analysis System for SOHO, *Solar Phys.*, **162**, 441, 1995.

Ho, G. C., et al., Enhanced solar wind $^3He^{2+}$ associated with coronal mass ejections, *Geophys. Res. Lett.*, **27**, 309, 2000.

Illing, R. M. E., and A. J. Hundhausen, Observation of a coronal transient from 1.2 to 6 solar radii, *J. Geophys. Res.*, **90**, 275, 1985.

Isenberg, P. A., On a difficulty with accelerating particles at slow-mode shocks, *J. Geophys. Res.*, **91**, 1699, 1986.

Kaghashvili, E. Kh., G. P. Zank, and G. M. Webb, Propagation of energetic charged particles in the solar wind:

Effects of intermittency in the medium, *Astrophys. J.*, **636**, 1145, 2006.

Kahler, S. W., Injection profiles of solar energetic particles as functions of coronal mass ejection heights, *Astrophys. J.*, **428**, 837, 1994.

Kahler, S. W., The correlation between solar energetic particle peak intensities and speeds of coronal mass ejections: Effects of ambient particle intensities and energy spectra, *J. Geophys. Res.*, **106**, 20,947, 2001.

Kahler, S. W., Energetic particle acceleration by coronal mass ejections, *Adv. Space Res.*, **32**, 2587, 2003.

Kahler, S. W., Solar fast-wind regions as sources of shock energetic particle production, *Astrophys. J.*, **603**, 330, 2004.

Kahler, S. W., The 20 January 2005 energetic particle event as a test of current models, *AGU Fall Meeting 2005*, abstract #SH21A-07, 2005a.

Kahler, S. W., Characteristic times of gradual solar energetic particle events and their dependence on associated coronal mass ejection properties, *Astrophys. J.*, **628**, 1014, 2005b.

Kahler, S. W., and D.V. Reames, Solar energetic particle production by coronal mass ejection-driven shocks in solar fast-wind regions, *Astrophys. J.*, **584**, 1063, 2003.

Kahler, S. W., and A. Vourlidas, Fast coronal mass ejection environments and the production of solar energetic particle events, *J. Geophys. Res.*, **110**, A12S01, doi:10.1029/2005JA011073, 2005.

Kahler, S. W., et al., Associations between coronal mass ejections and solar energetic proton events, *J. Geophys. Res.*, **89**, 9683, 1984.

Kallenrode, M.-B., and E. W. Cliver, Rogue SEP events: modeling, in: *Proc., 27th Int. Cosmic Ray Conf.,* August 7–15, 2001, Hamburg, Germany, p. 3318, 2001.

Kallenrode, M.-B., and G. Wibberenz, Particle injection following solar flares on 1980 May 28 and June 8: Evidence for different injection time histories in impulsive and gradual events? *Astrophys. J.*, **376**, 787, 1991.

Kallenrode, M.-B., and G. Wibberenz, Propagation of particles injected from interplanetary shocks: A black box model and its consequences for acceleration theory and data interpretation, *J. Geophys. Res.*, **102**, 22,311, 1997.

Kellogg, P. J., Fluctuations and ion isotropy in the solar wind, *Astrophys. J.*, **528**, 480, 2000.

Klecker, B., et al., Observation of energy-dependent ionic charge states in impulsive solar energetic particle events, *Adv. Space Res.*, in press, 2006.

Klein, K.-L., et al., Coronal phenomena at the release of solar energetic electron events, *Astron.Astrophys.*, **432**, 1047, 2005.

Klimchuk, J. A., Coronal mass ejections, in: *Space Weather*, Geophysical Monograph 125, eds. P. Song, G. Siscoe, and H. Singer, p. 143, American Geophysical Union, Washington D.C., 2001.

Knock, S. A., I. H. Cairns, and P. A. Robinson, Type II radio emission predictions: Multiple shocks ripples and dynamic spectra, *J. Geophys. Res.*, **108**, doi: 10.1029/2003JA009960, 2003.

Kohl, J. L., et al., Ultraviolet spectroscopy of the extend solar corona, *Astron. Astrophys. Rev.*, doi: 10.1007/s00159-005-0026-7, 2006.

Koutchmy, S., et al., The August 11th, 1999 CME, *Astron. Astrophys.*, **420**, 709, 2004.

Krucker, S., et al., On the origin of impulsive electron events observed at 1 AU, *Astrophys. J.*, **519**, 864, 1999.

Laivola, J., J. Torsti, and K. Kocharov, A statistical study of ^{3}He enhancement in the high energy solar particles, in: *Proceedings of the 28th International Cosmic Ray Conference,* July 31–August 7, 2003, Trukuba, Japan, eds. T. Kajita et al., 3305, 2003.

Lario, D., B. Sanahuja, and A. M. Heras, Energetic particle events: Efficiency of interplanetary shocks as 50 keV < E <100 MeV proton accelerators, *Astrophys. J.*, **509**, 415, 1998.

Lario, D., et al., Radial and longitudinal dependence of solar 4–13 MeV and 27–37 MeV proton peak intensities and fluences: Helios and IMP-8 observations, submitted to *Astrophys. J.*, 2006.

Larson, D. E., et al., Using energetic electrons to probe the topology of the October 18–20, 1995 magnetic cloud, *Adv. Space Res.*, **20**, 655, 1997.

Leamon, R. J., et al., Observational constraints on the dynamics of the interplanetary magnetic field dissipation range, *J. Geophys. Res.*, **103**, 4775, 1998.

Leamon, R. J., R. C. Canfield, and A. A. Pevtsov, Properties of magnetic clouds and geomagnetic storms associated with eruption of coronal sigmoids, *J. Geophys. Res.*, **107**, SSH 1-1, doi:10.1029/2001JA000313, 2002.

Lee, M. A., Coupled hydrodynamic wave excitation and ion acceleration at interplanetary shocks, *J. Geophys. Res.*, **88**, 6109, 1983.

Lee, M. A., Particle acceleration and transport at CME-driven shocks, in*: Coronal Mass Ejections*, Geophysical Monograph 99, eds. N. Crooker, J. A. Joselyn, and J. Feynman, p. 227, American Geophysical Union, Washington D.C., 1997.

Lee, M. A., Acceleration of energetic particles on the Sun, in the Heliosphere, and in the Galaxy, in: *Acceleration and Transport of Energetic Particles Observed in the Heliosphere: Proc., ACE-2000 Symp.,* January 5–8, 2000, Indian Wells, CA, AIP Conf. Proc. 528, eds. R.A. Mewaldt et al., p. 3, AIP Publishing Services, Melville, NY, 2000.

Lee, M. A., Coupled hydromagnetic wave excitation and ion acceleration at an evolving corona/interplanetary shock, *Astrophys. J. Supp.*, **158**, 38, 2005.

Lepping, R. P., J. A. Jones, and L. F. Burlaga, Magnetic field structure of interplanetary magnetic clouds at 1 AU, *J. Geophys. Res.*, **95**, 11,957, 1990.

Lepri, S. T., et al., Iron charge distribution as an identifier of interplanetary coronal mass ejections, *J. Geophys. Res.*, **106**, 29,231, 2001.

Li, G., and G. P. Zank, Mixed particle acceleration at CME-driven shocks and flares, *Geophys. Res. Lett.*, **32**, L02101, doi:10.1029/2004GL021250, 2005.

Li, G., G. P. Zank, and W. K. M. Rice, Energetic particle acceleration and transport at coronal mass ejection-driven shocks, *J. Geophys. Res.*, **108**, SSH 10-1 doi 10.1029/2002JA009666, 2003.

Li, G., G. P. Zank, and W. K. M. Rice, Acceleration and transport of heavy ions at coronal mass ejection-driven shocks, *J. Geophys. Res.*, **110**, A06104, doi:10.1029/2004JA010600, 2005a.

Li, G., et al., Particle acceleration and transport at coronal eass ejection-driven (CME-driven) shocks: A case study, in: *Particle Acceleration in Astrophysical Plasmas: Geospace and Beyond*, Geophysical Monograph Series 156, eds. D. L. Gallagher et al., American Geophysical Union, Washington D.C., 2005b.

Lin, J., and T. G. Forbes, Effects of reconnection on the coronal mass ejection process, *J. Geophys. Res.*, **105**, 2375, 2000.

Lin, R. P., Energetic solar electrons in the interplanetary medium, *Solar Phys*., **100**, 537, 1985.

Lin, R. P., et al., Energetic electrons and plasma waves associated with a solar type III radio burst, *Astrophys. J.*, **251**, 364, 1981.

Linker, J. A., et al., Models of coronal mass ejections: A review with a look to the future, in: *Solar Wind Ten: Proc., Tenth Int. Solar Wind Conf.*, AIP Conference Proceedings, Vol. 679, p. 703, 2003.

Liu, Y., and K. Hayashi, The 2003 October–November fast halo coronal mass ejections and the large-scale magnetic field structures, *Astrophys. J.*, **640**, 1135, 2006.

Low, B. C., Magnetohydrodynamic processes in the solar corona: Flares, coronal mass ejections, and magnetic helicity, *Phys. Plasmas*, **1**, 1684, 1994.

Low, B. C., Coronal mass ejections, magnetic flux ropes, and solar magnetism, *J. Geophys. Res.*, **106**, 25,141, 2001.

Lugaz, N., W. B. Manchester, IV, and T. I. Gombosi, Numerical simulation of the interaction of two coronal mass ejections from Sun to Earth, *Astrophys. J.*, **634**, 651, 2005.

Lynch, B. J., et al., Observable properties of the breakout model for coronal mass ejections, *Astrophys. J.*, **617**, 589, 2004.

Maia, D. J. F., and M. Pick, Revisiting the origin of impulsive electron events: Coronal magnetic restructuring, *Astrophys. J.*, **609**, 1082, 2004.

Manchester, W. B. IV, et al., Coronal mass ejection shock and sheath structures relevant to particle acceleration, *Astrophys. J.*, **622**, 1225, 2005.

Mancuso, S., et al., UVCS/SOHO observations of a CME-driven shock: Consequences on heating mechanisms behind a coronal shock, *Astron. Astrophys.*, **383**, 267, 2002.

Mancuso, S., et al., Plasma properties above coronal active regions inferred from SOHO/UVCS and radio spectrograph observations, *Astron. Astrophys.*, **400**, 347, 2003.

Mann, G., et al., Formation and development of shock waves in the solar corona and the near-Sun interplanetary space, *Astron. Astrophys.,* **400**, 329, 2003.

Manoharan, P. K., et al., Influence of coronal mass ejection interaction on propagation of interplanetary shocks, *J. Geophys. Res.*, **109**, A06109, doi:10.1029/2003JA010300, 2004.

Marubashi, K., Interplanetary magnetic flux ropes and solar filaments, in: *Coronal Mass Ejections*, Geophysical Monograph 99, eds. N. U. Crooker, J. A. Joselyn and J. Feynman, p. 147, American Geophysical Union, Washington D.C., 1997.

Mason, G. M., J. E. Mazur, and J. R. Dwyer, ^{3}He enhancements in large solar energetic particle events, *Astrophys. J.*, **525**, L133, 1999.

Mason, G. M., J. R. Dwyer, and J. E., Mazur, New properties of ^{3}He-rich flares deduced from low energy particle spectra, *Astrophys. J.*, **545**, L157, 2000.

Mason, G. M., et al., Energetic particles accelerated by shocks in the heliosphere: What is the source material? in: *The Physics of Collisionless Shocks: 4th Ann. Int. Astrophy. Conf.*, eds. G. Li, G. P. Zank, and C. T. Russell, AIP Conference Proceedings 781, p. 219, AIP Publishing Services, Melville, NY, 2005.

Mazur, J. E., et al., Interplanetary magnetic field line mixing deduced from impulsive solar flare particles, *Astrophys. J.*, **532**, L79, 2000.

McComas, D. J., et al., Ulysses' return to the slow solar wind, *Geophys. Res. Lett.*, **25**, 1, 1998.

McKibben, R. B., et al., Simultaneous observations of solar energetic particle events by IMP8 and the Ulysses COSPIN high energy telescope at high solar latitudes, *Space Sci. Rev.*, **20**, 257, 2001.

Mewaldt, R. A., et al., Impulsive flare material: A seed population for large solar particle events? in: *Proc., 28th Int. Cosmic Ray Conf.,* July 31–August 7, 2003, Trukuba, Japan, eds. T. Kajita, et al., p. 3229, 2003.

Mewaldt, R. A., et al., The source material for large solar energetic particle events, Presentation at the *AGU Chapman Conf. on Solar Energetic Plasmas and Particles*, August 2–6, 2004, Turku, Finland, 2004.

Mewaldt, R. A., et al., Solar-particle energy spectra during the large events of October–November 2003 and January 2005, in: *Proc., 29th Int. Cosmic Ray Con.,* August 3–10, Pune, India, 2005a.

Mewaldt, R. A., et al., Proton, helium, and electron spectra during the large solar particle events of October–November 2003, *J. Geophys. Res.*, **110**, A09S18, doi: 10.1029/2005JA011038, 2005b.

Mewaldt, R. A., et al., The source material for large solar energetic particle events, in: *Solar Eruptions and Energetic Particles*, Geophysical Monograph Series, eds. N. Gopalswamy, R. A. Mewaldt, and J. Torsti, in press, American Geophysical Union, Washington, D.C., 2006.

Michalek, G., et al., Arrival time of halo coronal mass ejections in the vicinity of the Earth, *Astron. Astrophys.*, **423**, 729, 2004.

Miller, J. A, et al., Critical issues for understanding particle acceleration in impulsive solar flares, *J. Geophys. Res.*, **102**, 14,631, 1997.

Moore, R. L., et al., Onset of the magnetic explosion in solar flares and coronal mass ejections, *Astrophys. J.*, **552**, 833, 2001.

Mulligan, T., and C. T. Russell, Multispacecraft modeling of the flux rope structure of interplanetary coroanl mass ejections: cylindrically symmetric versus nonsymmetric topologies, *J. Geophys. Res.*, **106**, 10,581, 2001.

Murphy, N., et al., Chromospheric observation in the helium 1083 nm line: A new instrument, in: *Proc., Conf. Solar Wind 11—SOHO 16,* Connecting the Sun and Heliosphere*,* June 12–17, 2005, Whistler, Canada, ed. H. Lacoste, ESA SP-592, 2005.

NASA, *The Vision for Space Exploration*, p. 5, NP 2004-01-334-HQ, February 2004.

NASA, *Solar Probe: Report of the Science and Technology Definition Team*, Tech. Memo. 2005-212786, NASA Goddard Space Flight Center, Greenbelt, MD, 138 pp., 2005.

Ng, C. K., D. V. Reames, and A. J. Tylka, Effect of proton-amplified waves on the evolution of solar energetic particle composition in gradual events, *Geophys. Res. Lett.*, **26**, 2145, 1999.

Ng, C. K., D. V. Reames, and A. J. Tylka, Modeling shock-accelerated solar energetic particles coupled to interplanetary Alfvén waves, *Astrophys. J.*, **591**, 461, 2003.

NOAA, *NOAA Service Assessment: Intense Space Weather Storms October 19–November 7, 2003*, U.S. Dept. of Commerce, Washington, D.C., April 2004.

Odstrcil, D. and V. J. Pizzo, Three-dimensional propagation of coronal mass ejections (CMEs) in a structured solar wind flow, 1. CME launched within the streamer belt, *J. Geophys. Res.*, **104**, 483, 1999a.

Odstrcil, D., and V. J. Pizzo, Three-dimensional propagation of coronal mass ejections in a structured solar wind flow 2. CME launched adjacent to the streamer belt, *J. Geophys. Res.*, **104**, 493–504, 1999b.

Odstrcil, D., and V. J. Pizzo, The distortion of the interplanetary magnetic field by three-dimensional propagation of coronal mass ejections in a structured solar wind flow, *J. Geophys. Res.*, **104**, 28,225, 1999c.

Odstrcil, D., et al., Merging of coronal and heliospheric numerical two-dimensional models, *J. Geophys. Res.*, **107**, SSH 14-1, doi:10.1029/2002JA009334, 2002.

Odstrcil, D., P. C. Riley, and X. P. Zhao, Numerical simulation of the 12 May 1997 interplanetary CME event, *J. Geophys. Res.*, **109**, doi:10.1029/2003JA010135, 2004.

Palmer, I. D., Transport coefficients of low-energy cosmic rays in interplanetary space, *Rev. Geophys.*, **20**, 335, 1982.

Plunkett, S. P., et al., Simultaneous SOHO and ground-based observations of a large eruptive prominence and coronal mass ejection, *Solar Phys.*, **194**, 371, 2000.

Ragot, B. R., On the quasi-linear transport of magnetic field lines, *Astrophys. J.*, **525**, 524, 1999.

Raymond, J. C., Spectroscopic diagnostics of CME material, in: *SOHO-11 Symp.: From Solar Min to Max: Half a Solar Cycle with SOHO*, ESA SP-508, ed. A. Wilson, p. 421, ESA Noordwijk, 2002.

Raymond, J. C., et al., SOHO and radio observations of a CME shock wave, *Geophys. Res. Lett.*, **27**, 1439, 2000.

Reames, D. V., Solar energetic particles: A paradigm shift, *Rev. Geophys. Supp.,* U.S. National Report to IUGG 1991–1994, 585–589, 1995.

Reames, D. V., Solar energetic particles: sampling coronal abundances, *Space Sci. Rev.*, **85**, 327, 1998.

Reames, D. V., Particle acceleration by CME-driven shock waves, in: *Invited, Rapporteur, and Highlight Papers of the 26th ICRC (Salt Lake City)*, eds. B. L. Dingus, D. B. Kieda, and M. H. Salamon, AIP Conf. Proc. 516, p. 289, 2000.

Reames, D. V., Magnetic topology of impulsive and gradual solar energetic particle events, *Astrophys. J.*, **571**, L63, 2002.

Reames, D. V., and C. K. Ng, Streaming-limited intensities of solar energetic particles, *Astrophys. J.*, **504**, 1002, 1998.

Reames, D. V., T. T. von Rosenvinge, and R. P. Lin, Solar ^{3}He-rich events and non-relativistic electron events: a new association, *Astrophys. J.*, **292**, 716, 1985.

Rice, W. K. M., G. P. Zank, and G. Li, Particle acceleration and coronal mass ejection driven shocks: shocks of arbitrary strength, *J. Geophys. Res.*, **108**, SSH 5-1, doi:10.1029/2002JA009756, 2003.

Richardson, I. G., and H. V. Cane, The fraction of interplanetary coronal mass ejections that are magnetic clouds: Evidence for solar cycle variation, *Geophys. Res. Lett.*, **31**, L18804, doi:10.1029/2004GL020958, 2004.

Richardson, I. G., et al., Quiet-time properties of low-energy (<10 MeV per nucleon) interplanetary ions during solar maximum and solar minimum, *Astrophys. J.*, **363**, L9, 1990.

Richardson, I. G., et al., Are CME "interactions" really important for accelerating major solar energetic

particle events? *Geophys. Res. Lett.*, **30**, 8014, doi:10.1029/2003GL017277, 2003.

Richardson, J. D., and C. Wang, Voyager observations of interplanetary shocks, in: *The Physics of Collisionless Shocks: 4th Annual International Astrophysics Conference*, eds. G. Li, G. P. Zank, and C. T. Russell, AIP Conference Proceedings 781, p. 278, AIP Publishing Services, Melville, NY, 2005.

Richter, A. K., Interplanetary slow shocks, in: *Physics of the Inner Heliosphere II*, eds. R. Schwenn and E. Marsch, Springer Verlag, p. 23, 1991.

Riley, P., and N. U. Crooker, Kinematic treatment of coronal mass ejection evolution in the solar wind, *Astrophys. J.*, **600**, 1035, 2004.

Riley, P., J. A. Linker, and Z. Mikic, An empirically driven global MHD model of the solar corona and inner heliosphere, *J. Geophys. Res.*, **106**, 15,889, 2001.

Roberts, D. A., et al., Origin and evolution of fluctuations in the solar wind: Helios observations and Helios-Voyager comparisons, *J. Geophys. Res.*, **92**, 12,023, 1987.

Roberts, D. A., et al., Velocity shear generation of solar wind turbulence, *J. Geophys. Res.*, **97**, 17115, 1992.

Rosenbauer, H., et al., A survey on initial results of the HELIOS plasma experiment, *J. Geophys. Res.*, **42**, 561, 1977.

Roussev, I. I., et al., A three-dimensional model of the solar wind incorporating solar magnetogram observations, *Astrophys. J.*, **595**, L57, 2003.

Roussev, I. I., et al., A numerical model of a coronal mass ejection: Shock development with implications for the acceleration of GeV protons, *Astrophys. J.*, **605**, 73, 2004.

Ruffolo, D., W. H. Matthaeus, and P. Chuychai, Trapping of solar energetic particles by the small-scale topology of solar-wind turbulence, *Astrophys. J.*, **597**, L169, 2003.

Ruffolo, D., et al., Relativistic solar protons on 1989 October 22: Injection and transport along both legs of a closed magnetic loop, *Astrophys. J.*, **639**, 1186, 2006.

Rust D. M., et al., A tunable, solid, Fabry-Perot ETALON for solar seismology, in*:* Instrumentation in Astronomy VI, *SPIE Proc., 627*, p. 39, 1986.

Rust, D. M., et al., Comparison of interplanetary disturbances at the NEAR spacecraft with coronal mass ejections at the Sun, *Astrophys. J.*, **621**, 524, 2005.

Ruzmaikin, A., S. Martin, and Q. Hu, Signs of magnetic helicity in interplanetary coronal mass ejections and associated prominences: Case study, *J. Geophys. Res.*, **108**, doi:10.1029/2002JA009588, 2003.

Saiz, A., et al., Relativistic particle injection and interplanetary transport during the January 20, 2005 ground level enhancement, in: *Proc., 29th Int. Cosmic Ray Conf.,* August 3–10, 2005, Pune, India, 2005a.

Saiz, A., et al., On the estimation of solar energetic particle injection timing from onset times near Earth, *Astrophys. J.*, **626**, 1131, 2005b.

Schwenn, R., Large-scale structure on the interplanetary medium, in: *Physics of the Inner Heliosphere I*, eds. R. Schwenn and E. Marsch, p. 99, Springer Verlag, Berlin, Germany, 1990.

Schwenn, R., et al., The association of coronal mass ejections with their effects near the Earth, *Ann. Geophys.*, **23**, 1033, 2005.

Sheeley, N. R. Jr., et al., Coronal mass ejections and interplanetary shocks, *J. Geophys. Res.*, **90**, 163, 1985.

Shimojo, M., and K. Shibata, Physical parameters of solar X-ray jets, *Astrophys. J.*, **542**, 1100, 2000.

Shodan, S., et al., Counterstreaming electrons in magnetic clouds, *J. Geophys. Res.*, **105**, 27,261, 2000.

Simnett, G. M., The timing of relativistic proton acceleration in the 20 January 2005 flare, *Astron. Astrophys.*, **445**, 715, 2006.

Simnett, G. M., E. C. Roelof, and D. K. Haggerty, The acceleration and release of near-relativistic electrons by coronal mass ejections, *Astrophys. J.*, **579**, L854, 2002.

Snyder, C. W., M. Neugebauer, and U. R. Rao, The solar wind velocity and its correlation with cosmic-ray variations and with solar and geomagnetic activity, *J. Geophys. Res.*, **68**, 6361, 1963.

Steinolfson, R. S., Coronal shock waves, in: *Study of the Solar-Terrestrial System*, ESA SP-346, ESA Publ. Div., ESA Noordwijk, p. 51, 1992.

Szabo, A., Multi-spacecraft observations of interplanetary shocks, in: *The Physics of Collisionless Shocks: 4th Annual International Astrophysics Conference*, eds. G. Li, G. P. Zank, and C. T. Russell, AIP Conference Proceedings 781, p. 37, AIP Publishing Services, Melville, NY, 2005.

Tomczyk, S., et al., An instrument to observe low-degree solar oscillations, *Solar Phys.*, **159**, 1, 1995.

Townsend, L. W., Implications of the space radiation environment for human exploration in deep space, *Radiat. Prot. Dosimetry*, **115**, 44, 2005.

Tu, C.-Y., and E. Marsch, MHD structures, waves, and turbulence in the solar wind: observations and theories, *Space Sci. Rev.*, **73**, 1, 1995.

Tylka, A. J., New insights on solar energetic particles from Wind and ACE, *J. Geophys. Res.*, **106**, 25,333, 2001.

Tylka, A. J., D. V. Reames, and C. K. Ng, Observations of systematic temporal evolution in elemental composition during gradual solar energetic particle events, *Geophys. Res. Lett.*, **26**, 2141, 1999.

Tylka, A. J., et al., Evidence for remnant flare particles in the source population of solar energetic particles in the 2000 Bastille Day event, *Astrophys. J.*, **558**, L59, 2001.

Tylka, A. J., et al., Onsets and release times in solar particle events, in: *Proc., 28th Int. Cosmic Ray Conf.,* July

31–August 7, 2003, Trukuba, Japan, eds. T. Kajita et al., 3305, 2003.

Tylka, A. J., et al., Shock geometry, seed populations, and the origin of variable elemental composition at high energies in large gradual solar particle events, *Astrophys. J.*, **625**, 474, 2005.

Usmanov, A. V., et al., A global MHD solar wind model with WKB Alfvén waves: Comparison with Ulysses data, *J. Geophys. Res.*, **105**, 12,675, 2000.

van Ballegooijen, A. A., and P. C. H. Martens, Formation and eruption of solar prominences, *Astrophys. J.*, **343**, 97, 1989.

Vandas, M., and D. Odstrcil, Acceleration of electrons by interacting CMEs, *Astron. Astrophys.*, **415**, 755, 2004.

Vandas, M., D. Odstrcil, and S. Watari, Simulation of magnetic cloud propagation in three dimensions, in: *Proc., SOLPSA: The Second Solar Cycle and Space Weather Euroconference,* September 24–29, 2001, Vico Equense, Italy, ESA SP-477, p. 293, 2002.

Venkatakrishnan, P., and B. Ravindra, Relationship between CME velocity and active region magnetic energy, *Geophys. Res. Lett.*, **30**, SSC 2-1, doi:10.1029/2003GL018100, 2003.

Vourlidas, A., et al., 2003, Direct detection of a coronal mass ejection-associated shock in Large Angle and Spectrometric Coronagraph experiment white-light images, *Astrophys. J.*, **598**, 1392, 2003.

Vrsnak, B., and N. Gopalswamy, Influence of aerodynamic drag on the motion of interplanetary ejecta, *J. Geophys. Res.*, **107**, 1029, 2002.

Wang, L., et al., Evidence for double injections in scatter-free solar impulsive electron events, *Geophys. Res. Lett.*, **33**, L03106, 2006.

Wang, Y.-M., and N. R. Sheeley, Jr., Coronal white-light jets near sunspot maximum, *Astrophys. J.*, **575**, 542, 2002.

Wang, Y. M., P. Z. Ye, and S. Wang, Multiple magnetic clouds: Several examples during March–April 2001, *J. Geophys. Res.*, **108**, doi:10/1029/2003KA009850, 2003.

Wang, Y.-M., M. Pick, and G. M. Mason, Coronal holes, jets, and the origin of ^{3}He-rich particle events, *Astrophys. J.*, **639**, 495, 2006.

Webb, D. F., The origin and development of the May 1997 magnetic cloud, *J. Geophys. Res.*, **105**, 27,251, 2000.

Webb, G. M., et al., Multidimensional Green's functions and the statistics of diffusive shock acceleration, *Astrophys. J.*, **453**, 178–206, 1995.

Wibberenz, G., and H. V. Cane, Multispacecraft observations of solar flare particles in the inner heliosphere, *Astrophys. J.*, submitted, 2006.

Wiedenbeck, M. E., et al., How common is energetic ^{3}He in the inner heliosphere? *Solar Wind 10*, AIP Conference Proceedings 679, eds. M. Velli, R. Bruno, and F. Malara, p. 652, AIP Publishing Services, Melville, NY, 2003.

Withbroe, G. L., et al., Analysis of coronal H I Lyman alpha measurements from a rocket flight on 1979 April 13, *Astrophys. J.*, **254**, 361, 1982.

Zank, G. P., W. K. M. Rice, and C. C. Wu, Particle acceleration and coronal mass ejection driven shocks: A theoretical model, *J. Geophys. Res.*, **105**, 25079, 2000.

Zank, G. P., et al., Particle acceleration at quasi-perpendicular shock waves: Model and observations, *J. Geophys. Res.*, **111**, A06108, doi:10.1029/2005JA011524, 2006.

Zhang, M., J. R. Jokipii, and R. B. McKibben, Perpendicular transport of solar energetic particles in heliospheric magnetic fields, *Astrophys. J.*, **595**, 493, 2003.

Zurbuchen, T. H. and I. Richardson, In-situ solar wind and magnetic signatures of ICMEs, *Space Sci. Rev.*, in press, 2006.

Appendix A: Inner Heliospheric Sentinels Analyses and Key Trade-Off Studies

1. X-Band HGA Technologies

Detailed mechanical models were developed for several types of antennas to determine the optimum choice based on size, mass, DC power, and ease of implementation. The antennas studied included a paraboloidal solid dish antenna, a parabolic cylinder wire reflector, an electronically scanned flat array, and a mechanically scanned flat array. All antennas were sized to provide the peak gain of a 0.8-m-diameter parabolic dish minus pointing and passive losses. The assumed pointing loss was due to a 0.75° pointing error. All antennas, including associated radomes, had to be compatible with the intense thermal environment of the mission to be considered in the study.

Table A-1 summarizes the findings of the study. An HGA utilizing a paraboloidal solid dish antenna was the heaviest implementation. The mass of this configuration is driven by the mass of the radome and the radome support structure. The radome provides thermal protection and a constant solar pressure as a function of antenna pointing. A similar, although smaller, radome is required for the two flat array antennas.

The parabolic wire cylinder HGA, similar to that flown on Helios, is linearly polarized and therefore has twice the aperture size of the other antennas. This antenna has the highest pointing loss because of the large aperture size, and overcoming this higher pointing loss, in turn, requires increased antenna aperture. Although the parabolic wire cylinder does not require a radome and therefore has the lowest mass by a slight margin, the mass saving is more than offset by the increase in spacecraft structure mass required to accommodate the larger antenna. The parabolic wire cylinder antenna also poses the greatest development risk, as there are no existing X-band antennas of this design.

The two phased array antennas incorporate slotted waveguides similar to those used on the MESSENGER phased array antenna. The electrically steered array uses electronic phase shifters for pointing the beam over the limited range of elevation angles required to maintain Earth contact. The phase shifters, however, must be located down on the despun platform surface for thermal reasons, resulting in 12 transmission paths between the phase shifters and antenna. Each path includes a rotary joint required for gimbaling the antenna into position at the start of the mission.

The mechanically steered phased array requires no phase shifters and is therefore electrically less complicated than the electrically steered antenna. Only two RF transmission paths between the despun platform and the antenna are required (one for each redundant TWTA signal). The mechanically

Table A-1. Summary of technology trade studies for the Inner Heliospheric Sentinels high-gain antenna (HGA).

Antenna Technology	Mass (kg)	Antenna Construction	Bus Power (W)	Net Gain after Pointing Loss and Antenna-Specific Passive Loss (dBic)	Area (m^2)
Paraboloidal dish	34.9	Reflector material is graphite epoxy composite	0.2[a]	33.5	0.5 (0.8-m dia)
Parabolic cylinder (wires)	17.9	Wire material is a platinum-rhodium alloy, wire diameter is 0.2 mm, wire spacing is 2 mm	0.2[a]	33.7	1.56[b] (1.2 × 1.3 m)
Electronically scanned phased array	19.1	Antenna consists of WR90 thin-wall waveguide mounted on an aluminum plate	0.5[c]	33.4	0.36 (0.6 × 0.6 m)
Mechanically scanned phased array	20.1	Same as electronically scanned phased array	0.2[a]	33.7	0.3 (0.55 × 0.55 m)

Notes:
(a) Bus power for elevation angle gimbal electronics.
(b) Size may decrease if future DSN capability includes linear polarization reception to avoid a 3 dB linear-to-circular polarization mismatch loss.
(c) Bus power for electronic phase shifters.

steered array can be designed with passive redundant TWTA inputs. Because of its simpler architecture, low size and mass, and the availability of flight-qualified X-band slotted waveguide array technology, this antenna architecture was chosen as the baseline.

2. X-Band Versus Ka-Band Science Downlink

A detailed study was performed to examine the potential benefit of operating the science downlink at Ka-band (32 GHz) instead of X-band. The potential benefit can be viewed either as a smaller HGA for a given science return or as a higher science return for a given antenna size. A parabolic reflector model was used for this trade study. The Ka-band advantage is measurable in decibels. **Figure A-1** shows the benefit of Ka-band relative to X-band as a function of HGA size and pointing error. For the 1-m-diameter class of HGA being considered for the Inner Heliospheric Sentinels (IHS), the pointing error must be less than 0.3° to enable a significant benefit from Ka-band operation.

A preliminary HGA pointing budget for the IHS spacecraft indicates a worst-case error of 0.8°, which drove our science downlink design to X-band. This pointing error could be improved substantially by placing a star camera on the despun platform; however, the temperature range of the platform currently exceeds that of a star camera, and the field of view from that location may be inadequate. Secondary benefits of an X-band science downlink design include a single-frequency HGA, compatibility with existing space weather ground stations, and overall lower cost relative to Ka-band.

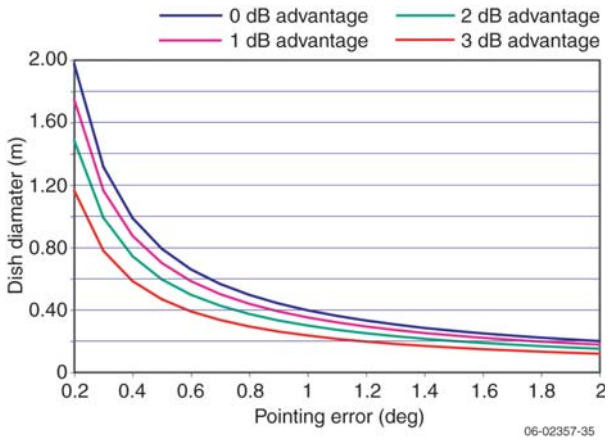

Figure A-1. Ka-band advantage over X-band as a function of pointing error and HGA size.

3. HGA Size Versus DSN Contact Time

The HGA size requirement can be traded off as a function of DSN contact time for a given science return capability. This trade-off is basically one of spacecraft mass (and associated cost) versus Phase E mission operations cost. A deep space aperture costing formula, available on the DSN website effective April l8, 2005, was used for this analysis. **Table A-2** shows the DSN cost as a function of contact frequency assuming that the four IHS spacecraft are tracked separately and independently. The corresponding HGA antenna size was determined through a combination of RF link analysis and detailed science return analysis.

Based on interactions with the DSN Advanced Planning Office, usage of the 34-m antennas at a loading of one to two contacts per spacecraft per week is reasonable for the Sentinels mission. From that information and the information in **Table A-2,** the size of the IHS antenna can be narrowed down to a range of 0.7 to 1 m in diameter. A parabolic reflector model was used for this trade study. To minimize DSN cost and loading, we have adopted a contact frequency of once per week per spacecraft, resulting in the need for an HGA having performance equivalent to that of a 1-m diameter dish (about 36 dB of gain at X-band).

4. ELV Separation Strategy

Spacecraft deployment from the launch vehicle will involve seven separate deployments, one for each of the four spacecraft and three inter-spacecraft structures. Different scenarios were evaluated in making this final decision, as there was a desire to minimize the number of deployments, or at the very least minimize the number of immediate deployments so as to reduce the possibility of contact between the various pieces.

One option involved leaving the inter-spacecraft structure attached to the bottom of each spacecraft. This would reduce the number of deployments to four. Due to thermal considerations, however, the structure would eventually need to be separated from the spacecraft. Thus the question became one of early operations with the structure attached. In this configuration the aft low-gain antenna (LGA),

Table A-2. Deep Space Network usage cost versus high-gain antenna size.

DSN Contacts per Spacecraft each Week	Total DSN Contacts each Week	Yearly Cost ($M)	Parabolic HGA Diameter (m)
0.25	1	0.5	2
0.5	2	1.1	1.4
1	4	2.6	1
2	8	6.7	0.7

Notes:

DSN Assumptions:
- Fiscal year 2005 costs
- Each pass includes 8 hours of science downlink plus 1 hour of pre/post pass calibration.
- 34-m DSN antennas
- Spacecraft are tracked separately and independently
  - Not co-located within beamwidth of the DSN antenna
  - Not tracked sequentially during a pass

RF Link Assumptions
- X-band operation
- 75 W_{RF} (150 W_{DC}) TWTA
- HGA overall efficiency = 55%
- 5 kbps continuous science plus 30% margin returned from each spacecraft.

located on the bottom of the spacecraft, would almost certainly require a deployed boom, adding the undesirable complication of a boom deployment. Moreover, the structure would block the star scanner, and the spacecraft–structure combination may not be a major-axis spinner. Additional analysis and design would be required to resolve the stability question.

A possible resolution to these issues would be to make the inter-spacecraft structure a truss design, potentially alleviating the need for a boom deployment. However, without going into a detailed analysis of this type of design, it was unknown if the LGA could provide enough gain through the structure. It was also questionable as to whether the star scanner field of view would still be partially obstructed, and whether a truss-structure could meet the launch vehicle modal frequency requirements for a stacked configuration.

Leaving the structure attached to the top of a spacecraft was another option considered. This would alleviate issues with the aft LGA and star scanner, but there could still be issues with spin stability (not a major-axis spinner). The structure would eventually still need to be deployed, since the HGA on the top of the spacecraft would be blocked by the structure.

The decision to have seven deployments was felt to be technically viable and to reduce complications with spacecraft design and operations. Collision avoidance is mitigated by requiring the launch vehicle to alter the direction in which the various pieces are ejected. Additionally, the launch vehicle already has the power switching resources to control the individual separations, thus alleviating the need for these services to be added to the spacecraft.

5. Spacecraft Post-Separation Distances

The four IHS spacecraft and three inter-spacecraft structures are stacked on a single launch vehicle. The separation sequence consists of seven separations, one each for the four spacecraft and three inter-spacecraft structures. The nominal release scenario starts at approximately L + 2 hours and ends 2 hours later, with spacecraft released every 40 minutes and the three adapter rings released in between. In this nominal scenario, the release of all of the spacecraft should occur within view of a DSN station. The spacecraft release (ΔV) directions would nominally be 5° to 10° apart to increase any possible close approach distances to an acceptable level (close to the separation distance at release). This release scenario has been discussed with Kennedy Space Center personnel and appears feasible with an Atlas V or Delta IV launch vehicle.

Spacecraft release and separation analysis was performed for the release scenario just described. Four spacecraft with masses assumed to be 750 kg each were released from a stacked configuration. An Atlas V second-stage mass of 2200 kg was assumed for this analysis. In addition, the analysis assumed that the spring release mechanism nominally provided a ΔV of 1.0 m/s to a single spacecraft in the direction of ecliptic normal (relative to the pre-release state). It was also assumed that the spring applied an equal total impulse in the opposite

direction during the release. If the spacecraft release ΔV error could be reduced to less than about 5% to 6% for this scenario, there should be no post-release close approaches of the spacecraft even if the spacecraft were all released in the same direction. Larger release ΔV errors can result in post-release close approaches if the spacecraft release ΔΩs are applied in the same direction. However, if the spacecraft release ΔV directions are offset by 5° to 10°, post-release close approach distances can be increased significantly to a level not much smaller than the release distance, and this is the release scenario that would nominally be used. **Figure A-2** shows the IHS-to-IHS range with spacecraft release ΔVs of 1.0 m/s normal to the ecliptic plane; the ranges for other combinations of spacecraft as a function of time are larger. **Figure A-3** shows the effect of a 5° offset in release ΔV direction on the post-separation close approach distance resulting from a difference in the spacecraft release ΔV magnitudes relative to the pre-release state (–10% and +10% errors, respectively). **Figures A-2 and A-3** were generated using the September 4, 2015, launch case trajectory data. This analysis did not include the release of the three connecting rings in addition to the four spacecraft, but the release scenario proposed above should be effective for that scenario as well.

6. Spacecraft Flip Maneuver

The science team has expressed the possible desire to perform a flip of the spacecraft, in which the spin-axis direction is flipped 180°. This type of maneuver could be possible with the IHS spacecraft, but the tank capacity would have to be slightly increased to ensure there was sufficient propellant to do so. A technique that will minimize the propellant required to do the flip has been identified.

First, this maneuver will require a significant amount of time, potentially days. As the spacecraft spin-axis precesses, the 20-m wire booms will not immediately follow. It will take some time for them to "catch up." If the maneuver is performed too quickly the wire booms could become entangled. As a result, the flip would have to be divided into small segments where the spacecraft precesses, and then time is allotted for the wire booms to stabilize.

Second, the flip maneuver requires a substantial amount of propellant. Precessing a spacecraft spinning at 20 rpm would require many thruster firings. One way to reduce the number of firings, and thus the amount of propellant required, is to lower the spin rate. **Table A-3** shows the current best estimate of the propellant required to perform the flip at various spin rates and two spacecraft masses, the nominal mass and the mass with 30% margin. The propellant shown in the table includes the propellant mass needed to spin down, flip the spacecraft, and

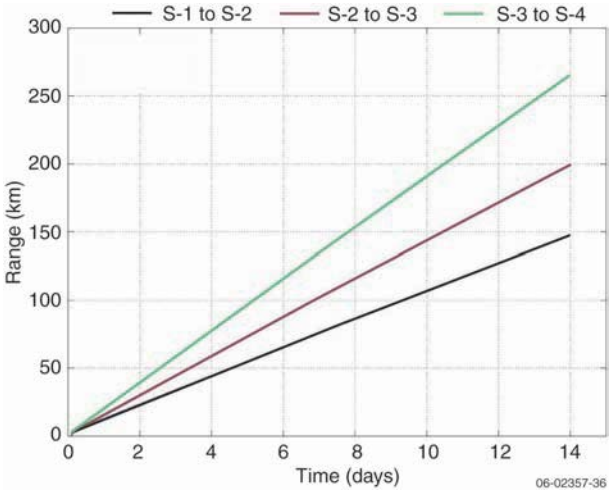

Figure A-2. Inner Heliospheric Sentinels spacecraft post-release separation distance. S-1 through S-4 denote the first though fourth spacecraft released. Release ΔV = 1 m/s normal to ecliptic plane for all IHS spacecraft; separation range is over 2 weeks. Time is referenced to launch.

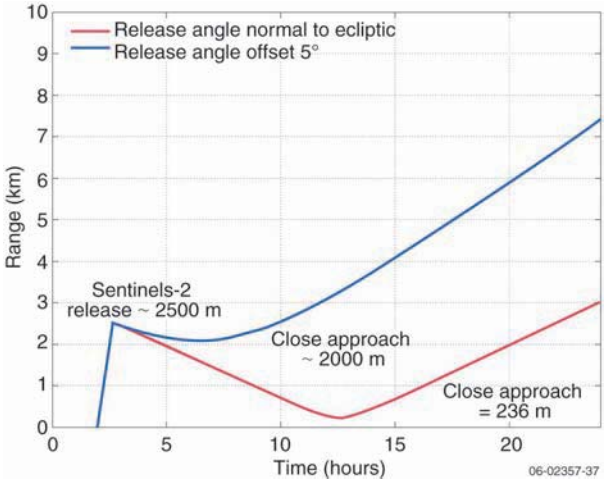

Figure A-3. Inner Heliospheric Sentinels spacecraft post-release separation distance showing range between Sentinels-1 and Sentinels-2 with 5° offset in release ΔV direction. Release ΔV = 0.9 m/s and 1.1 m/s for Sentinels-1 and Sentinels-2, respectively.

Table A-3. Current best estimate of propellant required to flip the IHS spacecraft based on minimum spin rate during maneuver and spacecraft mass.

Minimum spin rate during maneuver (rpm)	Propellant required with nominal spacecraft mass (kg)	Propellant required including 30% mass margin (kg)
3	3.3	4.2
5	4.1	5.3
10	6.0	7.8
20	10.0	12.9

spin back up to 20 rpm. Propellant usage is a function of the number of thruster pulses and the on-time for each pulse. The number of pulses required for the flip varies with the square of the spin rate, while the on-time is inversely proportional to spin rate.

There are restrictions on when the flip maneuver can be performed. The spin rate cannot be reduced when the spacecraft is close to the Sun due to thermal issues. It also cannot be reduced when the solar array output is close to the load power.

The proposed IHS propulsion subsystem allows an extra 2.0 kg of propellant (total) to be loaded into the tanks. As **Table A-3** shows, the current design would not accommodate a flip maneuver.

7. Minimum Perihelion Distance

An optimization study was performed to characterize the Sentinels mission trade space in terms of key parameters in an optimal relationship to one another. The result of this study reveals the sensitivity of spacecraft mass to perihelion distance. An Excel-based model was built to determine optimal structure and solar array form factors in order to minimize structure mass.

The model determines optimum spacecraft and solar array form factors in order to minimize overall spacecraft mass. Key variables are spacecraft body diameter and height and solar array length. Driving parameters include:

- Perihelion distance
- Thermal characteristic for specific form factor at perihelion distance
- Expendable launch vehicle (ELV) C_3 capability
- Four spacecraft on single ELV
- ELV fairing constraints
- Spacecraft power load
- Inertia ratio to ensure major axis spinner

The minimum perihelion distance is the largest driver of spacecraft mass. At a perihelion of 0.23 AU and with the spacecraft power load expected for the IHS mission, solar cell technology is on the edge of feasibility. As the perihelion distance is reduced, a larger fraction of solar array area must be allocated to Optical Surface Reflectors (OSRs) to maintain acceptable panel temperatures. As a result, the solar array area must increase in order to supply the same amount of power. For example, the solar array area doubles from 0.25 to 0.20 AU due to this relationship. **Figure A-4** illustrates the relationship between spacecraft mass and perihelion distance. Based upon this optimization study, the perihelion distance for the IHS mission was selected to be 0.25 AU so that four-spacecraft mission (from a mass standpoint) could launch on an affordable ELV. A reduced perihelion becomes feasible if an ELV with a greater lift capability is used. Reduced perihelion has additional effects not considered in the model used to relate spacecraft mass to perihelion distance. The thermal environment for components exposed to the Sun becomes more severe. This applies to instrument apertures, antennas, thrusters, and Sun sensors. Solar pressure increases, but this is not likely to be a concern.

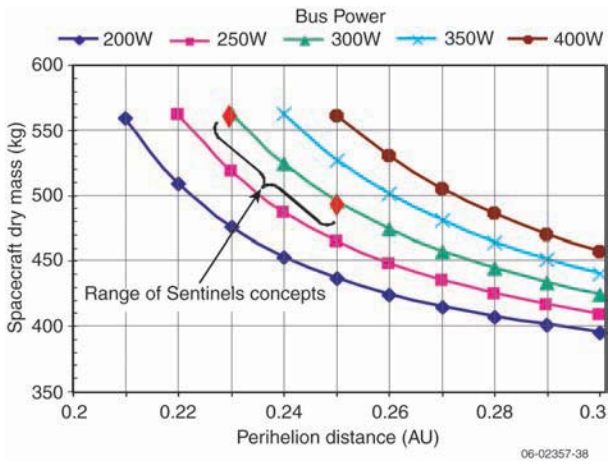

Figure A-4. Inner Heliospheric Sentinels spacecraft mass sensitivity to perihelion.

8. Radial versus Stacked Configuration

Two spacecraft configuration concepts were studied: stacked and radial. The selected stacked configuration stacks the spacecraft on top of one another, with a jettisoned inter-spacecraft structure between spacecraft. The radial configuration has the four spacecraft sitting side by side on top of a common launch vehicle dispenser. The dispenser includes four spin-up tables to spin up the spacecraft prior to deployment. The radial spacecraft configuration is narrower and taller than the stacked version. **Figure A-5** illustrates the radial configuration before and after deployment. **Figure A-6** illustrates the dispenser configuration. **Table A-4** compares the system parameters for the radial and stacked configurations.

The areas where the stacked configuration is superior make the stacked configuration inherently simpler and lower in risk than the radial configuration. The areas where the radial solution are superior are less important (e.g., differences in structure thickness between spacecraft), or they indicate minor concerns with the stacked configuration that can be managed (180° rotation of HGA and potential for contact between spacecraft at separation). The stacked configuration was selected because it carries the lower risk and is the simpler solution.

9. Selection of Heliocentric Spacecraft Orbits

Various final heliocentric spacecraft orbit configurations were analyzed. Originally, low C_3 Venus trajectories using a single Venus flyby were analyzed; final heliocentric orbits of 0.50 to 0.95 × 0.72 AU were achieved. The Sentinels science team felt it would be desirable to have perihelion of at least one of the spacecraft in the 0.20- to 0.30-AU range. Using higher C_3 Venus trajectories (maximum of ~30 km^2/s^2) with higher hyperbolic excess velocities (~10 km/s or more) at the Venus flybys and using three Venus flybys, perihelions as low as ~0.23 AU were achieved. After more detailed thermal analysis the minimum perihelion was constrained to 0.25 AU. Initially, the spacecraft performed between one and three Venus flybys and achieved final orbits between ~0.25 × 0.72 and 0.51 × 0.93 AU. The Sentinels science team felt it would be desirable to have perihelion of all of the spacecraft at approximately 0.25 AU and to achieve more significant heliocentric separation of the spacecraft early in the mission; this resulted in the current baseline

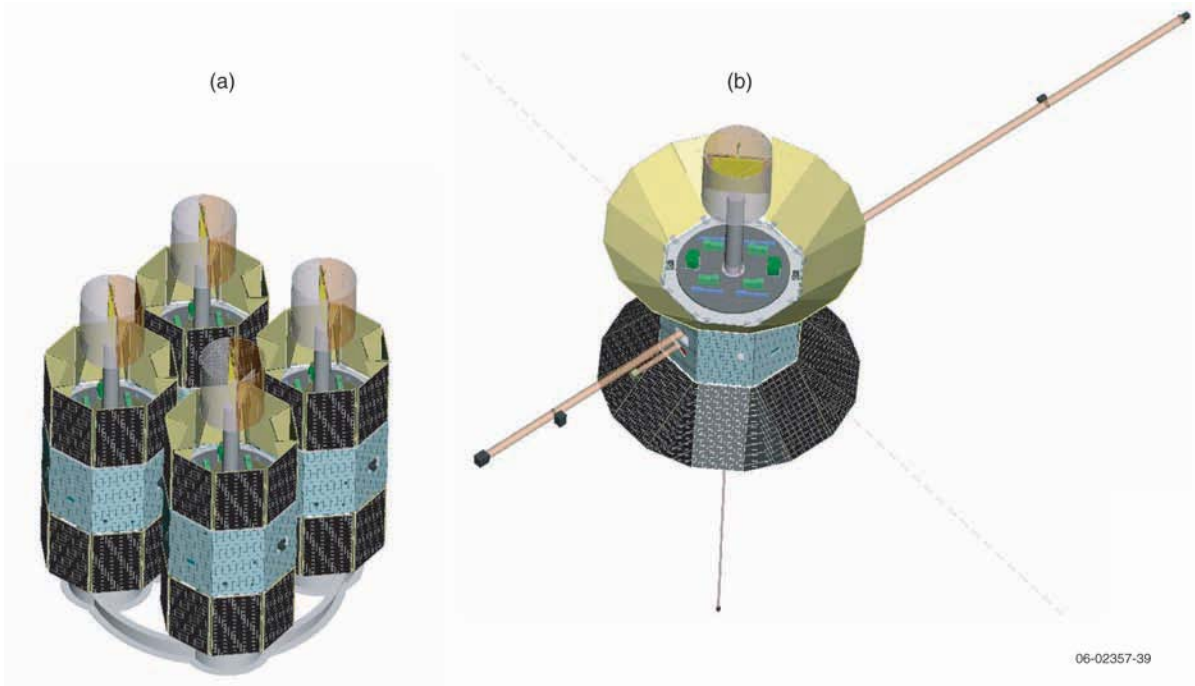

Figure A-5. Radial configuration of the Inner Heliospheric Sentinels spacecraft in (a) launch configuration, and (b) deployed configuration.

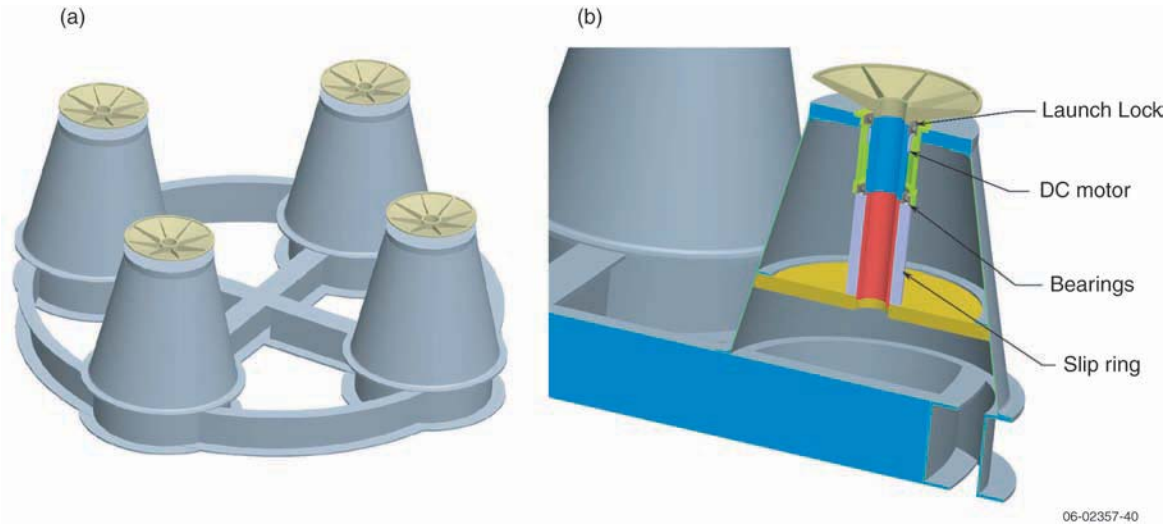

Figure A-6. (a) Dispenser for radial configuration; (b) radial dispenser spin-up mechanism.

Table A-4. Comparison between stacked and radial spacecraft configurations.

System Parameter	Stacked Configuration	Radial Configuration	Winner
Solar array	Fixed	Deployed with complicated baffle	Stacked
Thermal design	Large area for radiator on bottom deck	Small area for radiator on bottom deck	Stacked
Major axis spinner	Yes, at separation	Only after booms deployed, requires active nutation control	Stacked
Launch vehicle (LV) adapter complexity	Simple rings to interface stack to LV and between spacecraft	Complicated, one large adapter that incorporates four spin tables	Stacked
Separation Sequence	Requires seven serial deployments; uses LV rotation to spin up spacecraft. Design must ensure no contact between spacecraft when separating	Deploy spacecraft in pairs; LV must power up spin tables to spin up spacecraft. Reduced concern for contact between spacecraft during separation.	Radial
HGA configuration	Requires 180° rotation to get HGA into operational configuration	Does not require 180° rotation to get into operational configuration (but gimbal still needed to point HGA)	Radial
Mass	Greater average spacecraft mass (706 kg), but comparable total launch mass (3192 kg)	Lower average spacecraft mass (563 kg), but comparable total launch mass (3100 kg)	Even
Spacecraft similarity	The thickness of each spacecraft's internal support structure is different	All spacecraft have identical internal support structures	Radial

scenario with two of the spacecraft performing three Venus flybys and the other two spacecraft performing four Venus flybys. The science team requested significant heliocentric separation of the 0.25 AU perihelion right ascensions. This was achieved by modifying the Venus flyby scenarios.

10. Eclipses and Earth Occultation During Venus Flybys

Eclipses of excessive duration during Venus flybys could cause the required battery capacity to increase. For Type 1 trajectories (2012 launch), flyby periapsis moves toward the sub-solar point (the point at which the Sun is directly overhead) during the multiple flyby scenario; there should be no Venus eclipse periods for these trajectories. For Type 2 trajectories (2014, 2015, 2017 launches), flyby periapsis moves away from the sub-solar point during the multiple flyby scenario; Venus eclipse periods are possible for these trajectories. For an August 21, 2015, launch case, shadow periods were analyzed for the Sentinels-1 trajectory. There

were umbra periods on flyby 2 (1385-s duration) and on flyby 3 (933-s duration) for the Sentinels-1 spacecraft. Similar maximum shadow durations would be expected for other Type 2 trajectories since they have similar geometry. For the February 8, 2014, launch case, the maximum umbra duration was 1424 s on flyby 2 for the Sentinels-1 spacecraft. The battery (sized for the launch load requirement) can easily accommodate eclipses of these durations. In order to minimize the load on the battery, prior to the eclipse the spacecraft would be placed in a low-power mode by turning the instruments off and selecting the medium-power transmitter.

Earth occultation during Venus flybys is a potential concern, because communications with the Earth would be disrupted. Earth occultation during the Venus flybys was not analyzed in detail; however the maximum duration of Earth occultation events (if there are any) would be similar to that of the shadow events. Since no critical events such as maneuvers would occur during the Venus flybys (see **Table 4-3**), these events would not have a significant effect.

11. High-Gain Antenna Gimbal Angles Based on Orbit Trajectories

The angle between the heliocentric orbit plane and the spacecraft-to-Earth line determines the range of operation for the spacecraft high-gain antenna (HGA) gimbal. This parameter was analyzed for the 2/18/2014, 8/26/2015, 9/4/2015, 3/9/2017, and 3/19/2017 launch trajectory cases. For the spacecraft with the largest heliocentric ecliptic inclinations (2/8/2014, 3/9/2017, and 3/19/2017 launch cases), that angle was approximately 5° to 9° in the days after launch and decreased to less than 1° at the first Venus encounter. Between Venus flybys 2 and 3 of Sentinels-3 and Sentinels-4 (the period of higher ecliptic inclination), that angle was approximately 6.4° maximum. With a heliocentric ecliptic inclination of 1.3° and with maximum heliocentric ecliptic declination near aphelion, the maximum value of that angle after the final flyby would be approximately 5.4°.

The spacecraft can accommodate large positive gimbal angles (HGA pointing upward from the spacecraft body), but the maximum negative gimbal angle that can be accommodated is restricted to –7°. This was not an issue with the trajectories studied, but it could be a concern for other trajectories. Large gimbal angles always occur when the spacecraft–Earth distance is small, which is when maximum downlink rate can be achieved and a large volume of data can be dumped from the solid-state recorder (SSR). If the required gimbal angle exceeds the gimbal capability, SSR playback would be effectively halted during these high-data-rate periods because downlink communications must use the medium-gain antenna (MGA) instead of the HGA. For these trajectories, the determination of whether the IHS constellation is deployed "upside down" (HGA on the ecliptic south side of the spacecraft) or "right side up" could be based on minimizing the duration of large negative gimbal angles in order to enhance science data return.

12. Antenna Assembly Gimbal Design

An antenna assembly consisting of an HGA, an MGA, and one low-gain antenna (LGA) is gimbal-mounted within a radome on the despun platform. During the mission the antenna assembly is gimbaled in elevation by up to +15°/–7° to keep the HGA pointed at Earth. The gimbal does double duty by holding the antenna assembly in a compact position during launch and, after separation and early operations, rotates the antenna assembly approximately 180° into an operational state with a clear field of view past the solar arrays at all necessary gimbal angles. **Figure A-7** illustrates the gimbal design. The gimbal rotation is accomplished by a gear linkage mounted inside the center support tube powered by a drive actuator at the base of the tube. This design provides a benign thermal environment for the actuator. The actuator is a space-qualified motor from CDA InterCorp. A bearing shaft is attached to the drive actuator and is held in place by a set of precision bearings. At the opposite end of the bearing shaft is a gear shaft also held in place with bearings having a spur gear mounted to the tip. The spur gear will drive the antenna assembly about its rotation axis using a bevel gear attached to the RF rotary coupler housing.

13. Determination of Solar Array Tilt Angle

The IHS solar arrays are tilted relative to the spin axis. The optimum tilt angle is primarily driven by its effect on spacecraft radiator effectiveness. Radiator panels placed on the bottom spacecraft deck view the back of the hot solar arrays. As the tilt angle

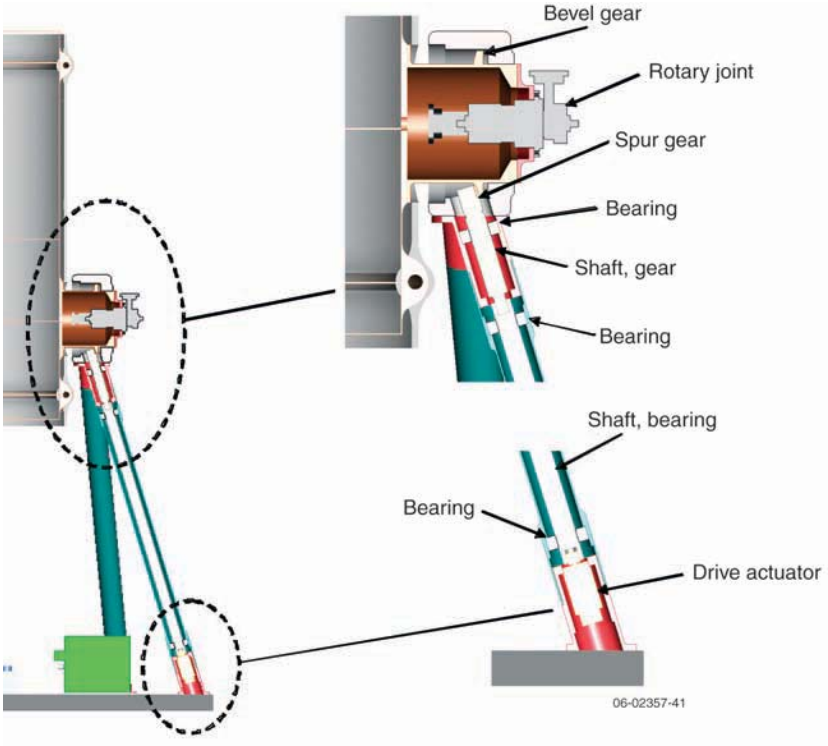

Figure A-7. Antenna assembly gimbal design shown with thermal blankets removed.

increases, the radiators have an improved view of deep space and will run cooler, which enhances removal of heat from the spacecraft bus. However, if the tilt angle is made too large, the power generation effectiveness of the solar arrays drops too much and the solar array would become unacceptably massive. A second factor is that for a given tilt angle, the temperature of the solar array will decrease as the solar cell packing factor is decreased (and the fraction of optical solar reflectors increases). As the solar array runs cooler, the radiator sink temperature also decreases. As a further constraint, the combination of tilt angle and packing factor must limit the solar array temperature to no more than 180°C at perihelion. The process used to determine the optimum tilt angle was to find the minimum angle at which the radiator sink temperature and solar array temperature were acceptable for a reasonable packing factor.

Four solar array tilt geometries were modeled in order to quantify the radiator sink temperature as a function of solar array tilt angle and packing factor. **Figure A-8** illustrates the results of this analysis. Solar array tilt angles less than 45° translate into radiator sink temperatures well above 0°C, which would not permit effective cooling of the spacecraft. A tilt angle of 45° would allow a reasonable packing factor of ~0.5 and an acceptable radiator sink temperature. As shown in **Figure A-9**, the solar array temperature is also acceptable with a tilt angle of 45°. Therefore, the spacecraft was designed with a solar array tilt angle of 45°. It is possible that a tilt angle slightly more or less than this would be better in terms of spacecraft mechanical design, solar array mass, radiator effectiveness, and instrument fields of view, but feasibility has been demonstrated with this angle.

Figures A-8 and **A-9** are based on simple analyses done early in the IHS study. For example the final spacecraft diameter was not used and the effect of the HGA blocking the back of the upper solar arrays (and causing their temperature to increase) was not included. **Figure 5-18** in the report more accurately shows how the packing factor varies with perihelion in order to maintain panel temperature at or below 180°C.

14. Inner Heliospheric Sentinels Initial RF Acquisition Strategy

The post-launch initial RF acquisition of four IHS spacecraft will present unique challenges to the

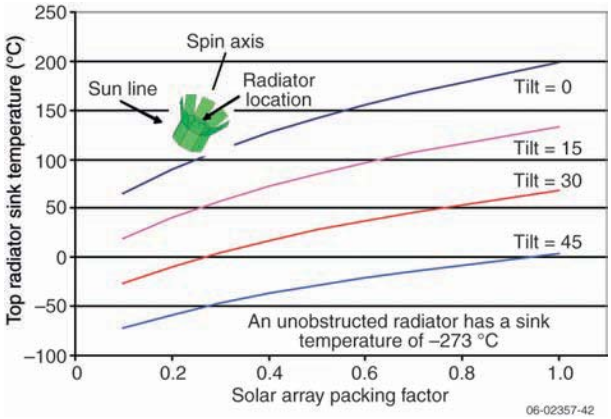

Figure A-8. Radiator sink temperature vs. packing factor and tilt angle.

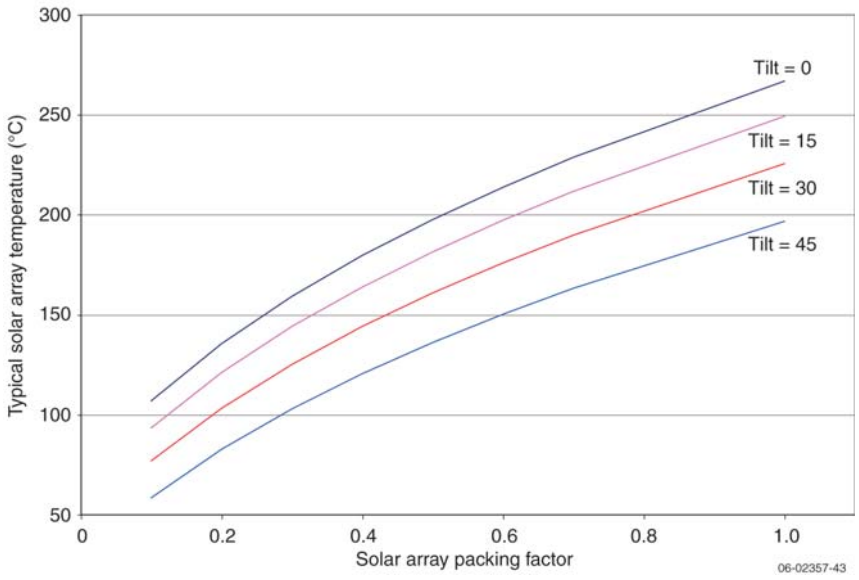

Figure A-9. Solar array temperature vs. packing factor and tilt angle.

Deep Space Network (DSN) and mission operations team. Of principal concern during the launch and initial acquisition process is to monitor the health and safety of each spacecraft. In the unlikely event of a detected anomaly, commanding of the spacecraft maybe necessary or desirable to resolve or troubleshoot the anomaly before proceeding to normal operations. Finally, radiometric tracking is also critical to determine the magnitude of any launch error that may have been imparted by the launch vehicle. Radiometric tracking is used to effectively point the DSN antenna and to determine any critical maneuvers that may be necessary as the result of the launch error.

Of primary of concern to the initial acquisition phase will be the availability of limited ground station resources to support command, telemetry, and radiometric tracking of four spacecraft. The analysis shown below is for a single launch opportunity of September 4, 2015; the entire launch window and launch opportunities were not analyzed. The resources identified herein are currently available in 2006. During the first 24 hours of operation, DSN has insufficient capability to remain in simultaneous contact with all four spacecraft. The initial acquisition strategy outlined use both DSN and Universal Space Network (USN) resources to support telemetry, command, and radiometric tracking of all four IHS spacecraft during initial RF acquisition and early operations.

Figure A-10 shows the relative separation distance of each spacecraft for the September 4, 2015, launch opportunity. The top graph shows the relative separation distance for the first 14 days from launch and the bottom plot shows a more refined view of the first 24 hours from launch. All four spacecraft can be viewed from a single DSN complex over this 2-week period based on the beamwidth of a 34-m antenna, the known Earth distance, and the small separation distance.

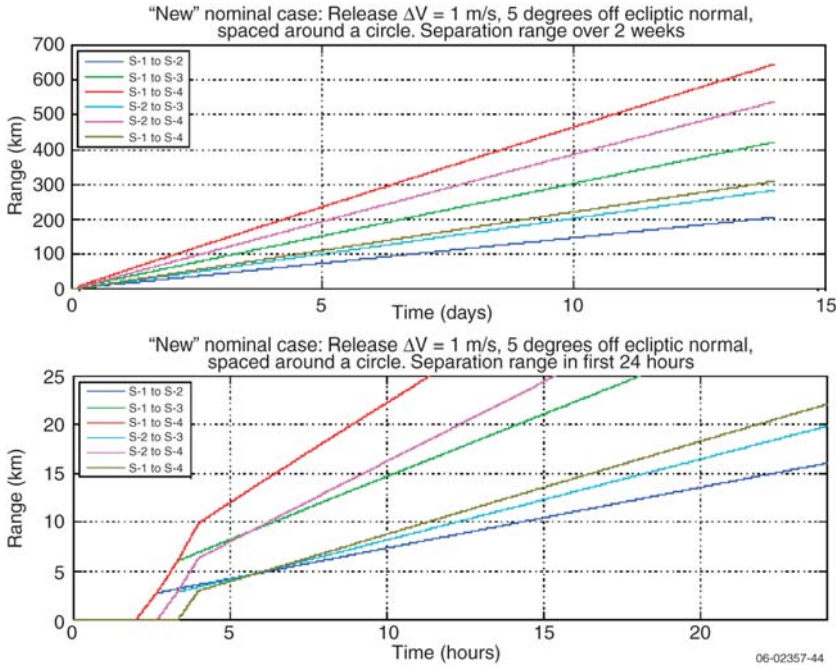

Figure A-10. Relative separation distance (km) of Sentinels-1 through 4 for the first 14 days after launch (top). The bottom plot shows the first 24 hours after launch.

Figure A-11 shows an initial acquisition strategy for first contact. Since the number of DSN-compatible ground station assets available for spacecraft commanding, telemetry reception, and radiometric tracking exceeds the resources available, a "round-robin" approach was developed. The spacecraft separate from the launch vehicle at 40-minute intervals. Two 34-m antennas (DSS-34 and DSS-45) at the DSN Canberra station and antennas at the USN Dunagara and Hartebeesthoek stations will be used for initial contact with the four spacecraft. USN stations have previously supported the early operations for deep space missions such as New Horizons. The USN stations have no X-Band uplink command or radiometric capability and will be used solely for telemetry reception.

Both the DSS-34 and DSS-45 antennas will acquire Sentinels-1 when it separates from the launch vehicle. The USN Dunagara station will provide backup real-time telemetry for Sentinels-1. When Sentinels-2 separates from the launch vehicle, the DSS-45 antenna will transition from Sentinels-1 to Sentinels-2. The USN Hartebeesthoek station will provide backup real-time telemetry for Sentinels-2. DSS-34 and Dunagara will continue to track Sentinels-1. At this point uplink and downlink capability for the first two spacecraft will be established through DSN antennas, and backup telemetry established through USN antennas.

When Sentinels-3 separates from the launch vehicle, the DSS-34 antenna will transition from Sentinels-1 to Sentinels-3, providing uplink and downlink capability for Sentinels-3. Real-time telemetry from the USN Dunagara station will continue to supply the health of Sentinels-1 but this station cannot provide a command capability. Radiometric tracking of Sentinels-1 will have been collected for 80 min and a solution of the launch errors could now be pursued to aid in DSN and USN antenna pointing.

When Sentinels-4 separates from the launch vehicle, the DSS-45 antenna will be released from Sentinels-2. Real-time telemetry from Sentinels-2 will continue to be received at the USN Hartebeesthoek station to allow monitoring of critical spacecraft health and safety, but as with Sentinels-1, there will no longer be a command capability. At this point, uplink and downlink capability have been established with Sentinels-3 and 4, but downlink capability only with Sentinels-1 and 2. The European Space Agency (ESA) station at New Norica, Western Australia, is an additional asset that could be used for uplink commanding and radiometric tracking of Sentinels-1 or 2 during this period.

The USN stations identified (as well as others at other locations on Earth) can continue to receive spacecraft telemetry out to a spacecraft range of 0.002 AU, which corresponds to 12 h after launch. These stations, together with DSN stations, can provide simultaneous telemetry coverage of all four spacecraft, and uplink commanding and radiometric coverage of two spacecraft at a time. After day

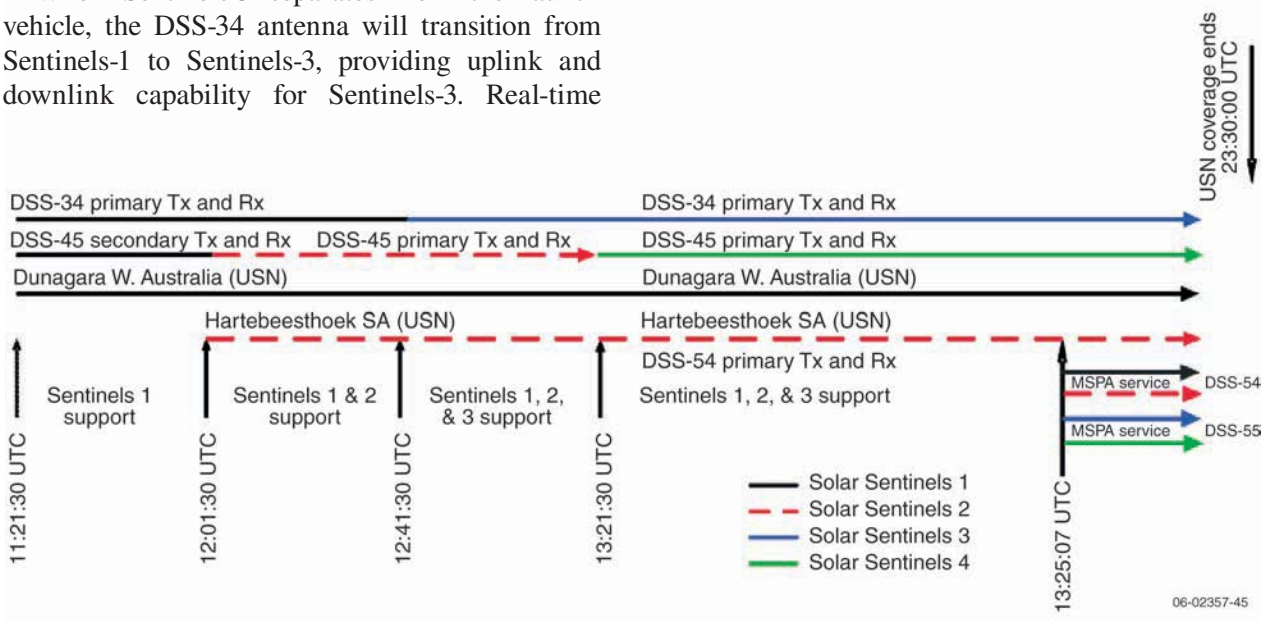

Figure A-11. Initial RF acquisition strategy for the IHS spacecraft using DSN and Universal Space Network (USN) assets.

L + 12 h, in order to achieve continuous telemetry coverage of all four spacecraft, the program must utilize the Multiple Spacecraft Per Aperture (MSPA) capability of DSN stations. MSPA allows a single antenna to process two or more downlink signals, but is limited to a single command uplink. After the spacecraft separate beyond the beamwidth of a 34-m antenna, this service will not longer be possible. At this point it will only be possible to remain in contact (uplink and downlink) with two spacecraft at a time by utilizing two 34-m dishes at each DSN station.

15. Bearing and Power Transfer Assembly (BAPTA)

The bearing and power transfer assembly (BAPTA) is an important component of the spacecraft. It allows the top platform to be despun from the rest of the spinning spacecraft so that the HGA and MGA can be pointed toward Earth. The BAPTA also allows the passage of three RF and up to 55 non-RF signals between the spinning spacecraft and the despun platform. The proposed BAPTA design from Boeing as shown in **Figure A-12** has a redundant brushless DC motor and resolver. The control electronics are redundant, but physically separate from the BAPTA. Components having heritage from other flight programs include the resolver, preload spring, slip-ring structure and slip-ring brush/ring interface for the non-RF channels, and bearings. The motor and the RF rotary joint will be slightly modified from their heritage designs. Since all of the parts are either re-used without changes or slightly modified from heritage designs, the BAPTA presents a low risk to the mission. The average lifespan (to date) of all BAPTAs produced by Boeing since 1972 for spinning spacecraft is about 13 years, well in excess of the IHS mission life goal of 5 years. This average lifespan has been limited by the spacecraft lifetime; all of the BAPTAs were operating at the retirement of the spacecraft.

The BAPTA control performance greatly exceeds what is necessary. It is capable of controlling the phase of the despun platform to an accuracy of 10 arcsec. This accuracy could degrade by an order of magnitude and the HGA pointing accuracy requirement of 0.8° would still be met.

Two of the BAPTA RF channels are waveguide based and can easily accommodate the power level of the high-power traveling wave tube antenna (TWTA). The third channel is coax-based and can support the medium-power TWTA continuously. The high-power TWTA can be accommodated on the coax channel for short periods (approximately 5 min). This allows ample time for the spacecraft autonomy system to correct the configuration of the RF subsystem if it were to be inadvertently commanded to an invalid state with a high-power TWTA connected to the MGA or LGA on the despun platform.

16. Study of Alternate RF Subsystem Configurations

The baseline design for the Inner Heliospheric Sentinels RF subsystem locates all the RF subsystem electronics (except for the antennas) on the lower deck of the spacecraft. A block diagram of the baseline RF subsystem is shown in **Figure A-13**. This topology requires three RF channels through the bearing and power transfer assembly (BAPTA) for the signals going to the antennas on the despun platform.

The baseline RF subsystem design was chosen after comparing designs containing a single RF channel BAPTA and a dual RF channel BAPTA. The single-channel case has all the subsystem electronics mounted to the despun platform. The dual- and

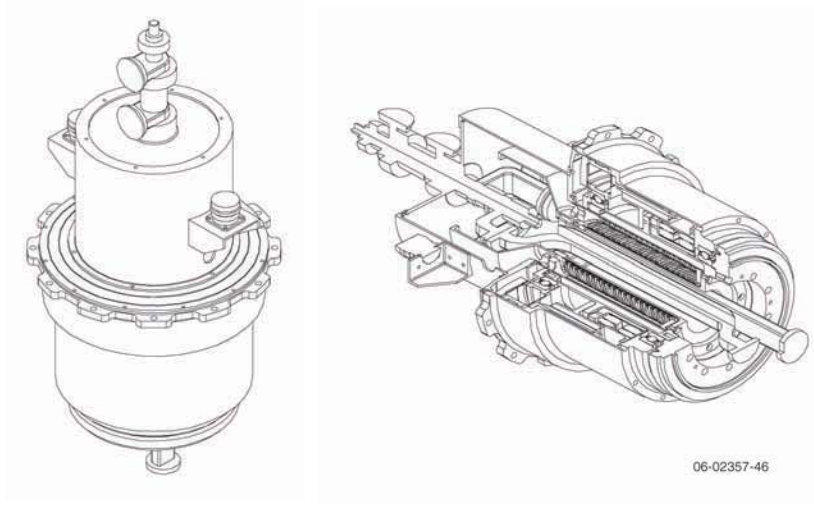

Figure A-12. Proposed BAPTA design from Boeing.

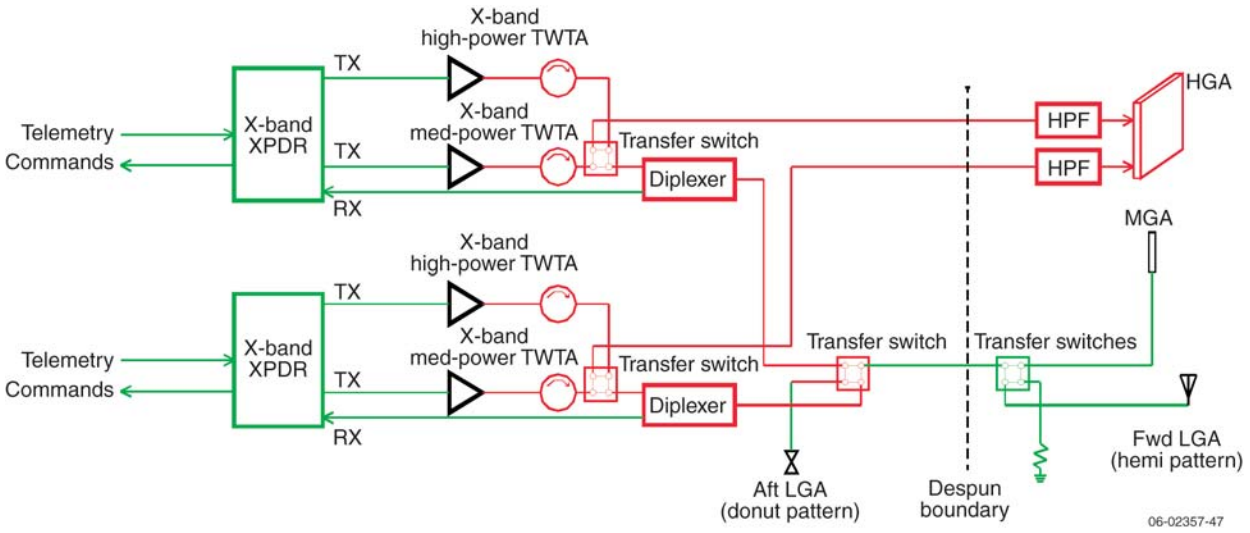

Figure A-13. Baseline IHS telecom system block diagram with three-channel BAPTA.

three-RF channel BAPTA allows the RF subsystem electronics to be moved off the despun platform; this results in significant advantages

Location of RF subsystem electronics: spacecraft body vs. despun platform

Locating RF subsystem electronics on the spacecraft body provides the following benefits:

1. **Simplified despun platform:** The despun platform no longer has to be designed to radiatively couple ~100 W of dissipation on the platform to the spacecraft body. The platform no longer has to accommodate a network of heat pipes to spread the heat across the platform. The mass of the platform can be decreased. The platform no longer has to be thermally isolated from the BAPTA.
2. **Increased transmitter power:** The high-power transmitters can be conductively coupled through the spacecraft structure to radiators on the bottom deck rather than radiatively coupled to the spacecraft body from the platform. This allows the transmitter power to be increased and to utilize the excess power available from the solar arrays.
3. **Increased science data rate:** The high-power transmitter power can be increased, allowing more the return of more science data. If the high-power transmitter was located on the platform, it would be thermally limited to 150 W, and the science data rate would be limited to 5000 bps (rather than the baseline 5900 bps).
4. **Reduced number of non-RF signals in the BAPTA:** The number of non-RF signals that the BAPTA must accommodate is reduced from ~100 to ~50. This also allows the elimination of a despun platform multiplexer electronics box that would be required to squeeze all of the required I/O needed for a one-channel BAPTA configuration into only 100 channels.

RF Subsystem with One Channel BAPTA and Dual-Feed HGA

A block diagram of the RF subsystem with a one-channel BAPTA is shown in **Figure A-14**. All of the RF subsystem electronics are located on the despun platform. A despun platform multiplexer (DPM) is required to reduce the number of non-RF signals to ~100. The basic RF subsystem topology is identical to the baseline RF subsystem configuration except that the despun boundary has been moved.

RF Subsystem with Two-Channel BAPTA and Dual-Feed HGA

A block diagram of the RF subsystem with a two-channel BAPTA is shown in **Figure A-15**. All of the telecom equipment except the antennas is on the spacecraft body shown to the left of the despun

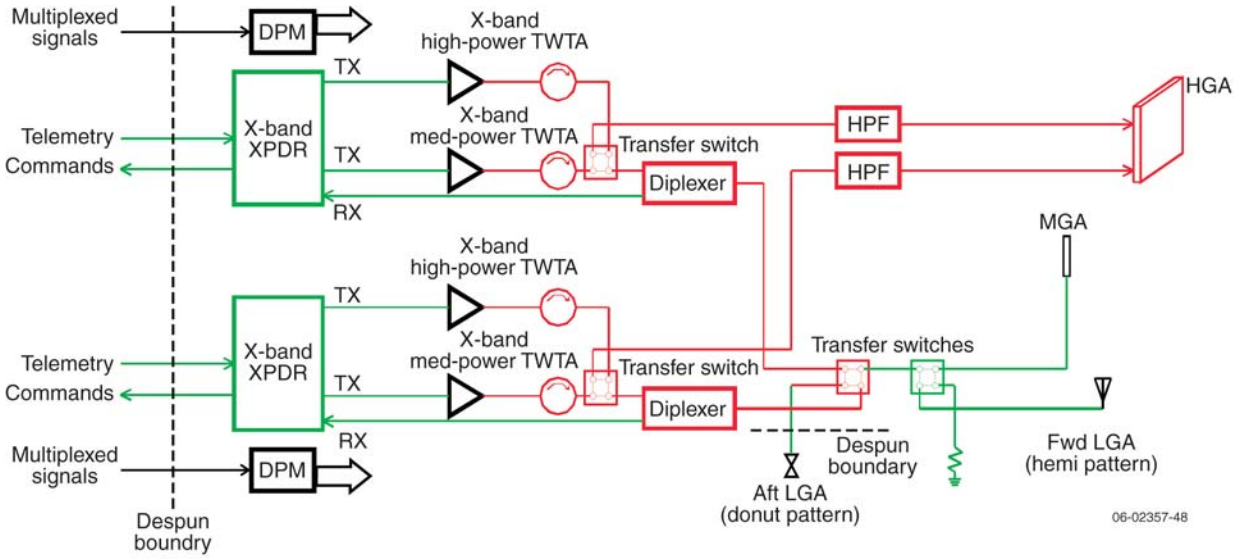

Figure A-14. Block diagram of telecom system with one-channel BAPTA.

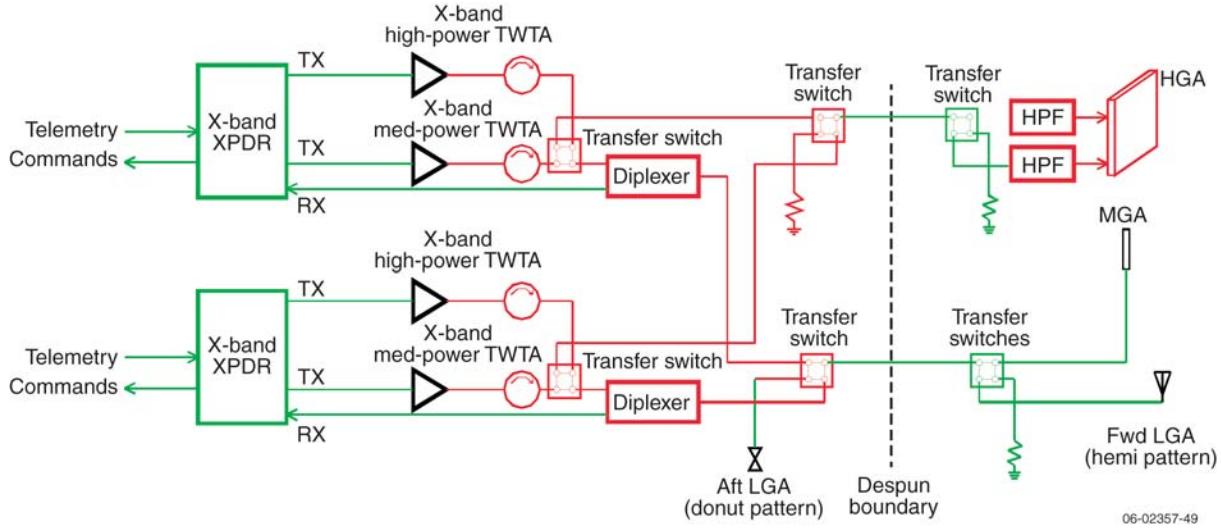

Figure A-15. Block diagram of telecom system with two-channel BAPTA.

boundary. Two additional transfer switches are needed in the connections to the HGA.

RF Subsystem with Two-Channel BAPTA and Single-Feed HGA

A block diagram of the RF subsystem with a two-channel BAPTA but also with a single-feed high gain antenna is shown in **Figure A-16**. All of the electronics are on the spacecraft body. An additional switch is needed compared to the baseline design, and the HGA only has one input.

Conclusion

The three-channel BAPTA configuration appears to be optimal. The reliability of a two-channel BAPTA is not believed to be significantly better than a three-channel BAPTA. The height of the three-channel BAPTA does not drive the spacecraft height. The reliability of a dual-feed versus a single-feed HGA needs to be evaluated. The pros and cons of the four potential RF subsystem configurations are summarized in **Table A-5**.

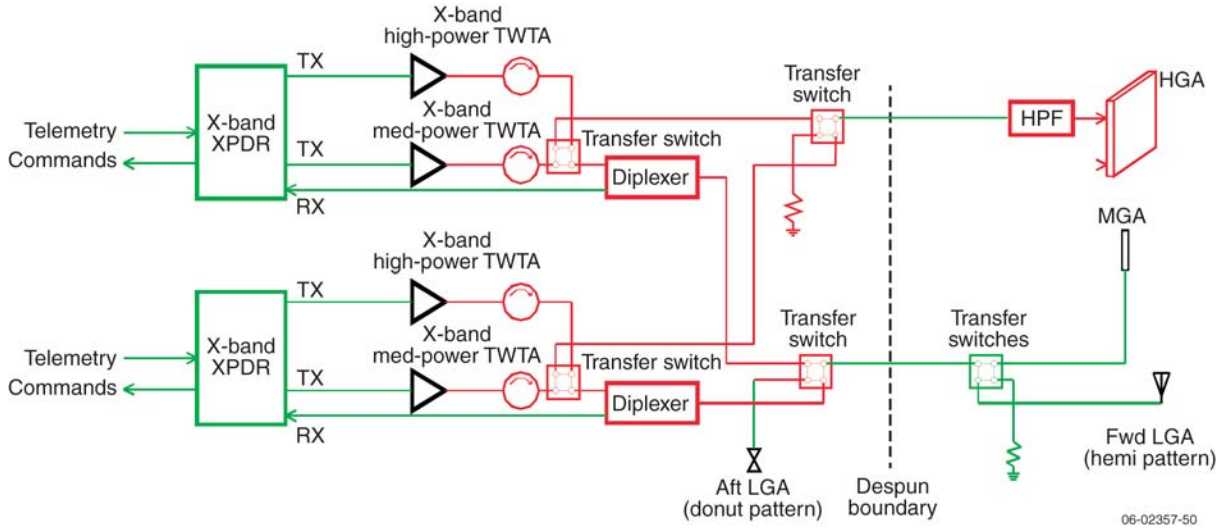

Figure A-16. Block diagram of telecom system with two-channel BAPTA and single-feed high gain antenna.

Table A-5. RF subsystem configuration tradeoff summary.

RF Subsystem Configuration	Pro	Con
1-channel BAPTA, dual-feed HGA	• Simplest RF rotary joint	• Complex platform design requires heat pipes • Platform power must be dissipated by radiating to spacecraft body • High-power transmitter limited by thermal constraints, reduces science data rate • Platform must be thermally isolated from BAPTA • BAPTA must accommodate ~100 non-RF signals • A redundant despun platform multiplexer is needed to accommodate all of the signals needed by the components on the platform
2-channel BAPTA, dual-feed HGA	• Simplifed thermal design • Transmitter power and science data rate can be increased • BAPTA only has to accommodate ~50 non-RF signals • A despun platform multiplexer is not required	• Two additional switches in HGA feed • Introduction of potential single-point failures
2-channel BAPTA, single-feed HGA	• Simplifed thermal design • Transmitter power and science data rate can be increased • Minimizes number of RF switches • BAPTA only has to accommodate ~50 non-RF signals • A despun platform multiplexer is not required	• One additional switch in HGA feed • Introduction of potential single-point failures
3-channel BAPTA, dual-feed HGA (baseline design)	• Simplifed thermal design • Minimizes number of RF switches • Transmitter power and science data rate can be increased • BAPTA only has to accommodate ~50 non-RF signals • A despun platform multiplexer is not required	• Most complicated RF rotary joint

17. Alternate IHS Spacecraft Mechanical Configurations

The baseline IHS design has fixed (non-deployed) solar arrays and an HGA that is simply rotated to become operational. This design is simple and low risk because there are essentially no spacecraft deployables, although a jettisoned spacer cylinder is required between each spacecraft. Other stacked configurations were studied that would reduce the launch mass by utilizing a folding HGA and folding solar arrays. Two of these configurations are compared to the baseline IHS configuration.

Cartoons of the IHS spacecraft baseline configurations and two alternative configurations are shown in **Figure A-17**. For each, the launch and deployed configurations are shown. The configurations are compared in **Table A-6**.

A fourth configuration was studied that further reduced the stowed size of the solar array by adding a second hinge to each solar array panel. This configuration did not provide any additional overall mass reduction due to the mass of the additional hinges and deployment mechanisms required, and so it was not studied further.

The alternative spacecraft configurations have two advantages:

- Total launch mass is reduced.
- The three inter-spacecraft cylinders and associated separation systems are not needed.

The alternative spacecraft configurations have several disadvantages, however:

- HGA mechanical complexity is greatly increased; the HGA must be folded up and stowed for launch, including a folded and deployed radome.
- Solar array complexity is greatly increased; solar arrays must be folded up and stowed for launch, including additional mechanisms.
- A solar array baffle must be deployed along with the solar array to block sunlight from illuminating the backs of the solar array panels after they are deployed.
- The aft LGA must be on a deployed mast instead of a fixed mast (in the baseline configuration, the aft LGA mast on an upper spacecraft is nestled within the HGA radome of a lower spacecraft).
- Some of the solar array panels will be shaded until the spacecraft is separated from the upper stage and the panels deployed. This may increase the required battery capacity compared with the baseline configuration.
- Some of the thrusters are blocked with the body-fold configuration prior to solar array release.

The baseline configuration was selected even though it requires a slightly more capable launch vehicle because spacecraft complexity and risk are reduced relative to the alternative configurations.

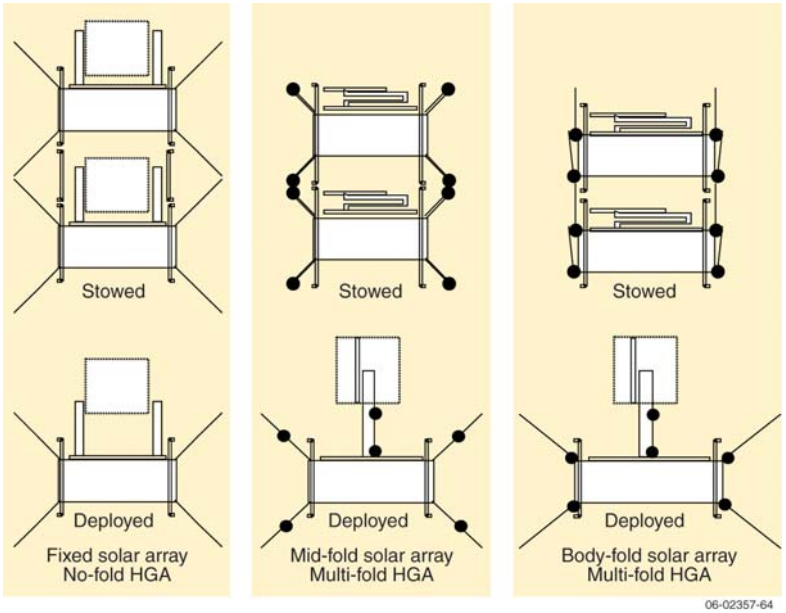

Figure A-17. IHS Baseline and alternate mechanical configurations.

Table A-6. Comparison of IHS mechanical configurations.

Parameter	Spacecraft Configuration		
	Baseline IHS	**Mid-Fold Solar Array**	**Body-Fold Solar Array**
Primary structure material	Isogrid aluminum panels	Aluminum honeycomb panels	Aluminum honeycomb panels
Solar array	Fixed, non-deployed	Deployed, hinge in middle	Deployed, hinge at S/C mount
Solar array baffle	Not needed	Simple (Kapton between solar array panels)	Complex
HGA mechanical complexity	Simple: 180° rotation but no hinges or deployment mechanisms required	Complex: multiple hinges and deployment mechanisms; limited space; deployed radome	Complex: multiple hinges and deployment mechanisms; very limited space; deployed radome
Aft LGA	Nondeployed	Deployed	Deployed
Spacer cylinders & separation systems	Spacers needed, 6 separation systems	No spacers needed, 3 separation systems	No spacers needed, 3 separation systems
Total launch mass	3192 kg	2774 kg	2697 kg
Mass reduction compared with baseline	–	418 kg	495 kg
Solar array power available before separation from stack	Full power from array	Reduced power from array	Reduced power from array
Thruster impact	None	None	Blocked until solar array deployed
Fairing needed	5-m or possibly 4-m	4-m	4-m
Launch vehicle required (minimum) for C_3 26.5 km^2/s^2	Atlas V (531) or Atlas V (431)	Atlas V (421)	Atlas V (421)

18. Summary of Major Mission and Spacecraft Trade-Off Studies

The major IHS trade-off studies are summarized in **Table A-7**. Most of the listed studies were presented in more detail in the preceding sections of Appendix A or in Chapter 4.

Table A-7. Summary of major IHS trade studies.

Issue	Trade Space	Selection	Primary Rationale
Spin axis orientation	a. Orbit normal b. Sun pointed	Orbit normal (essentially ecliptic north)	Only orbit normal satisfies science requirements.
Spin rate	1 to 25 rpm	20 rpm	Satisfies science and thermal requirements.
Minimum perihelion distance	0.20 to 0.35 AU	0.25 AU	Solar array area and spacecraft mass and volume greatly increase at perihelion distances under 0.25 AU.
Most favorable balance between spacecraft downlink capability and DSN pass time to return the required volume of science data	a. Robust spacecraft downlink capability, reduced DSN pass time b. Less capable spacecraft downlink capability, additional DSN pass time	Robust spacecraft downlink capability, reduced DSN pass time	A constellation of four spacecraft could tax DSN capabilities (and become costly) if overly reliant on downlink time to return science data; the baseline spacecraft downlink capability can return all science data with one 8-h pass per week per spacecraft.
Primary structure	a. Isogrid aluminum panels b. Thin-walled cylinder	Isogrid aluminum panels	Removable panels permit installation of propulsion subsystem by subcontractor and provide access to spacecraft interior during I&T.
Mechanical configuration of inter-spacecraft spacer cylinders	a. Incorporate cylinders into bottom of each spacecraft structure b. Jettison cylinders	Jettison cylinders	Incorporated cylinders block radiators and the aft LGA, and cause solar heating of the spacecraft.

Table A-7. Summary of major IHS trade-off studies (continued).

Issue	Trade Space	Selection	Primary Rationale
Launch configuration	a. Radial b. Stacked	Stacked	Radial requires a deployed solar array; is not a major axis spinner at separation; and requires a complicated launch vehicle adapter. Stacked configuration is simpler and lower risk.
Solar array and HGA configuration	a. Fixed b. Deployed	Fixed	Simpler, lower-risk spacecraft.
Solar array tilt angle	0° to 45°	45°	Optimal for radiator effectiveness, solar array temperature, and power generation.
Downlink frequency	a. X-band b. Ka-band	X-band	An X-band system is simpler than a Ka-band system and can return the required science data. A Ka-band system has tighter pointing requirements that would require a star tracker to be added to the G&C subsystem. Accommodation of a star tracker would be difficult (e.g., accommodating FOV, additional mass) and expensive.
HGA technology	a. Parabolic dish b. Parabolic wire cylinder c. Electronically scanned phased array d. Mechanically scanned phased array	Mechanically scanned phased array	Low mass, volume, and risk; the HGA gimbal does double duty by both deploying and pointing the HGA.
Location of RF components	a. Despun platform b. Spacecraft body	Spacecraft body	Superior thermal design; transmitter power can be increased; lower mass.
Number of transmitter power levels	One to three power levels	Two power levels	The medium-power transmitter is sized to support the emergency mode link; the high-power transmitter utilizes the increase in solar array output as the solar distance decreases; there is negligible benefit from a third transmitter.
High-power transmitter RF output power level	37 to 125 W	100 W	100-W transmitter maximizes science data return without requiring an increase in solar array size; thermal analysis shows that a 100-W transmitter can be accommodated.
Mission redundancy	a. Four spacecraft with redundant systems b. Five spacecraft with nonredundant systems	Four spacecrat with redundant systems	A nonredundant spacecraft is only ~5% lower in mass than a redundant spacecraft, so the mass of four redundant spacecraft is much less than the mass of five nonredundant spacecraft.
Spacecraft redundancy	a. Single string b. Partial redundancy c. Full (use redundant components or components with fault tolerance)	Full	Full redundancy necessary to satisfies 3-year lifetime requirement and 5-year lifetime goal
Mitigation of spin axis precession due to CM–CP offset	a. Thrusters b. Movable mass or solar sail	Thrusters	Only 1 kg of propellant is required to correct a 10 cm CM-CP offset for a 5-year mission.
Accommodation of growth in payload power beyond 30% of CBE	a. Increase solar array area b. Decrease solar distance that entire payload is turned on	Decrease solar distance that entire payload is turned on	Spacecraft design can power the entire payload at a solar distance of 0.88 AU with 30% payload power margin.

Appendix B: Inner Heliospheric Sentinels Mass and Power Estimates

Table B-1: Mass estimates.

Component	Mass (kg)
Instruments	
Dual Magnetometer	0.5
Dual Mag Boom	10.0
SW Electrons	1.5
Search Coil	0.5
SW/SC Boom	5.0
Protons/Alpha	4.0
Composition	6.0
Radio	4.7
Low Energy Ions	3.5
High Energy Ions and electrons and Boom	8.0
SEP Q-States and SEP DPU	10.5
Energetic Electrons & Suprathermals	2.0
Neutron Spectrometer	3.8
XR Imager	2.0
Gamma Spectrometer	2.2
Common DPU	3.0
DPU components	1.8
Purge system	0.1
Instrument harness	1.4
Instruments subtotal	70.5
Attitude Determination and Control	
Star scanner (2)	8.2
Accelerometers (2)	2.0
Sun sensors (2)	2.5
Attitude subtotal	12.7
Command & Data Handling	
IEM & OCXO -A	5.6
IEM & OCXO -B	5.6
Command subtotal	11.2
Power	
Solar arrays	41.6
Solar array hinges/brackets	5.1
Power distribution unit	14.0
Power system electronics	8.6
Junction box	1.5
Battery	10.0
Power subtotal	80.7
Structure	
Honeycomb decks and fasteners, average mass	57.7
Load-bearing structure, average mass	69.7
Despun platform	7.3
RF radiators with mounts	1.9
Secondary structure	9.7
Fasteners	2.3
Spin balance mass (no Cg offset)	13.0
Structure subtotal	161.6

Component	Mass (kg)
Propulsion	
Propellant tank (2)	7.4
Thrusters 4.4N (12)	4.8
Latch and service valve	1.3
Propellant filter	0.4
Pressure transducer	0.8
Cabling and connectors	3.4
Tubing/fasteners/tube clamps/etc.	5.1
Propulsion subtotal	23.2
RF Communications	
HGA	4.9
RF support structure	4.6
BAPTA & Electronics Box	20.9
HGA Actuator	2.3
Forward LGA and MGA	0.9
Aft LGA and boom	11.1
Rotary joints (2)	3.5
TWTA (4)	9.2
Transponder (2)	6.0
Waveguide RF Transfer Switches (3)	2.0
Waveguide diplexer (2) and Isolators (4)	2.0
Radome, pressure baffle, support	3.4
Waveguide runs	1.2
Coax transfer switch, filters	1.2
RF subtotal	73.1
Thermal	
MLI blankets	5.0
Radiator	4.0
Thermal curtains	0.5
OSRs	5.2
OSR Panels	5.4
Louvers	5.0
Despun thermal spacer	0.3
Heaters and miscellaneous	0.1
Thermal subtotal	25.5
Harness	
S/C harness, 9% dry mass	45.3
Harness subtotal	45.3
Spacecraft dry mass total (average)	**503.7**
Launch	
Wet mass with margin (average)	697.8
Usable propellant	42.5
Trapped propellant and pressurant	0.5
Dry mass with margin (average)	654.8
Dry mass with margin (top spacecraft)	614.1
Dry mass with margin (bottom spacecraft)	695.9
Margin on dry mass (average), kg	151.1
Margin on dry mass %	30.0
Bottom spacecraft wet with margin	738.9
Mid-Lo spacecraft wet with margin	709.2
Mid-Hi spacecraft wet with margin	686.3
Top spacecraft wet with margin	657.1
Mass of 4 observatories	2791.3
Jettisoned support cylinders w/ 30% margin	89.0
Separation and jettison systems w/ 30% margin	312.0
Total Launch Mass	**3192.4**

Table B-2: Power estimates.

Subsystem/Component	Average Power (W)				
	Launch Configuration	Platform Off, Instr. Off, Med-Pwr Downlink On	Platform On, Instr. Off, Med-Pwr Downlink On	Platform On, Instr. On, Med-Pwr Downlink On	Platform On, Instr.On, High-Pwr Downlink On
Instruments					
Dual Magnetometer	0.0	0.0	0.0	1.0	1.0
SW Electrons	0.0	0.0	0.0	1.5	1.5
Protons/Alpha	0.0	0.0	0.0	4.0	4.0
Composition	0.0	0.0	0.0	6.0	6.0
Radio	0.0	0.0	0.0	3.0	3.0
Search Coil	0.0	0.0	0.0	0.2	0.2
Low Energy Ions	0.0	0.0	0.0	3.0	3.0
High Energy Ions and Electrons	0.0	0.0	0.0	5.0	5.0
SEP Q-States	0.0	0.0	0.0	4.0	4.0
SEP DPU	0.0	0.0	0.0	6.5	6.5
Energetic Electrons and Suprathermals	0.0	0.0	0.0	2.0	2.0
Neutron Spectrometer	0.0	0.0	0.0	3.0	3.0
XR Imager	0.0		0.0	2.0	2.0
Gamma Spectrometer	0.0		0.0	0.5	0.5
Common DPU	0.0		0.0	3.3	3.3
Instruments subtotal (assume 65% conv eff)	0.0	0.0	69.0	69.0	
Attitude Determination and Control					
Star scanner—power provided by IEM	0.0	0.0	1.0	1.0	1.0
Accelerometers (3)—power provided by IEM	0.0	0.0	0.0	0.0	0.0
Sun sensor	0.0	0.0	1.0	1.0	1.0
Attitude subtotal	0.0	0.0	2.0	2.0	2.0
Command & Data Handling					
IEM A (includes OCXO)	21.0	21.0	21.0	24.0	24.0
IEM B	3.0	3.0	3.0	3.0	3.0
IEM subtotal	24.0	24.0	24.0	27.0	27.0
Power					
Power distribution unit	18.0	18.0	18.0	18.0	18.0
Power system electronics	6.0	6.0	6.0	6.0	6.0
Solar array junction box	0.0	0.0	0.0	0.0	0.0
Battery recharge	0.0	20.0	20.0	20.0	20.0
Power subtotal	24.0	44.0	44.0	44.0	44.0
Propulsion					
Thrusters—assume 2 x 1 lb thrusters	0.0	0.0	0.0	0.0	0.0
Cat bed heaters—4 for launch, 2 for maneuvers	16.0	0.0	0.0	0.0	0.0
Pressure sensors (4 at 0.9 W each)	3.6	3.6	3.6	3.6	3.6
Propulsion subtotal	19.6	3.6	3.6	3.6	3.6

Table B-2: Power estimates. (Cont.)

Subsystem/Component	Average Power (W)				
	Launch Configuration	Platform Off, Instr. Off, Med-Pwr Downlink On	Platform On, Instr. Off, Med-Pwr Downlink On	Platform On, Instr. On, Med-Pwr Downlink On	Platform On, Instr.On, High-Pwr Downlink On
RF Communications					
Receiver A	5.6	5.6	5.6	5.6	5.6
Receiver B	5.6	5.6	5.6	5.6	5.6
Exciter	0.0	4.0	4.0	4.0	4.0
Med/high power transmitter	0.0	50.0	50.0	50.0	200.0
BAPTA & BAPTA Electronics	0.0	13.5	13.5	13.5	13.5
HGA actuator	0.0	3.0	3.0	3.0	3.0
RF subtotal	11.2	65.2	81.7	81.7	231.7
Thermal					
Thruster valve heaters (12 @2.2 W each)	8.8	26.4	26.4	26.4	26.4
Fuel line heaters (0.1 W per foot)	0.0	4.0	4.0	4.0	4.0
Fuel tank heater	0.0	10.0	10.0	10.0	10.0
Instrument operational heaters	0.0	0.0	0.0	0.0	0.0
Instrument survival heaters (need when instr off)	0.0	20.0	20.0	0.0	0.0
Battery heater	0.0	7.5	7.5	7.5	7.5
Thermal subtotal	8.8	67.9	67.9	47.9	47.9
Harness					
IR loss (1.5% of load power)	1.3	3.1	3.3	4.1	6.4
Total Current Best Estimate (CBE)	88.9	209.8	226.5	279.4	431.6
Total CBE Plus 30% Margin	115.6	272.7	294.5	363.2	561.1

Appendix C: Inner Heliospheric Sentinels Spacecraft and Launch Stack Dimensions and Mechanical ICD

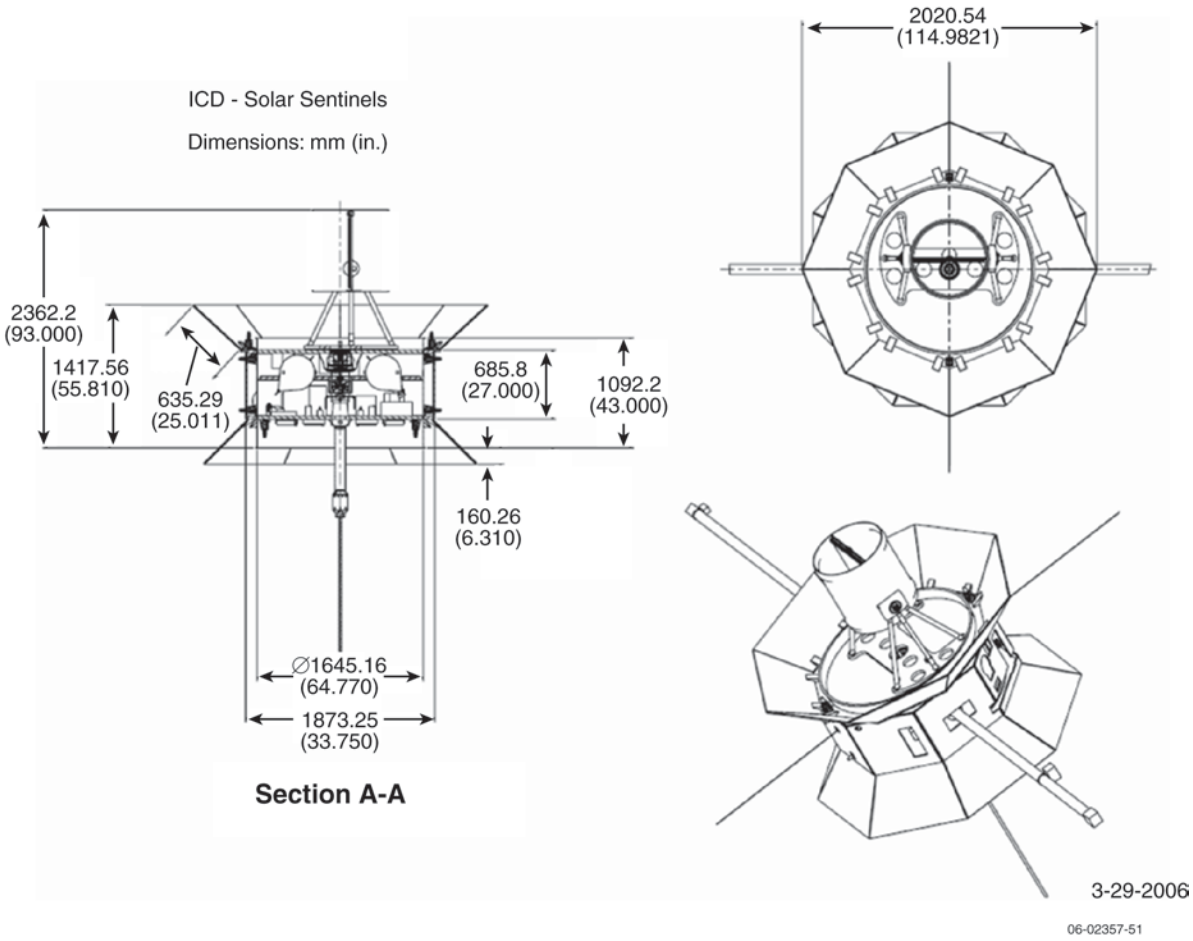

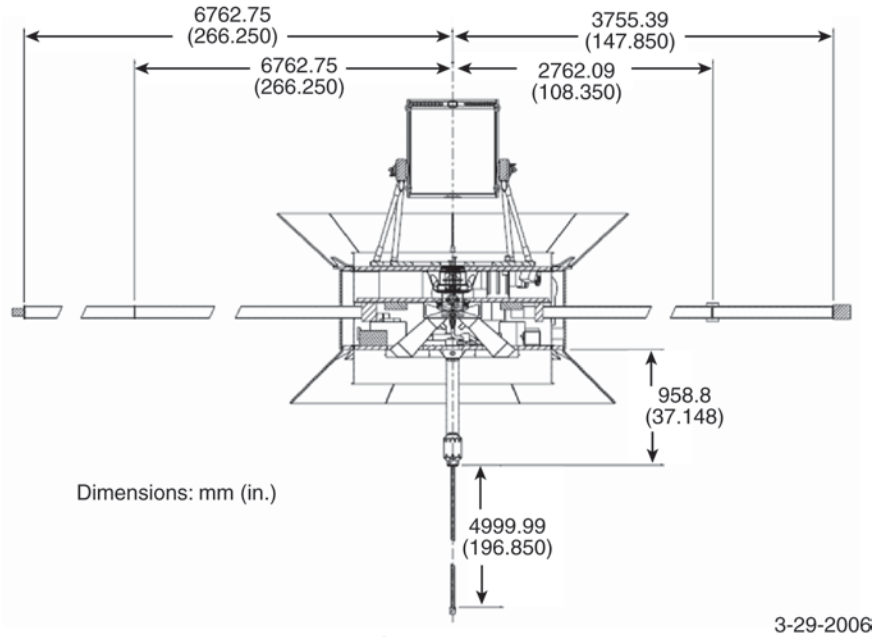

Section B-B

06-02357-52

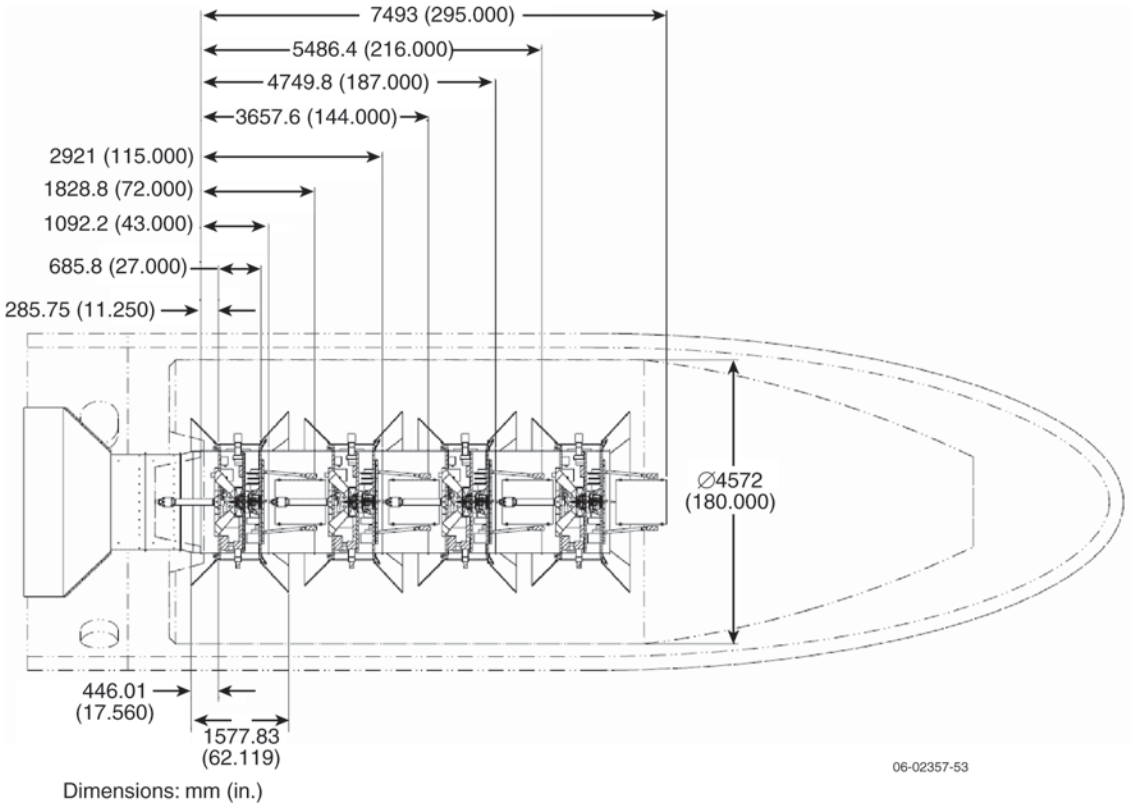

Dimensions: mm (in.)

Appendix D: Farside Sentinel: Report of the Science and Technology Definition Team

The Farside Sentinel (FSS) is designed to complement the Inner Heliospheric Sentinels (IHS) mission, which is tasked with probing the characteristics of the solar environment to within 0.3 AU of the Sun. While the four IHS spacecraft will conduct detailed in-situ investigations, FSS will provide a global context for these local measurements by studying the Sun from near 1.0 AU in conjunction with observations from the Earth. Thus, the more comprehensive view provided by the FSS mission will contribute to an improved understanding of the overall solar dynamics.

This section provides a high-level summary of the work completed in support of the Sentinels Science and Technology Definition Team (STDT). This summary is divided into two principal areas, as outlined below. Section D.1 provides an overview of the major design drivers and the overall mission trade space, and Section D.2 reviews a specific point design that fulfills the mission objectives consistent with a six-instrument suite. Additionally, a one-instrument design (using only the magnetograph) is presented as a comparison and possible "floor" option.

The geometry of the FSS mission is outlined in **Figure D-1**, which shows an ecliptic view of the mission. A single spacecraft would be placed into an Earth-leading orbit (~1 AU heliocentric range) that provides solar visibility from 60° to 180° ahead of the Earth. Additionally, a second spacecraft (nearly identical to the first) may be launched into an Earth-trailing orbit. Although this latter option was not studied, the major design drivers and spacecraft design presented in this section would generally apply to both the leading and trailing spacecraft with small design changes and less development risk for the second spacecraft.

One of the principal mission requirements is to provide overlap with the science phase of the IHS mission. The IHS mission was studied in parallel to this report, requiring several assumptions. It is assumed for this section that the earliest IHS launch would occur in January of 2014. IHS cruise would last 1 year followed by 4 years of science operations. Furthermore, the earliest FSS launch would occur in 2016 (2 years after the IHS launch), allowing a maximum overlap with the IHS mission of 3 years.

D.1 Major Design Drivers

The FSS system design is driven by the science objectives, as identified by the STDT. In particular, the instrument payload and trajectory have a major impact on the design. Depending on the instrument suite, its development can be nearly as complex and labor intensive as the spacecraft bus. Part of this complexity is due to the addition of the guide telescope, which is required by several instruments and imposes a need for precise pointing knowledge. The other principal driver is the set of derived requirements from the trajectory. The trajectory design process endeavors to fulfill the viewing requirements, including overlap with IHS, while trading launch vehicle size, flight times, magnitude of ΔV, and type of propulsion. The requirements derived from this process drive the use of a redundant spacecraft design (due to a longer flight time) and a more capable launch vehicle. Combined, the instrument payload and trajectory design directly drive the majority of the mission budget.

A secondary design driver is the science collection data rate. This data rate may fluctuate between 37.3 and 500 kbps, depending on desired science. While the data rate was found to be a less influential system driver, it is included in this analysis given the general desire to collect additional science data.

Table D-1 presents a summary of the principal design drivers, including the baseline used for this report, other options considered, and the type of analysis employed. The primary mission driver is

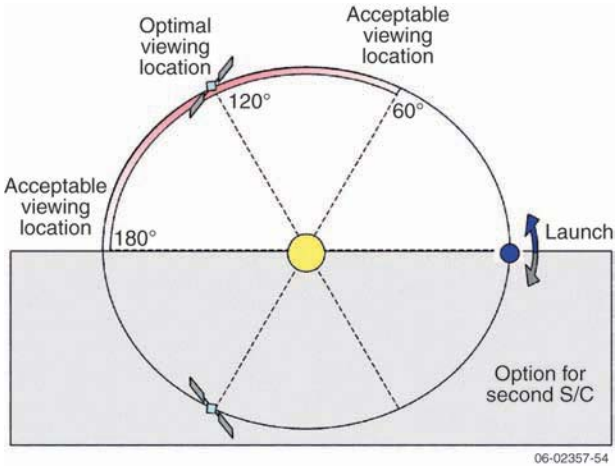

Figure D-1. Imaging Sentinels mission overview.

Table D-1. Summary of major design drivers.

Design Driver	STDT Report	Other Options	Type of Analysis
1. Instrument payload	Six-Instrument Suite: Magnetograph + Coronagraphs + In Situ	• Magnetograph only • Helioseismology • Magnetograph and Coronagraphs	Point designs system trade studies
2. Trajectory	0° to 180° drifting with lunar gravity assists	• 120° Fixed • Optimal 60° to 180° • 0° to 180° drifting (slow) • 0° to 180° drifting (fast)	Trajectory analysis system trade studies
3. Science data collection rate	115.6 kbps	• 37.3 to 500 kbps	Telecom analysis system trade studies

the instrument payload, which offers the greatest flexibility in reducing mission complexity. While the six-instrument suite studied in this report would be ideal, descoping to a one-instrument option would provide significant savings. Additionally, the trajectory provides an opportunity to trade mission complexity with the orbit location and duration of IHS overlap. Although a 0° to 180° drifting orbit is suboptimal for science collection, it allows a smaller Taurus launch vehicle to be used. Finally, the data rate may be varied from 37.3 to 500 kbps, depending on the desired science and available launch vehicle margin.

D.1.1 Science objectives. There are four instrument options that were identified by the STDT and considered here as part for the FSS mission trade space. These four options are outlined below and collectively build on each other. The minimum mission would be a simple magnetograph mission, whereas an ideal mission would be the magnetograph, two coronagraphs, and a package of in-situ instruments.

- ***Magnetograph***—Map the photospheric magnetic field from a different heliospheric longitude than Earth.
- ***Helioseismology—***Map the photospheric magnetic field from a different heliospheric longitude than Earth; also, provide Doppler measurements to allow helioseismology studies.
- ***Magnetograph + Coronagraphs***—Map the photospheric magnetic field from a different heliospheric longitude than Earth; also, observe coronal mass ejection (CME) propagation, high-speed streamers, electron jets, and other coronal structures from the solar surface to 60 R_S.
- ***Magnetograph + Coronagraphs + In Situ***—Map the photospheric magnetic field from a different heliospheric longitude than Earth, observe CME propagation, high-speed streamers, electron jets, and other coronal structures from the solar surface to 60 R_S; also, measure the in-situ plasma, magnetic field and energetic particle populations.

An instrument summary of these options is included in **Table D-2**. The table illustrates the instrument suite for each option. The first six instruments are science instruments, whereas the last two (the guide telescope and electronic boxes) are engineering components. Although a suggested data rate is listed below each option, this rate is flexible (that is, more is better), making it a separate design consideration.

D.1.2 Trajectory objectives. To be at the desired location at the right time for science data acquisition is a critical design driver. Attaining an orbit with the necessary Earth-relative phasing requires considerable cruise time and/or a larger launch vehicle. While there is some flexibility in the trajectory design, the resulting minimum acceptable mission duration is in excess of 3 years, requiring the use of redundancy in the flight system design. Similarly, escaping Earth's gravity requires more capability from the launch vehicle. Preferred trajectories (fully responsive to science desires) require the use of a Delta II launch vehicle. However, using trajectories with suboptimal flight path characteristics and/or minimizing the payload allow the use of a less costly Taurus launch vehicle.

Four trajectory options are presented in **Figure D-2**. They are selected as examples because they present performance suitable across several categories of requirements, including solar viewing positioning, overlap with IHS, and launch mass capability. Key mission parameters are presented in this table, illustrating how mission drivers (such

Table D-2. Summary of instrument options.

Instrument	Magneto-graph	Helio-seismology	Magnetograph + Coronagraphs	Magnetograph + Coronagraphs + In Situ (STDT Report)
Magnetograph	X		X	**X**
Enhanced Magnetograph		X		
Inner Coronagraph			X	**X**
Outer Coronagraph			X	**X**
Magnetometer				**X**
Solar Wind Proton & Electron				**X**
SEP Telescope				**X**
Guide Telescope			X	**X**
Electronic Boxes			X	**X**
Total mass	5.0 kg	7.0 kg	48.0 kg	**66.5 kg**
Total power	4.0 W	8.0 W	115.0 W	**130.0 W**
Total data rate	37.3 kbps	158.0 kbps	111.9 kbps	**115.6 kbps**

as ΔV and flight time) may be traded. Additionally, a fifth option is discussed, which is a derivative of the other trajectories, but includes two lunar gravity assists to increase the launch mass injection capability.

- ***120° fixed***—This trajectory design is driven by the desire to place a spacecraft in an Earth-relative fixed location (120° Earth-leading) as fast as possible, while delivering a suitable science payload.
- ***Optimal 60° to 180° drifting***—This option maximizes the overlap time with IHS by increasing the cruise time to reach 60° Earth-leading, and then slowing the drift rate to match the remaining IHS mission duration.
- ***0° to 180° drifting (slow)***—This option minimizes the post-launch ΔV to allow the use of a smaller

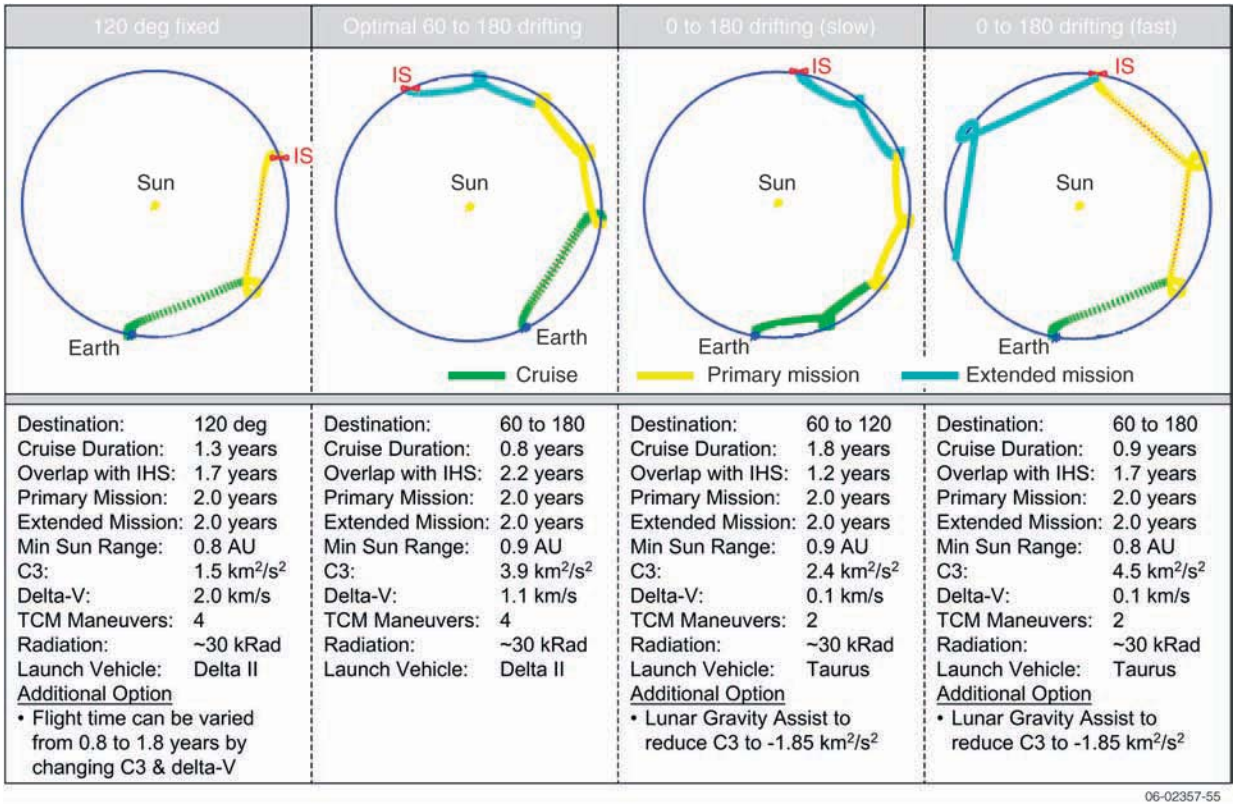

Figure D-2. Summary of trajectory options.

launch vehicle. The trajectory drifts slowly from Earth to the far side of the Sun over 6 years, which includes cruise, primary operations, and extended operations.

- ***0° to 180° drifting (fast)***—Like to the preceding option, this trajectory minimizes the post-launch ΔV, but the drift rate is faster, allowing the spacecraft to reach the far side of the Sun at the end of primary operations.
- ***0° to 180° drifting with two lunar gravity assists***—This option is a derivative of the third option, but includes two lunar gravity assists (LGAs). The LGAs lower the launch vehicle capability requirement (C3), but extend the cruise time.

D.1.3 Data acquisition strategy. Although the data rate is not a primary design driver, increases in data rate require the tailoring of the given flight system design to arrive at an optimal solution. Increasing or decreasing the data acquisition rate will drive the mass of the telecommunications and power subsystems. For the given options studied and depending on the launch vehicle margin, the data rate can sometimes be increased to use excess launch capability.

In general, the optimization method is to adjust the telecom/ground-system design for a given data rate while staying within the selected launch vehicle performance range. The transmitter size, high gain antenna (HGA), length and number of weekly Deep Space Network (DSN) passes, and DSN array are traded, emphasizing reduced mission operations, low flight system mass, and/or limited volume availability. For example, to accommodate a 500 kbps data rate and a Taurus launch vehicle, a 1.25 m HGA, two 8-hour passes/week, and 100 12-m DSN nodes are required. **Table D-3** summarizes the scope of the optimization parameters investigated.

D.1.4 Other design considerations. Beyond the principal design drivers, many other subsystem trades were considered, which contributed positively to the overall design. Of these trades, the attitude control (ACS) and propulsion subsystem trades are critical design considerations and are addressed in this subsection.

For this mission, there are three types of potential propulsion systems: monopropellant, bipropellant, and solar electric propulsion (SEP). Of these, monopropellant is the cheapest, but least efficient (Isp = 225 s). Bipropellant is slightly more expensive and more efficient (Isp = 325 s), and finally SEP is very expensive and highly efficient (Isp = 3100 s). Thus, a trade study was performed to determine what, if any, benefit might be realized from these three propulsion systems. The result was that a monopropellant system offers nearly equivalent performance at a lower price for all of the options considered.

Another trade study was conducted to determine what type of ACS system would provide the desired pointing and stabilization precision. The two primary options, both of which require the guide telescope pointing knowledge, were reaction wheels and warm-gas thrusters. The reaction wheels provide exceptional performance, but they are heavy and complex. In contrast, the warm-gas thrusters are a simpler solution. The result of this analysis showed that a warm-gas thruster system is feasible, which would significantly reduce mass and complexity. Additionally, the magnetograph, instead of the guide telescope, could provide the necessary pointing knowledge.

D.1.5 Mission trade space. To establish the mission trade space available within the constraints, three activities were conducted in parallel: (1) four "end-to-end" point designs were completed by the study team, (2) individual trajectory and subsystem trades were evaluated, and (3) the results were used to iteratively populate the Systems Trade Model (STM). The STM is a tool that models the payload, trajectory, subsystem, and ground system inputs. Once subsystems have been defined, characterized, and populated by the study team, the tool can

Table D-3. Summary of data rate options.

Science Data Rate Options	Telecom Subsystem Design & Ground Systems (optimized for design)			
	Transmitter Size	High Gain Antenna	Weekly Passes	DSN Coverage
37 to 500 kbps	25 to 250 W TWTA	0.85 to 1.5 m	4 to 8 hour duration 1 to 2 passes/week	36 to 100 12-m nodes (assumes new 200 node 12-m DSN array)

approximate alternative designs that are similar in nature to the existing point designs, modeling the downstream interactions and providing a trade space of insights. For this study, a trade space of hundreds of potential mission permutations was identified. Each permutation includes a mass equipment list, power budget (for three modes), and cost per element of the work breakdown structure (WBS), albeit additional validation is required to further consider individual options.[1]

In this context, the STM was used to support the FSS study. Specifically, the major design drivers were varied to produce an array of supporting mass, power, and schedule information. **Figure D-3** explicitly shows the impact from the four instrument options. The first and last options are based on point designs generated by the flight system team, whereas the middle options are an STM product. The result shows that the payload mass directly drives the flight system mass. More specifically, only the payload, structure, and cabling mass vary across the increasingly complex payload options. In contrast, the mass of the other subsystems remains nearly constant. As the options vary, component selections are adjusted within the power, attitude control, thermal, and telecom subsystems.

[1]Rather than validated point designs, the tool results are simply a guide for determining options for further study.

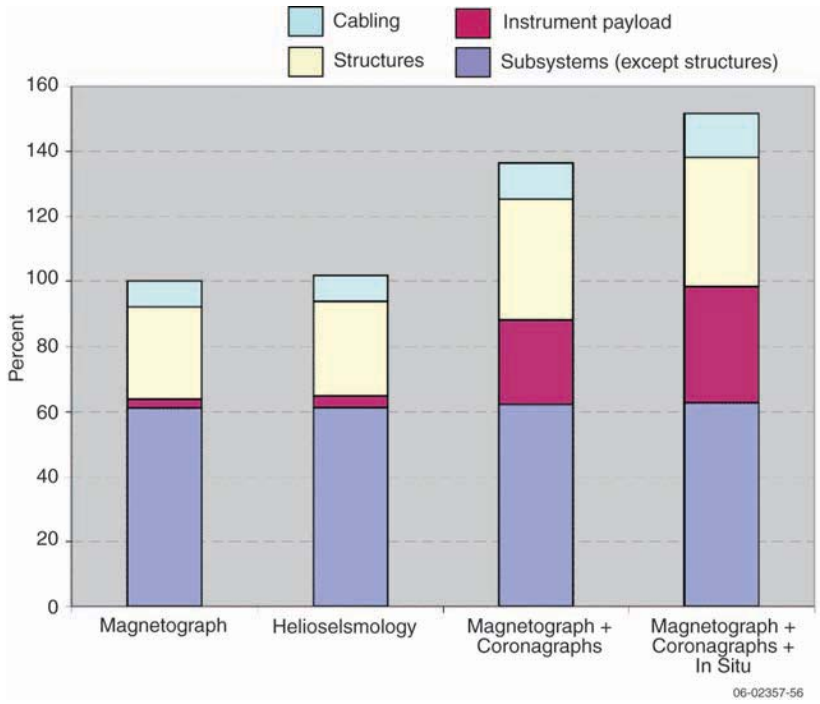

Figure D-3. Impact of instrument options on spacecraft dry mass.

Similarly, the modeling tool was used to consider mission launch mass with respect to payload, trajectory, and data rate. The results are shown in **Table D-4**, which provides a comprehensive understanding of the mission trade space. The matrix consists of the five trajectory options, four payload options, and two data rate options, resulting in 40 unique design concepts. These concepts are listed by total launch mass and color-coded by the approximate mission proposal class. Additionally, three of the point designs that were used to span this trade space are outlined in bold.

D.2 Mission Implementation: Six-Instrument Taurus Option

The science objectives for the Imaging Sentinel suggest a variety of mission concepts, which were examined in the previous section as part of the comprehensive mission trade space. Of these missions, the Six-Instrument Taurus Option was selected for this section. It is a point design (developed by the engineering study team), includes a full instrument suite, and fits on a Taurus launch vehicle. It uses a 0° to 180° drifting trajectory and a data rate of 115.6 kbps. Additionally, a second concept, the One-Instrument Taurus Option, is summarized as a comparison to the baseline mission. This second concept (also developed by the study team) is a point design that provides a simpler solution and satisfies the floor science requirements.

D.2.1 Instrument definition. The baseline mission concept includes six science and two engineering instruments, as defined by the STDT, which are characterized in **Table D-5** and **Table D-6**, alongside the One-Instrument Taurus Option. This instrument suite includes a magnetograph, inner and outer coronagraphs, magnetometer, solar wind proton and electron telescope, and solar energetic particle (SEP) telescope, along with the guide telescope and the camera and electronic boxes. This combined instrument suite provides the following capabilities:

Table D-4. Mission trade space.

Trajectory Options	Total Launch Mass (kg) Instrument Payload Options: Magnetograph	Helioseismology	Magnetograph + Coronagraphs	Magnetograph + Coronagraphs + In Situ
120° fixed	L: 510 kg	H: 580 kg	H: 737 kg	H: 765 kg
	VL: 458 kg	L: 517 kg	L: 674 kg	L: 742 kg
Optimal 60° to 180° drifting	L: 479 kg	H: 545 kg	H: 693 kg	H: 719 kg
	VL: 429 kg	L: 485 kg	L: 633 kg	**L: 697 kg (3)**
0° to 180° drifting (slow)	L: 273 kg	H: 328 kg	H: 357 kg	H: 429 kg
	VL: 243 kg	L: 276 kg	L: 349 kg	L: 370 kg
0° to 180° drifting (fast)	L: 273 kg	H: 328 kg	H: 349 kg	H: 429 kg
	VL: 243 kg (1)	L: 276 kg	L: 349 kg	L: 394 kg
0° to 180° drifting w/LGA	L: 273 kg	H: 328 kg	H: 394 kg	H: 395 kg
	VL: 243 kg	L: 276 kg	L: 364 kg	**L: 402 kg (2)**

Validated point designs					
(1) One-Instrument Taurus Option	**Mission cost**	**MIDEX class**			**Discovery class**
(2) Six-Instrument Taurus Option		VL	L	M	H	VH
(3) Six-Instrument Delta II Option	**Data rate**	VL = 37.3 kbps	L =115.6 kbps		H = 500 kbps	

Table D-5. Instrument payload overview.

Payload	Six-Instrument Taurus Option	One-Instrument Taurus Option[a]
Number of science instruments	6	1
Number of engineering instruments	2	0
Mass	66.5 kg	5.0 kg
Power	130.0 W	4.0 W
Science data collection rate	115.6 kbps	37.3 kbps

[a] The One-Instrument Taurus Option includes only the Magnetograph, which fulfills the first science capability of measuring the surface structure, solar dynamics, and solar magnetic flux.

Table D-6. Detailed instrument specifications.

Instruments	Mass (kg)	Power (W)	Data Rate (kbps)	Comments
Magnetograph	10.0	20.0	37.3	Unique magnetographs are used for each design
Inner Coronagraph	10.0	20.0	37.3	Pointing requirements: 20 arcsec control, 0.1 arcsec knowledge, <5 arcsec/s stability
Outer Coronagraph	10.0	20.0	37.3	
Magnetometer	2.5	1.0	0.5	Requires a 5-m boom
Solar Wind Proton & Electron	6.0	6.0	2.0	
SEP Telescope	10.0	8.0	1.2	
Guide Telescope	3.0	5.0	–	Engineering instrument, which provides 0.1 arcsec pointing knowledge
Camera & Electronic Boxes	15.0	50.0	N/A	Includes an instrument data processing unit (IDPU)
Total	**66.5**	**130.0**	**115.6**	

- Map the photospheric mag-netic field from a different heliospheric longitude than Earth
- Observe CME propagation, high-speed streamers, electron jets, and other coronal structures from the solar surface to 60 R_S
- Measure the in-situ plasma, magnetic field and energetic particle populations.

Table D-6 provides a detailed summary of the instrument specifications. It outlines the mass, power, and data rate specifications for the payload. Additionally, this table provides some information on the pointing requirements. Specifically, the inner and outer coronagraphs drive the pointing requirements. They require 20-arcsec control from the

spacecraft to locate the Sun-center. Once located, a pointing knowledge of 0.1 arcsec (provided by the guide telescope) is required along with stability of better than 5 arcsec/s. These fine pointing requirements and the complex interaction between the instrument suite and the attitude control subsystem require some atypical payload elements. First, the instruments should be mounted as an integrated payload module on a carbon optic bench, as they require careful alignment and integration. Second, an instrument data processing unit (IDPU) is required to coordinate data transfer with the guide telescope. This component is included in the electronic boxes. Finally, the magnetometer requires a 5-m boom in order to provide some separation from the spacecraft.

In the case of the One-Instrument Option, the payload is significantly reduced. The pointing requirements are relaxed such that the star cameras, Sun sensors and inertial measurement unit (IMU) can provide adequate pointing control and knowledge (eliminating the need for the guide telescope) and, similarly, the IDPU is unnecessary. The Magnetograph provides its own internal mechanization for jitter control.

D.2.2 Mission design. Reaching the far side of the Sun is on par with interplanetary travel. Consequently, the trajectory for this mission is a design driver. Several possible trajectories were investigated, including fixed orbits, drifting orbits, varying rates of speed, low-energy trajectories, and lunar gravity assists (LGAs). Of these, the 0° to 180° Drifting Orbit with LGAs was selected for two reasons. It results in a relatively long overlap with IHS (1.5 years), while maintaining a sufficiently low C3 (–1.85 km^2/s^2) to accommodate a Taurus launch vehicle. With 30% mass and power contingency and 3σ ΔV load, this combination may raise the risk, as the resulting launch vehicle margin is low (that is, <10 kg). If the spacecraft grows beyond the design contingency, then either a Delta II launch vehicle would be required; alternatively, reoptimization of the flight system and data return strategy might allow launch within the Taurus performance. **Table D-7** lists additional parameters related to mission design, along with a comparison to the One-Instrument Taurus Option, which uses a similar trajectory, but without the LGAs.

0° to 180° drifting trajectory with lunar gravity assists. The trajectory chosen for the baseline mission concept is shown in **Figure D-4**. Following launch from Earth, the trajectory uses two unpowered LGAs to escape Earth's orbit. The trajectory then becomes a solar elliptical orbit (0.85 × 1.0 AU), which results in a drift velocity of 60° per year and provides 1.5 years of overlap with the IHS mission. The primary mission ends after 2 years of science, when the spacecraft reaches the far side of the Sun. Beyond this location, the spacecraft has the option of entering an extended mission phase, as the spacecraft continues beyond 180° leading. If a 2-year extended mission is approved, the spacecraft would reach 300° Earth-leading (or 60° Earth trailing) at the conclusion of the 5.5-year mission. Additionally, a preliminary estimate of navigational ΔV shows the 85 m/s would be sufficient for this trajectory. (The STEREO mission, with a similar trajectory, uses 100 to 180 m/s for ΔV, depending on the launch date.)

Launch vehicle performance. **Figure D-5** shows the launch vehicle performance for the most likely range of launch vehicles, given a C3 of –1.85 km^2/s^2. Data for this graph was generated

Table D-7. Mission design overview.

Mission Design	Six-Instrument Taurus Option	One-Instrument Taurus Option
Destination	0 to 180 Drifting	0 to 180 Drifting
Lunar gravity assist?	Yes (×2)	No
Duration of IHS overlap	1.5 years	1.7 years
Maximum Sun range	0.85 AU	0.8 AU
Maximum Earth range	2.0 AU	2.0 AU
C3	–1.9 km^2/s^2	4.5 km^2/s^2
ΔV	85 m/s	85 m/s
Number of maneuvers	6	2
Launch vehicle (LV)	Taurus 3113 / Star 37F	Taurus 2130
Fairing size (inner diameter)	1.4 m	1.4 m
LV adapter (LV-side) included?	No	Yes
LV performance	445.0 kg	310.0 kg
LV margin	8.7 kg	67.3 kg

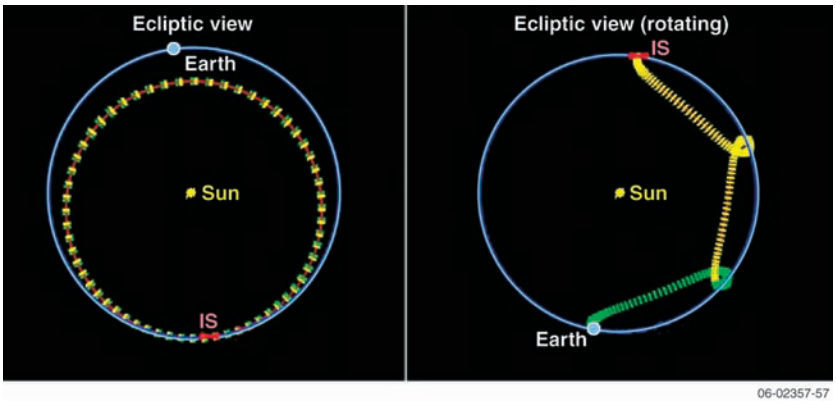

Figure D-4. 0° to 180° drifting trajectory with lunar gravity assists.

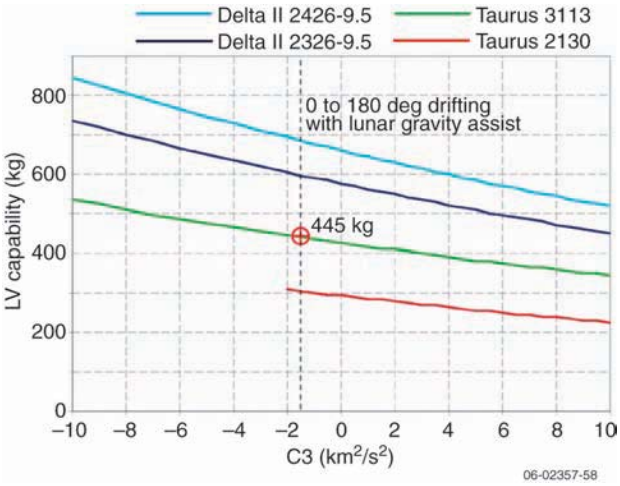

Figure D-5. Launch vehicle performance.

from the Kennedy Space Center (KSC) Launch Vehicle Site for the Delta II and Taurus 2130 options. However, for the Taurus 3113, unofficial estimates were used, given known launch vehicle parameters, combined with a Star 37 F solid rocket booster. Additionally, this capability (445 kg) does not include an adapter on the launch vehicle side (~30 kg), which has been accounted for separately in the mass equipment list.

Launch vehicle accommodation. The selection of a Taurus, particularly the Taurus 3113, adds a volume constraint within the fairing. Specifically, the fairing diameter is 1.4 m and the height (after providing for the Star 37 F motor) is 2.4 m. These constraints require a configuration design to ensure that adequate volume margin exists with the proposed mission concept. **Figure D-6** shows how this configuration works, along with the necessary design changes to accommodate this concept. The principal change was to the high gain antenna, which decreased from 1.5 m (on the Delta II) to 1.25 m to accommodate the smaller Taurus diameter. Additionally, deployment mechanisms were added to the four solar array panels, allowing them to be stowed during launch. Also shown in the figure below are the fourth and fifth stages of the Taurus 3113. The fourth stage is an Orion motor, and the fifth stage is the Star 37 F motor, which is housed within the payload fairing.

D.2.3 Flight system overview. FSS requires an interplanetary, dual-redundant flight system design that can accommodate a 66.5 kg and 130 W payload on a trajectory to the far side of the Sun. These requirements limit the potential use of an off-the-shelf industry spacecraft. Instead, a flight system

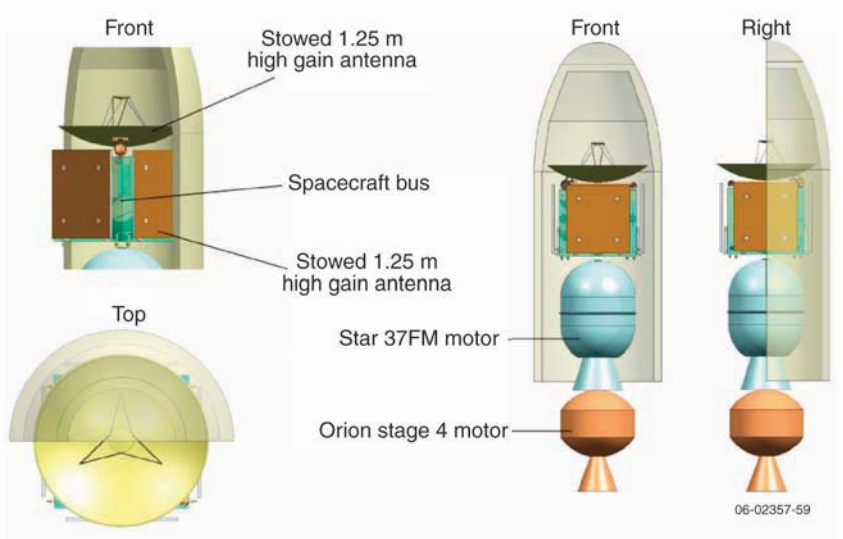

Figure D-6. Launch vehicle accommodation.

team generated a design that emphasizes available, high-heritage components, as outlined in this section.

Description. The key flight system parameters are listed in **Table D-8**. The spacecraft is an industry-subcontracted spacecraft with a lifetime of at least 3.5 years. It is primarily dual-string, except for specific components such as the high gain antenna and the instrument payload. It is radiation tolerant for an expected lifetime dose of 30 krad. It is cube-shaped with an aluminum honeycomb structure, four deployable solar arrays, a deployable high gain antenna, and a deployable 5-m boom for the magnetometer. The single internal hydrazine tank is located beneath the integrated instrument module.

The spacecraft dry mass is fairly light at 216.8 kg. However, once the payload, launch vehicle adapters, 30% contingency, and propellant are added, the total launch mass becomes 439.5 kg, which is just under the 445 kg launch vehicle capability. The peak power, including contingency, is 595.1 W, which is reached while operating the thrusters.

The spacecraft block diagram is shown in **Figure D-7**, which outlines the key spacecraft components. These components are further discussed as distinct subsystems in the following sections. In general, the

Table D-8. Flight system overview.

Flight System	Six-Instrument Taurus Option	One-Instrument Taurus Option
Mission class (A/B/etc.)	B	B
Mission lifetime	3.5 years	3.0 years
Redundancy	Dual-string	Dual-string
Total radiation dose	30 krad	30 krad
Peak power mode	Thruster control	Thruster control
Peak power (w/contingency)	595.1 W	431.6 W
Payload mass	66.5 kg	5.0 kg
Spacecraft dry mass	216.8 kg	160.1 kg
System dry mass (w/contingency)	368.3 kg	214.6 kg
Propellant mass	37.6 kg	30.9 kg
Total launch mass	439.5 kg	245.5 kg
Reserves	30%	30%

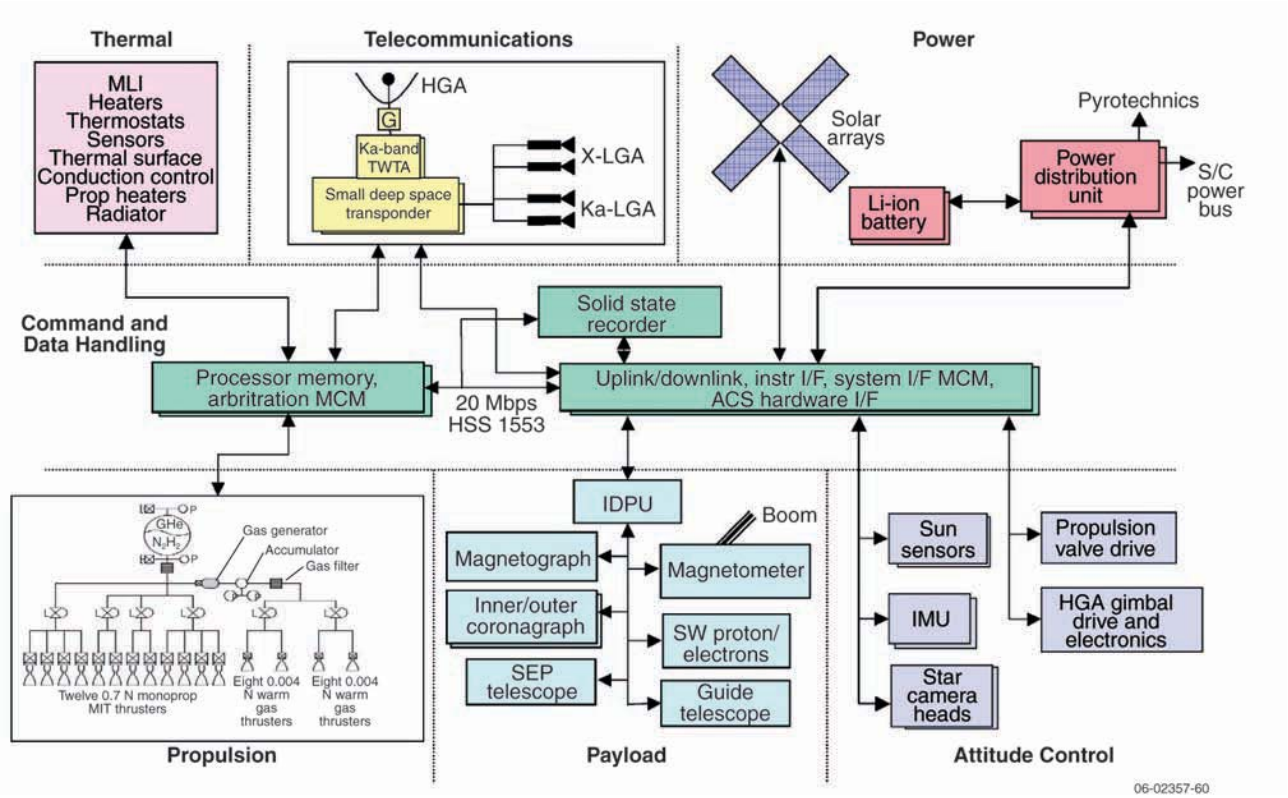

Figure D-7. Flight system block diagram for the Six-Instrument Option.

components are all high-heritage, flight-validated components that are either currently available or will be available by 2012 (4 years prior to the earliest launch date). Aside from the high gain antenna, dual-string redundancy is found throughout the system, including multiple low gain antenna horns, two batteries, two solid-state recorders, two flight computers, and redundant propulsion and ACS subsystems.

Mass and power budget. The mass budget is summarized is in **Table D-9**. These numbers are based on a detailed mass equipment list, which includes current best estimates for each component. These individual estimates are summarized in the table and include cabling and a spacecraft adapter. Additionally, the Taurus 3113 does not include a spacecraft adapter on the launch vehicle side. Therefore, it is included here as 33.6 kg (or 5% of the dry mass). The total launch mass, including 30% contingency for growth, is 439.5 kg.

The power budget is also summarized in **Table D-9**. These numbers are based on a detailed power mode sheet that considers when specific spacecraft components are operated and their respective power levels. The five power modes shown in the table were considered, along with modes for safing and science/telecom. From this analysis, the thruster control power mode is the highest power mode, as shown in the table. During this power mode, most subsystems are operational (including propulsion and telecom), while the instruments are powered off. Adding 30% contingency, the total power required is 595.1 W.

Mechanical design. The FSS mechanical design is a typical cubic spacecraft layout as described in **Table D-10**. Its dimensions allow it to tightly fit within the 1.4-m fairing of a Taurus launch vehicle. There are seven mechanisms, which are primarily used for deploying the four solar arrays, the high gain antenna, and the boom for the magnetom-

Table D-9. Mass and power budget.

Flight System Element	Power (W)
Payload	N/A
C&DH	6.5
Telecom	198.0
Attitude control	72.0
Power	41.6
Propulsion	52.7
Thermal	87.0
Structure	N/A
Subtotal	457.8
Power contingency	137.3 (30%)
Total	**595.1**

Summary of Power Modes	Power (W)
Science	369.2
Instrument calibration (array sizing)	570.8
Thrusters (highest power)	595.1
Cruise/telecom	492.1
Launch (battery sizing mode)	393.8

Flight System Element	Mass (kg)
Payload	66.5
C&DH	12.6
Telecom	22.0
Attitude control	8.8
Power	41.8
Propulsion	13.1
Thermal	19.3
Structure	99.3
Cabling	24.8
S/C adapter	6.5
Subtotal	283.3
Mass contingency	85.0 (30%)
Spacecraft dry mass	368.3
Propellant	37.6
Launch vehicle adapter	33.6 (5%)
Total launch mass	**439.5**
LV capability	445
LV margin	6 (1%)

Table D-10. Mechanical design overview.

Mechanical Design	Six-Instrument Taurus Option	One-Instrument Taurus Option
Spacecraft dimensions	0.97 x 0.97 x 0.97 m	< 0.97 x 0.97 x 0.97 m
High gain antenna diameter	1.25 m	1.25 m
HGA boom length	1.25 m	1.25 m
Magnetometer boom length	5.0 m	N/A
Number of mechanisms	Solar array deployment (4) HGA 2-axis articulation (1) HGA deployment (1) Mag. boom deployment (1)	SA deployment (4) HGA 2-axis articulation (1) HGA deployment (1)
Number deployments	Solar array deployment (1) HGA deployment (1) Mag. boom deployment (1)	Solar array deployment (1) HGA deployment (1)

eter. Only the high gain antenna requires additional articulation, allowing it to point toward Earth as the spacecraft drifts to the far side of the Sun. The solar arrays do not require articulation, since the spacecraft is continuously pointed at the Sun, except during launch, trajectory correction maneuvers (TCMs), and events where battery-backup is provided. The One-Instrument Option is similar, but would have a smaller bus size, and it would not have the boom or deployment associated with the magnetometer.

Figure D-8 illustrates the FSS flight system configuration. The solar array has four symmetric wings to minimize disturbances to the control of the flight system. Similarly, the high gain antenna and magnetometer boom are mounted at opposite ends. Internally, the instruments are mounted on a carbon optical bench, which is attached to the top of the spacecraft. Most instruments face outward, directly into the Sun.

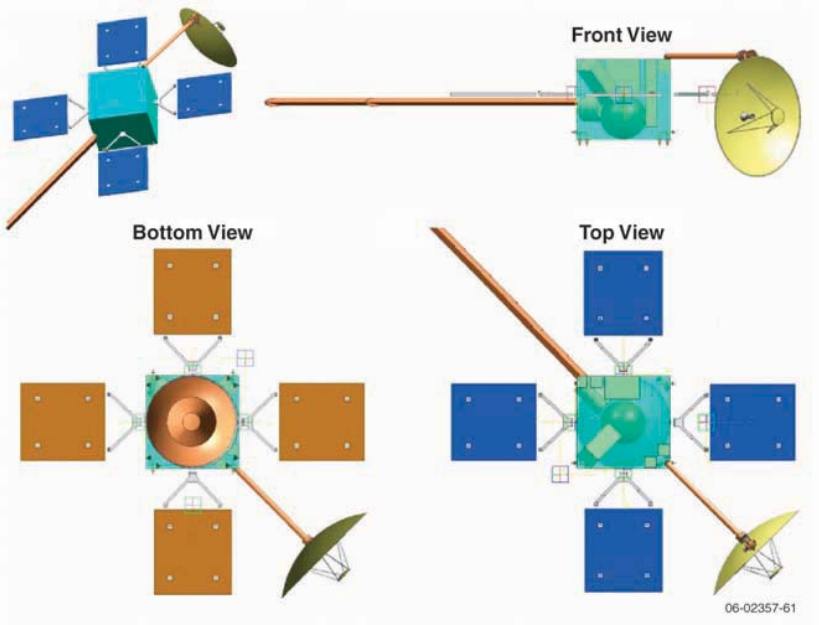

Figure D-8. Flight system configuration.

Thermal control. The thermal control for the spacecraft (**Table D-11**) ensures that all flight subsystems are maintained within their desired thermal ranges. This control accounts for external environmental influences (primarily the Sun between 0.85 and 1.0 AU) and internal power dissipation. Additionally, the science instrument thermal interfaces are monitored to ensure correct thermal control of the integrated instrument module.

To accomplish these objectives, various passive and active elements are used. Passive elements include lightweight multilayer insulation, thermal surfaces, conduction control, and a thermal radiator for the telecom system. Active elements include temperature sensors and electric heaters/thermostats for the propulsion elements, batteries, critical flight elements, and instruments.

Power. The three components of the power subsystem are the solar array, battery, and power electronics. The solar array is used nearly continuously, except during launch and trajectory maneuvers (as necessary). It is sized at 2.24 m^2 to accommodate a peak power of 589.5 W, assuming a maximum heliocentric range of 1.0 AU and the use of state-of-the-art triple-junction technology. Two 50-Ah lithium-ion batteries are used for reserve power and augmentation during high demand modes. These batteries are currently used on short-term missions and will be fully validated for long-term missions by 2012. The power electronics will be packaged in a 6U form factor and support power distribution, battery charge control, bus voltage control, and load-switching function. (See **Table D-12**.) The One-Instrument Option is similar, but relies on smaller 1.27 m^2 solar arrays and 30-Ah batteries to provide for a TCM peak power of 431.6 W.

Telecommunications. The design of the telecom subsystem (**Table D-13**) and DSN coverage are tightly coupled, such that the design can be

Table D-11. Thermal control subsystem parameters.

Thermal Control	Six-Instrument Taurus Option	One-Instrument Taurus Option
Number of thermostats	16	12
Number of heaters	20	18
RF out	27.0 W	9.0 W
Radiator size	0.33 m^2	0.31 m^2

Table D-12. Power subsystem parameters.

Power	Six-Instrument Taurus Option	One-Instrument Taurus Option
Solar array type	GaAs-TJ	GaAs
Solar array size	2.24 m^2	1.27 m^2
Battery type	Li-Ion	Li-Ion
Battery size	50 Ah	30 Ah
Power electronics	Power distribution, battery & solar array control, 6U form factor, provide redundancy and single fault tolerance	Power distribution, battery & solar array control, 6U form factor, provide redundancy and single fault tolerance

Table D-13. Telecommunications subsystem parameters.

Telecommunications	Six-Instrument Taurus Option	One-Instrument Taurus Option
Band (S/X/Ka/etc.)	X-band up Ka-band down	X-band up Ka-band down
Redundancy	Dual-string	Dual-string
High gain antenna size	1.25 m	1.25 m
TWTA power	90.0 W	30.0 W
Downlink data rate	2.8 Mbps	0.9 Mbps
Pointing accuracy	0.1°	0.1°
Margin	3.02 dB	3.42 dB

optimized for low mass, reduced DSN operations, or a combination thereof. Allowing for a science collection data rate of 115.6 kbps and the Taurus 3113 fairing, the telecom design was optimized to reduce both dry mass and DSN operations. Correspondingly, the minimum DSN coverage is employed, which consists of one 8-hour weekly pass with 36 12-m DSN antennas (using the new DSN array). For this coverage frequency and receiving aperture, a Ka-band downlink rate of 2.8 Mbps is accommodated. The downlink requirement coupled with a 1.25-m high gain antenna on the spacecraft requires a 90.0-W traveling wave tube amplifier (TWTA) to achieve an RF power of 45 W. A pointing accuracy of 0.1° (3σ) is required, which produces approximately 3 dB of margin. Additionally, there are two X-band low gain antenna horns for receiving and two Ka-band low gain antenna horns for transmitting during launch and emergencies. Finally, solar conjunction at the far side of the Sun is a concern, and limited communication should be expected for 20 to 30 days near the conclusion of the primary mission. The One-Instrument Option is similar, but the lower science data collection rate (37.3 kbps) requires only a 30-W TWTA.

Command and data handling (C&DH). The C&DH subsystem is identical for each of the FSS mission concepts considered. Given a technology cutoff date of 2012, the minimum set of avionics hardware identified provides sufficient data processing and storage for all of the options (see **Table D-14**). It is assumed that the multi-chip modules (MCMs) can be micro-packaged on two 6U cPCI cards, all science and ACS instruments will have their own microcontroller/FPGA and data buffer, and the next generation of MSAP (multiservice access platform) electronics will be available. Given these assumptions, the hardware listed in **Table D-14** is a reasonable extension of current technology. This subsystem is dual-string, requiring that each processor be mounted on a separate card and cross-strapped to the two solid-state recorders. This set of advanced electronics will have up to 256 analog channels with an expected design life of at least 8 years.[2]

Software. This mission is similar to a typical deep space mission with payloads nearly identical to STEREO and TRACE, resulting in some code reusability (20–30%) depending on the mission type (see **Table D-15**). The flight software (FSW) must be NASA and CMMI compliant with typical data management and commands for each subsystem. The ACS is the only exception; it requires additional complexity in providing very precise 3-axis stability using the guide telescope. The ACS and guide telescope are tightly linked to provide 20 arcsec of control and 0.1 arcsec of knowledge. The FSW also provides fault protection that monitors, analyzes, and responds to faults, resource management, and timing.

[2]Project should reference the "Design Principles Matrix ID-62432" regarding pre-Phase A design margins for memory allocation for boot code, flight image, hardware interfaces, power, mass, etc.

Table D-14. Command and data handling subsystem parameters.

Command & Data Handling	Six-Instrument Taurus Option	One-Instrument Taurus Option
C&DH redundancy	Dual-string	Dual-string
Flight computer	Arbitration MCM, Advanced PowerPC processor, 20 Mbps, 50-krad rad-tolerant, 128 analog channels (2)	Arbitration MCM, Advanced PowerPC processor, 20 Mbps, 50-krad rad-tolerant, 128 analog channels (2)
Cards	6U cPCI (2)	6U cPCI (2)
Solid-state recorder	MTO heritage (2)	MTO heritage (2)
Processor speed	240 MIPS	240 MIPS
Mass memory requirement	20.0 Gbits/day	10.0 Gbits/day
Onboard memory storage	360.0 Gbits	360.0 Gbits

Table D-15. Software parameters.

Software	Six-Instrument Taurus Option	One-Instrument Taurus Option
Autonomy?	No	No
Code reusability	20%	30%
Subsystem complexity	High ACS complexity	Med ACS complexity

Attitude control system (ACS). Given the tight pointing requirements (see **Table D-16**) and the coupling between the ACS and the instrument payload, the complexity and operation of the ACS is fairly high. Originally, reaction wheels were required to meet these requirements. However, a commercially available warm-gas thruster system may be used in conjunction with the hydrazine propulsion system, which significantly reduces complexity.

To accommodate the desired pointing requirements, various assumptions were necessary. The instruments should be integrated and tested as a separate module prior to being assembled to the spacecraft (similar to STEREO). Once the instruments are aligned on a common optical bench, the guide telescope becomes the key boresight reference for all science pointing control and knowledge functions. Thus, the spacecraft can be stabilized on the Sun-line (including pitch, yaw, and roll) using the warm-gas thrusters. Beyond this initial stabilization, the thrusters can use the guide telescope to satisfy the high pointing requirements for pitch and yaw, whereas roll can only be maintained to an accuracy of 20 arcmin (effectively preventing image blurring). This degree of accuracy must be maintained as the spacecraft orbits the Sun at a rate of approximately 1° per day.

It is critical that the instruments are aligned to within 30 arcsec on the integrated instrument module. Following launch, careful instrument calibration during cruise can eliminate this systematic bias. The guide telescope can provide sufficient pointing knowledge to calibrate the payload during cruise. It operates at 50 to 100 Hz with 0.1-arcsec-noise (1σ), which is filtered by the ACS to less than 0.1 arcsec (3σ). Additionally, the magnetograph may also be used in a similar fashion, to produce pointing knowledge (possibly degraded).

The warm-gas thrusters can adequately provide sufficient pointing to eliminate the need for reaction wheels. The gaseous hydrazine is metered by the 4.4-mN Moog thrusters at a feed pressure of 5 psia. The 1 bit (torque impulse bit) of coupled thrusters with 5 ms solenoid actuation time and 0.5 m moment

Table D-16. Attitude control subsystem parameters.

Attitude Control System	Six-Instrument Taurus Option	One-Instrument Taurus Option
Stabilization	3-axis	3-axis
Pointing control	20 arcsec	0.1°
Pointing knowledge	0.1 arcsec (using payload)	0.1° (instrument provides fine knowledge & stability)
Pointing stability	<5 arcsec/s	<5 arcsec/s
Hardware	Coarse Sun sensors (2) Star trackers (2) Internally redundant IMU Warm gas thrusters (16)	Coarse Sun sensors (2) Star trackers (2) Internally redundant IMU Warm gas thrusters (16)

arms is 22 μNms. Assuming a reasonable spacecraft inertia of 125 Nm^2, the minimum inertia rate is 0.15×10^{-6} rad/s, which is within the required 0.20×10^{-6} rad/s rate derived as the heliocentric angular rate of the instruments. The result is that the thruster one bit quantization satisfies the 20 arcsec control and 5 arcsec/s stability required by the inner and outer coronagraphs.[3]

Propulsion. Since this mission concept does not require large ΔV maneuvers to slow or stop the spacecraft, only a small propulsion system is required. This propulsion system should be sufficient to correct launch injection errors and provide slight adjustments for the lunar gravity assists. The necessary ΔV is estimated at 85 m/s and an additional 20 kg of hydrazine is required for ACS (see **Table D-17**).

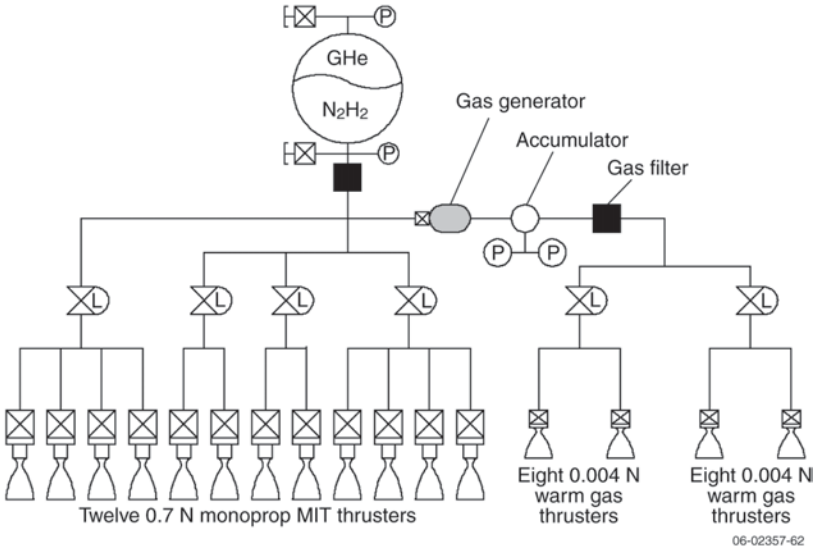

Figure D-9. Propulsion subsystem block diagram.

A block diagram of the propulsion system is shown in **Figure D-9**. A single hydrazine tank holds approximately 30 kg of propellant and pressurant. This fuel feeds to two separate thruster systems. The first thruster system contains two branches of four 0.7-N MIT thrusters that provide thrust for the ΔV burns and pitch/yaw attitude control and two branches of two 0.7-N MIT thrusters for maneuver roll attitude control for a total of 12 thrusters. The second thruster system includes two branches of eight warm gas 0.004-N thrusters for science orbit attitude control. These thrusters are fed by pressure from a warm gas accumulator tank that is maintained by passing hydrazine the through a gas generator based on pressure measurements on the downstream accumulator. The specific thrusters used for this warm gas system are the Moog cold gas thrusters.

[3]A Pointing Control Law will regulate the line-of-sight (LOS) angular rate and position relative to the solar centroid using the IMU and Star Cameras and Guide telescope inputs to a state estimation filter for full state feedback to the rate and position compensator loops that modulate the micro-thruster firings. A feed-forward angular rate signal also may be used based on the heliocentric orbital ephemerides determined by ground tracking and uploaded to the spacecraft.

D.2.4 Ground systems. As previously described, the ground system design and the telecom subsystem are tightly coupled with a necessary trade between increasing mass and power of the telecom transmitter versus adding DSN time and antennas. For the baseline mission concept, a science data collection rate of 115.6 kbps allows for both a relatively small telecom design and a maximum of a single 8-h weekly DSN pass of 36 12-m antennas during science operations (**Table D-18**).

Cruise tracking and operations occur for the 18 months prior to the start of science operations. During this period, one 4-h weekly DSN pass with a single 12-m antenna supports navigation tracking, routine spacecraft commanding, health-and-status assessment, and instrument calibration. Additionally, throughout the first 8 weeks after launch, greater 12-m array tracking may be

Table D-17. Propulsion subsystem parameters.

Propulsion	Six-Instrument Taurus Option	One-Instrument Taurus Option
Propulsion system	Monopropellant	Monopropellant
ACS propellant	20 kg	20 kg
Number of 0.7-N thrusters	12	12
Number of warm gas thrusters	16	16
Isp	225 s	225 s

Table D-18. Ground systems overview.

Ground Systems	Six-Instrument Taurus Option	One-Instrument Taurus Option
Engineering data rate (uplink)	0.5 kbps	0.5 kbps
Engineering data rate (downlink)	2.0 kbps	2.0 kbps
Data return overhead	15%	15%
Phase E: Cruise		
Link duration	4 h	4 h
Passes per week	1	1
Number of 12-m antennas	1	1
Downlink data rate	0.025 Mbps	0.025 Mbps
Phase E: Operations		
Link duration	8 h	8 h
Passes per week	1	1
Max number of 12-m antennas	36 (average of 33)	36 (average of 33)
Downlink data rate	2.8 Mbps	0.9 Mbps

necessary to support the correction of launch vehicle errors, lunar gravity assists, orbit determination, and flight system characterization. For most of cruise, a minimum spacecraft team is required to support instrument operations, gradually increasing as the instrument suite is calibrated prior to the start of science operations. Although a single DSN 12-m antenna should support this level of activity, it is possible that the DSN will only assign the antennas in larger blocks. If so, then the larger block would be used with biweekly 4-h passes, which is the minimum time required for a navigation orbital dynamics solution.

Primary science operations will last for 2 years with tracking provided by the DSN 12-m array. One 8-h weekly pass is required to support playback of science data, navigation tracking, routine spacecraft commanding, and health-and-status assessment. At the start of the prime mission, the number of required array nodes would increase to 29 12-m antennas, slowly increasing to a maximum of 36 antennas as the distance from Earth to the spacecraft increases. If the mission is further extended, the number of antennas will begin to drop as the spacecraft flies past the far side of the Sun and the range begins to decrease.

Figure D-10 presents a block diagram for the ground system design. There are three major elements, including the spacecraft, the mission operations control center, and the data processing and distribution center. These elements cleanly interact to deliver solar data from the instruments to the science team via the science data archiving system. Along with the delivery of this data, the health of the spacecraft must be continually assessed and commanded as necessary, as illustrated in the figure.

D.3 Schedule

The schedule for design, development, and operations is outlined in **Table D-19**. This schedule follows general Jet Propulsion Laboratory (JPL) design principles, slightly extended given the complexity of developing the integrated instrument module that is mounted on the spacecraft. (The One-Instrument Taurus option shows the recommended baseline mission schedule.) Although the schedule has not been further divided into milestones, testbed development, and hardware deliveries, it is sufficient at this resolution to provide insight into the development, providing additional margin to ensure adequate time for the critical path. Some compression would be possible in a more detailed schedule.

D.4 Summary

There are several potential concepts for the FSS mission, defined primarily by the trajectory and instrument payload options. The trajectories determine the length of overlap with the IHS mission (1.2 to 2.2 years), the minimum solar range (0.8 to 0.85 AU), and the ultimate destination (fixed at 120° or drifting from 60° to 180°). All of these options require interplanetary trajectories and long mission durations that drive the ultimate cost of the mission. The instrument suite is the second principal driver, contributing nearly as much to the development effort as the flight system. Four payload options were considered that range from a simple magnetograph to an instrument suite of the magnetograph,

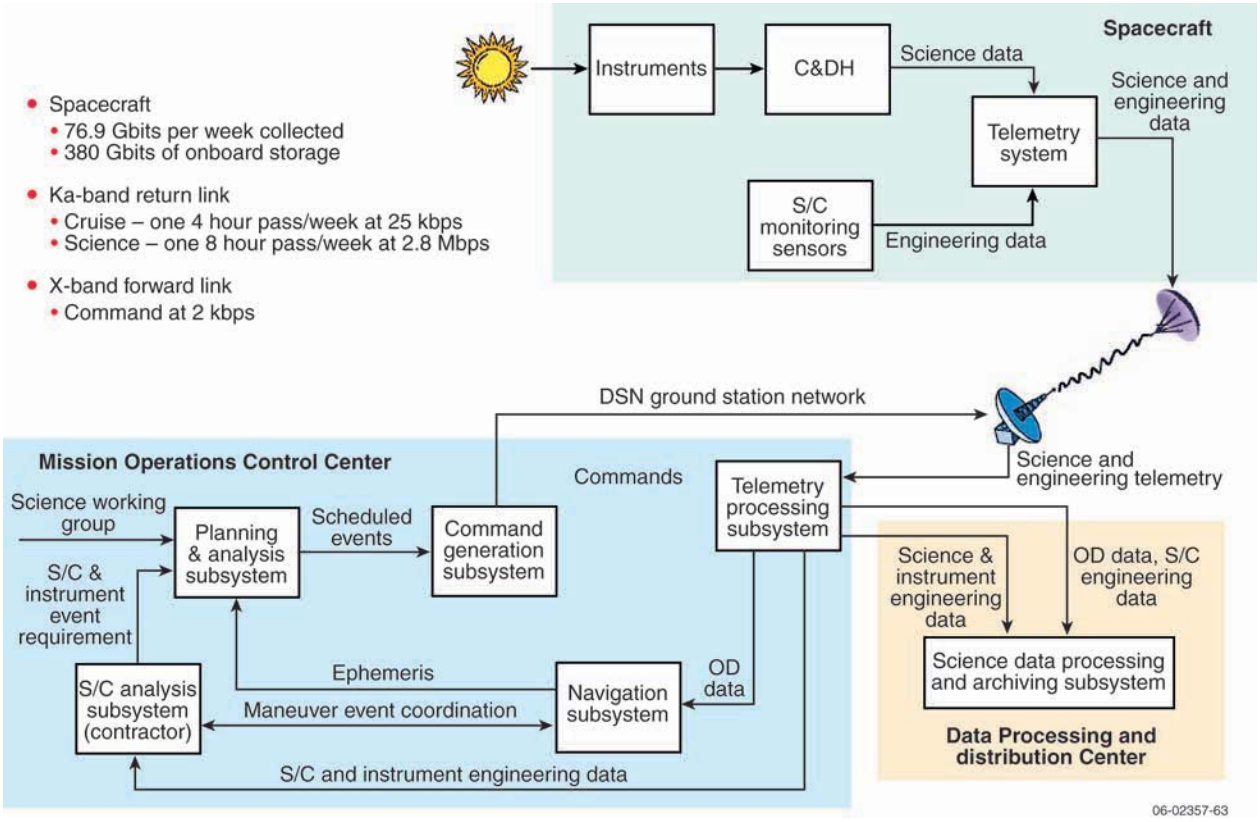

Figure D-10. Ground systems block diagram.

Table D-19. Schedule overview.

Schedule	Six-Instrument Taurus Option	One-Instrument Taurus Option
Phase A	7 months	7 months
Phase B	12 months	11 months
Phase C/D	41 months	36 months
Phase E: cruise	18 months	11 months
Phase E: operations	24 months	24 months
Phase E: data analysis	12 months	12 months

coronagraphs, and a package of in situ instruments. Independently from these payload options, data rate was considered as a secondary design driver. Data rates ranging from 37 to 500 kbps can be accommodated across all of the mission concepts, despite slight increases in mass and power.

In parallel, three concepts were studied to support the mission trade space. These options included two complete instrument payloads, differentiated by their trajectories and launch vehicles (Delta II versus Taurus). The third concept emphasized a minimum cost option of a single instrument payload (using a suboptimal trajectory and Taurus launch vehicle). Of these point designs, the Six-Instrument Taurus Option was presented in this report. It is a 3-axis stabilized, redundant flight system. A small propulsion system is required for 85 m/s of ΔV. The telecom system includes a 1.25-m high gain antenna for an X-band uplink and Ka-band downlink that communicates at a rate of 2.8 Mbps (given a continuous science collection data rate of 115.6 kbps). The attitude control system is tightly coupled with guide telescope instrument to provide the precise pointing required by the payload. The pointing control and stability is achieved through a warm-gas thruster system that is equivalent to but less complex than reaction wheels. As a comparison to this option, the key parameters for the One-Instrument Taurus Option were also presented, and additional information is available upon request.

Acknowledgments. Many team members greatly contributed to this effort, including the design and analysis of the payload options, trajectories, mission trade space, and validated point designs. The team members include Jim Chase (study lead), Janine Daughters and Luke Dubord (systems), Chen-wan Yen (mission design), Xiaoyan Zhou, Neil Murphy, Joe Davila, and Adam Szabo (payload), Jerry Flores (configuration), Bob Gustavson (ground systems), Mike Fong (cost), Juan Ayon (oversight), Ed Mettler (ACS), Vince Randolph (C&DH), Sal Distefano (power), Dick Cowley (propulsion), Yu-wen Tung (software), Gerhard Klose (structure), Dave Hansen (telecom), and Bob Miyake (thermal).

This research was funded by the NASA Living with a Star Program Office. It was carried out at the Jet Propulsion Laboratory, California Institute of Technology, under a contract with the National Aeronautics and Space Administration. Reference herein to any specific commercial product, process, or service by trade name, trademark, manufacturer, or otherwise, does not constitute or imply its endorsement by the United States Government or the Jet Propulsion Laboratory, California Institute of Technology.

Appendix E: Engineering Implementation of the Near-Earth Sentinel Payload

The role of the Near-Earth Sentinel (NES) is (1) to characterize the coronal source regions of solar energetic particles (SEPs) and coronal mass ejections (CMEs) and (2) to relate in-situ measurements by the Inner Heliospheric Sentinels (IHS) to the large-scale density structures in the inner heliosphere. NES measurements, when combined with the in-situ measurements by the IHS near 0.25 AU, will provide the information needed to guide the development of new, physics-based models of SEP acceleration and CME initiation. By tailoring the theoretical models to specific events and structures that are observed with remote-sensing and in-situ instrumentation, significant progress can be made in the development of a predictive capability for SEPs. Fully developed models would then be able to use the NES measurements close to the Sun to predict SEP, CME, and solar wind properties measured at the IHS spacecraft and beyond.

NES ultraviolet measurements of spectral line intensities and profiles will be used to determine thermal and non-Maxwellian velocity distributions, densities, and bulk flow velocities for ions and electrons in the extended corona (out to ~10 R_S). Polarized white-light brightness measurements will be used to determine electron densities and velocities of structures in the inner heliosphere (out to 60 R_S). The latter observations will include the inner portions of the IHS orbits and thereby provide a global context for the in-situ measurements of transients as they evolve during their passage through the inner heliosphere.

Combined UV spectroscopy and white-light polarimetry will provide information on SEP source regions, e.g., CME shocks and flare/CME current sheets. In the case of CME shocks, NES observations will be used to determine shock structure, speed, compression ratio, and angle. For flare/CME current sheets, NES observations will be used to determine the current sheet thickness, plasma density, temperature, ion distribution functions, plasma composition, and ion charge states and to estimate magnetic and electric field strengths, helicity, and reconnection rates.

E.1 Mission Summary

Ideally the remote-sensing NES spacecraft should fly in concert with IHS. The start of the primary science phase for NES should overlap as much as possible with the IHS primary mission. The optimal combined observational time period is near solar maximum when the rate of flare/CME events is at its maximum value. The baseline mission will use a launch vehicle capable of placing NES into a 650-km-altitude, Sun-synchronous orbit that provides a nearly continuous observation period without Earth eclipses while avoiding the additional cost associated with a geostationary or L1 mission. The NES spacecraft should be designed for a mission life comparable to that of the primary IHS mission (3 years).

The NES design is very similar to recent solar remote-sensing missions. Hence specific spacecraft bus (SCB) options were not studied in detail. The focus was placed on instrument feasibility studies aimed at extending UV spectroscopic coronagraph and white-light coronagraph capabilities. A Smithsonian Astrophysical Observatory (SAO) team studied improvements to a UV spectroscopic coronagraph, while a Naval Research Laboratory (NRL) team investigated white-light coronagraph implementations. The results of these engineering studies are summarized below.

E.2 Near-Earth Sentinel Baseline Payload

The NES baseline payload consists of a UV Spectroscopic Coronagraph (UVSC), a Wide- and Inner-Field Coronagraph (WIFCO), a Guide Telescope (GT), a Deployable Boom Assembly (DBA), and Instrument Remote Electronics (IRE). The instrument complement can work as individual instruments or as a suite of instruments controlled by a common data processing/instrument controller in the IRE. Details of the NES instrument complement are given in **Table E-1**.

E.2.1 Ultraviolet Spectroscopic Coronagraph (UVSC). The requirement on UVSC is to describe and characterize CMEs, including CME shocks and current sheets, which are believed to be the source regions of solar energetic particles. The instrument is required to have a high enough cadence to describe the evolution of fast CME events. For detailed studies of CMEs, flare/CME current sheets, corona streamers and polar plumes, its spa-

tial resolution should be at least 5 arcsec. Also, UVSC should have a high enough spectral resolution to determine proton and minor ion velocity distributions (thermal and non-Maxwellian). Doppler shifts would also be used to determine bulk velocities along the line of sight. Determination of elemental abundances and charge states of ions in coronal plasmas would be used to identify the origin of particles detected in situ with the IHS spacecraft. In addition, UVSC should be capable of measuring coronal electron temperatures, including departures from a Maxwellian velocity distribution. When combined with white-light density measurements, UVSC observations would be used to determine bulk outflow velocities with the Doppler dimming/pumping technique.

The SAO team determined that a large-aperture, high-sensitivity coronagraph with a filed of view (FOV) that extends from 1.2 to 10 R_s and has an external linear occulter at the end of a 13-m boom can provide the required resolution and cadence. This instrument will have up to 2 orders of magnitude higher sensitivity and a wider spectral range than UVCS on SOHO. This improved performance will allow the determination of line profiles for atoms and ions of many different charge-to-mass ratios, including helium, the most dominant species after hydrogen. The instrument's large aperture and superior stray light suppression permit observations of coronal structure and SEP source regions as close as 1.2 R_S from Sun-center, which is significantly closer to the disk than earlier space-based coronagraphs have been able to achieve. This is particularly important for characterizing CMEs and their associated current sheets right after their formation close to the coronal base. A possible design for UVSC is shown on **Figure E-1**. The overall mass of the instrument, including electronics, is estimated as 265 kg (with 20% margin and 20% reserve). The instrument requires about 135 W average operational power. The technical characteristics for UVSC are provided in column 2, **Table E-1**.

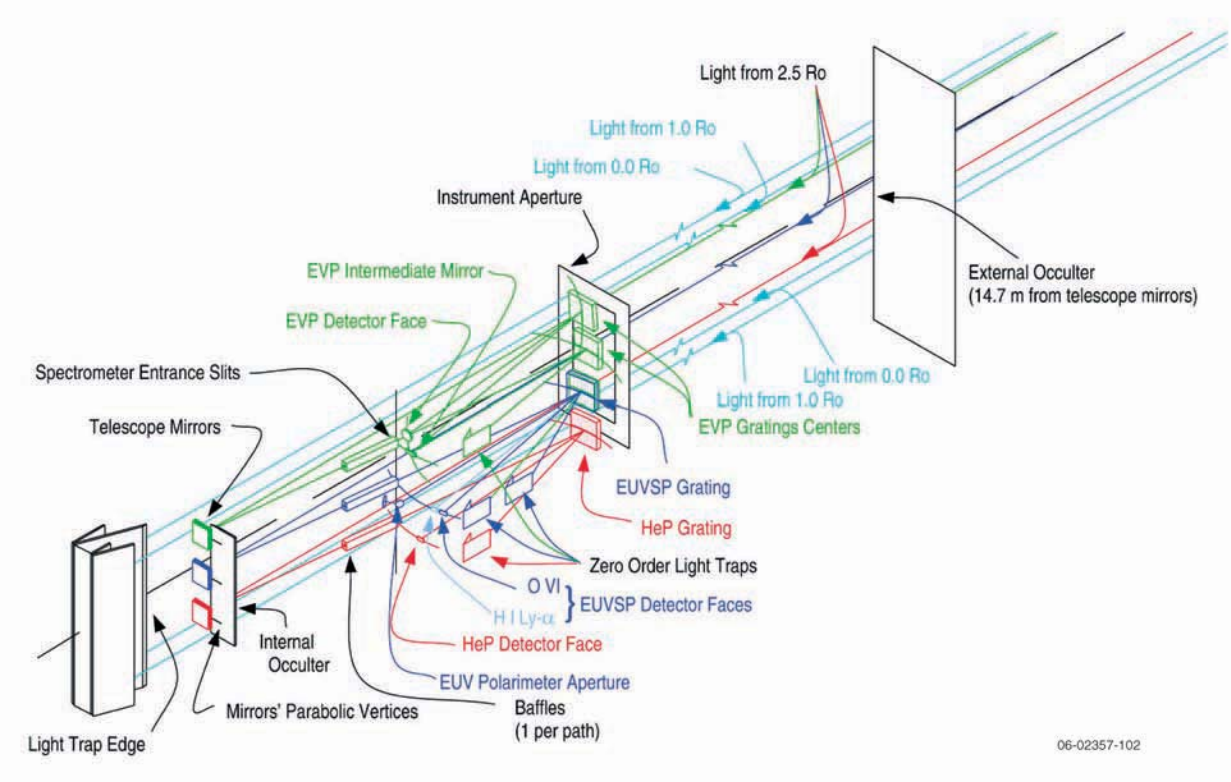

Figure E-1. Ultraviolet Spectroscopic Coronagraph Concept. UVSC has three optical paths, each with an internally occulted telescope mirror, spectrometer entrance slit, grating(s), and a detector. The paths are optimized for measurements of (1) He II 30.4 nm, (2) H I Lyα/OVI 103 nm, and (3) electron scattered H I Lyα. Note that the distance to the external occulter is not shown to scale.

Table E-1. NES instrument characteristics and technical requirements

Parameter/Characteristics	UVSC (Instrument 1)	VLC (Instrument 2)	IFC (Instrument 3)	WFC (Instrument 4)	3 IREs	Comments
Allowable Physical Interfaces						
Unit (launch) volume	230 × 90 × 70 mm	220 × 40 × 110 mm	800 × 470 × 295 mm	800 × 470 × 295 mm	0.35 × 0.35 × 0.35 m enclosure w/cabling (each IRE)	Physical envelopes are based on preliminary launch fairing analyses and are applicable to instrument launch configurations. X axis is the Sun-pointing axis. Electronics volume shown is for a single instrument.
Alignment requirements	Instruments 1, 2 and 3 must have definitive aperture planes and be capable of being coaligned w.r.t. other instrument units, the GT, and the deployable boom (if applicable).				N/A	
Sensor unit (operational)	All instrument deployable cover hardware must reside behind Instrument aperture plane when fully-deployed.				N/A	
Instrument Mech. Interfaces						
Interface mount	Flat-panel hard mount	Flat-panel hard mount	Flat-panel hard mount	Flat-panel hard mount	N/A	Instrument interface, deployable boom, and guide telescope mounts shown are for single instrument mounting.
Boresight w.r.t. SCB roll axis	0°	0°	0°	0°	N/A	
Clear field of view (FOV)	2.5 R_S(Y) × (1.1–10) R_S(Z)	2.5 R_S(Y) × (1.1–10) R_S(Z); (1.1–5.0) R_S (outside UVSC FOV)	1.3-4 R_S	5-60 R_S	N/A	
Deployable boom	4-point hard mount	4-point hard mount	None	None	None	
Guide telescope	If applicable, two 2-point hard mounts (approx. 0.75 m apart)	If applicable, two 2-point hard mounts (approx. 0.75 m apart)	None	None	None	
Instrument Elec. Interfaces						
Command/housekeeping data	See IRE	See IRE	See IRE	See IRE	MIL-STD-1553 bus for each IRE	Power and data interfaces shown are for single instruments.
Science data	See IRE	See IRE	See IRE	See IRE	16-bit parallel bus for each IRE	
Power	See IRE	See IRE	See IRE	See IRE	Reg & Unreg 28-V DC power busses per IRE	
Allowable Mass						
Sensor unit	265 kg	105 kg	20 kg	12.7 kg	N/A	Best estimate plus 20% margin and 20% reserve.
Electronics unit	N/A	N/A	2 kg	2 kg	25 kg per IRE	
Allowable Power						
Average (operational)	135	45	45	45	20 W per IRE	Best estimate plus 20% margin and 20% reserve. The nonop heater power values do not include reserve and margin.
Nonoperational (survival)	85	27	19	19	10 W per IRE	
Imaging Requirements						
FOV	2.5 R_S × (1.2–10) R_S	2.5 R_S × (1.2–10) R_S; (1.2–5.0) R_S (outside UVSC FOV)	1.3-4 Rs	5-60 Rs	N/A	The UVSC instrument requires spacecraft roll maneuvers around the spacecraft–Sun line for pointing.
Spatial resolution element	5.0 × 5.0 arcsec	5.0 × 5.0 arcsec	3.75 arcsec	28 arcsec	N/A	
Pointing Performance						
Absolute pointing (pitch/yaw)	1 arcmin	1 arcmin	50 arcsec	50 arcsec	N/A	
Knowledge (pitch/yaw)	30 arcsec	30 arcsec	30 arcsec	30 arcsec	N/A	
Stability (pitch/yaw over 50 min.)	1.5 arcsec	1.5 arcsec	4 arcsec	4 arcsec	N/A	
Drift (pitch/yaw over 24 h)	10 arcsec	10 arcsec	N/A	N/A	N/A	
Absolute pointing (roll)	40 arcmin	40 arcmin	40 arcmin	40 arcmin	N/A	
Knowledge (roll)	20 arcmin	20 arcmin	20 arcmin	20 arcmin	N/A	
Stability (roll over 50 min)	2 arcmin	2 arcmin	N/A	N/A	N/A	
Drift (roll over 24 h)	12 arcmin	12 arcmin	N/A	N/A	N/A	
Occulting Performance						
Absolute occulting (pitch/yaw)	20 arcsec	20 arcsec	50 arcsec	50 arcsec	N/A	The occulting performance numbers shown here are the total requirements which are allocated among the instruments, the deployable boom, and the SCB. The SCB provides roll and offset pointing maneuvers and achieves stability 30 s after maneuver is completed. Absolute roll pointing is determined by spacecraft roll pointing.
Knowledge (pitch/yaw)	10 arcsec	10 arcsec	30 arcsec	30 arcsec	N/A	
Stability (pitch/yaw over 24 h)	5 arcsec	5 arcsec	4 arcsec	4 arcsec	N/A	
Absolute occulting (roll)	N/A	N/A	40 arcmin	40 arcmin	N/A	
Knowledge (roll)	N/A	N/A	20 arcmin	20 arcmin	N/A	
Stability (roll over 24 h)	N/A	N/A	N/A	N/A	N/A	
Thermal						
Operating temperature range	10 to 30°C	10 to 30°C	10 to 30°C	10 to 30°C	0 to 40°C	The SCB/Instrument thermal interface assumes a highly isolated design in which radiative and conductive coupling are minimized.
Standby temperature range	10 to 30°C	10 to 30°C	10 to 30°C	10 to 30°C	0 to 40°C	
Survival temperature range	0 to 40°C	0 to 40°C	0 to 40°C	0 to 40°C	–10 to 50°C	
Data Rates						
Housekeeping	3.00×10^3 bps	2.00×10^3 bps	2.00×10^3 bps	2.00×10^3 bps	N/A	
High-speed science data	5.60×10^6 bps	8.00×10^6 bps	1×10^6 bps	1×10^6 bps	N/A	
Average data rate	1.60×10^6 bps	5.40×10^6 bps	2.30×10^5 bps	2.30×10^5 bps	N/A	

UVSC = Ultraviolet Spectroscopic Coronagraph; VLC = Visible Light Coronagraph; IFC = Inner Field Coronagraph; WFC = Wide Field Coronagraph; IRE= Instrument Remote Electronics; SCB = Spacecraft Bus

E.2.2 Wide- and Inner-Field Coronagraph (WIFCO). WIFCO consists of a Wide Field Coronagraph (WFC) and an Inner Field Coronagraph (IFC) combination. As noted below, there is an option to replace the IFC with a more capable large-aperture visible light coronagraph (VLC).

Wide Field Coronagraph (WFC). The Sentinels science objectives require concurrent in-situ and remote observations of the same heliospheric structures. WFC should be able to image shocks and CMEs to heliocentric distances of ~60 R_S (~0.3 AU), which overlaps a portion of the IHS orbits (perihelion of ~0.25 AU). The temporal resolution should be sufficient to track the evolution of shocks and fast CMEs associated with the acceleration of SEPs. The fastest of the 10,000 CMEs recorded by LASCO had a speed of 3200 km/s, on November 10, 2004; the second-fastest traveled at 2800 km/s; and 36 CMEs have had speeds above 2000 km/s. Since the maximum proper motion of a 2000 km/s CME is 1 R_S in 5.8 min, these structures would be well recorded with WFC cadences of 2 min inside 6 R_S, 10 min inside 12 R_S, and 20 min from 12 to 60 R_S.

Image quality can be expressed in terms of exposure, spatial resolution, exposure time, and masking of coronal structure by energetic particles during radiation storms. Exposure sufficient to detect CMEs and shocks in the outer field of view can be estimated by scaling from LASCO/C3, which detects shocks to about 25 R_S. The required exposure, where both signal and background profiles are taken into account, is about 12 times that achieved in 19 s with LASCO/C3. Spatial resolution required to detect CME and shock structures is ideally about 30 arcsec per pixel, where spatial resolution is dominiated by detector pixelation; but it could be as high as about 100 arcsec, since the structures are relatively broad. Exposure time short enough to avoid image smear beyond about 30 arcsec for fast CMEs and shocks is about 10.8 s. Energetic particles incident on the WFC image detector can mask CME and shock data during SEP events. The radiation storm of 22 November 2001, associated with a flare and halo CME, was the sixth-ranked proton storm from 1976 to 2003, and had a peak >10 MeV proton flux equal to 0.44 of the largest storm in the 27-year period. The corresponding peak masked pixel fraction for the LASCO CCD was 0.8 with a 19-s exposure time, 22-s read time, and 21 × 21 µm pixels. Good WFC imagery can be maintained during the worst storms with multiple short 3-s exposures (peak masked fraction ~0.1; 13.5 × 13.5 µm pixel), obtained within the image blur time, that are efficiently scrubbed onboard for energetic particles before summing to a single final image.

A WFC instrument concept (**Figure E-2**) was developed by an NRL team consistent with the above requirements by scaling from the 33 R_S half FOV SOHO/LASCO/C3 to 60 R_S. A larger 21-mm diameter entrance aperture, A1, was chosen to increase light-gathering power by nearly a factor of 6, partially satisfying the exposure requirement, while image summing was introduced to both satisfy the remaining exposure requirement and accomplish the energetic particle scrubbing. A single 3-s exposure will be adequate to 25 R_S Five 3-s exposures summed onboard will be adequate for 60 R_S.

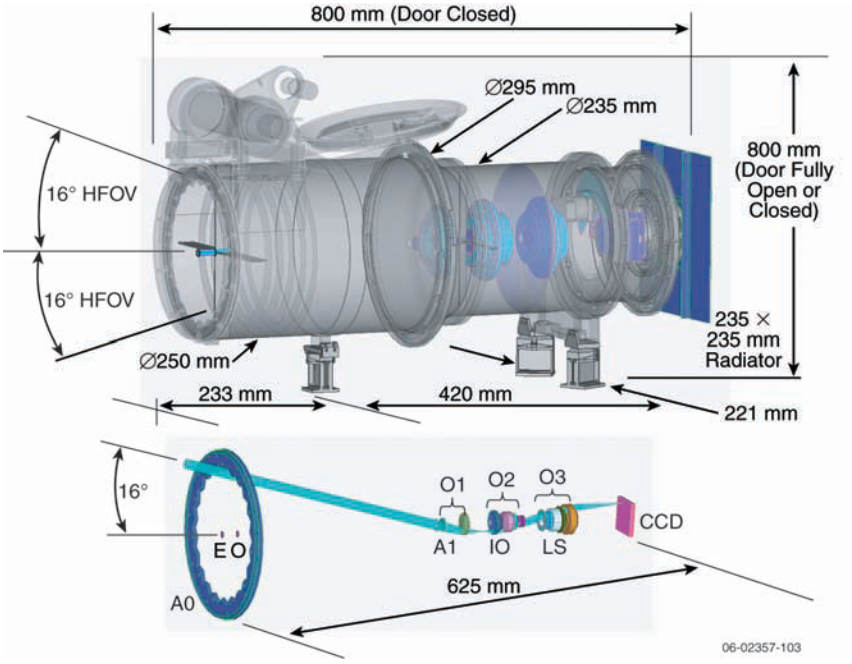

Figure E-2. Wide Field Coronagraph (WFC) concept showing the envelope and optical layout. EO = external occulter; A0 = first aperture; A1 = entrance aperture; LS = Lyot stop; CCD = charge couple device; O1, O2, and O3 = lens subassemblies 1, 2, and 3.

ZEMAX ray trace analysis was performed to define the optical train and its image performance. Instrumental stray light over the field of view would be comparable to LASCO/C3. A polarization analysis capability is recommended to improve knowledge of the three-dimensional distribution of the CMEs and shocks with respect to the IHS.

The CCD image reading, scrubbing, and summing are assumed to take place in a camera electronics box (CEB) located near the detector. All other mechanisms, as well as thermal control, are assumed to be located in a common instrument processing unit. The WFC technical characteristics are provided in column 5, **Table E-1**.

Inner Field Coronagraph (IFC). Rather than requiring WFC to observe coronal structure down to the lower corona, the separate IFC is suggested to cover the range from ~1.3 to 4 R_S The IFC is a high spatial and temporal resolution instrument that records the onset, structure, and initial acceleration of CMEs and possibly shocks in SEP source regions low in the corona and near the solar limb. It has a Sun-centered circular field of view that should, at its inner limit, approach the solar limb to capture events that are out of the plane of the sky. The spatial resolution should be better than 10 arcsec to detect CME substructure. The timing of CME onset should be accurate to about 1 min in order to relate the coronagraphic observations with SEP timing analysis using IHS data. The acceleration and velocity of the fastest CMEs should be observable, since these are associated with shocks and SEP acceleration.

A classical Lyot coronagraph will detect the required CME and shock density signatures in the electron, or K-corona, with a simple and compact instrument operating with a broad passband in the visible region of the spectrum where the K-corona signal peaks. Internal occultation is required to achieve high spatial resolution near the inner field limit (~1.3 R_S). With a compact instrument, this type of occultation limits the outer field cutoff to about 4 R_S due to the scatter of solar disk light by the objective into the coronal image.

The flight-qualified STEREO/SECCHI/COR1[1] is typical of a coronagraph that could be built and operated to satisfy the NES requirements. **Figure E-3** is a conceptual design of this instrument. The coronagraph uses a polarization analyzer to enhance the contrast of the polarized K-corona Thomson scattered photospheric photon signal in the presence of the unpolarized scene F-corona and instrumental backgrounds. The exposure time is short enough that fast CME image smear and energetic particle masking of the image at the CCD are minimal. We use a nominal value of 2000 km/s for a "fast" CME. CMEs with velocity above 2000 km/s are observable with some small image degradation. Approximately eight images of a fast CME can be used to determine velocity and acceleration before it passes beyond the outer 4-R_S FOV cutoff. The instrument technical characteristics for IFC, as determined by the NRL team, are provided in column 4, **Table E-1**.

[1]Thompson, W. T., et al., COR1 inner coronagraph for STEREO-SECCHI, in: *Innovative Telescopes and Instrumentation for Solar Astronphysics*, SPIE Proceedings Vol. 4853, eds. S. L. Keil and S. V. Avakyan, p.1, SPIE, Bellingham, WA, 2003.

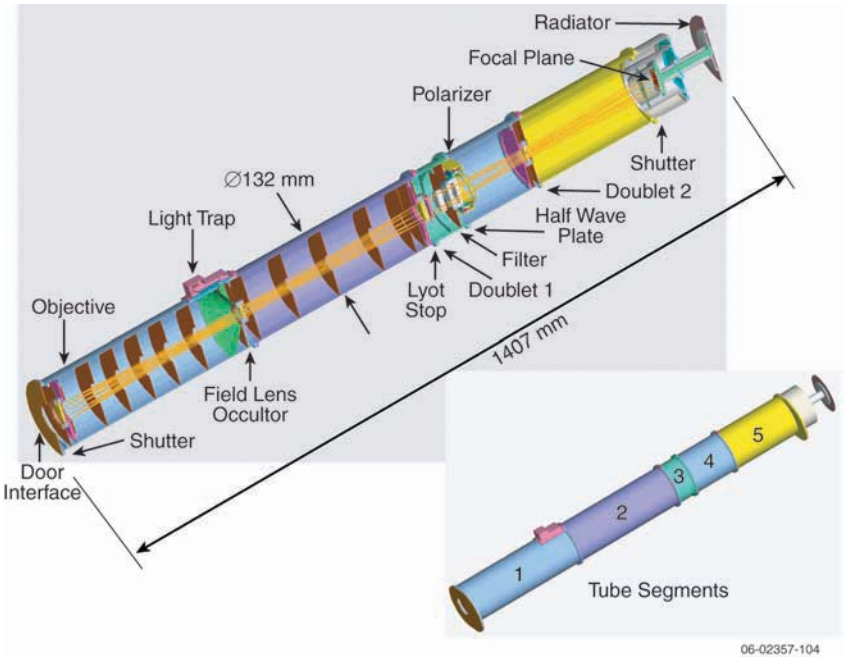

Figure E-3. Inner Field Coronagraph (IFC) concept. The section view of the IFC reveals the standard Lyot design beginning with the 36-mm diameter objective lens, which is followed by the internal occulter, field lens, Lyot stop, bandpass filter, polarization analyzer, transfer lens, shutter, CCD detector and CCD radiator.

Optionally, a more capable large-aperture coronagraph that takes advantage of the UVSC occulting boom could be used instead of the IFC. The Visible Light Coronagraph (VLC), studied by the SAO team, is a large-aperture, broadband visible light coronagraph that will provide a time series of polarized brightness images of the corona from 1.2 to 10 R_S. These data are used to provide high-spatial-resolution (5 arcsec) and high-temporal-resolution (10-s cadence) maps of the electron density distribution in coronal holes, streamers, and CMEs. The externally occulted VLC has superior stray light suppression and a spatial resolution in the radial direction (inside of 2 R_s) that is an order of magnitude better than any previously flown coronagraph. The external occulter supported by a 13-m boom allows the optical system to resolve structures such as the tops of CME flux ropes with "eclipse-like" clarity. The VLC would provide information on the coronal density structure and bulk flows that could be used with spectroscopic data provided by the UVSC to characterize CME, SEP, and solar wind source regions. The high time cadence is required for detailed studies of CME evolution and would be used to investigate the wave propagation of density perturbations in coronal structures. Technical specifications of this instrument are given in column 3 of **Table E-1**.

E.2.3 Guide Telescope (GT). The GT provides error signals to the spacecraft attitude control system (ACS) for maintaining the overall required pointing control. Its design is based on the guide telescope used for the STEREO mission. It provides 5-arcsec absolute accuracy and knowledge and, when combined with the spacecraft attitude control system, provides a 1-arcsec (3σ) pitch/yaw and 5 arcmin (3σ) roll stability. It is to be mounted on one of the instrument structures to ensure precise alignment and control. The required GT characteristics are provided in **Table E-2**.

E.2.4 Deployable Boom Assembly (DBA). The DBA has a 13-m boom with an external occulter system used by the UVSC. At launch the DBA is in a compact retracted configuration but is deployed by the spacecraft bus shortly after launch and remains deployed for the duration of the mission. It carries a linear occulter for UVSC. If a VLC were used in place of the IFC, the boom would also carry a circular occulter. These remote external occulters create an artificial eclipse with an umbra large enough to accommodate the telescope primary mirror while subtending a small enough solid angle to allow observations at 1.2 R_S from the Sun center. The small angular spread of diffracted light from the external occulter also results in exceptional stray light suppression. The WFC and IFC will be co-aligned to the UVSC but do not require the boom. The physical properties, dynamic characteristics, and positional stability requirements are listed in **Table E-3**.

Table E-2. Guide Telescope (GT)—fine-pointing sensor.

GT Parameter/Characteristics	Value	SCB Provisions/Comments
Physical/Resource Properties		
Volume	2.00 × 0.3 × 0.3 m	Mass does not include thermal control materials or associated cabling (SCB provided).
Field of view	2° × 2°	
Mass	3.5 kg	
Power	5 W	
Sensing Performance		
Absolute accuracy	5 arcsec	The GT sensing performance shown here has to be combined with the SCB pointing performance to determine the overall absolute pointing performance.
Knowledge	5 arcsec	
Bias magnitude	30 ± 3 arcsec	
Bias drift	±1 arcsec/month	

Note: SCB = Spacecraft Bus.

Table E-3. Deployable boom assembly (DBA) (SCB = Spacecraft Bus).

DBA Parameter/Characteristics	Value	SCB Provisions/Comments
Physical/Resource Properties		
Volume (stowed)	1.3 × 0.5 × 0.5 m	Cannister has circular cross-section of about 0.5 m diameter.
Mast cross-section	12 × 12 in. (17-in. diagonal)	
Mass	37 kg	
Length	13 m	
Tip mass (maximum at mast end)	5 kg	
Power (deployment)	30 W continuous, 60 W peak	
Dynamic Characteristics		
Deployment rate	< 0.5 in./s	
Structural frequency (stowed)	> 35 Hz	
Structural frequency (deployed)	1.1 Hz	
Design life	280 cycles	
Tip Positional Stability		
Pitch/yaw (long-term)	2 arcmin	
Roll (long-term)	4 arcmin	
Pitch/Yaw (50 min)	20 arcsec	
Roll (50min)	3 arcmin	

Note: SCB = Spacecraft Bus.

APPENDIX F: ACRONYMS AND ABBREVIATIONS

ACE	Advanced Composition Explorer
ACS	Attitude Control System
AIA	Atmosphere Imaging Assembly on SDO
APL	The Johns Hopkins University Applied Physics Laboratory
ATST	Advanced Technology Solar Telescope
AU	Astronomical Unit
BAPTA	Bearing and Power Transfer Assembly
bps	Bits per Second
BWG	Beam Waveguide
C&DH	Command and Data Handling
C_3	Maximum Required Launch Energy
CCD	Charge-Coupled Device
CCSDS	Consultative Committee for Space Data Systems
CPU	Central Processing Unit
CFDP	CCSDS File Delivery Protocol
CIR	Co-rotating Interaction Region
CISM	Center for Integrated Space Weather Modeling
CM	Center of Mass
CME	Coronal Mass Ejection
CMMI	Capability Maturity Model Integration
CP	Center of Pressure
CZT	Cadmium-Zinc-Telluride
DC	Direct Current
DDOR	Delta-Differential One-way Ranging
DOD	Depth of Discharge
DPM	Despun Platform Multiplexer
DPU	Data Processing Unit
DSAD	Digital Solar Aspect Detector
DSN	Deep Space Network
EIT	Extreme Ultraviolet Imaging Telescope on SOHO
ELV	Expendable Launch Vehicle
EMC	Electromagnetic Cleanliness
EPI	Energetic Electron and Proton Instrument
ESA	European Space Agency
EUV	Extreme Ultraviolet
FASR	Frequency-Agile Solar Radiotelescope
FAST	Fast Auroral Snapshot Explorer
FIP	First Ionization Potential
FOV	Field of View
FPGA	Field-Programmable Gate Array
FPI	Fabry-Perot Interferometer
FSM	Farside Sentinel Magnetograph
FSS	Farside Sentinel
FSW	Flight Software
FUV	Far Ultraviolet
G&C	Guidance and Control
GLE	Ground Level Event
GOES	Geostationary Operational Environmental Satellite
GRS	Gamma-Ray Spectrometer
GSFC	NASA Goddard Space Flight Center
HICA	High-Energy Ion Composition Analyzer
HGA	High-Gain Antenna

HPF	High Pass Filter
ICME	Interplanetary Coronal Mass Ejection
IDPU	Instrument Data Processing Unit
IEM	Integrated Electronics Module
IFC	Inner-Field Coronagraph
IHS	Inner Heliospheric Sentinel
IMF	Interplanetary Magnetic Field
IMP	Interplanetary Monitoring Platform
IMU	Inertial Measurement Unit
ISEE	International Sun–Earth Explorer
IST	Interdisciplinary Science Team
JHU/APL	The Johns Hopkins University Applied Physics Laboratory
JPL	Jet Propulsion Laboratory
kbps	Kilobits per Second
KSC	Kennedy Space Center
LASCO	Large Angle and Spectrometric Coronagraph on SOHO
LGA	Low-Gain Antenna
LICA	Low-Energy Ion Composition Analyzer
LV	Launch Vehicle
LVPS	Low Voltage Power Supply
LWS	Living With a Star
MAG	Magnetometer
MC	Magnetic Cloud
MCM	Multi-Chip Module
MESSENGER	MErcury Surface, Space ENvironment, GEochemistry, and Ranging
MGA	Medium-Gain Antenna
MHD	Magnetohydrodynamics
MIPS	Millions of Instructions per Second
MLI	Multilayer Insulation
MOF	Magneto-Optical Filter
MOI	Moment of Inertia
MURI	Multidisciplinary University Research Initiative
MWA-LFD	Mileura Widefield Array—Low Frequency Demonstrator
N/A	Not Applicable
NASA	National Aeronautics and Space Administration
NES	Near-Earth Sentinel
NOAA	National Oceanic and Atmospheric Administration
NS	Neutron Spectrometer
OCXO	Oven Controlled Crystal Oscillator
OSO	Orbiting Solar Observatory
OSR	Optical Solar Reflector
PDU	Power Distribution Unit
PI	Principal Investigator
PPT	Peak Power Tracking
PSE	Power System Electronics
Q/A	Charge-to-Mass
QTN	Quasi-Thermal Noise
RF	Radio Frequency
RHESSI	Reuven Ramaty High Energy Solar Spectroscopic Imager
rpm	Revolutions per Minute
R_S	Solar Radius
RX	Receiver
S/C	Spacecraft
S/N	Signal-to-Noise Ratio

SAMPEX	Solar Anomalous and Magnetospheric Particle Explorer
SCB	Spacecraft Bus
SCM	Search Coil Magnetometer
SDO	Solar Dynamics Observatory
SDRAM	Synchronous Dynamic Random Access Memory
SEP	Solar Energetic Particle
SEPQ	Solar Energetic Particle Composition and Charge State Analyzer
SMM	Solar Maximum Mission
SOHO	Solar and Heliospheric Observatory
Solwind	White-Light Coronagraph on Air Force Satellite P78-1 (1979–1985)
SPE	Solar Particle Event
SSD	Silicon Semiconductor Detector
SSR	Solid-State Recorder
STDT	Science and Technology Definition Team
STEREO	Solar-TErrestrial RElations Observatory
STM	Systems Trade Model
SWComp	Solar Wind Composition Analyzer
SWE	Solar Wind Electron Analyzer
SWI	Solar Wind Ion Analyzer
STE	Suprathermal Electron Instrument
TCM	Trajectory Correction Maneuver
TOF	Time of Flight
TRACE	Transition Region and Coronal Explorer
TR&T	Targeted Research and Technology
TSS	Thermal Synthesizer Model
TWTA	Traveling Wave Tube Amplifier
TX	Transmitter
USN	Universal Space Network
UVCS	Ultraviolet Coronagraph Spectrometer on SOHO
UVSC	Ultraviolet Spectroscopic Coronagraph on the Near-Earth Sentinel
VGA	Venus Gravity Assist
VHP	Venus Hyperbolic Excess Velocity
VLC	Visible Light Coronagraph
VSE	Vision for Space Exploration
WAVES	Radio and Plasma Waves Instrument
WFC	Wide-Field Coronagraph
WIFCO	Wide- and Inner-Field Coronagraph
XEPF	Extended Payload Fairing
XMTR	Transmitter
XPDR	Transponder

REPORT DOCUMENTATION PAGE

Form Approved
OMB No. 0704-0188

1. REPORT DATE *(DD-MM-YYYY)*	2. REPORT TYPE	3. DATES COVERED *(From - To)*
31-08-2006	Technical Memorandum	

4. TITLE AND SUBTITLE

Solar Sentinels:
Report of the Science and Technology Definition Team

5a. CONTRACT NUMBER

5b. GRANT NUMBER

5c. PROGRAM ELEMENT NUMBER

6. AUTHOR(S)

The LWS Sentinels Science and Technology Definition Team

5d. PROJECT NUMBER

5e. TASK NUMBER

5f. WORK UNIT NUMBER

7. PERFORMING ORGANIZATION NAME(S) AND ADDRESS(ES)

Goddard Space Flight Center
Greenbelt, MD 20771

8. PERFORMING ORGANIZATION REPORT NUMBER

2006-01518-0

9. SPONSORING/MONITORING AGENCY NAME(S) AND ADDRESS(ES)

National Aeronautics and Space Administration
Washington, DC 20546-0001

10. SPONSORING/MONITOR'S ACRONYM(S)

11. SPONSORING/MONITORING REPORT NUMBER

TM-2006-214137

12. DISTRIBUTION/AVAILABILITY STATEMENT

Unclassified-Unlimited, Subject Category: 88
Report available from the NASA Center for Aerospace Information,7121 Standard Drive, Hanover, MD 21076. (301)621-0390

13. SUPPLEMENTARY NOTES

14. ABSTRACT

The goal of NASA'sLiving With a Star (LWS) program is to develop the scientific understanding necessary to effectively address those aspects of the connected Sun–Earth system that directly affect life and society. Along with the other elements of LWS, Solar Sentinels aims to discover, understand, and model the heliospheric initiation, propagation, and solar connection of those energetic phenomena that adversely affect space exploration and life and society here on Earth. The Solar Sentinels mission will address the following questions: (1) How, where, and under what circumstances are solar energetic particles (SEPs) accelerated to high energies and how do they propagate through the heliosphere? And (2) How are solar wind structures associated with these SEPs, like CMEs, shocks, and high-speed streams, initiated, propagate, evolve, and interact in the inner heliosphere? The Sentinels STDT recommends implementing this mission in two portions, one optimized for inner heliospheric in-situ measurements and the other for solar remote observations. Sentinels will greatly enhance the overall LWS science return.

15. SUBJECT TERMS

Solar energetic particles, coronal mass ejections, interplanetary shocks, solar flares, heliospheric plasma, and magnetic fields

16. SECURITY CLASSIFICATION OF:			17. LIMITATION OF ABSTRACT	18. NUMBER OF PAGES	19b. NAME OF RESPONSIBLE PERSON
a. REPORT	b. ABSTRACT	c. THIS PAGE			Haydee M. Maldonado
Unclassified	Unclassified	Unclassified	Unclassified	176	19b. TELEPHONE NUMBER *(Include area code)* (301) 286-6762